A Ph.D. Dissertation on

Shape Memory Alloy Based Stiffening of Horizontal Axis Wind Turbine Blade for Vibration Control and Fatigue Life Enhancement

submitted by

Mohamed Sajeer M.

(156104029)

under the supervision of

Dr. Arunasis Chakraborty

DEPARTMENT OF CIVIL ENGINEERING

INDIAN INSTITUTE OF TECHNOLOGY GUWAHATI

August, 2021

Certificate

It is certified that the work contained in the dissertation entitled **"Shape Memory Alloy Based Stiffening of Horizontal Axis Wind Turbine Blade for Vibration Control and Fatigue Life Enhancement"**, by **Mohamed Sajeer M. (156104029)** for the partial fulfilment of the requirements for the award of the *Doctor of Philosophy* (*Ph.D.*) in *Civil Engineering* with the specialization in *Structural Engineering* at the *Indian Institute of Technology Guwahati, India* is an authentic work. This dissertation has been performed under my sole supervision and not submitted elsewhere to award a degree.

Dr. Arunasis Chakraborty
Associate Professor
Department of Civil Engineering
Indian Institute of Technology Guwahati
Guwahati - 781039, India

Date:

Acknowledgements

I would like to express wholesome gratitude to my research supervisor and mentor, *Dr. Arunasis Chakraborty*, for accepting me as his student. I owe him a great tribute for foreseeing my skills and for his visionary plan to uplift me. Throughout my PhD, his support, encouragement, and motivations have helped me achieve more than I thought I could. His vast insight and ample expertise have inspired me all the time of my research and daily life. It is a great honour and privilege for me to work and learn under him. Moreover, his feedbacks on my presentations and writing has helped to improve that over time. I would like to thank him for his patience, empathy, and friendship that gave me freedom and peace to complete the work in a better way.

Sincere thanks to the Doctoral Committee members, *Prof. Sudip Talukdar*, *Prof. Konjengbam Darunkumar Singh*, *Prof. Satyajit Panda* and my supervisor for their critical reviews, suggestions and encouragement, which helped me to move forward. I would like to express my special gratitude to the Faculty of Civil Engineering and the staff fraternity for an unforgettable stay at this institute. Also, the financial assistance from the Department of Civil Engineering, Indian Institute of Technology Guwahati, India, is gratefully appreciated to carry out this research.

I wish to thank my seniors, *Dr. Amit Kumar Rathi*, *Dr. Swaroop Mahato*, for motivation, insightful discussions and cooperation. I also thank my colleagues, especially *Mr. Arka Mitra*, *Mr. Sourav Das* and *Dr. Saptarshi Sarkar*, for providing the technical support, and my all friends for making the stay memorable. I wish a great future for all of my friends and colleagues.

I would also like to thank my family for their constant support and motivation; without that, it would be difficult to finish my thesis in the last few years. Especially, my father who encouraged education amid his struggles. Also, a special thanks to my elder brother, who motivated me to choose engineering and encouraged throughout the career. Last but not least, my wife, who is my backbone, supporting during all my ups and downs with tremendous understanding and motivation.

Mohamed Sajeer M.
(156104029)
Department of Civil Engineering
Indian Institute of Technology Guwahati
Guwahati - 781039, India

Date:

This thesis is dedicated to
all mentors in my career.

Abstract

The last few decades have witnessed a tremendous increase in energy demand to support global socio-economic development. The worldwide climate change and depleting fossil fuel with ever-increasing carbon footprint have forced humankind to search for the alternate green energy sources. Natural sources like sun, wind, biological process, waves etc., have become viable alternatives for power generation. Wind energy has remained a popular source among them due to its commercial viability, and the net power production in this sector has undergone a steady growth in the recent past.

The power production and efficiency of a wind farm are mostly influenced by the forces acting on the turbines, which vary considerably over different geographical regions. In this context, wind turbines are of two types depending upon their location, i.e. onshore and offshore. Onshore wind turbines are easily accessible than offshore turbines and can be readily connected directly to local power grids. The wind speed in the onshore environment generally fluctuates due to various reasons, including its geographical features. Therefore, detailed analysis (i.e. micro-siting) is necessary to select the wind farm location to ensure availability of wind throughout the year, less impact on human settlement and nearby environment. Offshore turbines, on the other hand, are more profitable in the long run compare to its onshore version due to various factors (e.g. steady flow of wind over the years, availability of vast space for large wind farms, less noise pollution to the nearby settlements). Nevertheless, the construction, installation, and grid connection cost depends on the depth of water and site distance from the shore. However, the steady and higher wind speed in the marine environment has made offshore turbines commercially attractive, with ∼50% more power generation than an onshore turbine of similar size. Although they produce more power, they are exposed to a severe environment that demands a stringent design requirement for safe and sustained operation. The turbines in marine environment experience significant structural vibrations due to the combined effects of wind and wave.

The power produced by a wind turbine is proportional to its rotor area. Thus, modern megawatt turbines have a larger rotor diameter with flexible blades that undergo significant vibration when exposed to aerodynamic loads. Due to this reason, blades suffer fatigue and need regular maintenance. Besides fatigue and other associated issues, excessive deformation of the blade in the along-wind direction can lead to collision with the tower. In general, pre-cone angles are provided along with a tilted drivetrain to address this issue. However, pre-conning the rotor and tilting of the slow-moving shaft in the drivetrain develops additional stress on the gear tooth and root of the blade that ultimately induces damage and downtime for maintenance. The problem is more intense as the aerodynamic loads acting on the blades are cyclostationary in nature. Therefore, control and health monitoring are essential components to ensure safety during its operation to protect them against vibration-induced structural and mechanical damage.

For this purpose, researchers developed different vibration control strategies for wind turbines. Most of the vibration controllers are designed to operate in either flapwise or edgewise direction independently. This motivates to develop a controller that can reduce vibration in two orthogonal directions. A single controller that enhances the performance of a blade in both these directions without influencing the aerodynamics of the airfoils is indeed in demand. Thus, the present study proposes longitudinal stiffening of blades using a tendon made of shape memory alloy. The rationale behind selecting this smart material is due to its ability to offer excellent thermo-mechanical behaviour at low strain. A discrete reduced-order model considering the dominant modes of the tower, drivetrain and blade is developed with this stiffener for response analysis. It is based on using the distributed properties of tower and blade given for National Renewable Energy Laboratory (NREL) 5 MW benchmark turbine. The mode shapes are obtained from BModes, where the tower and blades are modelled as Euler-Bernoulli cantilever beams.

The three-dimensional wind field passing through the rotor plane is simulated using TurbSim package freely available from NREL. From this field, the aerodynamic loads are computed in MATLAB® using a modified version of Blade Element Momentum (BEM) theory. These aerodynamic loads are validated

with widely used software AeroDyn. The wind turbines in the offshore environment are exposed to wave in addition to the aerodynamic loads. These wave loads are simulated using Morison's equation, where the wave time histories are generated from the Joint North Sea Wave Project (JONSWAP) spectrum considering two-dimensional wave propagation. The response of a benchmark wind turbine is simulated using these loads and validated with FAST. Further, this model is utilized to study the performance of the proposed control strategy. The non-linear material behaviour of the stiffener is modelled by combining the principles of thermodynamics with the constitutive models of SMA found in the literature (i.e. Liang-Rogers model). Thus, the super-elastic effects are utilized in semi-active mode (i.e. using Joule heating with the current flow) to apply actuation force that opposes blade deformation. An efficient switching algorithm is developed along with performance curves that enable the designer to select an optimal heating mode depending upon the operational scenario.

The numerical results presented in this thesis established the fact that different performance parameters (i.e. peak, peak-to-peak, mean, *rms* deformation of blade) are significantly reduced by the proposed stiffening strategy. Therefore, the proposed longitudinal stiffening offers an efficient solution reducing the dependence on tilt and pre-cone angle. Thus, the blade reliability against excessive deformation and subsequent collision with the tower is improved. For this purpose, a level crossing problem in the light of cyclostationary blade response is carried out using Rice formula, where the failure is modelled as a Poisson process. Sensitivity analysis is carried out to demonstrate the performance envelop of the proposed control strategy over the operational range of the benchmark 5 MW wind turbine for different diameter of the tendon.

Further, the impact of proposed stiffening strategy on fatigue life of a blade is investigated. For this purpose, a detailed spinning finite element model of the blade is developed by considering gyroscopic and Coriolis effect with respect to a non-rotating reference frame, where the displacement fields are evaluated using Hermitian shape functions. Modal analysis of the stiffened blade is carried out using this spinning finite element model, which shows significant improvement of bending stiffness. The variation of natural frequencies of the stiffened blade within its operational window (i.e. cut-in to rated rpm) are also studied using the Campbell diagram.

The impact of the proposed longitudinal stiffener on the stress profile and fatigue life of the blade are studied to show its performance under different design load cases as per IEC 61400-3. The fatigue damages at various locations is estimated using Palmgren-Miner's linear summation utilizing the cycle count obtained from the rainflow algorithm and S-N curve of Glass Fiber Reinforced Plastic (GFRP) material. Goodman diagram is used for the mean correction of stress response to obtain the allowable number of cycles from the S-N curve. The fatigue life of the blade using short-term damage under rated wind speed is improved $\sim$2 times with passive stiffener while its semi-active version shows $\sim$3 times increase. A sensitivity analysis based on peak stress and fatigue life reduction for different diameters of the tendon is also presented. Usually, wind turbines are exposed to various aerodynamic loads during their design life depend upon the environmental conditions. Hence, a long-term fatigue analysis is also carried out under different design load cases. The fatigue life of the blade with passive stiffener is improved by $\sim$60% while its semi-active version shows an increase by $\sim$13 times. Further, the damage equivalent stresses are evaluated for each design load cases. Also, the impact of the proposed stiffener on the reliability of blade against fatigue damage is studied. The numerical results obtained from this analysis highlights the performance enhancement in terms of serviceability (i.e. deformation of blades) and design against longitudinal stress, fatigue life and reliability.

List of Publications

Journal Articles:

1. S. Das, M. M. Sajeer and A. Chakraborty, Vibration control of horizontal axis offshore wind turbine blade using SMA stiffener, *Smart Materials and Structures*, 2019, 28(9), 095025. doi:10.1088/1361-665x/ab1174.

2. M. M. Sajeer, A. Mitra and A. Chakraborty, Spinning finite element analysis of longitudinally stiffened horizontal axis wind turbine blade for fatigue life enhancement, *Mechanical Systems and Signal Processing*, 2020, 145, 106924. doi:10.1016/j.ymssp.2020.106924.

3. M. M. Sajeer, A. Chakraborty and S. Das, An efficient vibration control strategy for reliability enhancement of HAWT blade, *Smart Structures and Systems*, 2020, 26(6). doi:10.12989/sss.2020.26.6.703.

4. S. Das, M. M. Sajeer, A. Chakraborty, and S. Sarkar, Shape memory alloy-based centrifugal stiffening for response reduction of horizontal axis wind turbine blade, *Structural Control and Health Monitoring*, 2020, 28(3). doi:10.1002/stc.2669.

5. M. M. Sajeer and A. Chakraborty, Long-term fatigue reliability enhancement of horizontal axis wind turbine blade. *Wind and Structures*. (*Revision Recommended*)

Related Articles:

6. M. M. Sajeer, A. Mitra and A. Chakraborty, Multi-body dynamic analysis of offshore wind turbine considering soil-structure interaction for fatigue design of monopile, *Soil Dynamics and Earthquake Engineering*, 2021, 144, p.106674. 10.1016/j.soildyn.2021.106674.

7. G. Yamini, S. Das, M. M. Sajeer and A. Chakraborty, On Optimal Tuning of Mass-Damper for Passive Vibration Control of Horizontal Axis Wind Turbine Tower. (*Manuscript Under-preparation*)

8. A. Kumar, M. M. Sajeer and A. Chakraborty, Secondary power generation from horizontal axis wind turbine blade using piezoelectric energy harvester. (*Manuscript Under-preparation*)

Contents

List of Figures

List of Tables

List of Abbreviations

1D	One Dimensional
2D	Two Dimensional
3D	Three Dimensional
ALP-STMD	Adaptive-Length Pendulum Smart Tuned Mass Damper
ATMD	Active Tuned Mass Damper
ATVA	Adaptive Tuned Vibration Absorber
ANN	Artificial Neural Networks
BEM	Blade Element Momentum
BEMT	Blade Element Momentum Theory
BVA	Ball Vibration Absorber
CCATMD	Cable Connected Active TMD
CCF	Cyclic Coherence Function
CDF	Cumulative Distribution Function
CFD	Computational Fluid Dynamics
CFRP	Carbon Fiber Reinforced Plastic
CLCD	Circular Liquid Column Damper
DBD	Dielectric Barrier Discharge
DEL	Damage-equivalent Load
DES	Damage-equivalent Stress
DOF	Degrees of Freedom
DRDM	Discrete Reduced Degrees of Freedom Model
DROM	Discrete Reduced Order Model
FE	Finite Element
FEA	Finite Element Analysis
FEM	Finite Element Method
FLAP	Force and Load Analysis Program
G-C	Graesser-Cozzarelli
GFRP	Glass Fiber Reinforced Plastic
GTR	Grow-The-Rotor

HAWT	Horizontal Axis Wind Turbine
IP	In-plane
IPCC	Intergovernmental Panel on Climate Change
JONSWAP	Joint North Sea Wave Project
LIDAR	Light Detection and Ranging
LQG	Linear Quadratic Gaussian
LQR	Linear Quadratic Regulator
MFC	Macro Fiber Composite
MR	Magnetorheological
MRE	Magnetorheological Elastomer
MCS	Monte Carlo Simulation
NREL	National Renewable Energy Laboratory
OLC	Optimal LQG Controller
OP	Out-of-plane
PI	Proportional Integral
PM	Pearson-Moskowitch
RBDO	Reliability-Based Design Optimization
RMS	Root Mean Square
RPM	Revolutions per minute
RSS	Rotationally Sampled Spectrum
SDAC	Stochastic Disturbance Accommodating Controller
SE	Super-Elastic Effect
SePCaT	Separate Pitch Control at the Tip
SFOWT	Spar-type Floating Offshore Wind Turbine
SIM	Stress-Induced Martensite
SLM	Simple Load Model
SMA	Shape Memory Alloy
SME	Shape Memory Effect
SMP	Shape Memory Polymer
STMD	Semi-active TMD
TEF	Trailing-Edge-Flap
TLCD	Tuned Liquid Column Damper
TLD	Tuned Liquid Damper
TSD	Tuned Sloshing Damper
TMD	Tuned Mass Damper
TVA	Tuned Vibration Absorber
VAWT	Vertical Axis Wind Turbine
VD	Viscous Damper

List of Symbols

a	Axial induction factor
a'	Tangential induction factor
A	Area
A_{cr}	Cross-sectional area
A_f	Austenite finish temperature of SMA
A_s	Austenite start temperature of SMA
A_{sur}	Surface area
c	Chord length
c_b^a	Aerodynamic damping of blade
c_t^a	Aerodynamic damping of tower
c_n	Constant for controlling the sharpness of transition from elastic to inelastic phase
c_p	Specific heat
c_s	Constant for controlling the slope of unloading stress path
c_T	Constant for controlling type and size of hysteresis
c_α	Constant that determines the slope of inelastic region
C	Damping matrix
C_d	Coefficient of drag force
C_l	Coefficient of lift force
C_m	Coefficients of fluid inertia force
C_n	Coefficients of normal force
C_p	Power coefficient
C_t	Coefficients of tangential force
C_T	Thrust coefficient
d	Diameter of tendon
D	Young's Modulus of SMA
D_A	Modulus of elasticity in the austenite phase of SMA
D_M	Modulus of elasticity in the martensite phase of SMA
D_p	Diameter of monopile
D_R	Diameter of rotor
D^L	Damage accumulated during design life

D^{ST}	Short-term damage accumulated during a given time history
f	Frequency
f^{eq}	Frequency of DES
f_b^{edge}	Blade edgewise frequency
f_b^{flap}	Blade flapwise frequency
$f_t^{\text{fore-aft}}$	Tower fore-aft frequency
$f_t^{\text{side-to-side}}$	Tower side-to-side frequency
f^L	Scaling factor
F_c	Centrifugal force
F_g	Gravitational force
F_L	Loss Factor
$F_{\text{loss}}^{\text{hub}}$	Hub-loss Factor
$F_{\text{loss}}^{\text{tip}}$	Tip-loss Factor
F_T	Control force in the tendon
g	Gravitational acceleration
h	Height
H	Enthalpy
h_c	Convective heat transfer coefficient
h_d	Height above ground where mean wind speed equal to zero due to obstacles
H_h	Hub height
h_o	Surface roughness length
h_r	Reference height
H_s	Wave height
H_t	Tower height
H_p	Monopile height
I_{e}	Second moment of area of the blade about edgewise axis
I_{f}	Second moment of area of the blade about flapwise axis
J_g	Generator inertia about high speed shaft
J_r	Rotational inertia of the rotor-hub about low speed shaft
K	Stiffness matrix
K_b	Thermal conductivity of a body
k_d	Equivalent torsional stiffness of drivetrain shaft
k_g	St. Venant torsional stiffness of high-speed shaft
k_r	St. Venant torsional stiffness of slow-speed shaft
L	Length
L_c	Characteristic length
l_e	Element length
L_K	Integral length scale of turbulence for Kaimal spectrum
L_M	Monin-Obukhov length

L_v	Integral length scale of turbulence for von-Karman spectrum
$m_{_T}$	Mass of the tendon
M	Mass matrix
M_b	Blade mass
M_f	Martensite finish temperature of SMA
M_p	Monopile mass
M_s	Martensite start temperature of SMA
M_t	Tower mass
M^{edge}	Bending moment in edgewise direction
M^{flap}	Bending moment in flapwise direction
n_{ji}	Rainflow cycle count during i^{th} stress reversal of j^{th} time history
N_{ji}	Number of cycle from S-N curve during i^{th} stress reversal of j^{th} time history
N_b	Number of blades
N_{Bi}	Biot number
P	Power
p_d^-	Pressure at downstream of disc actuator
p_d^+	Pressure at upstream of disc actuator
p_f	Probability of failure
P_e	Electric power
P_{in}	Peak in-plane displacement
P_{out}	Peak out-of-plane displacement
$P2P_{in}$	Peak-to-peak in-plane displacement
$P2P_{out}$	Peak-to-peak out-of-plane displacement
P_r	Rated power
P_w	Far downstream (atmospheric) pressure
P_∞	Far upstream (atmospheric) pressure
Q	Net heat transfer
Q_{gen}	Heat generated
Q_{out}	Heat emitted
$r_{_T}$	Radius of tendon
rms_{in}	RMS in-plane displacement
rms_{out}	RMS out-of-plane displacement
S_{JS}	Joint North Sea Wave Project spectrum
S_{PM}	Pearson-Moskowitch spectrum
S_u	Single sided power spectrum
T	Temperature
T_{amp}	Ambient temperature
T_d	Thrust on rotor disc
t_p	Monopile wall thickness

T_P	Peak spectral period
$\mathrm{T_w}$	Turbulence
v	Velocity
V	Voltage
$\bar{v}$	Mean velocity
v^*	Friction velocity
v_{ci}	Cut-in velocity
v_{co}	Cut-out velocity
v_d	Velocity at disc
v_r	Rated velocity
V_T	Volume of Tendon
v_w	Far wake velocity
v_∞	Far upstream velocity
α	Angle of attack
α_p	Power law exponent
$\alpha(\xi)$	Phase transformation tensor
β	Reliability index
Δh	Latent heat of transformation
ΔT	Change in temperature with respect to surrounding
η_e	Efficiency coefficient of electrical energy conversion
η_m	Efficiency coefficient of mechanical energy conversion
ϵ	Strain
ϵ_L	Maximum recoverable strain
γ_g	Gear ratio
κ	von-Karman constant
κ_u	Autocorrelation function
λ	Slope of S-N curve
λ_1, λ_2	S-N curve parameters
Λ	Phase transformation tensor
μ_{in}	Mean in-plane displacement
μ_{out}	Mean out-of-plane displacement
ω	Natural frequency
Ω	Rotational frequency
Ω_{ci}	Cut-in RPM
Ω_r	Rated RPM
ϕ	Mode shape
$\mathbf{\Phi}$	Standard normal CDF
Π_K	Kinetic energy
Π_P	Potential energy

Π_{P_0}	Potential energy of uncontrolled system
$\Pi_{K,T}$	Kinetic energy of tendon
$\Pi_{P,T}$	Potential energy of tendon
ψ	Stability function
ψ_k	Azimuth of k^{th} blade
ρ_a	Density of air
ρ_b	Density of blade material
ρ_p	Density of monopile material
ρ_r	Resistivity of SMA tendon
ρ_s	Density of SMA
ρ_w	Density of water
σ	Stress
σ^{a}	Alternating stress
σ^{ac}	Axial stress due to centrifugal force
σ^{ag}	Axial stress due to gravitational force
$\sigma^{\text{a}T}$	Axial stress due to tendon force
σ^{ea}	Equivalent alternating stress
σ^{fm}	Fixed mean stress
σ^{m}	Mean stress
σ^{u}	Ultimate stress
σ_β	Uni-axial back-stress
σ^L	Longitudinal stress
$\sigma^{\text{L}}_{\text{DE}}$	Lifetime damage-equivalent stress
$\sigma^{\text{ST}}_{\text{DE}}$	Short-term damage-equivalent stress
σ_Y	Stress threshold for phase transformation
σ_r	Solidity
σ_v	Standard deviation of velocity
θ_{f}	Fibre angle
θ_{ma}	Wind-wave misalignment angle
θ_p	Pitch angle
θ_{pt}	Combined pitch and twist angle
θ_t	Twist angle
Θ	Thermo-elastic tensor
ξ	Martensite volume fraction
ξ_A	Volume fraction at austenite state
ξ_b	Structural damping ratio of blade
ξ_M	Volume fraction at martensite state
ξ_p	Structural damping ratio of monopile
ξ_t	Structural damping ratio of tower

Chapter 1

Introduction

The requirement for electrical energy has increased manifold with the socio-economic development and the depletion of fossil fuel calls for new sources of renewable energy for power generation. There are many sources available for energy harvesting, among them solar and wind power are the most popular resources available to humankind. Offshore and onshore wind turbines are good examples of wind power generation and their importance is growing day by day. The power output from these turbines depend on the rotor area. Thus, the size of wind turbine blades keep on increasing to produce more power. With the advent of new materials, it is possible to construct bigger-sized rotors. But these structures experience significant vibration due to aerodynamic loads. Hence, proper modelling and analysis are required for safe and sustained operation of wind turbines.

Wind turbines convert inflowing wind energy (i.e. kinetic energy) into electrical energy or mechanical power [1–4]. Wind flows due to the uneven heating of the atmosphere by the Sun ray besides other atmospheric reasons [5]. The spatial variation of atmospheric heat creates the variation in atmospheric forces viz. pressure, Coriolis, inertial and frictional forces, which cause air movement. Centuries before, human civilization developed the technologies to use wind energy for different purposes like sailing, flying, and agriculture, among many others. Historical records show that wind energy was used in early 5000 B.C. for sailing boats, while simple windmills for pumping water started operation as early as 200 B.C. in China [6]. The reliance on wind energy has been increasing due to a few important factors, e.g. depletion of fossil fuel, availability of wind worldwide, and sustained research for more efficient means of power generation. Thus, wind energy is an alternative to fossil fuels, which does not produce carbon footprints or greenhouse gas during its operation and uses very little space. Intergovernmental Panel on Climate Change (IPCC) [7] forecasts an increase in mean sea level due to global warming, which directly advocates for a carbon-free alternate source of power generation. Wind energy is one of the popular carbon-neutral sources, which involves different turbines to extract energy from inflowing wind. This motivates the author of this thesis to investigate/study wind turbine for more efficient design and operation.

The kinetic energy of the wind turns the rotor connected to a slow-moving shaft. The spinning rotor turns the generator through a connecting shaft to create electricity. Wind turbines are mainly classified into two groups according to its axis of rotation [8, 9]. Turbines that rotate about its horizontal axis are called Horizontal Axis Wind Turbine (HAWT) and those rotating about the vertical axis are called Vertical Axis Wind Turbine (VAWT). HAWTs are further classified based on wind direction - upwind turbines where the rotor faces the wind first and downwind turbine having rotor at the downside of the tower. Nowadays, most of the HAWTs are designed as upwind turbines with a yaw mechanism to face the upcoming wind, and also to avoid tower shadow effect. Thus, downwind turbines often face power fluctuations due to this shadow effect.

HAWT can be designed with a different number of blades; however, a three-bladed rotor has been the optimal one. The system with less number of the blade can rotate faster for capturing the same energy produced by more blades, i.e. tip speed ratio changes with the number. Previous studies have shown that a three-bladed system has the advantage of least vibration and noise than one or two blade systems. Besides optimal tip speed ratio, the ability of pitch controller in modern HAWT allows it to operate over the maximum range of wind flow and hence, it is more efficient than VAWT [10]. On the other hand, VAWTs are smaller in size, easy to construct, transport and install. Therefore, it requires low initial and maintenance cost. Moreover, VAWT does not require a yaw mechanism and can work at low wind speed, but they also need small power to initiate rotation. It does not disturb the ecosystem and can be installed near a human

settlement with the least land use and noise. VAWT are mainly of three types, Savonius, Giromill and Darrieus VAWT. However, the horizontal axis turbines are more popular, as it can produce more power and is also commercially viable for a large population. These turbines can be installed on land or in the ocean, where a vast area is available with significant wind flow throughout the year. Therefore, wind turbines can be classified into two groups based on their installation location, i.e. onshore wind turbines and offshore wind turbines.

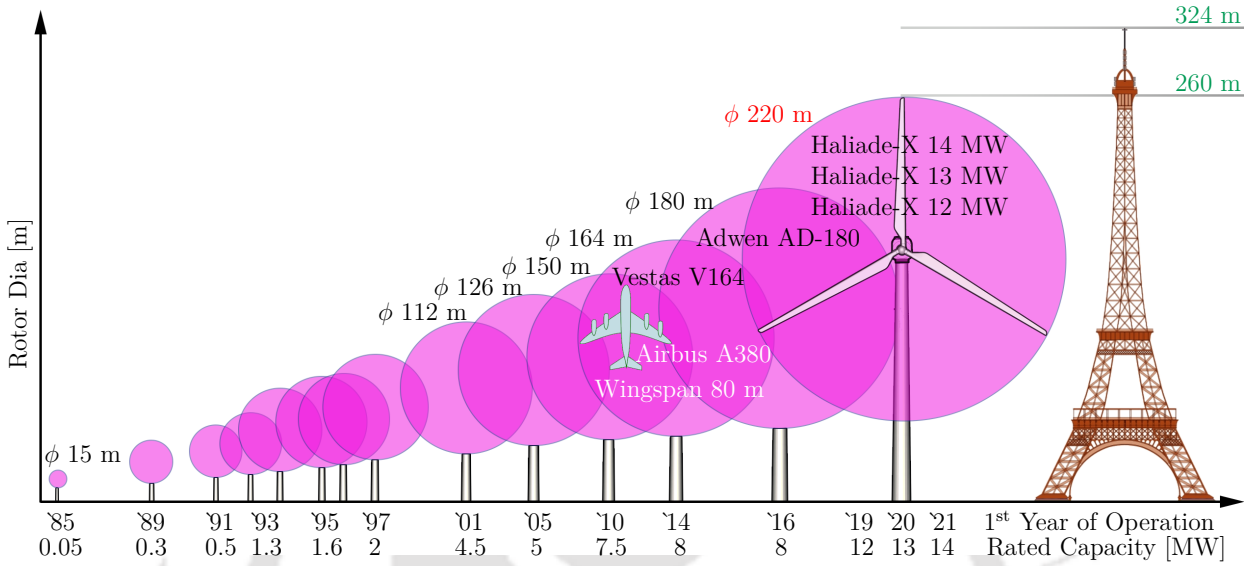

Figure 1.1: Evolution in size of the wind turbine.

The aerodynamics of wind turbine blade is similar to that of an aircraft wing. The airfoil shape of the blade creates a difference in velocity on its two sides. Using Bernoulli's principle, the pressure of moving fluid decreases when the velocity increases and vice versa. This pressure difference on either side of the rotor leads to the net lift force that turns the blade. Thus, the power produced by a wind turbine is given by

$$P = \frac{1}{2}\rho_a A C_p v^3 \tag{1.1}$$

where P is the power, ρ_a is the density of air, A is the rotor area, C_p the power coefficient of the wind turbine, and v is the velocity of incoming wind. The power coefficient is the ratio of power extracted by the turbine from the wind. For an ideal wind turbine, the maximum power coefficient is equal to 59.3%, as proved by German scientist Albert Betz [11]. This is the maximum amount of energy that can be extracted from the inflowing wind, which is hard to achieve in reality due to the losses by the drag and blade surface roughness [12,13]. Therefore, an actual wind turbine's power coefficient is around 35∼40%, which is evaluated as a function of tip speed ratio and the blade pitch angle. In general, the pitch angle is adjusted to maintain power output. Hence, the maximum C_p reduces with use of pitch angle. Further, the power loses due to electrical and mechanical inefficiencies are considered to find the final outcome. Thus, the amount of electrical power generated by the turbine is expressed as

$$P_e = \eta_e \eta_m P \tag{1.2}$$

where η_e and η_m are the coefficient of electrical and mechanical energy conversion, respectively. The power output of a wind turbine is proportional to the cube of the inflowing wind velocity, as shown in Eq. 1.1. Hence, identifying suitable sites using power resource assessment requires a critical understanding of its wind resource characteristics. The wind characteristics vary with space and time, so the geographical variations and climate changes affect the wind flow. For the same climatic region, the wind characteristics changes due to the variations in the geographical formation.

The electrical power produced by a wind turbine in Eq. 1.1 indicates that a bigger rotor size produces more power. At present, the World's largest wind turbine, Haliade-X 12 MW [14], has a rotor diameter of 220 m. It is a three-bladed offshore turbine whose first prototype was installed in Rotterdam port, the Netherlands, in 2019. Fig. 1.1 shows the evolution of wind turbines in terms of its size and power generation.

In general, turbines rotate with a blade tip speed of around 80∼90 m/s. As the tip speed ratio increases, turbines produce more noise due to friction with the air. Due to this reason, turbines of bigger size tends to make noise, which is more prominent in its nearby areas (around ∼50 m). A wind turbine's power efficiency reduces due to the energy loss caused by friction and blade vibration. This also causes damage to the blade, which requires frequent maintenance. Hence, vibration control of wind turbine blade is an essential component in its design and sustained operation to make this technology commercially viable.

1.1 Literature Review

The utilization of wind energy in its current form is achieved through the confidence gained by sustained research and development in the past decades. A major challenge in the technological development of wind energy originates from the structure that supports the rotor and other electrical equipment throughout its design life. This includes tower, nacelle and blades that experience structural vibration when they collectively face the upcoming wind. Therefore, keeping the vibration level as low as possible is a fundamental requirement for the safety and sustainability of the complete power generation unit, which is the motivation behind this thesis work. Thus, this study focuses on vibration control and its impact (i.e. fatigue life enhancement) on horizontal axis wind turbine. The following subsections illustrate the current state-of-the-art of HAWT modelling, blade vibration control, fatigue and reliability analysis.

1.1.1 Aerodynamics and Modelling

A brief review of various modelling and analysis techniques is presented in this subsection, which includes different development in structural load calculation, deterministic and stochastic modelling of the turbine.

1.1.1.1 Structural Load

Wind turbines are exposed to various external forces depending on the operating environmental conditions, as shown in Fig. 1.2, where blades are subjected to aerodynamic loads due to inflowing wind. Therefore, an accurate estimation of the aerodynamic load is essential for the design of wind turbine components.

The aerodynamic load are estimated using environmental conditions. IECWind [15] and TurbSim [16,17] are the commonly used tools for this simulation; both of them were developed by the National Renewable Energy Laboratory (NREL). IECWind generates the deterministic wind flow for the extreme conditions (i.e. gust wind, direction change, coherent gust with direction change, etc.) outlined in IEC 61400-1 [18] and IEC 61400-3 [19], whereas TurbSim simulates a stochastic full-field three-dimensional turbulent wind speed components.

Once the wind field is simulated, the aerodynamic loads are estimated using the geometric properties of a blade facing the inflowing wind. Thresher et al. [20] proposed a Force and Load Analysis Program (FLAP) in 1984 using quasi-steady linear aerodynamic model. They included wind shear and tower shadow effect along with gravity load and used power law to estimate the mean wind velocity above ground. This program was developed to estimate sophisticated time-dependent aerodynamic forces for a rigid-hub case. Later, it was modified for teetering-hub case using pinned boundary conditions for the asymmetric bending modes [21].

Blade Element Momentum (BEM) theory is the most popular tool for estimating aerodynamic forces acting on a rotating blade due to its efficiency and simplicity compared to other methods like Computational Fluid Dynamics (CFD). NREL developed a software called AeroDyn [22] for estimating aerodynamic loads from the simulated wind field using BEM theory. BEM theory assumes that aerodynamic forces on a blade element (i.e. airfoil) are independent (i.e. no interaction between the elements) and solely depend on its lift and drag coefficients. Therefore, few corrections were suggested in the literature for improving the accuracy of aerodynamic load estimation using BEM theory [23–26]. However, if the axial induction factor exceeds 0.5, the BEM theory fails, as the relation between axial induction factor and thrust coefficient is not valid in this case. To address this issue, Glauert [23] proposed an empirical relationship based on the experimental data. But this empirical curve does not accommodate tip and hub losses. Later, Buhl [24] extended this empirical solution with tip and hub loss corrections. With these corrections, the traditional BEM theory solves the induction factors iteratively, which frequently experiences numerical convergence issues. Ning [27] proposed a modified approach for solving the BEM theory with guaranteed convergence. In his method, the optimal flow angle is evaluated instead of induction factors by segmenting the BEM equation into three regions (i.e. momentum, empirical and propeller break) to enhance the convergence. He considered Buhls

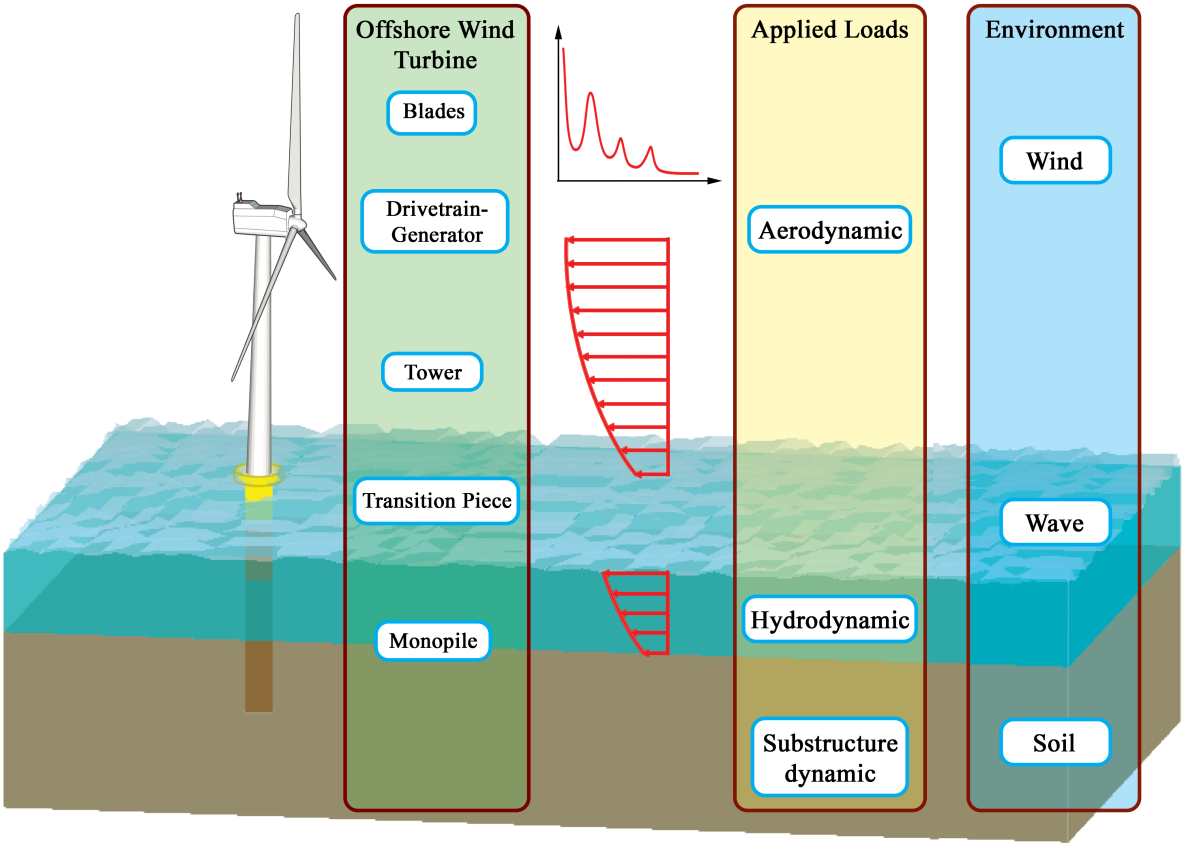

Figure 1.2: Offshore wind turbine and its components.

empirical relationship that incorporates various corrections to obtain a more accurate solution.

Simulation of the flow behaviour around the wind turbine blade using CFD received attention of many researchers in the last decade [28,29]. Duque et al. [30] developed a CFD code coupled with turbulence model using the Reynolds Averaged Navier-Stokes equations. Goundarzi [31] presented a comprehensive review of BEM theory and CFD analysis. He proposed CFD-BEM approach to estimate the aerodynamic loads more accurately at a low computational cost.

Many wind turbines are often built in offshore environments, which experience loads due to waves. Ocean wave profiles are generally simulated from the zero-mean Gaussian stationary power spectrum that correlates energy with the parameters essential for wave formation (e.g. fetch length, effective depth). Pearson and Moskowitch [32] proposed a mathematical formulation to fit the frequency spectrum for a fully developed sea state, which is known as Pearson-Moskowitch (PM) spectrum. Fully developed sea state happens only when the wind speed maintained for a large fetch length. But in most cases, it is small and results in an exaggerated peak in the frequency spectrum. Hasselmann et al. [33] developed a spectrum known as the Joint North Sea Wave Project (JONSWAP) spectrum using actual wave measurement. It is an improved version of the PM spectrum to model large waves, i.e. PM spectrum multiplied with a normalizing parameter and frequency dependant peak enhancement factor. Once the wave time history is simulated, the hydrodynamic loads acting on the structure are estimated using Morison's equation [19]. Jamieson et al. [34] presented the importance of considering wind and wave loading together in the design of offshore structures. The isolation of one load case from the other leads to over-conservative design.

1.1.1.2 Dynamics of HAWT

A dynamic system can be described using a set of governing differential equations involving inertial, damping and elastic forces besides external disturbance. These equations are obtained either from the analytical method (continuous parameter model) or from the numerical method (Finite element model). Hence, a physical system can be modelled as a continuous or discrete system. For the computational purpose, usually continuous systems are idealized as a discrete or lumped parameter models.

Leung and Fung [35] demonstrated the modal analysis of a rotating uniform cantilever beam using Finite Element Method (FEM). They compared spinning and non-spinning non-dimensional natural frequencies for horizontal, vertical and inclined (general) orientation of a beam. Hansen et al. [36] developed a dynamic analysis tool for wind turbines, i.e. Adams-WT using finite element method integrated with an aerodynamic load calculation module. Larwood [37] extended this work for curved wind turbine blade to find the mode shapes, further developed into a new software (i.e. CurveFAST) for dynamic analysis. He used non-linear equation of motion modelled in Kane's approach, where the mode shapes were evaluated using spinning FE model of the curved blade. Vollan and Komzsik [38] described the finite element modelling of a wind turbine and illustrated the variation in natural frequencies of the blade with an increase in rotational speed of the turbine using the Campbell diagram. They also extended this study for the analysis of a four-bladed aircraft propeller. Chortis [39] developed a non-linear finite element tool known as DAMPBEAM for dynamic analysis of large composite blades of the modern multi-megawatt wind turbines. The non-linear effects of large deformation and in-plane loads were included in his model and validated with experimental results on cross-ply composite beam. Ganguli [40] presented an extensive study on spinning FEM formulation with an example for modelling a rotating tapered beam in detail. He presented the formulation in the spectral finite element with the basics of the rotating system in the finite element framework. This study also provided a simple MATLAB code for modal analysis of rotating-beam based on finite element method. Later, he conducted a stability analysis of the helicopter blade using this model [41].

Finite element model of the complete wind turbine system is computationally exhaustive. Therefore, many researchers used reduced order models of wind turbine where the mode shapes from finite element models are used. In a reduced-order model, a few significant modes of the blade and tower are considered for the analysis. Burton et al. [42] presented a step-by-step procedure for developing a discrete reduced-order wind turbine model and its dynamic analysis. They derived an approximate expression for mass-proportional or equivalent modal aerodynamic damping of the turbine. They also demonstrated the variation of natural frequencies with an increase in rotational speed of the turbine using Campbell diagram for a 40 m blade. Zhang et al. [43,44] modelled the onshore wind turbine as a reduced-order system with 13 degrees of freedom (DOF), including drivetrain (i.e. 2-DOF), tower (i.e. 5-DOF), blades (i.e. each having 2-DOF). They added a 1-DOF vibration control device for each blade to reduce edgewise deformation. They also developed another 2-DOF non-linear blade model with the control device without considering blade-tower-drivetrain coupling. This model was computationally more efficient and further used to find optimum design parameters of the control device. Later, Dinh et al. [45] developed a reduced-order model of spar-type offshore floating wind turbine considering spar platform, nacelle and blades. The aerodynamic loads on the blades were estimated, and their coupling effect applied to the nacelle and spar. But this model needs to be validated with a more sophisticated program like FAST or any FEM software.

1.1.1.3 Cyclostationary Analysis of Rotating Body

Rotating mechanical systems often experience periodically varying non-stationary excitations. Although these systems can be studied using the general mathematical framework of non-stationary random vibration [46], their modelling comes under a special category of cyclostationary process. Gardner [47] studied the cyclostationarity in signal processing with a major emphasis on its advantage and possible applications. Holm et al. [48] investigated the level crossing rate of crack opening under cyclostationary load of a fillet welded steel plate to study its sequential effects on the fatigue life prediction. They determined the total damage from the level crossing rate of the stress time history rather than using load cycles. McCormick and Nandi [49] discussed the cyclostationary analysis of the rotating machines. They compared second-order model with stationary spectral analysis and first-order cyclic analysis (i.e. synchronous averaging) for different machine vibration. A comprehensive review on this topic may be found in Gardner et al. [50]. Antoni et al. [51] proposed a general guideline for modelling and analysis of rotating machines. They showed that time-cyclostationarity of the machine vibration occurred when the velocity fluctuation was periodic and stationary. They also derived the relationships between the angle and time-cyclostationarity for the vibrations experienced in mechanical systems. Antoni [52] studied the modelling and analysis of different cyclostationarity encountered in engineering applications. He explained how to perform cyclostationary analysis from theory to practice with a major emphasis on its advantages.

Chaari and Haddar [53] investigated spectral analysis of a wind turbine gear operating in the non-stationary environment. They concluded that the frequency-based study offered erroneous results when the speed was non-uniform. Therefore, they recommended a time-frequency analysis to model the variations in the frequency content of the response. Maheswari and Umamaheswari [54] reviewed trends in the condition assessment of wind turbine drivetrain using cyclostationary analysis. Ma et al. [55] presented bearing fault

diagnosis of wind turbine drivetrain using cyclostationary models. In this analysis, the acceleration response of the drivetrain bearings was used for fault detection in the inner and outer race through signal processing based on power spectrum and Cyclic Coherence Function (CCF). Teng et al. [56] applied CCF for fault analysis of wind turbine generator subjected to electromagnetic vibration and compared with the demodulation ability of spectral kurtosis and complex wavelet transform. They observed that CCF performed better than other methods available in the literature. They also studied the fault on a reassembled bearing to observe its failure due to the shaft current corrosion and discussed the failure mechanism resulting from electromotive forces generated in the shaft while intercepting asymmetric magnetic field due to the unbalance in the stator flux leakage or rotor eccentricity. Hence, they suggested providing a ground connection to the shaft for releasing the positive charges to avoid the corrodible tiny electric discharge points due to its transmission from shaft to framework through the inner race, ball roller and outer race.

1.1.2 Vibration Control

Wind turbines experience significant vibration during its operational life. Thus, various vibration control strategies/devices were proposed in the literature to enhance the performance of the turbine. The vibration control of wind turbine system includes mitigation of vibrations in foundation, tower or nacelle, drivetrain and rotor blades. Wind turbine blades primarily experience vibration in the flapwise and edgewise directions. The shape of the airfoils in a turbine blade is optimized in such a way that they experience minimum drag and maximum lift. Due to this shape optimization, flapwise motion experiences high aerodynamic damping. Hence, the deformation along this direction has large amplitude with significant static component due to the non-zero mean of the upstream wind flowing towards the rotor plane. Although aerodynamic damping is very high in this direction, it only reduces vibration to some extent with an unaltered mean component (i.e. static deformation) of the response. Contrary to the flapwise motion, aerodynamic damping in the edgewise direction is significantly less and results in small amplitude but high-frequency vibration [57, 58]. Under certain conditions, very low or negative damping is experiences in the edgewise direction, which leads to instability [59]. Moreover, prolonged exposure to large-amplitude vibration during its service life often causes structural failure of the blade. Besides these dominant blade modes, tower dynamics in the fore-aft and side-to-side directions are also coupled with blades causing significant blade-tower interaction. Murtagh et al. [60] studied the dynamics of wind turbine under blade-tower interaction and observed that displacement of the blade tip increased up to 256% due to this interaction. Even though the towers are made of strong materials, it experiences large amplitude vibrations due to their slenderness to accommodate modern multi-megawatt large blades with enough ground clearance. Therefore, many researchers initially proposed conventional Tuned Vibration Absorbers (TVAs) for reducing tower top motion and later extended its use for mitigating blade vibration. Fig. 1.3 shows the tree diagram of various control strategies/devices used to suppress wind turbine blade vibration.

Tuned vibration absorbers are the most commonly used motion control device in civil and mechanical systems from the beginning of the 20th century. Many researchers studied passive control techniques using tuned vibration absorbers (i.e. TMD, TLCD) for structural control of both onshore and offshore wind turbines. Multiple researchers studied tower vibration control using passive devices in the recent past. Among these options, Tuned Mass Damper (TMD) and Tuned Liquid Column Damper (TLCD) are the most common devices proposed in the literature. Murtagh et al. [61] used passive TMD at the tower top to reduce its fore-aft motion. They observed around 20% reduction in tower tip displacement using the TMD of mass ratio 1%, damping ratio 5% and tuning ratio 0.99. Colwell and Basu [62] studied the performance of TLCD for vibration control of the tower. They designed a TLCD placed at the top of the tower with 1% mass ratio and tuned to 99.2% of the fundamental frequency. They used wind and wave loading using Kaimal spectrum and JONSWAP wave spectrum, respectively and observed a 55% reduction in the peak displacement. However, in these studies, they ignored the aerodynamics of the blades. Lackner and Rotea [63] investigated passive TMD's performance for vibration control of offshore wind turbines using more realistic aeroelastic code, i.e. FAST (Fatigue, Aerodynamics, Structures and Turbulence). Lackner and Rotea [64] extended this work and developed a simulation tool for TMD based passive, active and semi-active control of an offshore floating wind turbine. These numerical studies using FAST showed that an active TMD performed better than its passive version. They observed 30% or more reduction in the fore-aft displacement using the active version of the controller. Fitzgerald and Basu [65] used Active Tuned Mass Damper (ATMD) for tower out-of-plane vibration control. They considered damage in the foundation due to soil stiffness degradation. They also noticed a 20% reduction in soil stiffness, causing 45% increase in peak-to-peak vibration of tower/nacelle without the controller, which was reduced by 52% using ATMD. Recently, Zhang et al. [66] studied the performance of Ball Vibration Absorber (BVA) for vibration control

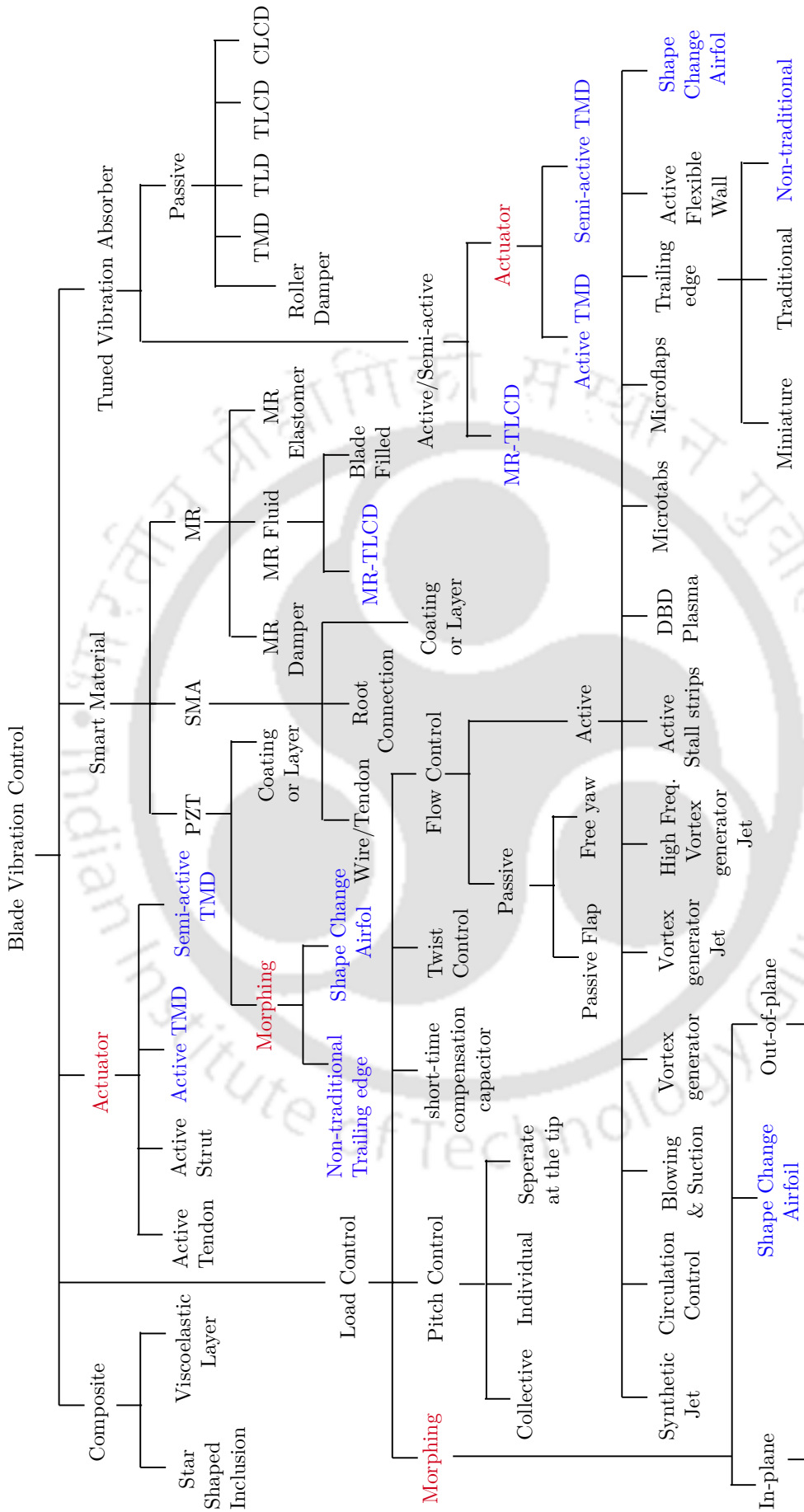

Figure 1.3: Tree diagram of strategies/devices used for wind turbine blade vibration control.

of offshore wind turbine tower using numerical and experimental models. They carried out a series of shake table tests on a scaled wind turbine model with and without BVA. Rezaee et al. [67] conducted a comparative study on the performance of TMD, Tuned Liquid Damper (TLD), TLCD and Viscous Damper (VD) for reducing tower top displacement and acceleration. Their study revealed that VD offered better performance, but the accommodation of VD required additional design considerations.

However, all these studies reported in the literature were focused on unidirectional control. Sun and Jahangiri [68] studied vibration control of offshore wind turbine using bi-directional pendulum TMD under misaligned wind, wave and seismic loadings. They compared the percentage reduction of Root Mean Square (RMS) and peak response of the tower top obtained by their method with the conventional unidirectional TMD for controlling the fore-aft and side-to-side motion and observed around 10% improvement in vibration control for the same mass ratio.

Besides tower vibration control, considerable research works in the recent past were aimed at blade vibration control. Anderson et al. [69] carried out edgewise control to avoid stall using Aerpac, a kind of tuned harmonic absorber that were installed in series near the tip of the blade. Their proposal was experimentally validated using a 600 kW wind turbine. Huang et al. [70] used multiple semi-active tuned mass dampers to control the edgewise vibration of offshore floating wind turbine tower and blades. They placed one TMD at the tip of each blade and another one over the tower. They used a control algorithm based on short-time Fourier transform to identify the dominant frequency of the system. Arrigan et al. [71] developed a frequency tracking algorithm based on Fourier transform for reducing flapwise displacement of the blade using Semi-active TMD (STMD) at the tip. They observed a significant reduction in flapwise displacement of the blade and extended this work to mitigate the edgewise vibration [72]. Dinh et al. [45] investigated edgewise vibration control of Spar-type Floating Offshore Wind Turbine (SFOWT) blades, nacelle and spar with passive and semi-active TMD. They observed instability due to excessive large strokes of the nacelle STMD at low tuning frequency compared to its passive version.

Fitzgerald et al. [73] compared passive and active TMDs for in-plane vibration control of the wind turbine blade. They observed a 37% reduction in peak-to-peak response using passive TMDs with 3% mass ratio whereas its active version with a Linear Quadratic Regulator (LQR) algorithm resulted in a 44% reduction. This study was also extended for a Cable Connected Active TMD (CCATMD) and the tip of the blade [74]. The modified version showed that CCATMD performed better than active or passive TMD. The authors assumed the availability of enough space for the movement of TMD inside the blade, having a significantly high mass ratio. Recently, roller dampers were used for passive control of edgewise vibrations of rotating turbine blades. Zhang et al. [75] proposed roller damper for mitigating edgewise vibration of the blade. The roller damper was located at a two-third length of the blade and modelled as an equivalent pendulum. They observed that roller damper performed better with larger centrifugal acceleration and mass at optimal frequency ratio. Although, theoretical models of these studies demonstrated impressive results, using these devices on a commercial basis in a full-scale turbine system was doubtful.

Zhang et al. [44] proposed non-linear tuned liquid (or sloshing) dampers (TLDs or TSDs) for mitigating edgewise vibration of the blade. They observed 40∼50% reduction in Fourier amplitude of edgewise blade tip vibration using 2-5% of mass ratio, i.e. the damper's performance increased with increasing mass ratio. Also, the study identified the optimum length of TLD. Later, the authors [43] extended this work with TLCD, which reduced peak displacement in edgewise direction by ∼20%. The TLCD performed better when placed towards the tip of the blade, with increasing fluid mass. Zhang and Nielsen [76] compared the performance of roller damper and tuned liquid column damper for edgewise vibration control of the blade. This study indicates that roller damper performed better than TLCD. Basu et al. [77] developed a liquid column damper that consists of a circular tube partially filled with liquid to control edgewise vibration of wind turbine blades. They used a non-linear reduced-order model for tuning Circular Liquid Column Damper (CLCD) under different rotational speeds. The magnitude of damping in this device could be altered by changing the orifice openings. The mass ratio of CLCD used in this study was around 1∼4%, which located at 45 m from the root on a 61.5 m long blade and obtained 25-33% reduction in the standard deviation of displacement at the tip. Although TVAs were proposed for tower and blade in the literature, they often suffer two major setbacks - (1) tuning the controller as the frequencies of a combined system are affected due to blade rotation and (2) spatial constraints for installing of these devices.

Apart from tuned vibration absorbers, many researchers developed sensor-actuator based controllers. Rice and Verhaegen [78] proposed multisensor-actuator control of blade in a close loop over a broader wind speed range. Krenk et al. [79] proposed collocated sensor-actuator in the form of an active strut mounted at the root of each blade, which changes the local curvature to control the edgewise motion. They studied the variation of dimensionless blade frequency with respect to rotor speed and observed a significant reduction of edgewise motion without any change in flapwise motion. Staino et al. [80] proposed active

actuators mounted inside the blade to control its edgewise motion. They proposed two linear actuators, which were supported by a truss within the airfoil. They used multi-blade coordinate transformation to convert a rotating framework into a non-rotating framework, and observed 65% of displacement reduction while applying a force equal to 28% of the blade weight. However, in reality, it is challenging to incorporate a truss inside the blades. Staino and Basu [81] investigated the impact of change in rotational speed on the edgewise motion of a blades with grid fault. They observed that their controller was robust with the variation of rotational speed. They extended this work with passive pitch control using the Pareto-optimality criteria [82]. This dual control strategy reduced the disadvantage of individual scheme, and a 63% reduction of blade vibration was observed with 15% of power loss. In comparison, individual pitch control application caused a 50% reduction in power, and active tendon alone required 40% extra control force, to achieve the same reduction. Cong et al. [83] presented the mitigation of edgewise motion using a Stochastic Disturbance Accommodating Controller (SDAC) developed with two actuators (active tendon) and wireless sensor. They observed a considerable reduction in edgewise motion but this proposal needed further validation with adequate experimental results. They also neglected mass and stiffness of the truss beside the difficulties of placing it inside the airfoil. Zhang et al. [84] proposed torsional viscous damper to enhance flutter instability of the turbine blades. Most of these research works were focused on unidirectional vibration control, while in reality, wind turbines blades are exposed to bi-directional motion due to vortex-induced crosswinds. Chen et al. [85] used viscous damper inside the blade to enhance its critical flutter speed.

Besides blade-tower interaction, the coupling between edgewise modes of blade and drivetrain also causes strong oscillation that affects power generation [86]. Therefore, in addition to the controllers mentioned above, various other control techniques are also proposed in the literature. Among them, load control is a popular technique used in the wind turbine industry to reduce the fatigue load and increase the life span of a blade and drivetrain. There are several approaches proposed in the literature that includes both passive (viz. free yaw movement) and active (viz. blade pitch control) load control strategies [87]. In this context, few advanced load control techniques are also proposed in the recent past, e.g. advanced pitch control, twist control, variable diameter rotor and active flow control [88]. Among them, advanced pitch control and generator torque control are the two most popular techniques used in the wind industry for structural load mitigation of modern variable speed wind turbines. In general, torque control is used below the rated speed to obtain maximum output. In contrast, a pitch controller is used above the rated wind speed to regulate the *rpm* to the desired value with a constant generator torque [42]. Generator torque is widely deployed to provide damping into the drivetrain, which reduces torsional vibration [86,89]. Van der Hooft et al. [90] and De Corcuera et al. [91] investigated active damping to control lateral tower vibration with generator torque. They explored a multi-variable controller based on H_∞ strategy to mitigate both torsional vibration of the drivetrain and lateral vibration of the tower. However, the torque transfer mechanism from the generator to the tower vibration and the effect of the generator torque on other wind turbine components were not studied in detail. Fleming et al. [92] carried out field tests on a 600 kW wind turbine to demonstrate the effect of active generator control on the drivetrain and lateral tower vibration. As the gearbox causes maximum downtime resulting in revenue loss, using a directly driven system to avoid overhauling (i.e. removing and re-installing gearbox) reduces the long-term operating cost of a turbine, thereby making electricity from the wind farms cheaper. In these literatures, the effect of generator torque on the wind turbine blade was ignored. In reality, edgewise vibrations of the blades are coupled with the torsional vibration of the drivetrain.

Likewise, Pitch control is one of the popular active load control technique often used in the wind turbine industry to reduce aerodynamic loads. There are various methods proposed in the literature for pitch control and to improve its effectiveness. Anderson and Bose [93] proposed pitch control to avoid damage of generator and gears during extreme wind and incorporated mode switching algorithm above the cut-off speed. Lackner [94] investigated load control using variable power collective pitch controller of a floating offshore wind turbine. They observed a 20% reduction of pitching motion of the platform, thereby increasing maximum power generation. Bossanyi [95] studied individual pitch control using Linear Quadratic Gaussian (LQG) and Proportional Integral (PI) scheme to achieve a significant reduction of aerodynamic loads. In another work, Bossanyi [89] also presented a comprehensive review of different control strategies including collective and individual pitch control. Kusiak et al. [96] demonstrated an intelligent pitch control technique based on a model integrating approach that involved data mining, evolutionary computation and model predictive control. They used five objectives with different weights to control the performance of a wind turbine. They designed the controller in such a way that it modified the objective function according to the wind condition and the electricity demand. With this controller, they regulated the power output, generator torque and *rpm* of the rotor in turbulent wind without compromising the power output. Zuo et al. [97] developed a computationally inexpensive robust adaptive variable pitch controller with memory-based compensation for

power tracking and fatigue load reduction for offshore wind turbines. The controller was adaptive to the system parameter variations and uncertainties. It was also robust against complex wind and wave loading, which reduced power fluctuations, platform vibration, and fatigue loads. Zhang and Nielsen [98] showed that advanced pitch control and generator torque control techniques effectively mitigate structural loads. Agarwala and Ro [99] observed a huge increase in power production using Separate Pitch Control at the Tip (SePCaT) of the blade. They compared the performance of blades with six different SePCaT lengths varying from 5% to 30% of the total length. This study was limited to the analytical investigation based on power production only, while its performance on vibration mitigation and fatigue life enhancement were not explored.

Apart from pitch control, various flow control techniques are also used in wind turbines. Active flow control is an advanced technique to improve the power generation of a wind turbine (e.g. trailing edge, synthetic jets, micro tabs, morphing and plasma actuators), which also mitigates blade vibration due to reduced aerodynamic loads [87]. Various researchers investigated the use of synthetic jet actuators [100], microtabs and trailing edge flaps [101,102] to control wind-induced vibrations. Bottasso et al. [103] proposed passive flaps, which moved opposite to the blade vibration and worked over a wider frequency range without affecting power production. The advantage of this strategy was that it could be integrated with any other controllers and did not require sensors and actuators. Zhang et al. [104] introduced active flaps in blades to mitigate three different response characteristics viz. flapwise acceleration, tip displacement and root moment. Their study in aero-servo-elastic framework showed 12∼22% reduction of fatigue load where the root bending moment was used for design. Wilson et al. [105] proposed microtabs along with collective and individual pitch control to alleviate extreme loads, thereby, preventing damage and producing more energy. Their proposal showed a 70% reduction of the root bending moment, which was also verified experimentally. Moreover, they [106] investigated the combined performance of different trailing edge devices, including microtabs, morphing trailing edge device and traditional trailing edge flaps along with collective pitch controller. They observed 20∼30% reduction in the standard deviation of the root bending moment. Pechlivanoglou et al. [107] carried out wind tunnel test to investigate the performance of flexible flaps as a load controller. In this experiment, standard DU96W180 airfoil and its modified version were used with flexible flaps using wind flow at a high Reynolds number (∼1,300,000). The test was conducted for both positive and negative deflections, which experienced significant variation in lift and drag coefficients. The lift-drag ratio decreased with the application of a positive flap, which increases both lift and drag. However, the increase of drag is more compared to the increase of lift under this condition.

The flow can also be controlled by ionising the surrounding air using Dielectric Barrier Discharge (DBD) plasma devices with high electric potential. In other words, DBD-plasma is a device, which produces body force on the surrounding fluid using an electric field. Nelson et al. [108] proposed a distributed DBD-plasma flow controller for wind turbine blades to increase its power output while reducing vibration. It produced an ionic wind as soon as the electric field was applied to drive the nearby fluid. Thomas et al. [109] experimentally investigated the performance of DBD-plasma to improve the aerodynamic flow at a higher Reynolds number.

Other than flow control strategies, morphing (i.e. optimal profile) was also studied by different researchers to reduce the structural load on a blade. It is an advanced technique often used to improve power production with an optimal profile. It is mainly classified into in-plane morphing and out-of-plane morphing depending upon the direction of the shape modification. Lachenal et al. [110] demonstrated this concept with the details of shape adapting materials. They discussed the possibilities of adapting different morphing concepts used in helicopter blades and aircraft wings. Berg et al. [111] investigated the effect of active aerodynamic load control using Grow-The-Rotor (GTR) and Trailing-Edge-Flap (TEF). GTR could retract the blade tip to reduce aerodynamic loads during extreme wind, which was extended to increase power generation during normal condition. Their study showed a 10-15% increase in power production with 10% increase of blade length. Capuzzi et al. [112–114] proposed a passive structural morphing technique with the variable elastic twist. It could adjust the angle of attack along the blade length in different wind conditions (i.e. below and above the rated speed), which improved the energy output. Besides variable angle of attack, it also had the gust load alleviation capability that significantly enhanced the dynamic performance of the blade. Wang et al. [115] proposed to apply a controllable linear blade twist along the length and compared its performance with morphing and pitch control. Their study concluded that blade morphing performed better than pitch control in terms of power production.

1.1.3 Advanced Materials

Besides continuous efforts to develop new control strategies, researchers in the recent past have focused their attention on developing new materials that are specifically tuned for different applications.

Hu et al. [116] designed a composite blade against ultimate limit state based on robust multi-objective optimization. They optimized the material type, orientation angle and thickness of the Glass Fiber Reinforced Plastic (GFRP) and Carbon Fiber Reinforced Plastic (CFRP) layers to reduce the weight and cost of a blade. But this minimum material design of the modern multi-megawatt wind turbine blades led to a thin-walled structure, which might face instability due to buckling and vibration. Thus, the researchers included buckling analysis and tip deformation in a multi-objective optimization framework. Cox and Echtermeyer [117] developed a lightweight hybrid composite blade with reduced tip deformation using glass and carbon fiber layers. They used carbon fibers to gain sufficient bending stiffness and glass fibers to achieve buckling resistance. Finite element analysis of this blade proved its performance against extreme loading conditions. They also presented a detailed description of structural components and their ply layups. Dal Monte et al. [118] proposed a multi-objective genetic algorithm for the optimal design of composite blades. They designed a blade with more advanced material, i.e. D155 instead of A130, which reduced the blade weight by 8.29%. They noticed a 12.04% reduction of flapwise displacement with 2.92% increase of edgewise deformation. This work required further modification with more appropriate multi-objective genetic algorithm so that there was no increase of blade deformation in any direction. Chortis [39] investigated the performance improvement of the blade using composite strip based on Kelvin visco-elastic model and Green-Lagrange non-linear formulation. Cheng et al. [119] studied vibration control of blade using fiber-reinforced composite with visco-elastic damping layers. This analytical study showed the application of sandwiched visco-elastic damping layer could effectively mitigate the vibration.

In the recent past, smart materials gained popularity in vibration control of dynamical systems. Hurlebaus and Gaul [120] discussed various smart materials with their modelling and applications. Piezoelectric material, Magnetorheological (MR) fluid, Shape Memory Alloy (SMA) or Shape Memory Polymer (SMP) were examples of such materials. Piezoelectric materials can generate electric energy when mechanical energy is applied and vice versa, i.e. applied voltage deforms the material. The precise response of a piezoelectric actuation upon voltage application brings them even in micro industries [121]. Mao and Pietrzko [122, 123] proposed a piezoelectric based passive shunt damper to control structural vibration. They compared the performance of different shunt circuits, i.e. RL series, RL parallel, RL-C parallel and pulse-switching shunt circuits. They optimized shunt circuit parameters for a fixed location of the piezoelectric patch and validated with experimental work on an aluminium cantilever beam. They obtained ∼70-81% reduction in velocity response of the beam. Later, it is studied for optimisation of piezoelectric patch location along with other two parameters (i.e. R and L), and further enhanced percentage reduction by ∼12-24% [124, 125]. Qiao et al. [126] proposed active vibration control of blade using piezoelectric layer with glass fiber composite. In this study, the stress-strain behaviour and dynamics of a blade were improvised using a piezoelectric actuator. This numerical study was conducted on a small wind turbine blade, which needs to be validated with experimental study and extended for large blades with a more sophisticated control algorithm. Tippmann and Scalea [127] experimentally investigated the performance of piezoelectric shunt circuit damping for blade vibration control. They used CX-100 blade with Macro Fiber Composite (MFC) transducer connected to a tuned passive resonant shunt circuit. The numerical results presented in this work showed a significant reduction of blade vibration using MFC shunt damping. This study focused on frequency domain result and was limited to impulse load only, which required further investigation with actual wind loading or wind tunnel experiment. Liu [128] studied piezoelectric active control against classical blade flutter of a single-cell thin-walled composite wind turbine blade using LQG theory. His work opened a new area of classical flutter control using piezoelectric actuator in wind turbines blades. He considered a small blade for this analysis. Thus, the application of piezoelectric actuator in large-span blades require more study. Liu and Liu [129] extended this work to design an Optimal LQG Controller (OLC) against the vibration-induced stall. The feedback from piezoelectric material was used to adjust the pitch controller for enhancing the aeroelastic behaviour. They discussed effects of varying ply angles and rotating speeds of rotating piezo-composite blades on its piezoelectric damping ratios. They conducted an experimental study using real-time OLC controller on a small scale blade and observed a significant improvement against the stall. Besides stall control, piezoelectric actuators were used for camber morphing in wind turbine blades, mainly using THUNDER® TH-R6 (Thin layer composite uni-morph ferro-electric driver and sensor). Pern [130] used TH-R6 for camber morphing using NACA 4415 airfoil with a latex rubber layer to increase its lift and drag ratio. The top surface of the airfoil (i.e. camber) in the flow separation region is oscillated to control the flow with the application of 30 V to the piezoelectric actuator (i.e. TH-R6), which results in minimising boundary layer

separation. They observed improved flow control using both experimental and CFD analysis.

Magnetorheological (MR) fluid exhibits a smart property where its viscosity increases when a magnetic field is applied. Saptarshi et al. [131] used magneto-rheological fluid in TLCD for semi-active vibration control of the tower in LQR framework. They applied clipping optimality of the control force to maintain the MR parameters within their feasible range. Their study focused on along-wind vibration control of the tower, and this needs to be investigated for the performance of MR-TLCD in the out-of-plane and in-plane direction using a fully coupled system. Bolat [132] proposed vibration control of wind turbine blade filled with MR fluid to achieve significant vibration control. They modelled the combined system by considering dynamic interaction between the electromagnetic actuator and the MR fluid. In this approach, they obtained considerable vibration control in a small scale model, but the performance of this control technique for large wind turbine blades required further investigation. Chen [133] employed MR-damper inside the blade to reduce its edgewise vibration using a fuzzy control law, which evaluated the optimal voltage requirement for the damper. They also compared single and multiple MR-dampers in semi-active and passive mode, which offered ∼24% reduction of peak displacement and ∼47% reduction of its standard deviation.

SMA is one of the smart materials that have gained popularity due to its ability to recover large strains. Nitinol (Nickel Titanium Alloy) is an example of SMA. It possesses a unique property of solid-solid transformation, which occurs due to thermal or mechanical changes. It undergoes the transformation between two stable phases (i.e. austenite and martensite) and has the ability to return to its original undeformed shape by the combined effect of change of temperature (i.e. shape memory effect) and by the removal of stresses (i.e. super-elasticity effect). The stress-strain behaviour of SMA produces large hysteresis that has better energy absorbing capability with the re-centering ability [134,135]. Also, it has excellent resistance to corrosion and fatigue. Various models exist in the literature to characterize the material properties of SMA. Graesser and Cozzarelli (G-C) [136,137] modelled the stress-strain behaviour, which was used in different applications. This model depicts the uniaxial super-elastic behaviour. G-C model considered the hysteretic behaviour under small strain amplitudes, excluding the martensitic hardening effect of SMA under large strain. Wilde et al. [138] proposed a novel smart bridge bearing system using shape memory alloy bars laminated with rubber to protect from earthquake hazards. For this purpose, they made an extension of G-C model, which included the hardening of SMA after the completion of phase transition to twinned martensite. The smart isolator offers a stiff link between the deck and the pier for a small external excitation. For higher external disturbance, besides improved stiffness, the SMA bars enhance the damping characteristics of the isolator due to the stress-induced martensitic transformation. Auricchio [139] developed three dimensional thermo-mechanical constitutive model of SMA. Their work focused on a novel inelastic model based on an internal-variable formalism to develop 1D and 3D constitutive models of SMA. This constitutive model simulated some of the fundamental features of SMA, such as superelasticity, material behaviour under tension and compression, and the reorientation of single variant-martensite. Liang and Rogers [140] proposed a uniaxial constitutive model for both shape memory and super-elastic behaviour of SMA using a thermo-mechanical (i.e. stress-strain-temperature) relationship. This constitutive model related the effect of stress on martensite volume fraction during the phase transformation. This model shows very well match with experimental results.

Various applications of SMA were reported in the literature using these models with different characteristics. SMA materials are widely used in biomedical applications to design advanced surgical instruments and artificial organs. Duerig et al. [141] developed a spinal vertebra spacer to produce a constant load regardless of patient position. Mantovani [142] discussed the properties and the application of SMA in various fields of medical science. Simon filter is an SMA based cardiovascular device developed to prevent pulmonary embolism. Some other important and smart applications of SMA includes reinforcement of arteries and veins, bone plates, dental wires, active endoscopes, eyeglass frames and robotic hands [143,144]. It is also used as sensors and actuators in many fields, including fire security systems and electrical connections [145,146]. Moorleghem and Otte [147] used SMA to detect the temperature variation in a fire security system and designed a gas valve to stop the gas flow when the fire occurred. SMA can monitor temperature rise and react mechanically against it at the same time by closing the valve. Hartl [148] discussed different applications of SMA in atmospheric and space flights. They described the impact of SMA properties along with the techniques to utilize them. Also, they discussed design challenges and modelling approaches for SMA. Dhanalakshmi et al. [149] proposed SMA in sliding mode control for dynamic systems. They conducted experiments using a cantilever beam with SMA actuator, which reduced significant vibration. Khan et al. [150] developed a passive vibration isolation system using SMA spring. They modelled pseudo-elasticity of SMA based on Preisach input-output relation. They concluded that vibration isolation is strongly dependent on the relative displacement of SMA springs, as it directly affects the degree of phase transition.

Choi et al. [151] and Walber et al. [152] used SMA actuator for the vibration control of flexible beams.

They conducted experiments to study the performance of different control strategies for SMA based vibration control. Shahin et al. [153] investigated the passive and active vibration control of building with SMA bracing. They noticed significant reduction of displacement response using SMA tendon. Choi et al. [154] used SMA restrainer in conjunction with sliding type base isolation device for bridges to improve its performance. This bearing effectively restricted relative displacement of the deck under strong ground motions and restored to its original shape. Song et al. [155] studied different applications of SMA as passive, active and semi-active control devices in structural engineering with operational mechanism and experimental results. Sharabash and Andrawes [156] proposed vibration control of cable-stayed bridges using SMA dampers, where optimal parameters for the control device were designed. Ozbulut et al. [157] proposed the design strategy to find optimal parameter range using genetic algorithm. Küçük et al. [158] studied the stress development when different SMA (viz. Ni-Ti, Cu-Zn-Al and Cu-Al-Ni) materials were used in turbine root connection. Their study showed that Nitinol gave a better performance than other SMA materials in terms of von-Mises stress and yield stress. Performance of SMA supplemented rubber bearing was studied by Gur et al. [159] and Das and Mishra [160] for vibration control of structures. They used stochastic structural optimization to design the optimal parameters [161]. Mondal et al.[162] demonstrated the use of SMA rubber bearings for seismic protection and compared its performance with conventional lead plug bearing for large amplitude pulse type near field motion. Recently, Dimitrios et al. [163] proposed high-performance SMA coatings over metallic components of aerospace structures to reduce the stress of the underlying components. Patriota et al. [164] investigated the control of fixed edge deformation of a flexible beam using SMA wire actuator and adopted classical control strategies such as P, PI and PID to check the controllability in close-loop. Haghdoust et al. [165] studied passive damping of large wind turbine blades using thin SMA layer over the spar. They modelled 89 m long DTU 10 MW wind turbine blade in ABAQUS, and applied a thin CuZnAl SMA layer over the spar in three different configurations, which significantly improved blade damping.

Pasala et al. [166] proposed pendulum TMD with SMA wire known as Adaptive-Length Pendulum Smart Tuned Mass Damper (ALP-STMD) for building vibration control, which could change the length of wire by adjusting the current flow. They developed a device to change the length of pendulum wire for tuning to the dominant frequency of the system and experimentally showed that the ALP-STMD could work for frequency invariant system. Contreras et al. [167] extended this work for a system whose frequency varied with time. They used SMA bracing to produce the frequency variation and noticed that ALP-STMD could adjust the tuning frequency with respect to system frequency change. Some researchers developed new controllers using different combination of smart materials. Kumbhar et al. [168] developed new Adaptive Tuned Vibration Absorber (ATVA) using Magnetorheological Elastomer (MRE) with SMA. They showed that ATVA gave a better performance than SMA alone, using analytical and experimental results.

Mouleeswaran et al. [169] conducted experiments to study the use of active SMA wire for vibration control of small domestic wind turbine blade. They made a blade prototype using glass fiber reinforced polymer with SMA wire embedded between the top and bottom layers. With this controller, the amplitude of vibration was reduced by 20% in passive mode and 61% in active mode. Jagadeesh et al. [170] studied the variation of natural frequency using SMA wire in a small scale wind turbine blade. They embedded different number of 0.5 mm diameter SMA wires inside the blade, and noticed 6.3% increase in natural frequency of the blade and ∼64.8% reduction in amplitude of vibration using 3 embedded SMA wires.

1.1.4 Fatigue Analysis and Design

The demand for sustainable energy sources has created a revolution in the wind turbine industry. Modern turbines are bigger, with a large rotor diameter that captures more wind to convert it into electricity. Besides length, wind turbine blade has evolved in shape and functionality to produce maximum output, which is more prone to fatigue damage as bigger blades are exposed to the aerodynamic loads that cause large amplitude vibration. Here, it is needless to mention that blades are the most critical component of wind turbines, and their damage leads to catastrophic failure of the whole system. Therefore, fatigue and reliability analysis of modern multi-megawatt wind turbine blade are extremely important, and the relevant review of previous research works are presented in the following subsection.

1.1.4.1 Fatigue Life Enhancement

There are plenty of studies published in the literature to estimate the fatigue life of wind turbine blades. Greaves et al. [171] performed dual-axis fatigue test for large blades considering the interaction between flapwise and edgewise modes. Chou et al. [172] reviewed the common causes of HAWT blade failure. They collected the details of blade damages from different sources and statistically classified them according to

their cause. They also identified the damage mechanism by analysing the structural behaviour of blades. Dervilis et al. [173] proposed the use of pattern recognition algorithms based on Artificial Neural Networks (ANN) for damage detection of wind turbine blades. They conducted continuous fatigue load test on a 9 m blade in-order to investigate the damage mechanism. Lee et al. [174] investigated fatigue damage of a composite blade using Finite Element (FE) modelling and simulations. They found that blade root fails due to delamination caused by bending. They also conducted fatigue load test on a full scale 3 MW wind turbine blade of length 56 m and observed similar failure at the root. Haselbach et al. [175] numerically simulated the load-carrying capacity of large wind turbine blades prior to delamination. They analysed blade under flapwise loading with various initial delamination of the spar using FE model, and found delamination growth under normal operational load that induced near-surface local buckling. Zhang et al. [176] proposed a method for estimating the fatigue damage of large composite blades during their service life. They evaluated the stress profile over the blade using FE analysis and estimated the number of stress cycles using fast Fourier transform. Tenghiri et al. [177] presented analysis and design of blade of a 11 kW wind turbine against fatigue using different methods. They compared the efficiency of Simple Load Model (SLM) method, NREL MLife and Ansys nCode DesignLife in fatigue life estimation. They observed that the SLM underestimated the fatigue life, but it was computationally efficient and good starting point for stress and fatigue estimation.

1.1.4.2 Reliability

In the recent past, several researchers also investigate the improvement of structural reliability of wind turbine components with various control schemes. Fitzgerald et al. [178] used active tuned mass dampers to enhance the reliability of a wind turbine tower. They modelled the wind turbine as a reduced-order dynamic system based on Euler-Lagrange formulation. They conducted fragility analysis in a probabilistic framework to estimate the reliability improvement with their controller. In this study, Fitzgerald et al. [178] considered uncertainty in the natural frequency and structural damping ratio of the corresponding modes for probabilistic analysis and modelled them as a uniform random variable. They obtained a significant improvement in the reliability of tower displacement. In another work, Sarkar et al. [179] investigated the reliability improvement of tower response using MR-TLCD, designed in semi-active mode of operation to fully utilize its smart properties. They estimated the aerodynamic damping of a wind turbine in both fore-aft and side-to-side directions. This study reported a 30∼40% reduction in side-to-side displacements of the tower with their controller and significant improvement in reliability.

Dimitrov et al. [180] drew a comprehensive view on the implementation of reliability-based wind turbine design and identified robust reliability analysis. They estimated the reliability of composite wind turbine blade against blade-tower collision and fatigue failure of the sandwich panel. They evaluated the safety factors using ultimate strength and fatigue limit state against the target reliability level. Their study based on model uncertainty shows a significant impact on reliability, and reduced model uncertainties result in improved structural reliability and subsequently less safety factor. Tao et al. [181] investigated the reliability improvement of a blade using active tendon controller. This work proposed a computationally efficient stochastic method to estimate the improvement in structural responses. They simulated stochastic wind fields based on the time-evolving phase spectrum and the phase delay in the spectrum model, and noticed that the effectiveness of the active tendon controller increased at higher wind speeds with maximum reliability improvement at the cut-out speed. Jiang et al. [182] presented a comprehensive review on structural reliability of wind turbine and discussed a general approach for reliability analysis of mechanical and electrical components of the wind turbine. They summarized a variety of failure mechanisms of different wind turbine components. The failure modes of rotor blades were due to large deformation, excessive bending stress, fatigue and buckling. They mentioned that the large deformation failure includes the failure due to blade-tower interaction. Hu [183] studied various advanced wind turbine design techniques and conducted reliability analysis for a lifespan of 20 years, considering uncertainty in wind load. This work also addressed the Reliability-Based Design Optimization (RBDO) of composite wind turbine blade under manufacturing and wind load uncertainty. He observed that the probability of failure reduced from 50% to 2.28% in reliability-based design optimization. Liu et al. [184] studied the reliability of offshore floating wind turbine against excessive blade tip deformation and fatigue. They investigated the effects of floating foundation on the failure probability of blade and compared with the fixed foundation. They also observed that the probability of failure was significantly higher in the case of floating turbines.

1.2 Motivation

The review of various methods to model structural loads and dynamics of HAWT are presented in Subsection 1.1.1. In this study, TurbSim [17] is selected for simulating wind field due to its ability to generate stochastic full-field 3D turbulent flow for a given mean wind speed at hub height. The aerodynamic load estimation using BEM theory is adopted based on Ning's [27] algorithm due to its guaranteed convergence and computational efficiency. Apart from aerodynamic loads, the dynamics of the HAWT system are modelled in a reduced-order framework for preliminary analysis due to its simplicity in modelling. In this study, the model proposed by Fitzgerald et al. [73] is modified to include multiple modes of blades and tower, drivetrain and monopile. Further, a more sophisticated spinning finite element model of the blade is used for detailed analysis.

In modern wind turbines, the large amplitude of blade vibration is one of the primary cause of fatigue failure. Also, the vibration of these structures usually creates huge noise, which affects the ecosystem close to the turbine. Hence, blade vibration control is a critical component of regular operation to enhance the fatigue life and overall performance of the system. Due to this reason, vibration control of large wind turbine blades has drawn the attention of many researchers and the literature available on this topic outlines different options for this purpose as described in Subsection 1.1.2. The selection of an explicit vibration control device relies upon its performance, safety, compactness, capital expense, operational expense and maintenance requirements. Due to these reasons, most of the control devices used in mechanical and civil structures are unsuitable for wind turbine blades. Most of the controllers proposed in the literature were inherently incapable of reducing large static blade deformation. Also, they were limited to control vibration in a particular direction, i.e. either in-plane or out-of-plane. Hence, a controller reducing both static and dynamic components of vibration in the orthogonal directions without affecting the aerodynamic profile of the blade is the need of the hour.

These blades often experience damage due to lightning strike [42, 185]. Therefore, modern blades are designed for lightning protection using metal conductors, which are customarily kept inside [186]. Usually, these conductors are connected to the anchors at the root and tip with guiding mechanism at regular interval to avoid hitting the spar or airfoil skin. They are also not used as a structural element in the design of the blade. Thus, these cables do not offer any stiffness against blade deformation. This thesis work aims to investigate the possibility of using the cable (separate from lightening protection) inside the blade for its strengthening against deformation. With this in view, an SMA tendon beside the existing lightning protector connecting the root and tip of the blade is proposed in this study, which will act as a vibration controller. For modelling the material behaviour of SMA, the Graesser-Cozzarelli model is considered for preliminary study due to its ability to capture the actual material behaviour in isothermal condition, and the Liang-Rogers model is used for deriving a new constitutive relation based on thermodynamic principles due to its accuracy, as discussed in Subsection 1.1.3.

Usually, wind turbines are designed for 15-20 years, but they are often damaged earlier, making the wind energy more expensive due to heavy maintenance [187]. Therefore, design engineers continuously look for better techniques to improve blade performance. There are various reasons for wind turbine failure, out of which lightning strike and extreme cyclic loading are the major cause of failure. Different techniques have been proposed in the literature to alleviate the extreme load on the blade to enhance its fatigue life. Subsection 1.1.4 through some light on fatigue design of wind turbine blade using various tools. In this study, the open-source code MLife [188, 189] by NREL is selected for fatigue life estimation due to its accuracy and compatibility with MATLAB. The literature review presented in Subsection 1.1.1 also highlights the importance of cyclostationary analysis, and Subsection 1.1.4 recommended the reliability design of wind turbines against blade-tower collision and fatigue failure. Hence, this study also aims to investigate the reliability enhancement of the blade with the application SMA stiffener against blade-tower collision and fatigue failure.

1.3 Objectives

The literature review presented above clearly outlines the research activities related to the modelling, vibration control, fatigue and reliability analysis of wind turbine tower and blade under different operational scenarios. These studies justify the need for further research on this topic to develop more efficient engineering solution. In this context, the amplitude of blade deformation in along-wind direction is very high due to large aerodynamic loads, where mean component predominates. It often leads to blade-tower collisions, which is avoided by tilting the rotor and providing pre-cone angle as recommended by IEC 61400-1 [18].

While tilting induces additional stress on the gear tooth leading to damage and downtime for maintenance, pre-cone angles cause additional bending stress at the blade root resulting reduced operational life. Due to these reasons, reliability against blade-tower collision and fatigue life enhancement of a blade need to be investigated. With this in view, the present study aims to demonstrate the concept of longitudinal stiffening of a wind turbine blade using SMA tendon. The objectives of this proposal are as follows

- Develop a discrete reduced order mathematical model of wind turbine considering the dominant modes of the tower, drivetrain and blades. The blades are proposed to be axially stiffened by SMA tendons. The idea behind this proposal is to exploit the high strength offered by SMA in its austenite phase. This smart material's ability to regain its original state with no residual strain makes it an ideal material for prolonged use. The main aim is to improve the out-of-plane performance of the blade to reduce the dependence on the tilting of the shaft and the pre-coning of the blade for avoiding blade-tower impact.
- Demonstrate the performance of this passive stiffening strategy using benchmark wind turbine data and realistic aerodynamic loads. Carry out a sensitivity analysis to study the performance envelope of the proposed strategy over the operational range of the benchmark wind turbine. Compare the performance of proposed stiffener with other passive controllers.

SMA materials can undergo large recoverable stress at a higher temperature above austenite finish. Therefore, a semi-active version of the stiffener is proposed to enhance the control force, which is attained by Joule heating using current flow without affecting the overall aerodynamics of the blade. Thus, the following issues are proposed to be studied

- Derive appropriate model for stress-strain-temperature relation that tells the precise magnitude of current flow required to attain maximum response reduction. In this context, Nitinol is proposed due to its remarkable thermo-mechanical properties to recover large strains. Due to this tailor-made properties, Nitinol based stiffener has been observed to offer resistance which is difficult from stiffener of similar dimension and made of other material.
- Study the performance of the proposed control strategy under different operational scenarios and carry out sensitivity analyses to demonstrate the performance envelope of the proposed axial stiffener. In this context, two separate cases are studied, i.e. with the current flow to utilize super-elastic effect, which is termed as semi-active here and without current flow when the material operates at ambient temperature which is termed as passive. The rationale behind the passive case is to study the minimum guaranteed reduction that the proposed axial stiffening can achieve in case of any power failure.

Few works of literature presented in section 1.1 highlights the importance of cyclostationary analysis to develop a smart rotor blade. Although it is a popular topic of research, the performance of the controller under cyclostationary loading has remained an open problem. In this context, excessive deformation of the blade often leads to blade-tower collisions. Hence, level crossing analysis is an integral part of the safe design and operation of these rotors. With this in view, the present study aims to address the following issues

- Develop an efficient switching algorithm for semi-active vibration control of large wind turbine blade using SMA based longitudinal stiffener. It is envisaged to maintain the temperature of the material to generate maximum allowable control force.
- Investigate the cyclostationary characteristics of blade response with and without any longitudinal stiffener. Wavelet-based time-frequency analysis is proposed for this purpose to quantify the instantaneous frequency content and the second-order moment statistics of the blade response.
- Inspect the reliability of the proposed blade stiffening against a collision with the tower. This involves the formulation of the level crossing problem in the light of cyclostationary nature of the blade vibration using modified Rice formula where failure is modelled as a Poisson process.

In addition to vibration control, the literature highlights the importance of design against fatigue life. In order to extend the design life of modern multi-megawatt wind turbine blades, the stiffness and fatigue resistance of it need to be enhanced [190]. Thus, this work aims to investigate fatigue life improvement by SMA-based longitudinal stiffening, which can significantly reduce vibration in both out-of-plane and in-plane directions. The key contributions of this work are as follows

- Develop the spinning finite element model of a wind turbine blade having longitudinal stiffener for modal, dynamic and fatigue analysis. The material property of SMA tendon is modelled with the

help of constitutive relation and thermodynamic principle to investigate its impact on the modal and dynamic characteristics of the blade.

- Simulate blade responses and evaluate the stress profile with and without stiffener. Compare the performance of the proposed controller in passive and semi-active mode to reduce the blade root bending moment and stress profile.
- Estimate the fatigue life of a wind turbine blade with and without the controller. Also, compare the fatigue life improvement using passive and semi-active modes of operation, investigate the variation in peak stress and fatigue life of the blade for different diameters of the tendon.
- Investigate the effect of longitudinal stiffening on the fatigue reliability of the blade. Estimate the variation of reliability index and probability of failure for a higher design life of the blade.

1.4 Organization of the Thesis

This thesis aims to develop an efficient blade stiffening strategy to enhance its dynamic performance, which in turn improves its reliability and fatigue life. In this context, the outlines of this thesis are given below

- The current chapter (i.e. 1st chapter) presents an introduction to this work, which summarizes the history of wind turbines and literature review on its modelling, dynamics, vibration control, fatigue analysis and design. Finally, the motivation behind this research work and the objectives are presented, followed by the organization of the thesis.
- The 2nd Chapter discusses the basics of wind energy assessment and estimation of structural loads acting on a wind turbine. The variation of wind speed with time and height are demonstrated using wind data at Muppandal wind farm, India. The modelling of aerodynamic loads from the 3D wind field using BEM theory and hydrodynamic loads using the JONSWAP spectrum is presented along with gravitational load calculation.
- In the 3rd Chapter, the discrete reduced-order model of onshore and offshore horizontal axis wind turbines are developed considering dominant modes of blades, drivetrain and tower. This chapter discusses the modelling of equivalent aerodynamic damping and hydrodynamic damping along with modal load calculations. Then, the responses of a wind turbine are simulated using these models, which are validated with FAST.
- In the 4th Chapter, the formulations for the proposed longitudinal stiffening of the blade is derived using different shape memory alloy model and thermodynamic principle. Then, the effectiveness of this stiffener in passive and semi-active modes of operation are presented in terms of reduction in all dynamic components of the blade vibration. Finally, various sensitivity analyses are carried out to demonstrate the performance envelop of the proposed stiffener.
- Based on SMA stiffener's performance, the 5th Chapter investigates the safety of the wind turbine blade against excessive deformation using a level crossing problem in light of the cyclostationary nature of the blade vibration. It also explores the power consumption during semi-active control using an efficient voltage switching algorithm.
- In 6th Chapter, a spinning finite element model of stiffened blade is developed to investigate the impact of proposed stiffening strategy on its modal and dynamic characteristics. Then, modal analysis of blade with and without stiffener are carried out to demonstrate the improvement in bending stiffness. Finally, the responses of a wind turbine are simulated using this model, which are validated with FAST, and studied the performance of blade with passive and semi-active stiffener.
- The detailed fatigue analysis of a longitudinally stiffened blade is presented in Chapter 7 based on IEC 61400-3 guidelines. For this purpose, the longitudinal stresses over the blade profile are evaluated and demonstrated its variations. The improvement in fatigue reliability and its variation with higher design life are also explored in this chapter.
- Finally, Chapter 8 concluded with a brief discussion on the major contributions of this study along with plausible future developments.

Chapter 2

Loads on Wind Turbine

2.1 Introduction

Wind turbines are usually subjected to aerodynamic and time-dependent gravitational loads. Among them, aerodynamic force on the rotor act as a torque on the drivetrain's low-speed shaft, which is transmitted to the generator to produce electrical energy. Therefore, explicit estimation of aerodynamic loads is extremely important for wind turbine system design and analysis. Besides aerodynamic and gravitational forces, an offshore wind turbine is also exposed to wave load. The combined effect of wind and wave loads make the design of an offshore wind turbine more challenging. Also, the understanding of wind resource is necessary for site selection and wind turbines design. In this chapter, the power resource assessment for a site and the structural loads are discussed.

2.2 Wind Resource Assessment

The power assessment is extremely important since the initial investment for a wind turbine is very high. Also, the wind resource knowledge is necessary for the design of horizontal axis wind turbine and its components. Therefore, the statistics of wind resource variations and its effect on power production must be well known for an efficient design. The variation of wind resources is generally measured in terms of mean wind velocity at a particular height. The wind velocity at a location is initially studied from the available meteorological data. After the preliminary study, met mast or measurement tower is installed for detailed investigation if the region exhibits enough wind resource. Met mast is a tower usually made of steel with the wind measuring equipment like anemometer and weather vane. The anemometer is used to measure the speed of the wind, whereas the weather vane measures its direction. Wind speed and its direction can also be detected with Light Detection and Ranging (LIDAR), which is generally used to measure the upstream wind that eventually hitting the blade for advanced applications like feedback control [191].

The power generation of a turbine depends on the velocity of inflowing wind, as described in Eq. 1.1. The natural features heavily affect wind velocity at a particular site, e.g., presence of mountains, type of vegetation, proximity of ocean. The topography of a land also has major impact on the wind speed, which is significant in high mountain compared to sea level. The variation of wind with time is due to the atmospheric temperature changes, which is recorded at different time intervals. For site resource assessment, the hourly wind data is usually used, and the daily, monthly and annual variations are studied by averaging hourly data accordingly.

The mean wind speed varies with the height and it depends on the surface friction of the earth. The surface friction alters from location to location depending on the type of vegetation and human settlement. The surface roughness of irregular shaped forest and buildings are higher than the regular surfaces like water body. The variation of mean wind speed with height is evaluated using Logarithmic or Power law.

2.2.1 Logarithmic Wind Profile

Logarithmic law is derived from Ludwig Prandtl's mixing length theory. It is generally used to evaluate the wind speed at a height in the lower atmospheric boundary layer. The mean wind speed $v(h)$ at height h from the ground using this law is given by [42]

$$v\left(h\right) = \frac{v^*}{\kappa}\left[\ln\left(\frac{h-h_d}{h_0}\right) - \psi\left(h, h_0, L_M\right)\right] \tag{2.1}$$

where v^* is the friction velocity and κ is the von-Karman constant, which is approximately equal to 0.41. In Eq. 2.1, h_d is the height above ground at which mean wind speed is equal to zero due to obstacles [192], where h_0 is the surface roughness length and ψ is the stability function. This function is equal to zero for neutral stable atmospheric condition [17]. L_M is Monin-Obukhov length used to define the buoyancy effects on turbulent flows. The wind speed $v\left(h\right)$ at height h with reference to known wind speed at height h_r is evaluated as

$$v\left(h\right) = \frac{\ln\left(\frac{h-h_d}{h_0}\right) - \psi\left(h, h_0, L_M\right)}{\ln\left(\frac{h_r-h_d}{h_0}\right) - \psi\left(h, h_0, L_M\right)} v\left(h_r\right) \tag{2.2}$$

2.2.2 Power Law Wind Profile

Power law is the most widely used empirical method for finding wind speed at a projected height from the reference data. The variation of wind speed using power law is defined as [42]

$$v\left(h\right) = \left(\frac{h}{h_r}\right)^{\alpha_p} v\left(h_r\right) \tag{2.3}$$

where $v(h_r)$ is the known wind speed at a reference height h_r and α_p is power law exponent. The power law exponent depends on the stability of the atmosphere and varies with terrain, season, time of the day and temperature. For a neutral stable atmosphere, α_p can be taken as 0.143. Few researchers have also used Logarithmic law parameters for estimating α_p. Justus [193] correlated α_p as a function of know velocity $v(h_r)$ and height h_r as follows

$$\alpha_p = \frac{0.37 - 0.088\ln\left(v(h_r)\right)}{1 - 0.088\ln\left(\frac{h_r}{10}\right)} \tag{2.4}$$

Also, Counihan [194] developed a correlation between α_p and surface roughness (h_0) in the following form

$$\alpha_p = 0.24 + 0.096\log_{10} h_0 + 0.016\left(\log_{10} h_0\right)^2 \tag{2.5}$$

In general, Power law for wind profile is not reliable compared to Logarithmic law for heights below 20 m whereas it is more reliable for heights above 100 m. However, both of them offer similar result for altitude between 20-100 m in neutral atmospheric condition.

For example, the wind speed for Muppandal Wind Farm, Kanyakumari, Tamil Nadu, India (Latitude = 8.2596°, Longitude = 77.5367°) is evaluated at 90 m hub height using Power Law with Justus Power Law exponent to investigate the potential of wind resource. For this purpose, the speed and direction of wind at 10 m height for this region are collected from the MERRA [195] as shown in Fig. 2.1. Fig. 2.2 shows the hourly and daily average of wind speed at hub height for Muppandal wind farm. Here, it may be noted that the mean wind speed at hub height for this wind farm is obtained as 7.67 m/s. Apart from mean wind speed, its probability distribution is required for various statistical analysis and turbine design. The variation of annual mean wind speed for year-to-year is difficult to predict since it is a long term variation. But the variations within an year can be characterized using probability distribution, e.g. Weibull or Rayleigh distribution. Weibull distribution shows good fit in hourly variations of wind speed for a year in most of the sites [42]. It helps to identify the most frequent wind speed at a particular site. For highly fluctuating climates, the optimum rated speed of wind turbines at a particular site also can be evaluated based on the monthly performance index using hourly mean wind speed data [196]. Fig. 2.3 shows the Weibull distribution of wind speed at the hub height for Muppandal wind farm. For this site, the Weibull scale and shape parameters are obtained as 8.563 m/s and 3.207, respectively.

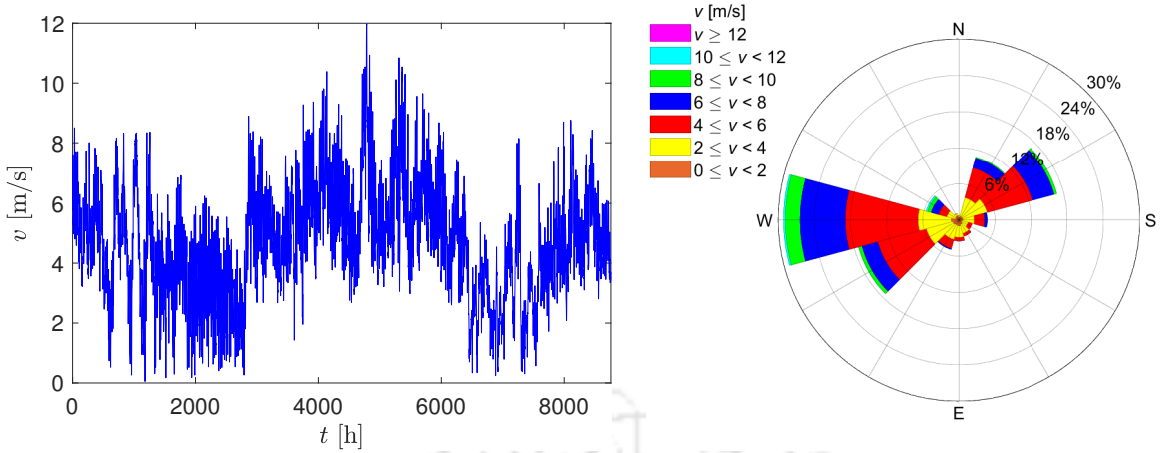

(a) (b)

Figure 2.1: Hourly average wind velocity at 10 m height of Muppandal wind farm from 1st January to 31st December 2019.; (a) time history and (b) wind rose.

2.3 Rotational Sampled Spectrum

The loads acting on a wind turbines are cyclic in nature. This is due to the fact that the force acting on a blade depends on its position. The fluctuating wind is generally simulated from stationary Rotationally Sampled Spectrum (RSS). It is based on the concept of Gust-Slicing by the airfoil of a rotor, which influences the flow variance corresponding to the rotational frequency and its harmonics. The RSS is obtained from the homogeneous and isotropic 1D flow spectrum (e.g. Kaimal or von-Karman). The power spectrum of wind approaching to a point on the rotating blade is given by the Fourier transform pairs [42], which are given by

$$S_u(f) = 4\int_0^\infty \kappa_u(\tau)\cos 2\pi f\tau d\tau \tag{2.6a}$$

$$\kappa_u(\tau) = \int_0^\infty S_u(f)\cos 2\pi f\tau df \tag{2.6b}$$

where f is the frequency in Hz. S_u and κ_u are the single sided power spectrum and autocorrelation function of wind speed fluctuations, respectively. The autocorrelation function κ_u is derived for a fixed point in space for longitudinal component of fluctuating turbulent wind from the input power spectrum (e.g. Kaimal or von-Karman) and then the relative autocorrelation functions for a rotating blade at different radial distances are evaluated. Finally, the rotationally sampled spectrum is obtained using Eq. 2.6a.

The input power spectrum for longitudinal component of the turbulence is obtained from commonly used Kaimal or von-Karman spectrum. The energy under Kaimal spectrum is spread over a frequency range with lower peak compared to von-Karman spectrum. The expression for Kaimal spectrum takes the following form

$$S_u(f) = \frac{4\sigma_v^2 L_K/\bar{v}}{(1+6fL_K/\bar{v})^{5/3}} \tag{2.7}$$

where L_K is the integral length scale of turbulence for Kaimal spectrum. $\bar{v}$ and σ_v are the mean and standard deviation of wind speed, respectively. The Kaimal spectrum provides a more appropriate atmospheric turbulence model, while von-Karman spectrum provides a better match for the wind tunnel test data. The expression for von-Karman spectrum is given by

$$S_u(f) = \frac{4\sigma_v^2 L_v/\bar{v}}{\left[1+70.8\left(fL_v/\bar{v}\right)^2\right]^{5/6}} \tag{2.8}$$

where L_v is the integral length scale of turbulence.

In this study, the turbulent wind flow is simulated using TurbSim [17], which modifies the simulation using horizontal and vertical wind shear along with its spatial coherence. Once the 3D wind field is simulated,

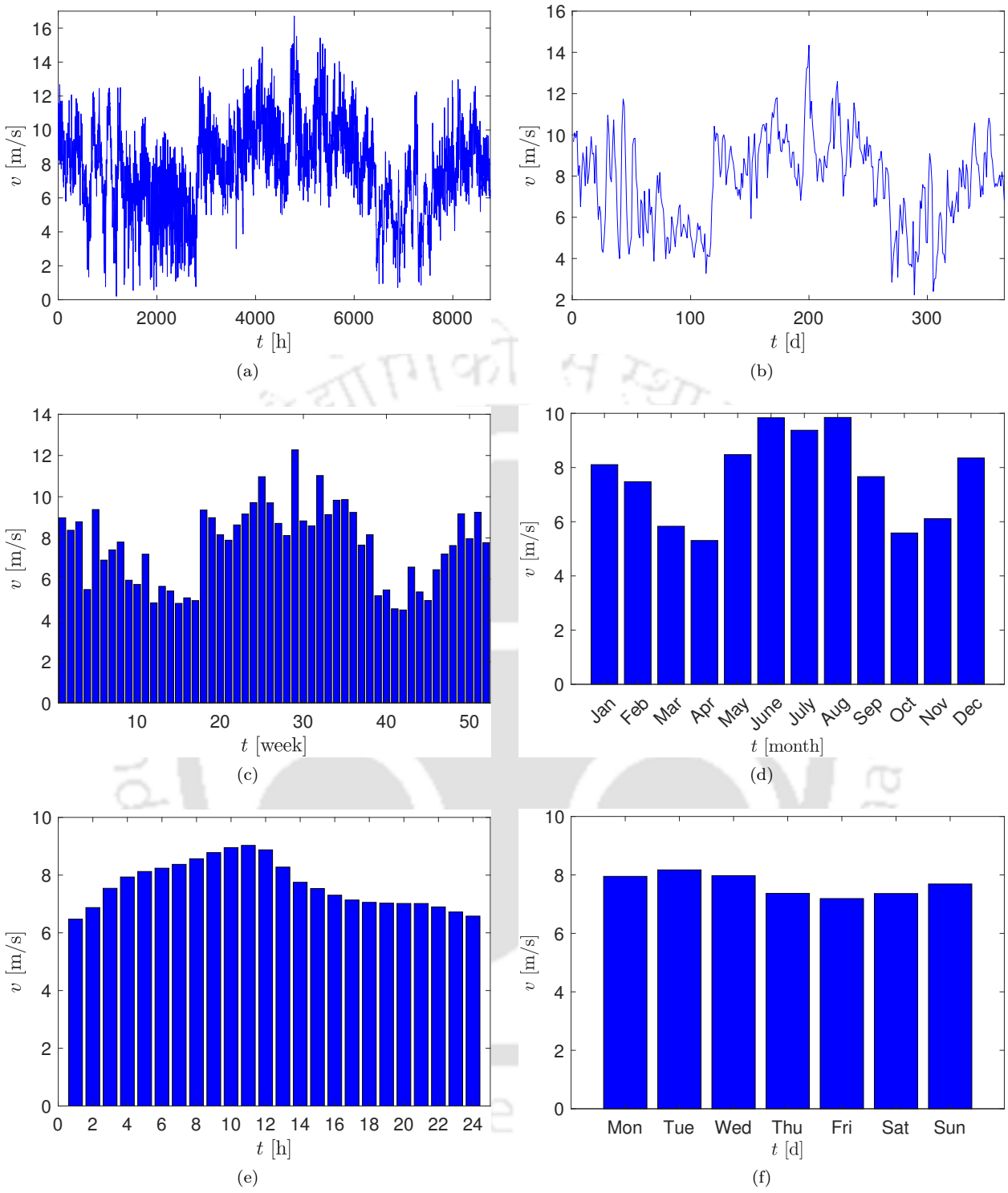

Figure 2.2: Wind speed at hub height of Muppandal wind farm from 1st January to 31st December 2019; (a) hourly average, (b) daily average, (c) weekly average, (d) monthly average, (e) daily ensemble average and (f) weekly ensemble average.

Blade Element Momentum (BEM) theory is applied to evaluate the aerodynamic load time history using the algorithm proposed by Ning [27].

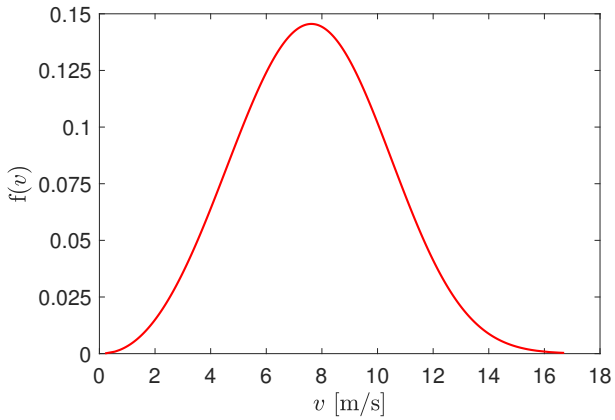

Figure 2.3: Weibull distribution of wind speed at hub height of Muppandal wind farm from 1st January to 31st December 2019.

2.4 Aerodynamics of Blade Airfoil

The lift and drag forces are generated as the wind passes over the airfoil shape of the blade. When the wind flows around the airfoil, it forces the blade to rotate due to the tangential component of the lift force and simultaneously the rotor forces the wind to move around is known as wake effect, where the wind speed is reduced. The flow in the wake having two components, one in axial direction and the other in tangential direction to the blade rotation, which causes rotation in the wake. The lift force acts in the plane of rotation of wind turbine, whereas the drag force acts parallel to the direction of the flow. The blade should have a high lift-drag force ratio to generate adequate rotational speed. Therefore, usually the blades are twisted to an angle to produce essential lift-drag force ratio. It is very important to estimate these aerodynamic forces accurately since the design of the whole turbine system depends on it.

In fluid dynamics, the rotating devices like wind turbine or windmill, aviation and marine propeller, helicopter rotor, etc. are usually represented by Rankine disk actuator for developing the mathematical model using momentum theory. The device which converts the fluid energy state from translation to rotation or vice versa about an axis is known as Rankine disk actuator. Following subsections describe the derivation of aerodynamic loads based on blade element momentum theory, which is combination of blade element theory and momentum theory (or actuator disc theory).

2.4.1 Stream-Tube and Actuator Disc Concept

Wind turbines rotate while converting the kinetic energy of the wind whose velocity is reduced (for a constant mass flow) at the downstream side. In this process, it is assumed that the energy of the wind flowing outside the swept area remains unaffected and separated from the mass of air passing through the rotor disc. Therefore, a stream-tube can be assumed by extending the boundary surface of the affected air, as shown in Fig. 2.4. The presence of actuator disc causes gradual slow down of fluid flow in the upstream such that the air meets the disc with a lower velocity (v_d) than the free stream velocity (v_∞). Since, the velocity of air within the stream-tube is reduced without affecting mass flow, the cross-sectional area of stream-tube should increase gradually to accommodate the slowly moving air for an in-compressible flow. In other words, the pressure at upstream of the disc (p_d^+) increases due to the velocity drop without any work done. Further, the air pressure dropped below atmospheric pressure at the disc due to the work done and it starts gradually increasing just after leaving the disc (i.e. downstream of the disc, p_d^-) due to velocity drop. This region of air flow with reduced velocity and pressure is known as wake. Finally, the static pressure of air at the downstream returns back to atmospheric pressure (p_∞) with a reduced velocity (v_w). Stream-tube and actuator disc concept relies on following assumptions

- the fluid passing through the stream-tube is homogeneous, in-compressible and steady state flow with no frictional drag.
- number of blades considered as infinite and uniform thrust acting over it.
- undisturbed air pressure at the upstream and downstream of the rotor.

- the disc doesn't cause swirl and the wake at the down stream is non-rotating.

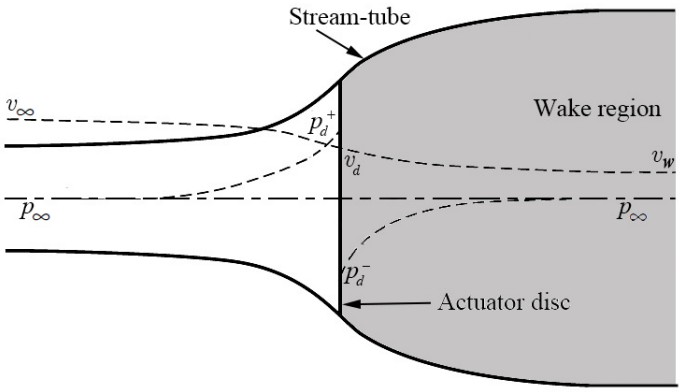

Figure 2.4: Schematic diagram of the stream-tube with actuator disc [42].

The mass flow rate ($\dot{m}$) through the cross section of the stream-tube is evaluated as

$$\frac{dm}{dt} = \rho_a A v \tag{2.9}$$

where ρ_a is the density of air and A is the cross-sectional area of the stream-tube and v is the velocity of flow. The mass flow rate $\dot{m}$ along the stream-tube must be same everywhere. Therefore, it is equated at the actuator disk (i.e. with the same in upstream and downstream) using Eq. 2.9, i.e.

$$\rho_a A_\infty v_\infty = \rho_a A_d v_d = \rho_a A_w v_w \tag{2.10}$$

where subscripts ∞, d and w denote the conditions at far upstream, at disc and far wake, respectively. Let us consider a fraction of free stream flow velocity induced by the disc, the ratio of decrease in flow velocity between the free stream and the disc is known as axial induction factor or inflow factor. Therefore, flow velocity at disc is given by

$$v_d = v_\infty(1-a) \tag{2.11a}$$

where

$$a = \frac{(v_\infty - v_d)}{v_\infty} \tag{2.11b}$$

2.4.2 Conservation of Linear Momentum

Using conservation of linear momentum, the rate of change of momentum or thrust due to overall change in velocity can be written as

$$T_d = \rho_a A_d v_d \left(v_\infty - v_w\right) \tag{2.12}$$

Bernoulli's principle is applied on either side of the disc with respect to the condition at disc to obtain the pressure difference. The potential energy due to gravity does not changes through out the stream-tube since the flow is in-compressible and horizontal. Therefore, Bernoulli's equation can be written as

$$p_\infty + \frac{1}{2}\rho_a v_\infty^2 = p_d^+ + \frac{1}{2}\rho_a v_d^2 \qquad \text{upstream} \tag{2.13a}$$

$$p_d^- + \frac{1}{2}\rho_a v_d^2 = p_w + \frac{1}{2}\rho_a v_w^2 \qquad \text{downstream} \tag{2.13b}$$

In the above equation, p_∞ and p_w are the pressure of the fluid at far upstream and downstream respectively whereas p_d is the pressure at the actuator disc. Assuming the flow is incompressible (i.e. $p_\infty = p_w$) and substituting their expression in Eq. 2.13 lead to the following form

$$\left(p_d^+ - p_d^-\right) = \frac{1}{2}\rho_a \left(v_\infty^2 - v_w^2\right) \tag{2.14}$$

$$T_d = \frac{1}{2}\rho_a A_d \left(v_\infty^2 - v_w^2\right) \tag{2.15}$$

Therefore, the far wake velocity is obtained by equating Eq. 2.12 and Eq. 2.15, which gives

$$v_w = v_\infty(1 - 2a) \tag{2.16}$$

That is, as the induced velocity (av_∞) at the disc increases, a increases and the wind speed reduces at the downstream side of the disc. If $a \geq 0.5$, the far wake velocity become zero or even negative as per Eq. 2.16. In that case, above mentioned method can not be used and an empirical modification of rotor thrust coefficient is applied. On substituting Eq. 2.16 and Eq. 2.11a in Eq. 2.12, the thrust force becomes

$$T_d = 2\rho_a A_d v_\infty^2 a\,(1 - a) \tag{2.17}$$

Therefore, the rate of work done by the force on the disc is given by

$$P_d = T_d v_d = 2\rho_a A_d v_\infty^3 a\,(1 - a)^2 \tag{2.18}$$

The power of inflowing wind, passing through the same area (i.e. A_d) in the absence of rotor disc, is expressed by

$$P_\infty = \frac{1}{2}\rho_a A_d v_\infty^3 \tag{2.19}$$

Therefore, power coefficient can be defined as

$$C_P = \frac{P_d}{P_\infty} = 4a\,(1 - a)^2 \tag{2.20}$$

At maximum value of C_P, its first derivative with respect to axial induction factor a is equal to zero. Therefore, corresponding axial induction factor can be obtained as

$$\frac{dC_P}{da} = 4\,(1 - a)\,(1 - 3a) = 0 \tag{2.21}$$

Solving above equation gives axial induction factor (a) corresponding to the maxima, which is equal to $\frac{1}{3}$ and the corresponding maximum value of C_P can be obtained as

$$C_{P_{max}} = \frac{16}{27} = 59.3\% \tag{2.22}$$

As discussed in the previous chapter, this maximum limit of power coefficient is known as Betz limit or Lanchester-Betz limit. Note that, this limit is not due to any limitations in design of the structure, e.g. deficiencies like mechanical or electrical efficiency factors. Similarly, the non-dimensional thrust coefficient can be obtained from Eq. 2.17 as follows

$$C_T = \frac{T_d}{T_\infty} = 4a\,(1 - a) \tag{2.23}$$

where $T_\infty = P_\infty v_\infty^{-1}$. Therefore, thrust coefficient C_T corresponding to the maximum power output is equal to $\frac{8}{9}$. The maximum thrust coefficient is observed at axial induction factor, $a = 0.5$ as shown in Fig. 2.5. It means the maximum thrust does not correspond to the maximum power output.

2.4.3 Stream-Tube with Rotor Disc Concept

The air passing through the rotor disc exerts a torque on it, and the rotor disc imposes an equal and opposite torque on the air [42]. This reaction causes the fluid in the downstream to rotate in an opposite direction of the disc rotation, as shown in Fig. 2.6a. Let us consider that a fraction of disc rotation velocity Ω causes the fluid in the downstream to rotate with velocity ω. The tangential velocity of the flow in the upstream of the disc is equal to zero. It gradually increases when the air passes over the airfoil and becomes equal to the tangential velocity of the disc at rotor plane (or middle of the rotor disc). It is formed in reaction to the

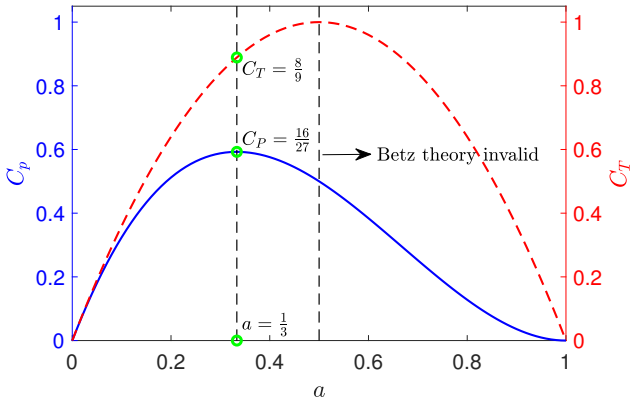

Figure 2.5: Variation of power coefficient, C_P and thrust coefficient, C_T with axial induction factor a.

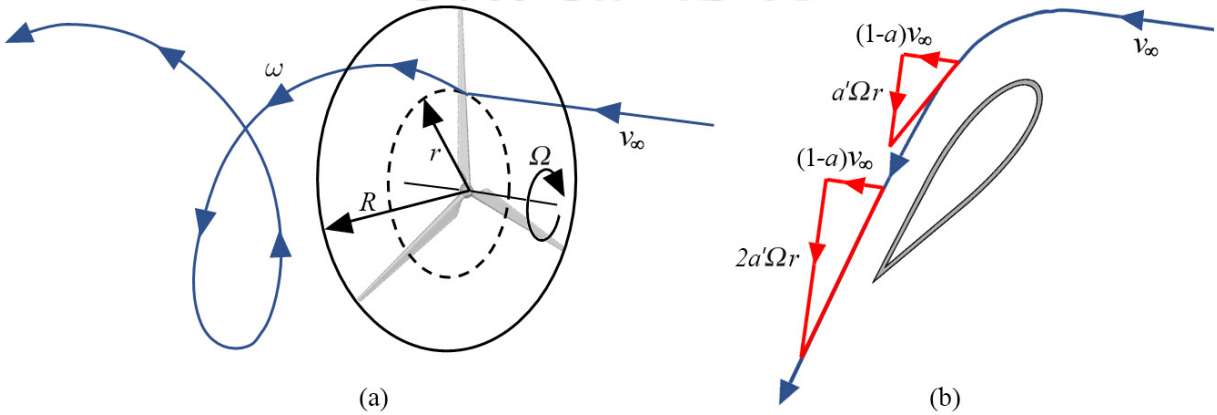

Figure 2.6: Air particle trajectory; (a) passing through the rotor disc and (b) tangential velocity growth.

torque of disc rotation. It further increases to twice of the tangential velocity of the disc at the downstream and becomes constant as the flow moves in the wake, which is shown in Fig. 2.6b. Therefore, the tangential induction factor can be written as

$$a' = \frac{\omega}{2\Omega} \tag{2.24}$$

2.4.4 Conservation of Angular Momentum

The tangential velocity of the rotor disc increases with the distance from the centre of rotation and the tangential velocity of air flow also varies with radial distance (refer Fig. 2.6a). Hence, an annular ring of the rotor disc at a distance r from the centre and radial width δr is considered for investigating the variation of both induced velocities (i.e. axial and tangential velocities). The thrust due to the axial momentum on the annular ring is obtained by modifying Eq. 2.17, which is given by

$$\delta T = 4\pi r \rho_a v_\infty^2 a\,(1-a)\,\delta r \tag{2.25}$$

Using conservation of angular momentum, the rate of change of angular momentum or torque due to overall change in velocity can be written as

$$\delta M = 4\pi r^3 \rho_a v_\infty \Omega\,(1-a)\,a'\delta r \tag{2.26}$$

2.4.5 Blade Element Momentum Theory

Blade Element Momentum (BEM) theory is the most popular tool for estimating aerodynamic forces on a rotating blade due to their computational efficiency as compared to other methods like Computational Fluid Dynamics (CFD). It models the behaviour of the rotor based on geometric and aerodynamic properties of the airfoil. The blade is assumed to be a collection of 2D airfoils along its longitudinal dimension and

the flow passing over each airfoil is modelled by balancing the momentum on the either side of the rotor plane. Thus, it is a combination of blade element and momentum theories. Blade element theory assumes the aerodynamic force on different blade elements are independent (no interaction between the elements) and solely depend on the lift and drag coefficients of the individual airfoil. On the other hand, momentum theory (or disk actuator theory) is based on the conservation laws in fluid dynamics. In other words, it is based on the momentum balance of the airflow about the rotor plane as discussed in Subsection 2.4.2 and Subsection 2.4.4. Aerodynamic forces acting at different points along the length of the blade change due to difference in chord length (c), rotational speed (Ωr) and twist angle (θ_t). Therefore, the blade is discretized into sufficiently large number of elements, as shown in Fig. 2.7 to evaluate the aerodynamic force at each element. The total load is evaluated by integrating them along the length of the blade. A set of equations are formed using these two theories, which are solved iteratively.

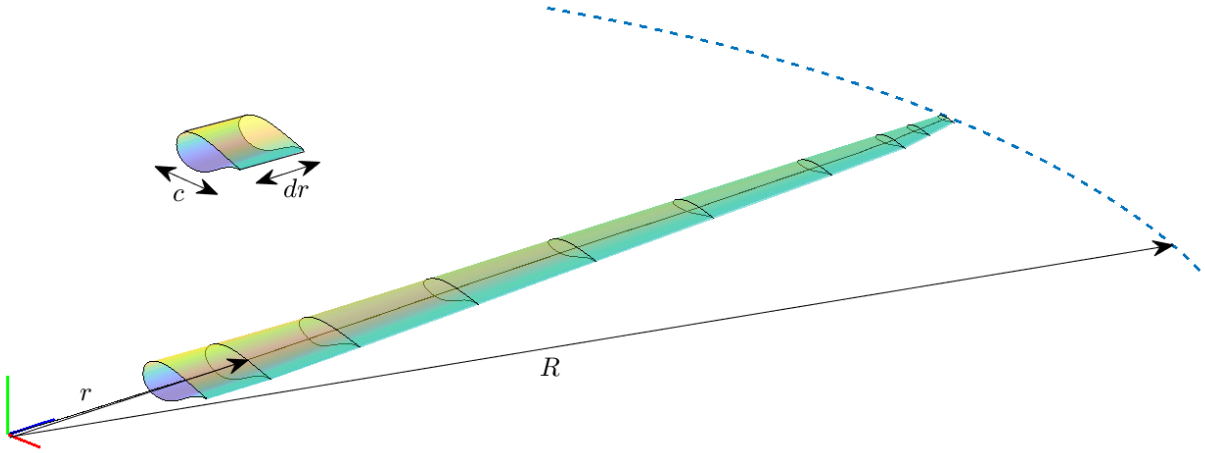

Figure 2.7: Schematic diagram of Blade Element Model.

The flow in the wake having two velocity components, one in the axial direction and the other in the tangential direction of the blade rotation as discussed in Section 2.4. Therefore, the velocity induced on the rotor plane has two components, as shown in Fig. 2.8. From this figure, the relative flow velocity v_{rel} can

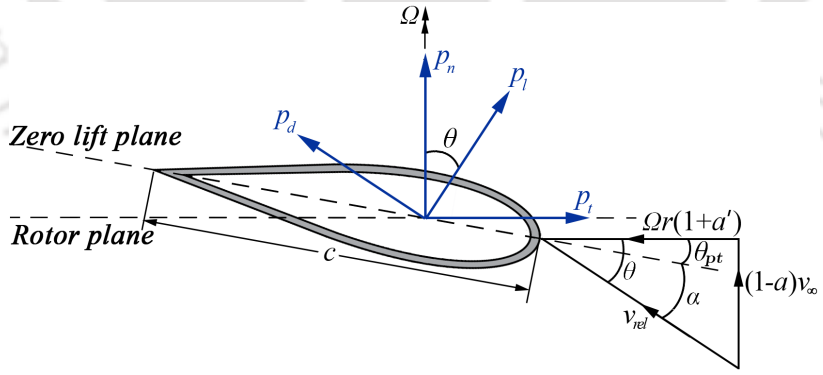

Figure 2.8: Schematic diagram of 2D airfoil with the velocity and force components.

be obtained as

$$v_{rel}(r,t) = \left[((1-a)v_\infty)^2 + ((1+a^{'})\Omega r)^2\right]^{1/2} \tag{2.27}$$

which acts at an angle θ with the rotor plane, which can be expressed by

$$\theta = \tan^{-1}\left[\frac{v_\infty(1-a)}{\Omega r(1+a')}\right] \tag{2.28}$$

The lift and drag forces are acting on the blade element along the perpendicular and parallel to the direction of incoming flow, as shown in Fig. 2.8. These forces on a radial length δr of the blade element can be

evaluated using coefficient of lift and drag, which are given by

$$\delta p_l = \frac{1}{2}\rho_a v_{rel}^2 c(r) C_l(\alpha)\delta r \tag{2.29a}$$

$$\delta p_d = \frac{1}{2}\rho_a v_{rel}^2 c(r) C_d(\alpha)\delta r \tag{2.29b}$$

In the above equation, ρ_a is the density of air and $c(r)$ is the chord length at a radial distance r from the center of rotation. The lift and drag coefficients C_l and C_d in the above equations depend on the angle of attack (α) of the respective airfoil. Thus, the normal and tangential forces acting on an annular ring of the rotor disc of a N_b bladed turbine are evaluated as

$$\delta p_n = \delta p_l \cos\theta + \delta p_d \sin\theta = \frac{1}{2} N_b \rho_a v_{rel}^2 c(r)[C_l(\alpha)\cos\theta + C_d(\alpha)\sin\theta]\delta r \tag{2.30a}$$

$$\delta p_t = \delta p_l \sin\theta - \delta p_d \cos\theta = \frac{1}{2} N_b \rho_a v_{rel}^2 c(r)[C_l(\alpha)\sin(\theta) - C_d(\alpha)\cos(\theta)]\delta r \tag{2.30b}$$

It can be noted that the axial thrust on an annular ring is equal to the normal force, i.e. $\delta T = \delta p_n$ while the torque can be evaluated by multiplying tangential force δp_t with the radial distance r, i.e. $\delta M = \delta p_t r$.

Further, equating the axial thrust acting on the annular ring from Eq. 2.25 and Eq. 2.30a gives the following form

$$N_b v_{rel}^2 c(r) C_n(\alpha,\theta) = 8\pi r v_\infty^2 a\,(1-a) \tag{2.31}$$

where $C_n(\alpha,\theta) = C_l(\alpha)\cos\theta + C_d(\alpha)\sin\theta$. Similarly, equating the torque acting on the annular ring using Eq. 2.26 and Eq. 2.30b (i.e. $\delta M = \delta p_t r$) gives the following form

$$N_b v_{rel}^2 c(r) C_t(\alpha,\theta) = 8\pi r^2 v_\infty \Omega\,(1-a)\,a' \tag{2.32}$$

where $C_t(\alpha,\theta) = C_l(\alpha)\sin(\theta) - C_d(\alpha)\cos(\theta)$. Solving Eq. 2.31 and Eq. 2.32 gives

$$a = \frac{\sigma_r C_n(\alpha,\theta)}{\sigma_r C_n(\alpha,\theta) + 4\sin^2\theta} \tag{2.33a}$$

$$a' = \frac{\sigma_r C_t(\alpha,\theta)}{4\sin\theta\cos\theta - \sigma_r C_t(\alpha,\theta)} \tag{2.33b}$$

where σ_r is the blade solidity, which is defined as the total blade area in an annular ring divided by the total area of the annular ring at a radial distance r, i.e. $\sigma_r = \frac{N_b c}{2\pi r}$. Since, the flow angle in Eq. 2.33 is a function of the flow induction factors as given in Eq. 2.28, an iterative procedure is adopted to find them, i.e. a and a'. Thus, the normal and tangential forces can be evaluated from Eq. 2.30a and Eq. 2.30b by substituting relative velocity obtained from Eq. 2.27 using these flow induction factors.

One of the major draw back of the BEM theory is that, it does not account for the effect of vortex shedding at the tip of the blade into wake. Therefore, some modifications are required in the formulations of BEM theory to account for various correction including tip and hub losses.

2.4.5.1 Corrections

The inflow angle in Fig. 2.8 becomes very small for a large axial induction factor and the contribution of lift force in the tangential direction also reduces. This is reflected in lower power production due to reduced torque, which generally occurs at the tip of the blade, i.e. tip-loss. The azimuthal variation of axial induction factor is required to incorporate this loss. Some correction factors are used with blade element momentum theory to address this issue.

Prandtl [197] proposed the behaviour of a particle in the downstream using wake-disc model and developed an approximate solution that account for tip-loss. This tip-loss correction factor is given by

$$F_{\text{loss}}^{\text{tip}}(r) = \frac{2}{\pi}\cos^{-1}\left[e^{-\frac{N_b(R-r)}{2r\sin\theta}}\right] \tag{2.34}$$

Similar to tip-loss correction, hub-loss (or root-loss) correction is obtained as [42]

$$F_{\text{loss}}^{\text{hub}}(r) = \frac{2}{\pi}\cos^{-1}\left[e^{-\frac{N_b(r-R_{hub})}{2r\sin\theta}}\right] \tag{2.35}$$

where R_{hub} is the hub radius. Thus, the complete tip/hub loss factor is $F_L = F_{\text{loss}}^{\text{tip}} \cdot F_{\text{loss}}^{\text{hub}}$. Therefore, the thrust and torque forces in Eq. 2.25 and Eq. 2.26 are modified in the following form

$$\delta T = 4\pi r \rho_a v_\infty^2 a\,(1-a)\,F_L \delta r \tag{2.36a}$$

$$\delta M = 4\pi r^3 \rho_a v_\infty \Omega\,(1-a)\,a' F_L \delta r \tag{2.36b}$$

where the flow induction factors are evaluated as

$$a = \frac{\sigma_r C_n(\alpha,\theta)}{\sigma_r C_n(\alpha,\theta) + 4F_L \sin^2\theta} \tag{2.37a}$$

$$a' = \frac{\sigma_r C_t(\alpha,\theta)}{4F_L \sin\theta\cos\theta - \sigma_r C_t(\alpha,\theta)} \tag{2.37b}$$

Further, Glauert proposed an empirical relationship for the thrust coefficient based on experimental data, when the axial induction factor is greater than 0.4. It has the following form

$$C_T = \begin{cases} 4a(1-a) & \text{if} \quad a \le a_c \\ 4(a_c^2 + (1-2a_c)a) & \text{if} \quad a > a_c \end{cases} \tag{2.38}$$

In the above equation, $a_c \simeq 0.2$. The flow induction factor using Glauert's correction can be evaluated as

$$a = \begin{cases} \frac{1}{1+K} & \text{if} \quad a \le a_c \\ \frac{1}{2}\left[2 + K(1-2a_c) - \sqrt{(K(1-2a_c)+2)^2 + 4\left(Ka_c^2 - 1\right)}\right] & \text{if} \quad a > a_c \end{cases} \tag{2.39}$$

where $K = \frac{4\sin^2\theta}{\sigma_r C_n(\alpha,\theta)}$. Similar to Glauert's empirical relationship, many others have proposed empirical curves to fit the same experimental data. But, these empirical curves do not consider the tip or hub losses. Few researchers recommended multiplying loss factor with axial induction factor to fix the curve, but this leaves mathematical discontinuity. In this context, Buhl [24] proposed a modified version of Glauert empirical curve to include tip and hub loss corrections for axial induction factor greater than 0.4 as

$$C_T = \frac{8}{9} + \left(4F_L - \frac{40}{9}\right)a - \left(4F_L - \frac{50}{9}\right)a^2 \tag{2.40}$$

2.4.5.2 Ning's Model

Though conceptually straightforward, solving BEM equations with high precision accurately and efficiently can be challenging. For numerically converging the axial and tangential induction factors, several solution techniques are available in the literature [198, 199]. In certain regions of the rotor blade design space, these approaches demand substantial computational cost to achieve convergence, else they suffer numerical instability. In this context, a solution technique proposed by Ning [27] assure convergence at a super-linear rate. In this proposal, the solution of the BEM equation is segmented into three regions (i.e. momentum, empirical and propeller break) to evaluate the optimal flow angle θ as opposed to traditional approach for optimal induction factors to enhance the convergence. Therefore, the number of equations to be optimized are reduced to one from two equations in BEM theory (i.e. Eq. 2.33a and Eq. 2.33b). The step by step procedure of Ning's BEM algorithm is given below

1. Assume an initial value for local inflow angle (θ)

2. Compute local angle of attack, i.e. $\alpha = \theta - \theta_{pt}$ as shown in Fig. 2.8
3. Estimate the lift and drag coefficients, i.e. $C_l(\alpha)$ and $C_d(\alpha)$ from the airfoil characteristics using angle of attack (α)
4. Find the coefficients of normal $C_n(\alpha, \theta)$ and tangential $C_t(\alpha, \theta)$ forces.
5. Evaluate the flow induction factors a and a' using Eq. 2.37
6. Check the residual error in the governing equation
7. Assume another value of local inflow angle until the residual error converges to zero. Brent's root finding technique is proposed here to find the solution.

The local thrust coefficient for an annular ring of the rotor disc is given by blade element theory as follows

$$C_T = \left(\frac{1-a}{\sin\theta}\right)^2 C_n(\alpha,\theta)\sigma_r \tag{2.41}$$

Axial induction factor with Buhl's correction can be evaluated by equating above equation with Eq. 2.40, which gives the following form after simplification

$$a = \frac{\gamma_1 - \sqrt{\gamma_2}}{\gamma_3} \tag{2.42}$$

where

$$\gamma_1 = \frac{2F_L}{K} - \left(\frac{10}{9} - F_L\right) \tag{2.43a}$$

$$\gamma_2 = \frac{2F_L}{K} - F_L\left(\frac{4}{3} - F_L\right) \tag{2.43b}$$

$$\gamma_3 = \frac{2F_L}{K} - \left(\frac{25}{9} - 2F_L\right) \tag{2.43c}$$

In the above expression, $K = \frac{4F_L \sin^2\theta}{\sigma_r C_n(\alpha,\theta)}$. This is valid for axial flow induction factor between 0.4 and 1. For axial flow induction factor greater than 1, the coefficient of thrust can be evaluated as

$$C_T = 4a(a-1)F_L \tag{2.44}$$

Thus, equating above equation with Eq. 2.41 and simplifying yields

$$a = \frac{1}{1-K} \tag{2.45}$$

2.5 Hydrodynamic Load

Ocean wave profiles are generally simulated from the zero mean Gaussian stationary wave spectrum that correlates energy with the parameters essential for wave formation (i.e. fetch length, effective depth). Commonly used spectrum for this purpose are Pearson-Moskowitch (PM) spectrum [32] and Joint North Sea Wave Project (JONSWAP) spectrum [33]. The PM spectrum represents fully developed sea states while JONSWAP spectrum is effective for developing sea states, which is used in this thesis to simulate the wave time history for a given wave height H_s and spectral peak period T_p. It is an improved version of the PM spectrum to model large waves. The PM spectrum is given by

$$S_{PM}(f) = 0.3125 H_s^2 f_p^4 f^{-5} \exp\left\{-1.25\left(\frac{f_p}{f}\right)^4\right\} \tag{2.46}$$

where f_p is the peak frequency. JONSWAP spectrum is obtained from this spectrum, which has the following form [19]

$$S_{JS}(f) = C(\gamma).S_{PM}(f).\gamma^{\alpha_h} \tag{2.47}$$

Here, it may be noted that $C(\gamma)$ and γ are the normalizing parameter and peak shape parameter, respectively. These parameters help to squeeze the PM spectrum within a narrow frequency band keeping the area under these two spectra same. Due to this reason, the variance corresponding to f_p is more in case of JONSWAP spectrum reflecting in large wave amplitude that represents high states. The expression for $C(\gamma)$ is given by [19]

$$C(\gamma) = \frac{\int_0^\infty S_{PM}(f)df}{\int_0^\infty \gamma^\alpha S_{PM}(f)df} = 1 - 0.287\ln(\gamma) \tag{2.48}$$

where γ depends on the wave height and peak period (i.e. H_s and T_p), which is given by

$$\gamma = \begin{cases} 5 & \text{for } T_p/\sqrt{H_s} \leq 3.6 \\ \exp\left(5.75 - 1.15T_p/\sqrt{H_s}\right) & \text{for } 3.6 < T_p/\sqrt{H_s} \leq 5.0 \\ 1 & \text{for } T_p/\sqrt{H_s} > 5.0 \end{cases} \tag{2.49}$$

Parameter α_h in Eq. 2.47 is given by the following expression

$$\alpha_h = \exp\left[-\frac{(f-f_p)^2}{2\sigma^2 f_p^2}\right] \tag{2.50}$$

where σ is a constant whose value is 0.07 for frequency less than or equal to the peak frequency and 0.09 when it is more [42]. Here, it may be noted that parameter γ correlates the peak time period T_p with the zero crossing time T_z, which is given by

$$T_z = T_P\sqrt{\frac{5+\gamma}{11+\gamma}} \tag{2.51}$$

Above expression of zero crossing time is for the 1D surface wave generated at a fixed point. However, sea wave at a fixed point also depends on the direction of propagation. Therefore, it is completely described by the directional spectrum, which is defined using the following form

$$S(f,\theta) = S(f).D(f,\theta) = S(f).D(\theta) \tag{2.52}$$

$$D(\theta) = \begin{cases} \frac{2}{\pi}\cos^2(\theta) & for \quad -\frac{\pi}{2} < \theta < \frac{\pi}{2} \\ 0 & \text{otherwise} \end{cases} \tag{2.53}$$

Function $D(\theta)$ in the above equation is deterministic and helps to simulate the 2D wave propagation. Once the directional spectrum is completely defined, wave time history can be simulated using linear superposition of infinite number of sinusoids, which is expressed in the following double summation

$$w(x,y,t) = \sum_{i=1}^{\infty}\sum_{j=1}^{\infty}\sqrt{2S(f_i,\theta_j)\Delta f_i \Delta\theta_j}.\cos[k_i x\cos(\theta_j) + k_i y\sin(\theta_j) - f_i t - \epsilon_{ij}] \tag{2.54}$$

In the above expression, $w(x,y,t)$ is the wave amplitude time signature at a location (x,y) at the surface and ϵ_{ij} is the uniformly distributed phase angle between 0 to 2π. The wave velocity and acceleration [i.e. $\dot{w}(x,y,t)$ and $\ddot{w}(x,y,t)$] can be evaluated by appropriately differentiating Eq. 2.54 or by simulating the time histories from the respective directional spectrum. Finally, the force acting on a static obstacle to the flow, say monopile, can be obtained from Morisson's equation, which is given by [19]

$$\delta F = \frac{\pi D_p^2 \rho_w}{4} C_m \ddot{w}\delta h + \frac{\rho_w}{2} C_d D_p \dot{w}|\dot{w}|\delta h \tag{2.55}$$

In the above equation, D_p is the diameter of the body objecting the flow while δh is the differential segment over which the force δF acts. The parameter C_m and C_d are the coefficients for fluid inertia and viscous drag forces, respectively.

2.6 Gravitational Load

Apart from aerodynamic and hydrodynamic forces, wind turbines are also subjected the force due to gravitational field. The components of gravitational force on the blade are time dependent sinusoids. As the blade rotates, in-plane bending moment acting on it varies due to gravity. The gravitational in-plane bending moment is maximum when the blade is horizontal. It is approximately 10 times more than the same due to wind (i.e. in-plane aerodynamic force). Therefore, gravitational force is a major source of fatigue load on a blade [42]. This force can be resolved into two components as shown in Fig. 2.9. The longitudinal

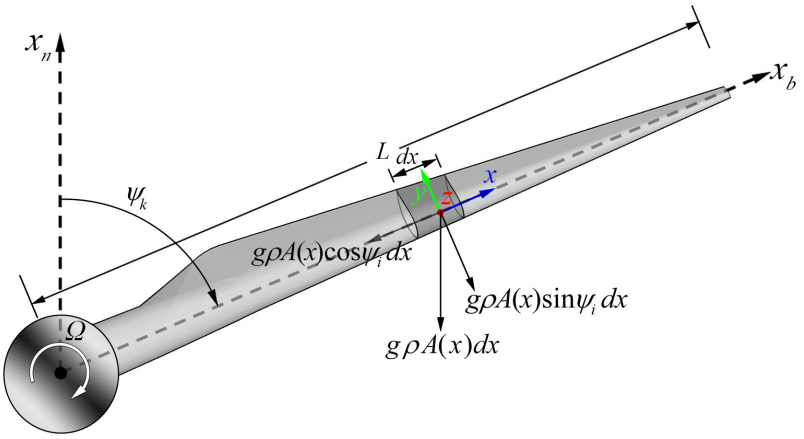

Figure 2.9: Schematic diagram of (a) gravitational load acting on the blade and (b) 2D airfoil with the velocity and force components.

component (i.e. along the length of the blade) and the component orthogonal to it can be evaluated as

$$F_{gx,i} = -g\cos\psi_i \int_0^{l_e} \rho_b A(x)dx \tag{2.56a}$$

$$F_{gy,i} = -g\sin\psi_i \int_0^{l_e} \rho_b A(x)dx \tag{2.56b}$$

where g is the gravitational force and $\psi_i = \Omega t + \frac{2\pi}{N_b}(i-1)$ for N_b bladed system, $i = 1, 2 \ldots N_b$. In Eq. 2.56, l_e and ρ_b are the element length and density of blade material, respectively. $A(x)$ is linearly varying cross section area of the blade.

2.7 Summary

This chapter deals with aerodynamics of wind turbine, i.e. wind energy assessment and aerodynamic load calculation. One of the important characteristic of the wind flow is its variability with geographical and temporal conditions. The variation of wind speed with time and height for the example case are studied using the wind data of India's largest wind farm, i.e. Muppandal wind farm. The wind speed also changes with the presence of turbine. This phenomenon is explained using stream tube and actuator disc concepts. The air passing through the rotor causes aerodynamic lift and drag forces on it, which drive the low-speed shaft of the drivetrain and subsequently high-speed shaft of the generator to produce the electrical energy. These aerodynamic forces acting on horizontal axis wind turbine blade are derived based on Blade Element Momentum (BEM) theory. Various modifications/corrections in BEM theory for tip and hub losses are also discussed along with Ning's approach for solution of BEM equations. Apart form aerodynamic loads, this chapter also gives an insight to the estimation of hydrodynamic and gravitational loads. The expression for hydrodynamic loads are derived using Morisson's equation, where the wave amplitude time history is modelled using JONSWAP spectrum and directional spectrum. Finally the gravitational loads on rotating blades are discussed in detail. These structural loads (i.e. aerodynamic, hydrodynamic and gravitational) on wind turbines are further used for various analysis in the following chapters.

Chapter 3

Discrete Reduced Order Model of HAWT

3.1 Introduction

This chapter demonstrates the modelling of wind turbine in discrete reduced order framework considering dominant modes of the tower, drivetrain and blades. Three-dimensional wind field passing through the rotor plane is simulated using TurbSim [17]. Aerodynamic loads are computed using modified blade element momentum theory and wave loads are simulated using Morison's equation where wave time-histories are simulated from the Joint North Sea Wave Project (JONSWAP) spectrum. Using these loads as input, the response of a benchmark wind turbine is simulated and validated with FAST.

3.2 Mathematical Model

In this section, the modelling of horizontal axis wind turbine is discussed for onshore and offshore environment. Offshore wind turbines are exposed to combined aerodynamic and hydrodynamic loads in the marine environment. The offshore wind turbines are supported over various types of foundations like monopile, gravity base, jacket/tripod and floating. Among them, monopiles are most commonly used. Therefore, a general Discrete Reduced Order Model (DROM) of an offshore wind turbine supported by monopile foundation is presented first. Then, the required changes for modelling an onshore wind turbine are discussed in the following subsections.

3.2.1 Offshore HAWT

The reduced-order model proposed by Fitzgerald et al. [73] is modified here to include multiple modes of blades and tower. Also, this improved model incorporates the drivetrain and monopile. The co-ordinate system for blade, tower and monopile assembly are shown in Fig. 3.1 along with the degrees of freedom used in this modelling, where x and y correspond to the fore-aft and side-to-side motions, respectively. Let $\mathbf{u}(t)$ be the displacement of the system, which is defined by

$$\mathbf{u}(t) = [u_{ij,x} \quad u_{4,x} \quad u_{5,x} \quad u_{ij,y} \quad u_{4,y} \quad u_{5,y} \quad u_{\bar{m}}]^T, \quad i = 1,2,3 \;\; j = 1,2 \;\; \bar{m} = 6,7 \tag{3.1}$$

In the above equation, subscript i represents the number of the blade while j corresponds to the modes and $\bar{m}$ denotes the degrees of freedom representing the drivetrain. Thus, in this notation, $u_{1j,x}(t)$, $u_{2j,x}(t)$, $u_{3j,x}(t)$ denote the tip displacement of three blades in the j^{th} mode along the out-of-plane direction and $u_{1j,y}(t)$, $u_{2j,y}(t)$, $u_{3j,y}(t)$ denote the same in the j^{th} mode along the in-plane direction. The blades are modelled as Euler-Bernoulli beam, whose bending stiffness in the flapwise and edgewise directions are represented by $EI_f(r)$ and $EI_e(r)$, respectively. The variable mass per unit length of each blade is denoted by $m_b(r)$, whose total length is R. The mass of the tower M^s is evaluated by summing the modal masses using variable tower mass $m_t(h)$ and the nacelle-hub mass M_n placed at the top. The monopile extending to the soil below the

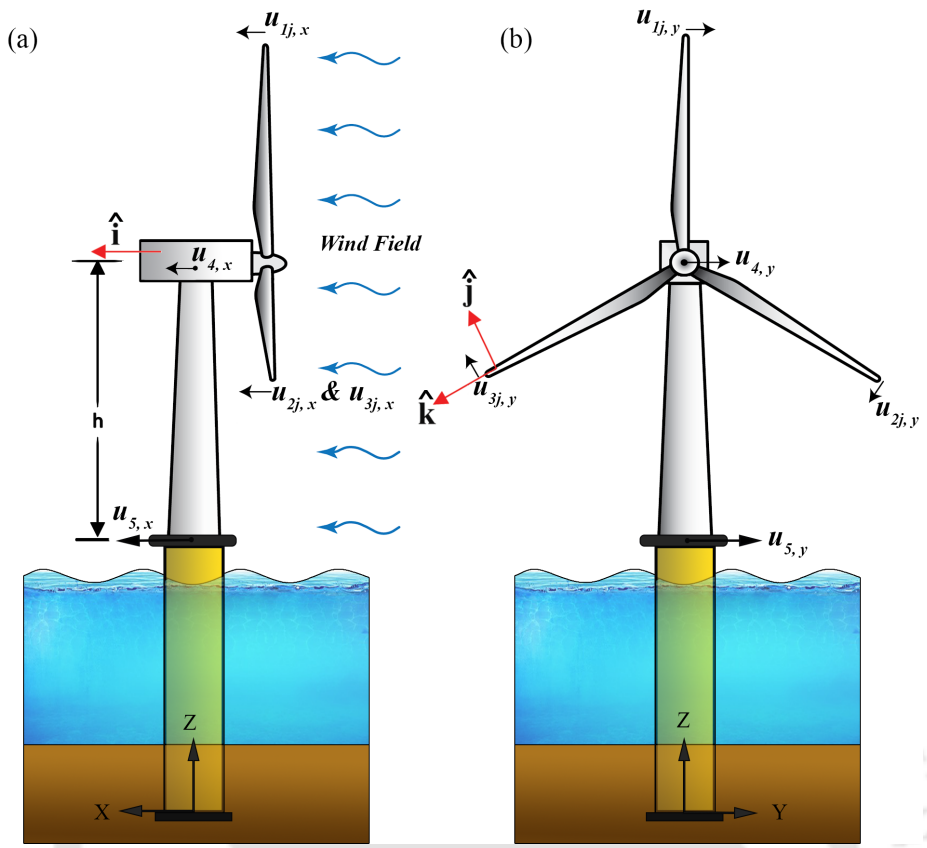

Figure 3.1: Monopile offshore wind turbine model; (a) out-of-plane direction and (b) in-plane direction.

sea bed is modelled by two degrees of freedom $u_{5,x}(t)$ and $u_{5,y}(t)$ denoting the translation at the top (i.e. platform level) along the fore-aft and side-to-side motion, respectively. Therefore, the displacement at the top of the monopile is given by

$$u_p = u_{5,x}.\mathbf{e}_x + u_{5,y}.\mathbf{e}_y + u_{5,z}.\mathbf{e}_z \tag{3.2}$$

The tower-nacelle together is modelled using two translational degrees of freedom, i.e. one in fore-aft and another in side-to-side direction and corresponding displacements are $u_{4,x}(t)$ and $u_{4,y}(t)$, respectively. Therefore, the relative deformation of the nacelle can be expressed as

$$u_n = (u_{4,x} + u_{5,x}).\mathbf{e}_x + (u_{4,y} + u_{5,y}).\mathbf{e}_y + (u_{4,z} + u_{5,z}).\mathbf{e}_z \tag{3.3}$$

Here, the monopile and tower motions in the vertical direction are assumed to be zero, i.e. $u_{4,z} = 0$ and $u_{5,z} = 0$. In this model, the drivetrain consists of a low-speed main rotor and a high-speed gear shaft, as shown in Fig. 3.2. The deformation of the main parts of the drivetrain are represented by $u_6(t)$ and $u_7(t)$ corresponding to the rotation of low and high-speed shaft, respectively. The blades rotate at a constant angular speed Ω rad/sec about its rotor axis. It may be noted that $u_6(t)$ and $u_7(t)$ are the rotations beyond the rigid body rotations of the respective shafts by an amount Ωt and $\gamma_g \Omega t$, respectively, where γ_g is the gear ratio. The azimuth angle of the i^{th} blade at any time instant is $\Psi_i(t) = \Omega t + (i-1)\frac{2\pi}{3}$. Using blade mode shapes $\phi^b_{j,x}$ and $\phi^b_{j,y}$, the displacements in out-of-plane and in-plane directions can be expressed as

$$u_{i,x}(r,t) = \sum_{j=1}^{n_x} u_{ij,x} = \sum_{j=1}^{n_x} \phi^b_{j,x}(r) q_{ij,x}(t) \tag{3.4a}$$

$$u_{i,y}(r,t) = \sum_{j=1}^{n_x} u_{ij,y} = \sum_{j=1}^{n_y} \phi^b_{j,y}(r) q_{ij,y}(t) \tag{3.4b}$$

Here, without loss of generality the number of modes along x and y are considered to be 2 (i.e. $n_x = n_y = n = 2$) as the participation factor for the higher modes are generally low. However, this can be extended for higher number of modes as per the requirement. The magnitude of blade mode shapes at the tip is considered to be unity in this analysis. Also, it may be noted that the flapwise and edgewise modes do not coincide with the out-of-plane and in-plane directions. The relative deformation of the blade evaluated with respect to the moving co-ordinates [i.e. $\hat{i}(t)\ \hat{j}(t)\ \hat{k}(t)$], with unit vectors $\hat{i}(t)$ is parallel to e_x, $\hat{k}(t)$ is along the length of the blade and $\hat{j}(t)$ is orthogonal to them. Using Eq. 3.1 and Eq. 3.4, the position vector of a given point on the i^{th} blade at a distance r from the hub can be written as

$$u_{b_i} = (u_{n_x} + u_{i,x}).\hat{i}(t) + (u_{n_y}\cos\Psi_i + u_{i,y}).\hat{j}(t) + (u_{n_y}\sin\Psi_i + r).\hat{k}(t) \tag{3.5}$$

where u_{n_x} and u_{n_y} are the tower top deformation in the fore-aft and side-to-side directions, respectively. Therefore, the velocity vector of i^{th} blade at a distance r from the hub is given by

$$\dot{u}_{b_i} = (\dot{u}_{n_x} + \dot{u}_{i,x}).\hat{i}(t) + (\dot{u}_{n_y}\cos\Psi_i + \dot{u}_{i,y} + \Omega r + u_6 r).\hat{j}(t) + (\dot{u}_{n_y}\sin\Psi_i - \Omega u_{i,y}).\hat{k}(t) \tag{3.6}$$

Once the displacement field and velocity vectors are defined, kinetic energy and potential energy of the system can be estimated. The total kinetic energy of a wind turbine system with N_b blades is given by

$$\Pi_K = \underbrace{\frac{1}{2}\sum_{i=1}^{N_b}\int_0^R m_b(r)\dot{u}_{b_i}^2(r,t)\,dr}_{\text{Blade}} + \underbrace{\frac{1}{2}M_n\dot{u}_n^2(H_t,t) + \frac{1}{2}\int_0^{H_t} m_t(h)\dot{u}_n^2(h,t)\,dh}_{\text{Tower}} + \underbrace{\frac{1}{2}J_r\dot{u}_6^2(t) + \frac{1}{2}J_g\dot{u}_7^2(t)}_{\text{Drivetrain}} + \underbrace{\frac{1}{2}M_p\dot{u}_p^2(t)}_{\text{Monopile}} \tag{3.7}$$

where J_r and J_g are the rotational inertia of the rotor-hub system and generator inertia of the high speed shaft, respectively while M_p is the mass of the monopile. The potential energy of the system is given by

$$\begin{aligned}
\Pi_P = &\underbrace{\frac{1}{2}\sum_{i=1}^{N_b}\int_0^R\left[\sum_{j=1}^{n}\sum_{k=1}^{n}\left\{EI_x(r)\left(\frac{\partial^2 u_{ij,x}}{\partial r^2}\right)\left(\frac{\partial^2 u_{ik,x}}{\partial r^2}\right) + EI_y(r)\left(\frac{\partial^2 u_{ij,y}}{\partial r^2}\right)\left(\frac{\partial^2 u_{ik,y}}{\partial r^2}\right)\right\} + 2\sum_{j=1}^{n} EI_{xy}\left(\frac{\partial^2 u_{ij,x}}{\partial r^2}\right)\left(\frac{\partial^2 u_{ij,y}}{\partial r^2}\right)\right]dr}_{\text{Blade (Elastic)}} \\
&+ \underbrace{\frac{1}{2}\sum_{i=1}^{N_b}\int_0^R\left[\sum_{j=1}^{n}\sum_{k=1}^{n}\left\{F_c(r)\left(\frac{\partial u_{ij,x}}{\partial r}\right)\left(\frac{\partial u_{ik,x}}{\partial r}\right) + F_c(r)\left(\frac{\partial u_{ij,y}}{\partial r}\right)\left(\frac{\partial u_{ik,y}}{\partial r}\right)\right\}\right]dr}_{\text{Blade (Centrifugal)}} \\
&+ \underbrace{\frac{1}{2}\sum_{i=1}^{N_b}\int_0^R\left[\sum_{j=1}^{n}\sum_{k=1}^{n}\left\{F_{gx}(r)\left(\frac{\partial u_{ij,x}}{\partial r}\right)\left(\frac{\partial u_{ik,x}}{\partial r}\right) + F_{gx}(r)\left(\frac{\partial u_{ij,y}}{\partial r}\right)\left(\frac{\partial u_{ik,y}}{\partial r}\right)\right\}\right]dr}_{\text{Blade (Gravitational)}} \\
&+ \underbrace{\frac{1}{2}k_{t,x}q_{4,x}^2 + \frac{1}{2}k_{t,y}q_{4,y}^2}_{\text{Tower}} + \underbrace{\frac{1}{2}k_{p,x}q_{5,x}^2 + \frac{1}{2}k_{p,y}q_{5,y}^2}_{\text{Monopile}} + \underbrace{\frac{1}{2}k_d(q_6 - \frac{1}{\gamma_g}q_7)^2}_{\text{Drivetrain}} - \underbrace{\sum_{i=1}^{N_b}\sum_{j=1}^{n} f_{gij,y}(t)q_{ij,y}}_{\text{Blade (Gravitational load)}} \\
&- \underbrace{\sum_{i=1}^{N_b}\sum_{j=1}^{n}\left(f_{ij,x}(t)q_{ij,x} + f_{ij,y}(t)q_{ij,y}\right)}_{\text{Blade (Aerodynamic load)}} - \underbrace{f_{4,x}(t)q_{4,x} - f_{4,y}(t)q_{4,y}}_{\text{Tower (Aerodynamic load)}} - \underbrace{(1-\nu)f_6(t)q_6 - f_7(t)q_7}_{\text{Drivetrain (Aerodynamic load)}} - \underbrace{f_{5,x}(t)q_{5,x} - f_{5,y}(t)q_{5,y}}_{\text{Monopile (Hydrodynamic load)}}
\end{aligned} \tag{3.8}$$

where EI_x and EI_y represent flexural rigidity of the blade in the out-of-plane and in-plane directions, respectively while EI_{xy} stands for the coupling between them [74]. The parameters $k_{t,x}$ and $k_{t,y}$ represent the elastic stiffness of the tower in the fore-aft and side-to-side directions, respectively whereas $k_{p,x}$ and $k_{p,y}$ represent the elastic stiffness of the monopile along these orthogonal directions. k_d is the equivalent torsional spring constant of the drivetrain. The aerodynamic forces acting on the blade are defined by $f_{ij,(.)}$, where the second subscript represent the appropriate direction. The same forces on the tower and monopile are represented by $f_{4,(.)}$ and $f_{5,(.)}$, respectively with appropriate subscript as described for blade. The aerodynamic forces on drivetrain are represented by f_6 and f_7 corresponding to the slow and fast moving shaft, respectively, where ν represents the friction coefficient [200]. In this equation, F_c represents the force due to the centrifugal acceleration, while F_{gx} and f_{gij} (i.e. $f_{gij} = \phi_{j,y}^b F_{gy,i}$) are the in-plane orthogonal forces due to the gravitational field. Substituting Eq. 3.4 in the above expressions of potential energy and

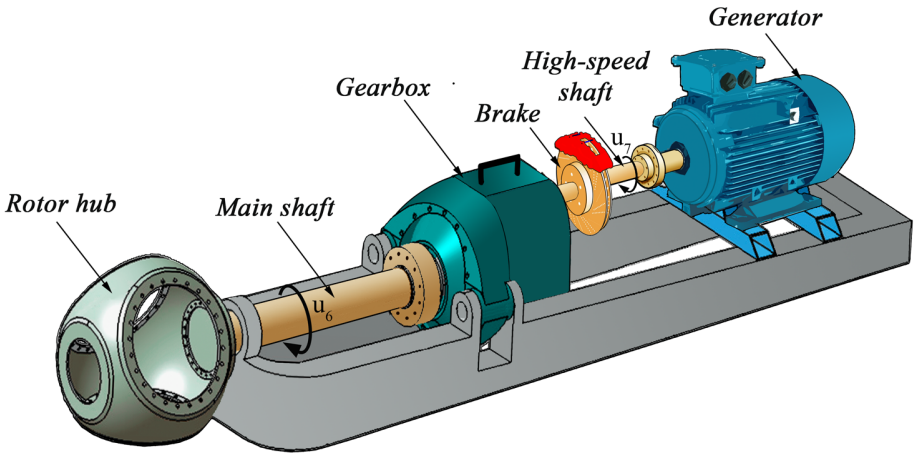

Figure 3.2: Schematic diagram of drivetrain.

simplifying it further gives

$$\begin{aligned}\Pi_P =& \frac{1}{2}\sum_{i=1}^{N_b}\left\{\sum_{j=1}^{n}\sum_{k=1}^{n}\Big(K_{e,jk,x}+K_{c,jk,x}+K_{g,jk,x}\cos\Psi_i\Big)q_{ij,x}q_{ik,x}\right\}+\sum_{i=1}^{N_b}\sum_{j=1}^{n}K_{xy,ij}q_{ij,x}q_{ij,y}\\ &+\frac{1}{2}\sum_{i=1}^{N_b}\left\{\sum_{j=1}^{n}\sum_{k=1}^{n}\Big(K_{e,jk,y}+K_{c,jk,y}+K_{g,jk,y}\cos\Psi_i\Big)q_{ij,y}q_{ik,y}\right\}+\frac{1}{2}\Big\{k_{t,x}q_{4,x}^2+k_{t,y}q_{4,y}^2\\ &+k_{p,x}q_{5,x}^2+k_{p,y}q_{5,y}^2+k_d(q_6-\frac{1}{\gamma_g}q_7)^2\Big\}-\sum_{i=1}^{N_b}\sum_{j=1}^{n}\Big\{f_{ij,x}(t)q_{ij,x}+\Big(f_{ij,y}(t)+f_{gij,y}(t)\Big)q_{ij,y}\Big\}\\ &-f_{4,x}(t)q_{4,x}-f_{4,y}(t)q_{4,y}-f_{5,x}(t)q_{5,x}-f_{5,y}(t)q_{5,y}-(1-\nu)f_6(t)q_6+f_7(t)q_7\end{aligned} \tag{3.9}$$

In Eq. 3.9, $K_{e,jk,x}$ and $K_{e,jk,y}$ are the bending stiffnesses in the appropriate directions. The details of $K_{e,jk,x}$ and $K_{e,jk,y}$ are not discussed here to avoid repetitions, which may be obtained from Staino et al. [80]. The sectional properties (i.e. I_x, I_y and I_{xy}) are obtained from the airfoil data (i.e. I_f and I_e) using proper coordinate transformation [201]. As the blade rotates with a constant speed Ω, the centrifugal force is exerted on it, which contributes to the geometric stiffness as

$$K_{c,jk,x}=\int_0^R F_c(r)\phi_{j,x}^{b'}(r)\phi_{k,x}^{b'}(r)dr \tag{3.10a}$$

$$K_{c,jk,y}=\int_0^R F_c(r)\phi_{j,y}^{b'}(r)\phi_{k,y}^{b'}(r)dr \tag{3.10b}$$

where $F_c(r)$ is the centrifugal force acting at a distance r on the blade, which is given by

$$F_c(r)=\Omega^2\int_r^R \mu(\xi)\xi d\xi \tag{3.11}$$

Besides centrifugal force, the gravitational force also acts on the blade that varies with blade rotation. The components of gravitational stiffness $K_{g,jk}$ arising due to blade rotation are given by

$$K_{g,jk,x}=\int_0^R\left(-g\int_r^R\mu(\xi)d\xi\right)\phi_{j,x}^{b'}(r)\phi_{k,x}^{b'}(r)dr \tag{3.12a}$$

$$K_{g,jk,y}=\int_0^R\left(-g\int_r^R\mu(\xi)d\xi\right)\phi_{j,y}^{b'}(r)\phi_{k,y}^{b'}(r)dr \tag{3.12b}$$

In this study, the drivetrain consists of a slow-speed main shaft, a gearbox and a high-speed shaft, as shown in Fig. 3.2. It modifies the torque transmitted from the blade to the generator. The equivalent torsional stiffness of the shafts in the drivetrain is given by [98]

$$k_d = \frac{\gamma_g^2 k_r k_g}{k_r + \gamma_g^2 k_g} \tag{3.13}$$

where k_r and k_g are the St. Venant torsional stiffness of the main shaft and the generator shaft, respectively. Using Eq. 3.7 and Eq. 3.9, the governing equation of motion can be derived from Lagrange's equation, which is given by

$$\frac{d}{dt}\left(\frac{\partial \Pi_K}{\partial \dot{q}_i}(t, \mathbf{q}(t), \dot{\mathbf{q}}(t))\right) - \frac{\partial \Pi_K}{\partial q_i}(t, \mathbf{q}(t), \dot{\mathbf{q}}(t)) + \frac{\partial \Pi_P}{\partial q_i}(t, \mathbf{q}(t), \dot{\mathbf{q}}(t)) = 0, \quad i = 1, 2, ..., N_{\mathbf{q}} \tag{3.14}$$

where $\mathbf{q}(t)$ is the degrees of freedom vector corresponding to the displacement $\mathbf{u}(t)$ and $N_{\mathbf{q}}$ is the total number of degrees of freedom. Following Eq. 3.14, the governing equation of motion can be expressed as

$$M(t)\ddot{q}(t) + C(t)\dot{q}(t) + K(t)q(t) = f(t) \tag{3.15}$$

In the above equation, system matrices M, C and K are the mass, damping and stiffness matrices, respectively. Here, it may be noted that these matrices are the function of time due to blade rotation. The stiffness matrix is the summation of elastic, centrifugal and gravitational components. The matrix C represents the combined structural and aerodynamic damping of the system. The details of these matrices are given in the Appendix A.

For an onshore wind turbine, the discrete reduced order model with fixity at the tower base can be developed by eliminating the degrees of freedom corresponding to monopile deformations in Eq. 3.1, i.e. $u_{5,x} = 0$ and $u_{5,y} = 0$. Finally, a numerical solution is opted to evaluate the responses where Eq. 3.15 is expressed in the state-space as follows

$$\dot{Z} = A(t)Z(t) + B(t)W(t) \tag{3.16}$$

In the above equation, $Z = [q \;\; \dot{q}]^t$ is the state vector, $W(t)$ represent external force due to wind, wave and gravity, $B(t)$ represents the influence vector. The matrices A(t) and B(t) have the following form

$$A(t) = \begin{bmatrix} 0 & I \\ -M^{-1}(t)K(t) & -M^{-1}(t)C(t) \end{bmatrix}, \quad B(t) = \begin{bmatrix} 0 \\ M^{-1}(t)I \end{bmatrix} \tag{3.17}$$

where I represents the identity matrix of appropriate dimension.

3.2.2 Structural Loads on HAWT

In the reduced order model, the loads acting on the blade are obtained by integrating over its length. The detailed estimation of structural loads are elaborated in Chapter 2. Following sections explains the loads used in the reduced order model and their estimation from the wind and wave time histories.

3.2.2.1 Aerodynamic Load

The aerodynamic loads acting on the blade elements are evaluated using Blade Element Momentum (BEM) theory as described in Section 2.4.5. Therefore, the total normal and tangential forces acting on the blade are obtained by summing up these elemental forces given in Eq. 2.30 along the length of the blade. Thus, the generalized wind induced forces acting on the blades are given by

$$f_{ij,x}(t) = \int_0^R \delta p_{n_i}(r,t)\phi_{j,x}^b(r)dr \tag{3.18a}$$

$$f_{ij,y}(t) = \int_0^R \delta p_{t_i}(r,t)\phi_{j,y}^b(r)dr \tag{3.18b}$$

where i denotes the blade number, i.e. $i = 1, 2, 3$. The aerodynamic forces acting on the tower are obtained from these blade loads using the following expression

$$f_{4,x}(t) = \sum_{i=1}^{N_b} \int_0^R \delta p_{n_i}(r,t)dr \tag{3.19a}$$

$$f_{4,y}(t) = \sum_{i=1}^{N_b} \int_0^R \delta p_{t_i}(r,t)dr \cos\Psi_i \tag{3.19b}$$

3.2.2.2 Hydrodynamic Load

The generalized form of hydrodynamic force corresponding to wave loading are derived in Eq. 2.55. Therefore, the in-plane and out-of-plane loads acting on the monopile are evaluated as

$$f_{5,x}(t) = \cos\theta_{\text{ma}} f_{\text{wave}} \tag{3.20a}$$

$$f_{5,y}(t) = \sin\theta_{\text{ma}} f_{\text{wave}} \tag{3.20b}$$

In above equation, $f_{\text{wave}}(t)$ is the wave force on the pile, which is evaluated by the following expression

$$f_{\text{wave}}(t) = \sum_{j=1}^{N_w} \left[\frac{\rho_w \pi D_p^2}{4} C_m \ddot{w} \Delta h + \frac{\rho_w}{2} C_d D_p \dot{w}|\dot{w}|\Delta h \right] \tag{3.21}$$

where θ_{ma} is the misalignment between the wind and wave forces, N_w is the number of monopile segments with diameter D_p under the water while Δh denotes the length of each segment.

3.2.3 Damping

The main components of damping in an offshore wind turbine are structural, aerodynamic and hydrodynamic, which are discussed below.

3.2.3.1 Structural Damping

In this study, the 5 MW National Renewable Energy Laboratory (NREL) benchmark wind turbine is used, which exhibits critical damping ratio of 0.477% and 1% in all modes of blade and tower, respectively. The structural damping ratio of concrete monopile is assumed to be approximately 2%.

3.2.3.2 Aerodynamic Damping

Aerodynamic damping is developed due to interaction between the blade aerodynamics and the structural motion. The aerodynamic damping of blade in their fundamental mode of vibration is given by [42]

$$c_b^a = \frac{1}{2}\rho_a \Omega \frac{dC_l}{d\alpha} \int_0^R rc(r){\phi_j^b}^2(r)dr \tag{3.22}$$

where ρ_a is the density of air, c is the chord of the blade, C_l and α are the lift coefficient and angle of attack, respectively. When the blade is not in stall, the rate of change of lift coefficient with angle of attack (i.e. $\frac{dC_l}{d\alpha}$) is equal to 2π. The aerodynamic damping of tower is mainly provided by N_b blades, which can be expressed as

$$c_t^a = \frac{1}{2}N_b \rho_a \Omega \frac{dC_l}{d\alpha} \int_0^R rc(r){\phi_j^b}^2(r)dr \tag{3.23}$$

3.2.3.3 Hydrodynamic Damping

The main components of hydrodynamic damping are wave radiation damping and viscous damping due to hydrodynamic drag [202]. The wave radiation is proportional to the wave velocity, whereas viscous damping is proportional to the square of the relative velocity [203]. Previous studies have reported 0.15% viscous damping [204] and 0.11% radiation damping [205] for similar structures. Tarp-Johansen et al. [206] have suggested 0.24% radiation damping after simulating the radiation component of wave using wave modeling program WAMIT. Shirzadeh et al. [203] have estimated 0.004% viscous hydrodynamic damping ratio using time domain solutions. From the above literatures, it can be concluded that hydrodynamic damping vary widely depending upon the depth. But, for offshore wind turbine located in relatively shallow water, hydrodynamic damping is very low compared to other damping. Hydrodynamic force can be calculated by two approaches - Morison's equation or potential flow theory considering interaction between the pile and seawater. Morison's equation deals with the viscous effect when flow separation is significant, whereas potential flow theory accounts for diffraction and radiation phenomena. Reader may refer Chen and Duffour [207] for further details on these issues.

- **Viscous Damping** - The damping ratio for a single pile subjected to viscous drag can be expressed as

$$\xi_{Hydro,Vis} = \frac{\int_{-H_{Pile}}^{0} \frac{1}{2}\rho_w D_{Pile} C_D \sqrt{\frac{8}{\pi}} \sigma_r(h) \phi^{t2}(h) dh}{2\omega \int_{-H_{Pile}}^{0} m_t(h) \phi^{t2}(h) dh} \tag{3.24}$$

  where σ_r(h) is the root mean square of the relative velocity between the water-wave particle and the pile.

- **Radiation Damping** - The radiation damping ratio is given by

$$\xi_{Hydro,Rad} = \frac{\int_{-H_{Pile}}^{0} C_{Rad} dh}{2\omega \int_{-H_{Pile}}^{0} m_t(h) \phi^{t2}(h) dh} \tag{3.25}$$

  where C_{Rad} is the radiation factor.

Chen and Duffour [207] have concluded that viscous damping ratio is 0.0006% using Eq. 3.24, whereas radiation damping ratio is 0.007% using Eq. 3.25 for the benchmark 5 MW offshore monopile supported wind turbine. Total hydrodynamic damping ratio is about 0.0076%, which is very less compared to other form of damping. Due to this reason, hydrodynamic damping is neglected for the simulation purpose in this study.

3.3 Numerical Results and Discussion

In this section, numerical simulation is carried out to illustrate the response for the benchmark NREL 5 MW wind turbine [201]. Its properties are summarized in Table 3.1. The height of the tower is 87.6 m that supports three 61.5 m long blades connected to a hub of diameter 3 m. The blades are made of 8 different airfoils, whose bending stiffness, mass per unit length, lift and drag coefficients are obtained from NREL Report [201]. The first two blade mode shapes in the flapwise and edgewise directions are shown

Table 3.1: NREL 5 MW Turbine Data.

Basic Descriptions		Blade (LM61.5 P2)		Tower		Drivetrain	
P_r	5000 kW	R	61.5 m	H_t	87.6 m	N	97
N_b	3	M_b	17740 kg	M_t	347460 kg	k_d	867637 kN-m/rad
D_R	126 m	f_b^{flap}	0.66, 2.07 Hz	$f_t^{\text{fore-aft}}$	0.324 Hz	J_g	534 kg-m^2
H_h	90 m	f_b^{edge}	1.08, 4.05 Hz	$f_t^{\text{side-to-side}}$	0.312 Hz		
v_{ci}, v_r, v_{co}	3 m/s, 11.4 m/s, 25 m/s	ξ_b	0.477%	ξ_t	1%		
Ω_{ci}, Ω_r	6.9 rpm, 12.1 rpm						

in Fig. 3.3. These modes shapes are obtained from the Finite Element (FE) analysis using BModes [208].

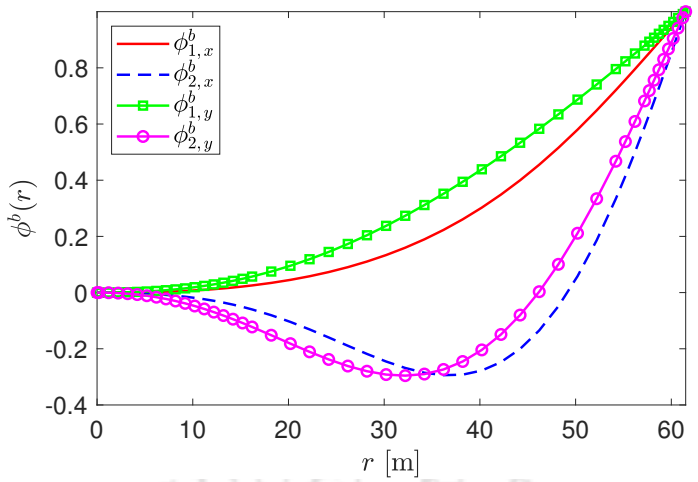

Figure 3.3: Flapwise and edgewise mode shapes of blade.

In this numerical study, three different mean wind speeds (i.e. cut-in, rated and cut-out) are considered at the hub height covering the full operational spectrum of the turbine. Using these properties and the mode shapes obtained from the FE analysis, system matrices are evaluated. Both aerodynamic and structural damping are considered in this analysis. The aerodynamic damping depends on the angular velocity and mass distribution of the blade. Modern blades are light and its airfoils are designed in such a way that they offer high aerodynamic damping. Usually, this damping is less in the edgewise direction compared to flap-wise direction. The equivalent modal aerodynamic damping is estimated using flow parameters and blade mode shape as discussed in Eq. 3.22, whose values at the rated speed in the first two modes along the flap-wise direction are found to be 70.87% and 2.86%, respectively while the same in the edgewise direction are 1.16% and 0.05%, respectively. Fig. 3.4 shows the variation of frequency and aerodynamic damping ratio of the blade for different wind speeds.

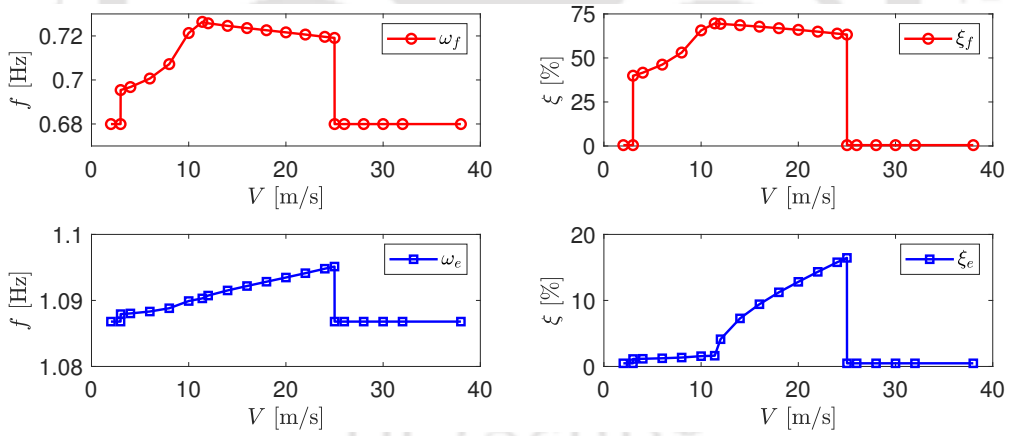

Figure 3.4: Variation of flapwise and edgewise blade frequency and aerodynamic damping of NREL 5 MW wind turbine during different wind speeds.

Using these parameters, the simulated response of the DROM is validated with FAST results. For this purpose, aerodynamic loads acting on the blades and nacelle are evaluated using BEM theory as explained in Section 3.2.2.1. TurbSim [16, 17] is used to generate 100 samples of turbulent wind fields for different mean wind speeds at the hub height. In this numerical study, the level of turbulence is assumed to be 15%. Three different mean wind speeds are considered with appropriate pitch angles, as recommended by NREL [201]. Once the pitch angle is selected for a particular mean speed, it is not changed during the simulation. The fixed-pitch angle is zero below the rated speed. In this validation exercise, first the aerodynamic loads are verified where AeroDyn [22] is used for steady flow while FAST [209] is referred for turbulent flow. In this context, FAST uses proper aeroelastic simulation that has inherent mechanism to model aerodynamic damping instead of equivalent modal values as used in this numerical analysis. Thus, FAST uses AeroDyn at every time instance for load evaluation based on the blade response in real-time. On the other hand, BEM

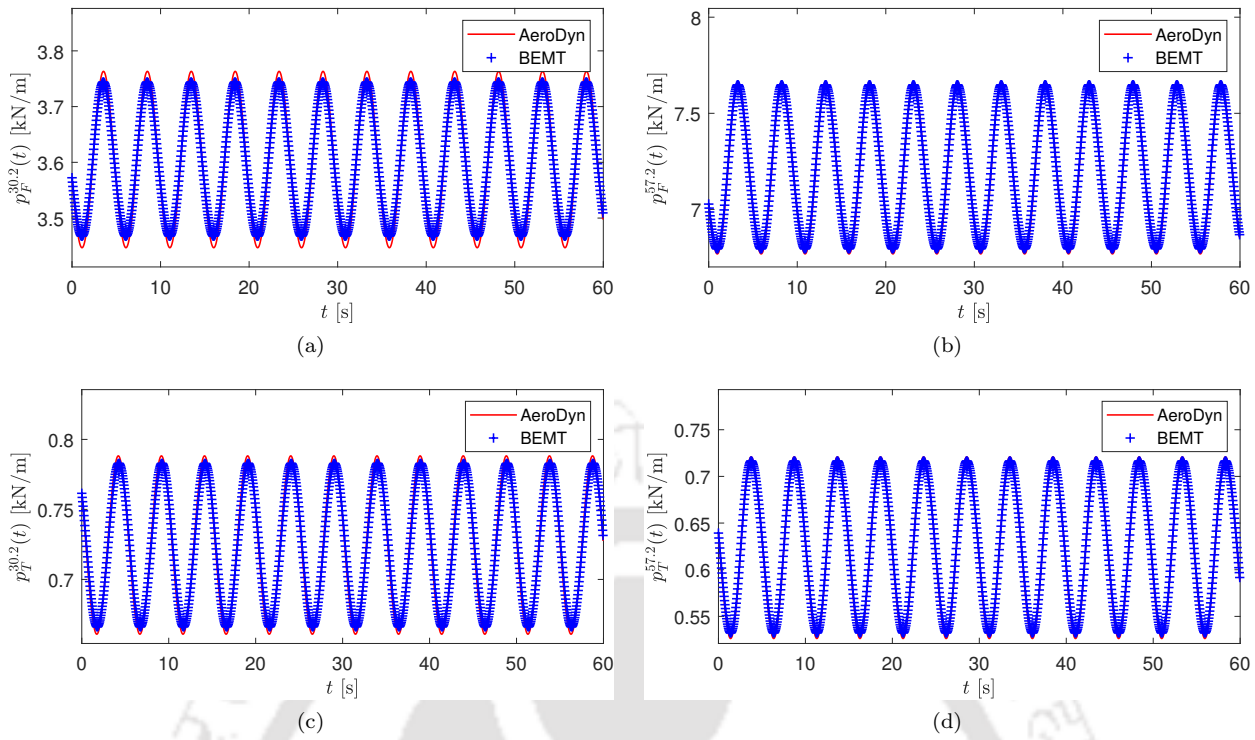

Figure 3.5: Thrust and torque at the rated speed steady flow; (a) at $r = 30.2$ m in out-of-plane direction, (a) at $r = 57.2$ m in out-of-plane direction, (c) at $r = 30.2$ m in in-plane direction and (c) at $r = 57.2$ m in in-plane direction.

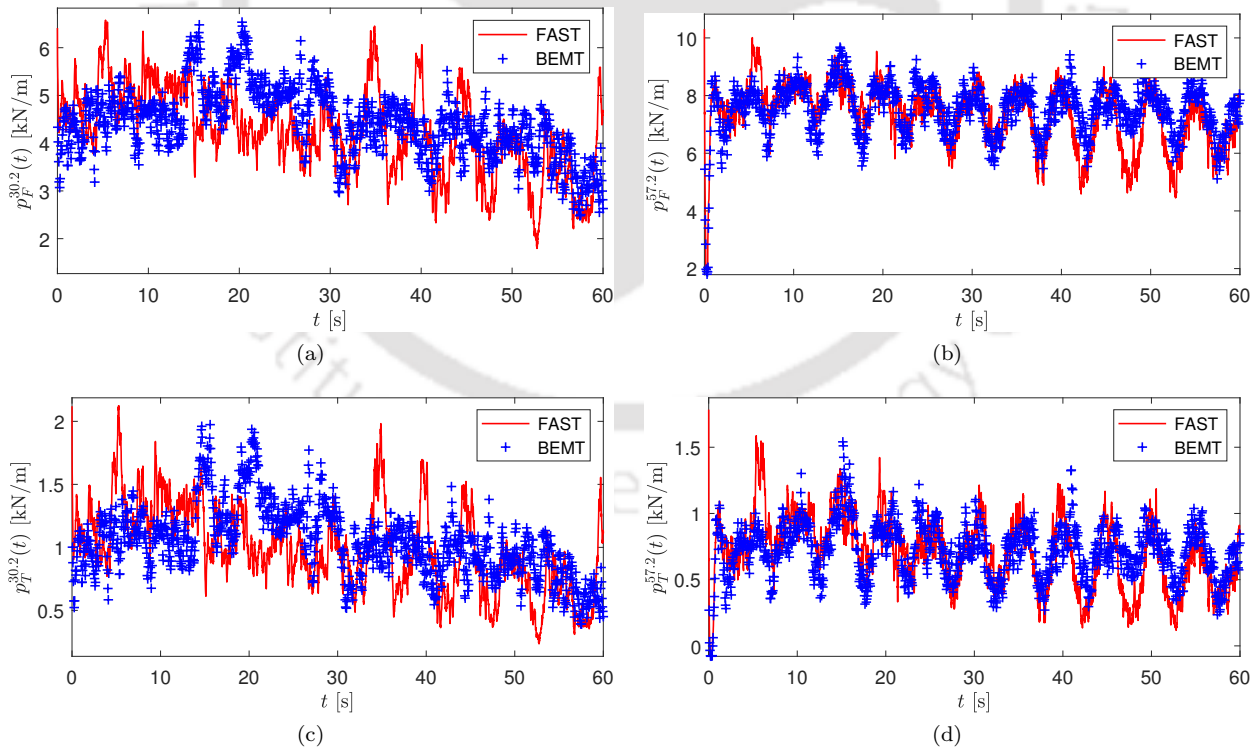

Figure 3.6: Thrust and torque at the rated speed with 15% turbulent flow; (a) at $r = 30.2$ m in out-of-plane direction, (b) at $r = 57.2$ m in out-of-plane direction, (c) at $r = 30.2$ m in in-plane direction and (d) at $r = 57.2$ m in in-plane direction.

theory is used in this study to simulate the loads prior to its use in the response calculation. Thus, loads at every airfoil is simulated, however, the location at 30.2 m and 57.2 m are arbitrarily chosen for comparison. Fig. 3.5 and Fig. 3.6 show the loads obtained from the BEM theory (which is referred as BEMT in the figure) for steady flow and with 15% turbulence, respectively. From Fig. 3.5, it can be observed that the loads during steady flow exactly match with each other indicating the accuracy of the BEMT code developed for this numerical analysis. For turbulent flow case (i.e. Fig. 3.6), the loads from BEMT also follow the same pattern (i.e. amplitude and dominant frequency) with FAST. However, the difference in amplitudes in this case is due to the difference in aero-elastic simulation as described above. Due to this reason, loads are not supposed to match in this case. However, the overall load pattern in the two orthogonal directions are close to each other.

Using these aerodynamic loads at different locations on the blades, modal loads are evaluated for further response validation. Fig. 3.7a and Fig. 3.7c show the aerodynamic loads acting in the first flapwise and

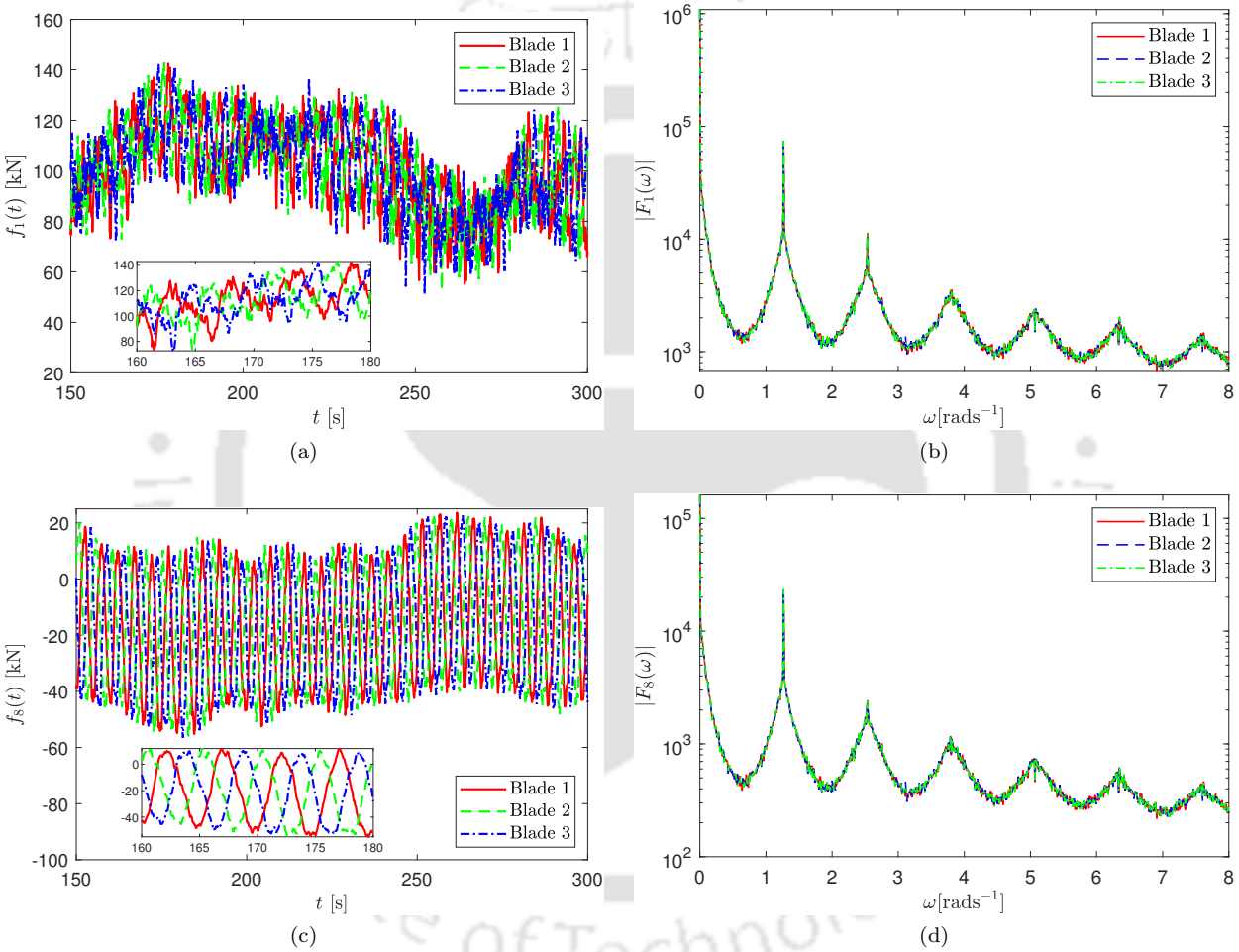

Figure 3.7: Total aerodynamic blade loads at the rated speed; (a) time history in out-of-plane direction, (b) Fourier amplitude spectrum in out-of-plane direction, (c) time history in in-plane direction and (d) Fourier amplitude spectrum in in-plane direction.

edgewise modes at the rated wind speed. As the blades are 120^o apart from each other, similar phase differences are observed in these load time histories. Fig. 3.7b and Fig. 3.7d show the corresponding Fourier amplitude spectrum of these loads. From these figures, it can be observed that the rotational frequency and its integer multiples dominate the load spectrum. It is due to sampling of the wind flow in the rotor plane as the blades move with a constant angular speed. Aerodynamic loads acting on the tower are obtained by summing up the blade loads that are transmitted through the hub.

Using these modal loads, blade responses are simulated in MATLAB by ODE45 solver. Fig. 3.8 shows the time histories and corresponding Fourier amplitude spectrum of the blade responses in the out-of-plane and in-plane directions and are compared with FAST results. The blade responses obtained from DROM match well with FAST results at the rotational frequency (i.e. 1P in Fig. 3.8b and Fig. 3.8d) that dominates in the

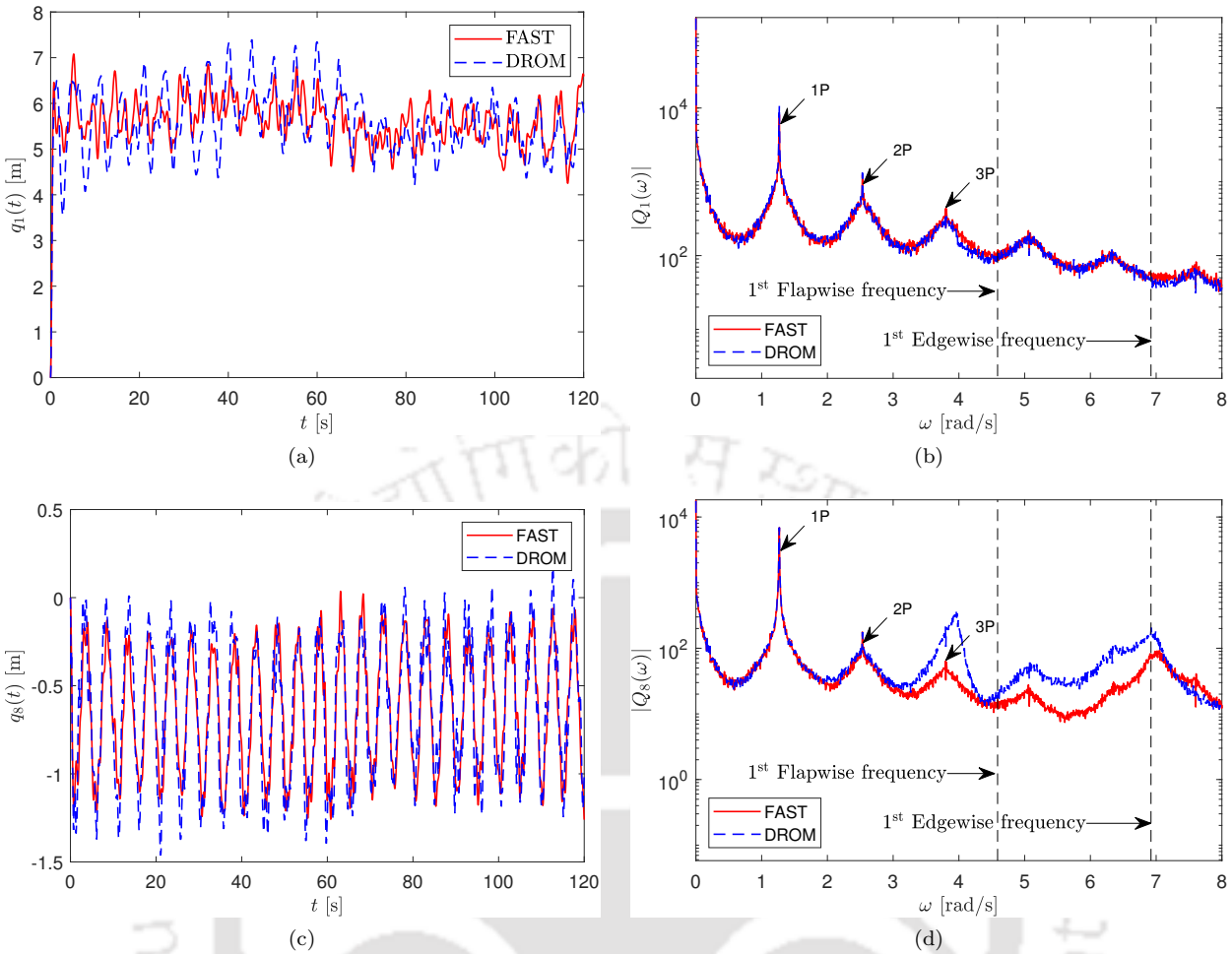

Figure 3.8: Blade tip displacement; (a) time history in out-of-plane direction, (b) Fourier amplitude spectrum in out-of-plane direction, (c) time history in in-plane direction and (d) Fourier amplitude spectrum in in-plane direction.

responses. However, the difference in blade responses at higher frequencies are envisaged due to the different approaches in modelling techniques, aerodynamic damping and the limitations of the reduced-order model to capture the responses at higher frequencies (i.e. 3P) accurately. The responses at the 1st flapwise and edgewise frequencies are less compared to the response at first three harmonics of the rotational frequency. Since the responses at 1P (i.e. dominant frequency) match well, the overall response simulation using DROM may be considered adequate for further analysis.

3.4 Summary

The details of mathematical modelling of onshore and offshore wind turbine using discrete reduced order model are presented in this chapter. For this purpose, the blades are modelled as Euler-Bernoulli beam using their distributed properties, which are connected to tower-nacelle-hub system. In this model, the rotations of low-speed and high speed shaft beyond their rigid body rotations are also considered. This chapter also provides an insight to the estimation of aerodynamic and hydrodynamic damping along with the modal load calculation for DROM. Using this formulation, the NREL 5 MW benchmark wind turbine is modelled and the responses are compared with FAST. The mode shapes of the blades and tower are estimated using finite element model in BModes. Then, the time dependant mass, stiffness and damping matrices are evaluated. It is observed that the frequency and aerodynamic damping of the turbines depend on its rotational speed. Before response analysis, the aerodynamic loads are evaluated using Blade Element Momentum (BEM) theory in the non-aeroelastic framework. The simulated loads are compared with AeroDyn and FAST for steady and turbulent wind flow, respectively. Then, the total aerodynamic loads are evaluated and the

responses are simulated using equivalent aerodynamic damping in each mode of vibration. The Fourier amplitude spectrum of loads and responses clearly show that the dominant frequencies are the integer multiple of turbine's rotational frequency. The responses obtained using DROM closely match with FAST and hence the proposed model can be used for further analysis. The deformation of the blade in the out-of-plane direction at the rated speed is significantly higher and reducing their amplitude are bound to enhance the performance of the blade in terms of reliability and fatigue life. These are discussed in the upcoming chapters.

Chapter 4

Longitudinal Stiffening of Blades for Vibration Control

4.1 Introduction

In this chapter, the study aims to reduce the deformation of large horizontal axis wind turbine blades using Shape Memory Alloy (SMA) based longitudinal stiffening. The discrete reduced order model presented in the previous chapter is used to demonstrate the performance of the proposed stiffening strategy. Firstly, a passive stiffener is proposed where the behaviour of SMA is characterized by Greaser-Cozzarelli model. Later, it is extended for semi-active mode of operation to obtain better performance by Joule heating where the behaviour of SMA is modelled by deriving a constitutive relationship based on Liang-Rogers model and thermodynamic principles. The responses are simulated using equivalent aerodynamic damping, which are estimated in each mode of vibration. Various sensitivity analysis are also carried out to demonstrate the performance envelop of the proposed stiffening strategy over the operational range of the benchmark 5 MW wind turbine. The study clearly highlights the performance enhancement in terms of deformation in two orthogonal directions and design in terms of longitudinal stress that ultimately improve the serviceability of the blade. The formulation of the proposed stiffening strategies are systematically developed as presented in the following sections.

4.2 Modelling of Stiffened Blades

In this section, the reduced-order model proposed in Chapter 3 is modified to include longitudinal stiffener, which is the main contribution of this work. Fig. 4.1 shows the SMA tendon along the longitudinal axis

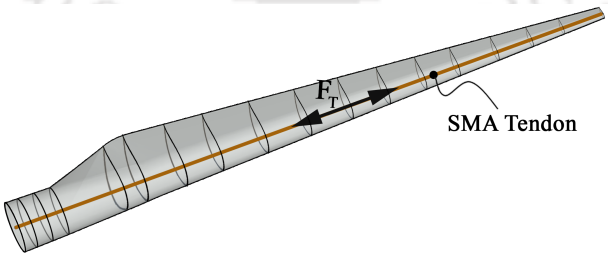

Figure 4.1: Proposed longitudinal stiffener in blade.

of the blade. It runs from the hub up to the tip of the blade. Here, it may be noted that proper guiding arrangement at a regular interval can be made within the spar of the blade so that the tendon follows the deformed profile. The tendon experiences an axial force F_T as the blade deforms. Therefore, the potential

energy of the proposed system is defined as

$$\Pi_P = \Pi_{P_0} + \underbrace{\frac{1}{2}\sum_{i=1}^{3}\int_0^R \left[\sum_{j=1}^{n}\sum_{k=1}^{n}\left(F_T\left(\frac{\partial u_{ij,x}}{\partial r}\right)\left(\frac{\partial u_{ik,x}}{\partial r}\right) + F_T\left(\frac{\partial u_{ij,y}}{\partial r}\right)\left(\frac{\partial u_{ik,y}}{\partial r}\right)\right)\right] dr}_{\text{Longitudinal Stiffening}} \tag{4.1}$$

where Π_{P_0} is the potential energy evaluated for uncontrolled system in Eq. 3.8 and the term underlined in above equation represents the proposed longitudinal stiffening of the blade. It may be noted that the tendon force F_T acts in the axial direction, which helps to reduce the deformation in both x and y directions. Using the expression of displacement field in different direction, the potential energy can be rearranged in the following form.

$$\Pi_P = \Pi_{P_0} + \frac{1}{2}\sum_{i=1}^{N_b}\sum_{j=1}^{n}\sum_{k=1}^{n}\left(K_{T,jk,x}q_{ij,x}q_{ik,x} + K_{T,jk,y}q_{ij,y}q_{ik,y}\right) \tag{4.2}$$

In Eq. 4.2, $K_{T,jk,x}$ and $K_{T,jk,y}$ are the stiffnesses of the blade due to tendon force in the out-of-plane and in-plane directions, respectively. The proposed tendon force acts in the opposite direction of the centrifugal force F_c(r). Hence, the stiffness arising due to this force can be obtained by replacing $F_c(r)$ with F_T in Eq. 3.10a and Eq. 3.10b, respectively i.e.

$$K_{T,jk,x} = \int_0^R F_T\Phi'_{j,x}(r)\Phi'_{k,x}(r)dr \tag{4.3a}$$

$$K_{T,jk,y} = \int_0^R F_T\Phi'_{j,y}(r)\Phi'_{k,y}(r)dr \tag{4.3b}$$

Using Eq. 3.7 and Eq. 4.2, the governing equation of motion can be derived by Euler-Lagrange equation (i.e. Eq. 3.14), which takes the following form on simplifying

$$M(t)\ddot{q}(t) + C\dot{q}(t) + K_s(t)q(t) = f(t) \tag{4.4}$$

In the above equation, $K_s(t)$ is a time dependent stiffness matrix of the controlled system, i.e. $K_s(t) = [K(t) + K_T(t)]$. The details of this matrix are given in the Appendix A.

4.3 SMA Material Model for Longitudinal Stiffening

In this study, the blades are stiffened by SMA tendon as shown in Fig. 4.1. The tendon is placed along the longitudinal axis of the blade whose two ends are anchored at hub and tip. SMA changes its underlying micro-structural orientation when exposed to temperature or electro-magnetic field. It has a unique characteristics to regain its predefined shape upon the application of heat is known as Shape Memory Effect (SME) while the ability to recover from large strain is known as the Super-Elastic Effect (SE), which are briefly described here. Fig. 4.2 shows the typical stress-strain-temperature behaviour of SMA where the path A-B-C-D-E-F-A shows the shape memory effect while the path G-H-I-J-K-L-G shows the super-elastic effect. These are mainly due to the crystal orientation during high temperature austenite phase and low temperature martensite phase. Furthermore, depending upon different crystal orientation, martensite phase has two more sub-phases (i.e. twinned martensite and detwinned martensite). During these phase transformations, molecular orientation changes from its parent state (i.e. high energy austenite) to a highly deformed state (i.e. low energy martensite).

In Fig. 4.2, the path A-B shows the classical elastic deformation of SMA. As the strain increases, it undergoes significant inelastic shear deformation and the molecular orientation start changing from twined martensite to detwinned martensite state. Beyond this point (i.e. C), permanent plastic deformation can set in. Path C-D shows the elastic unloading in detwinned martensite phase with some residual strain depending on the level of loading. In other words, the unloading alone can not trace back the stress-strain path at this stage, which is only possible by Joule heating i.e. path D-E-F. During heating, the molecular structure starts changing from detwinned martensite to austenite at a temperature above austenite start, i.e. A_s. The

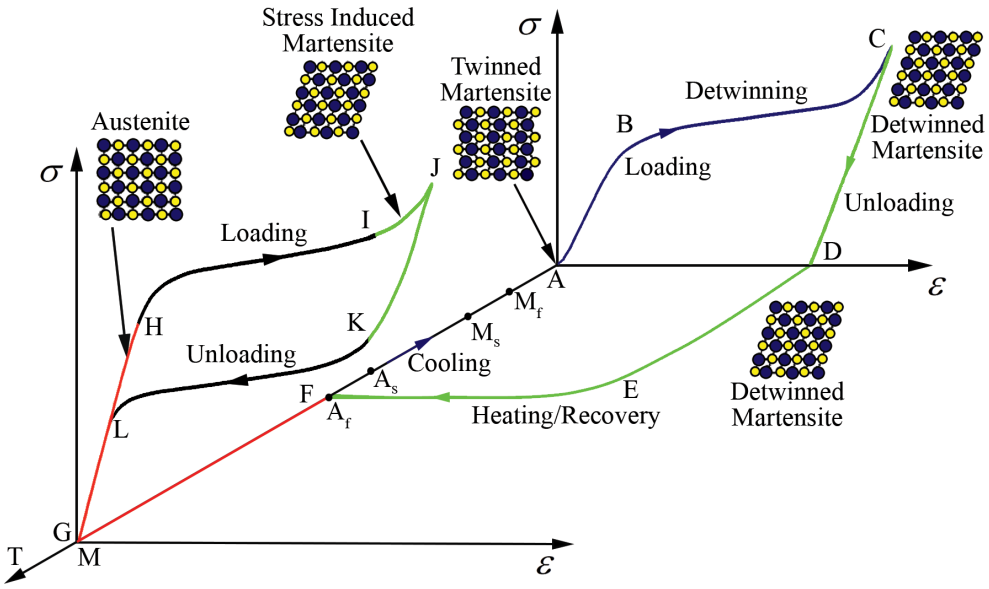

Figure 4.2: Typical stress-strain-temperature behaviour of SMA.

material is heated beyond austenite finish temperature, i.e. A_f to regain its undeformed shape. Finally, path F-A, the cooling of SMA below martensite start temperature (i.e. M_s) upon free stress condition begins the molecular structure transformation from austenite to twinned martensite and regains fully after the temperature reaches below the martensite finish temperature (i.e. M_f).

Super-elastic mechanism exhibits strain development during loading and strain recovery upon unloading when the temperature is above A_f. In other words, the stress-strain relation follows hysteresis upon loading and unloading in an isothermal condition above A_f, where path G-H shows classical elastic deformation in the austenite phase under moderate loading. Further increase of loading above the critical stress introduces Stress-Induced Martensite (SIM) phase in the path H-I, and majority of the austenite has converted to SIM by the end this path. However, loading above this point leads to inelastic deformation of SIM along the path I-J, followed by unrecoverable plastic deformation of the material. Path J-K shows unloading of the stress so that thermodynamically stable austenite phase introduced by the end of this path. Further unloading brings the material to austenite phase with the large recovery of strain (i.e. path K-L). Path L-M shows an ideal case of the strain recovery upon unloading. Usually, some residual strain exist in most of the superelastic recovery, i.e. points M and G do not overlap. Reader may refer to Rao et al. [210] for further details of this micro-structural behaviour of SMA.

Among various shape memory alloys available in the market for different end usage, Nitinol (i.e. Ni-Ti alloy) is popular for its excellent thermo-mechanical and thermo-electrical properties. Here, it may be noted that the behaviour of SMA depends on various factors viz. stress, strain, temperature, phase fraction, creep and visco-plasticity.

4.3.1 Graesser and Cozzarelli Model

As this study aims to utilize the super-elastic property of Nitinol in passive mode of operation first, Graesser-Cozzarelli model [137] is used to trace this behaviour of SMA tendon. In this model, the 1D stress-strain relationship is defined as

$$\dot{\sigma} = D_A \left[\dot{\epsilon} - |\dot{\epsilon}| \left| \frac{\sigma - \sigma_\beta}{\sigma_Y} \right|^{c_n - 1} \left(\frac{\sigma - \sigma_\beta}{\sigma_Y} \right) \right] \tag{4.5a}$$

$$\sigma_\beta = D_A c_\alpha \left[\epsilon - \frac{\sigma}{D_A} + c_T |\epsilon|^{c_s} \operatorname{erf}(c_r \epsilon) \right] \tag{4.5b}$$

where σ and ϵ are the uni-axial stress and strain, respectively, D_A is the elastic modulus in austenite phase, σ_β is uni-axial back-stress, σ_Y is the threshold for phase transformation. In the above equation, $c_\alpha = \frac{E_y}{D_A - E_y}$ is a constant that determines the slope of the inelastic region, E_y is the slope of the stress-strain diagram

after yielding, c_n is a constant that controls the sharpness of transition from elastic to inelastic phase, c_T controls type and size of the hysteresis. The two constants c_r and c_s control the extent of elastic recovery during unloading and the slope of unloading stress path. The error function, $\mathrm{erf}(x)$ is given by

$$\mathrm{erf}(x) = \frac{2}{\sqrt{\pi}} \int_0^x e^{-t^2} dt \tag{4.6}$$

4.3.2 Liang and Rogers Model

Besides passive control, this work extends the vibration control model for semi-active operation. Thus, in order to achieve maximum possible control force, Joule heating of tendon is proposed. For this purpose, a constitutive relation is derived based on Liang and Rogers [140] model of SMA and thermodynamic principles. In their model, the behavior of SMA is characterized by the relation between stress (σ), strain (ϵ), temperature (T) and the phase transformation (ξ) as

$$\dot{\sigma} = D\dot{\epsilon} + \Lambda\dot{\xi} + \Theta\dot{T} \tag{4.7}$$

Over dot in this expression represents derivative with respect to time. The parameter D in the above equation represents the Young's modulus of SMA, which is a linear function of martensite volume fraction considering a mechanical model equivalent to the Voigt scheme i.e.

$$D(\xi) = D_A + \xi(D_M - D_A) \tag{4.8}$$

Here, D_A and D_M represent the modulus of elasticity in the austenite and martensite phase, respectively. In Eq. 4.7, Λ represents the phase transformation tensor and Θ corresponds to the thermo-elastic tensor. The phase transformation tensor Λ is defined as

$$\Lambda(\xi) = -\epsilon_L D(\xi) \tag{4.9}$$

where ϵ_L represents the maximum recoverable strain. In Eq. 4.7, the martensite volume fraction ξ can be defined as a function of stress and temperature i.e. $\xi = \xi(\sigma, T)$. In this context, Fig. 4.3b shows a typical

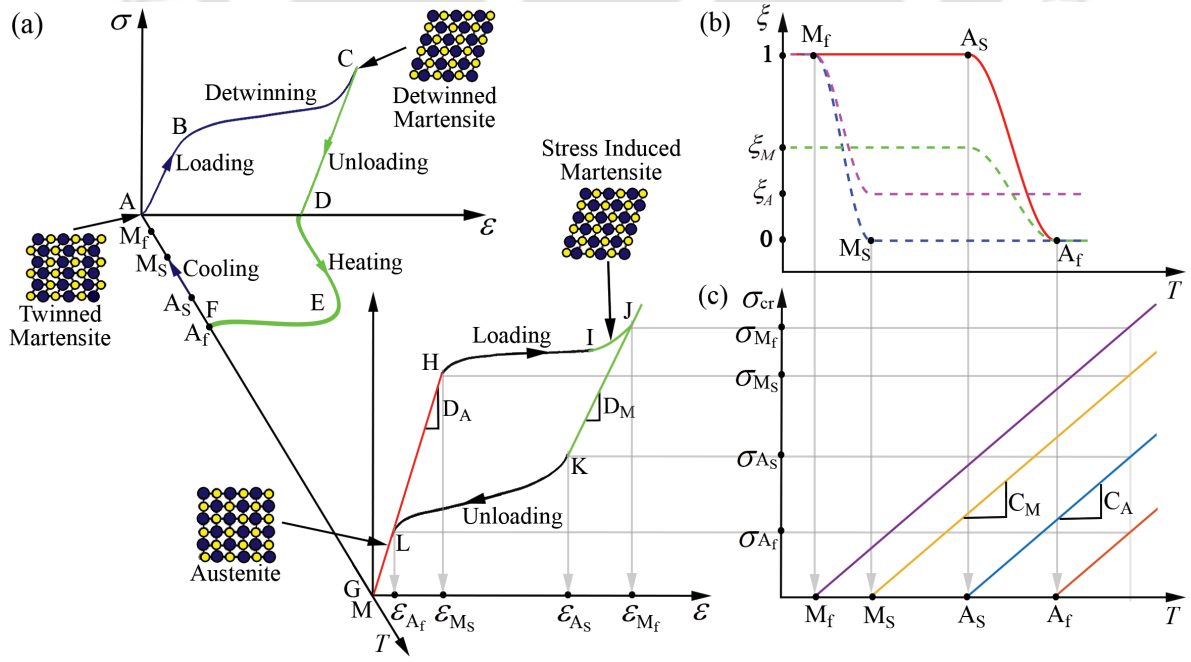

Figure 4.3: Schematic representation of behaviour of SMA in Liang-Rogers model (a) stress-strain-temperature behaviour of SMA (b) variation of martensite volume fraction and (c) variation of critical stress with respect to temperature.

variation of martensite volume fraction with respect to temperature under free stress condition. Liang

and Rogers [140] proposed a cosine formula to describe this change in volume fraction during the phase transformation under free stress condition and a linear stress-temperature relationship as shown in Fig. 4.3c. Here, it may be noted that the transformation temperatures (i.e. M_f, M_s, A_s and A_f) also vary linearly with stress and forms new boundaries (i.e. M_f^σ, M_s^σ, A_s^σ and A_f^σ), which may be obtained from the slope C_M and C_A. Using this model, the volume fraction for the phase transformation from martensite to austenite is expressed as

$$\xi = 0.5\xi_M\{\cos[A_A(T - A_s) + B_A\sigma] + 1\} \tag{4.10}$$

where T is the temperature of the current state when the phase transformation takes place. As the temperature decreases from M_s to M_f, the volume fraction is defined as

$$\xi = 0.5(1 - \xi_A)\cos\left[A_M(T - M_f) + B_M\sigma\right] + 0.5(1 + \xi_A) \tag{4.11}$$

In Eq. 4.10 and Eq. 4.11, A_A, B_A, A_M and B_M are the material parameters, which are function of transition temperature A_s, A_f (i.e. austenite formation start and finish temperature), M_s and M_f (i.e. martensite formation start and finish temperature). The rate of change of martensite volume fraction during forward (i.e. A_S^σ to A_f^σ) and backward (i.e. M_S^σ to M_f^σ) transformation can be evaluated by differentiating the above equations with respect to time. For all other cases, it is equal to zero (i.e. $\dot{\xi} = 0$ and $\dot{\xi}_S = 0$).

The above mentioned constitutive model is used in this study along with the law of thermodynamics for tuning the control force developed in SMA tendon by the application of heat. The applied heat on SMA tendon may exchange with the surrounding to maintain the equilibrium. Thus, the rate of net heat transfer to the tendon is expressed using the first law of thermodynamics as

$$\dot{Q} + \dot{W} = \dot{\Pi}_{K,T} + \dot{\Pi}_{P,T} + \dot{H} \tag{4.12}$$

In the above equation, Q is the net heat transfer and W is the work done, $\Pi_{K,T}$ and $\Pi_{P,T}$ represent the kinetic and potential energy of the tendon while H is the enthalpy. The rate of change of heat flow with respect to time depends on the rate of change of heat generated on the tendon by the application of electric current and the heat emitted with respect to time i.e.

$$\dot{Q} = \dot{Q}_{gen} - \dot{Q}_{out} \tag{4.13}$$

As the current passes through the tendon, electrical energy is transformed into the thermal energy. The rate of heat generated due to the flow of current with voltage V is given by

$$\dot{Q}_{gen} = \frac{V^2 A_{cr}}{\rho_r L} \tag{4.14}$$

where ρ_r, L and A_{cr} are the resistivity, length and cross-sectional area of SMA tendon, respectively. If the surrounding temperature is assumed to be T_{amb}, heat loss to the surrounding due to convection is

$$\dot{Q}_{out} = h_c A_{sur}(T - T_{amb}) \tag{4.15}$$

where h_c is the convective heat transfer coefficient and A_{sur} is the surface area of the tendon exposed to the surrounding. The variation of heat can be measured in terms of Biot number [211], which is the ratio of the conductive heat transfer resistance within the tendon and the external convective heat transfer resistance at the surface of the body $\left[\text{i.e. } N_{Bi} = L_c h_c K_b^{-1} = V h_c (A_{sur} K_b)^{-1}\right]$. The work input into the tendon is zero as the displacement of the blades is perpendicular to the force applied by the tendon. Therefore, the left side of Eq. 4.12 can be modified by substituting Eq. 4.14 and Eq. 4.15 as

$$\dot{Q} + \dot{W} = \frac{V^2 A_{cr}}{\rho_r L} - h_c A_{sur}(T - T_{amb}) \tag{4.16}$$

The change in enthalpy during the transformation is assumed to be a function of the martensite volume fraction [153]. For simplicity, it is assumed that the specific heat of these materials have mean and fluctuating

components, which are proportional to the martensite volume fraction i.e.

$$\dot{H} = m_{_T}\left[c_p\dot{T} - \Delta h\dot{\xi}\right] \tag{4.17}$$

where $m_{_T}$ is the mass of the tendon, c_p and Δh represent the specific heat of the wire and the latent heat of transformation, respectively. The first term represents the rate of enthalpy due to the changes of temperature while the second term represents the rate of enthalpy due to the phase transformation. The rate of change of potential energy is due to the amount of the strain energy stored in the SMA tendon. The change in kinetic energy is a function of product of strain rate and its rate of change. Therefore, the contribution to the total energy is negligible or $\dot{\Pi}_{K,T} \approx 0$ and the rate of potential energy is given by

$$\dot{\Pi}_{P,T} = \sigma A_{cr}\dot{L} \tag{4.18}$$

Therefore, Eq. 4.12 can be modified into the following form

$$(\rho_r L)^{-1}V^2 A_{cr} - h_c A_{sur}\Delta T = m_{_T}\left(c_p\dot{T} - \Delta h\dot{\xi}\right) + \sigma A_{cr}\dot{L} \tag{4.19}$$

The volume fraction in the above equation is a function of stress and temperature. Combining all these features, a generalized formula can be developed for the rate of change of stress and temperature with Joule heating as follows

$$\dot{\sigma} = \gamma_1\dot{\epsilon} + \gamma_2\dot{T} \tag{4.20}$$

$$\dot{T} = {\tau_2}^{-1}\left[V^2 A_{cr}(\rho_r L)^{-1} - h_c A_{sur}(T - T_a) - \sigma A_{cr}\dot{L} - \tau_1\dot{\epsilon}\right] \tag{4.21}$$

In the above equation, $\gamma_1 = D(1 - \epsilon_L DE_2)^{-1}$ and $\gamma_2 = (\Theta + \epsilon_L DE_1)(1 - \epsilon_L DE_2)^{-1}$ while $\tau_1 = m_{_T}\Delta h E_2\gamma_1$ and $\tau_2 = m_{_T}c_p + m_{_T}\Delta h(E_1 + E_2\gamma_2)$. As the temperature increases, the material changes from martensite to austenite with $E_1 = A_A\chi$ and $E_2 = B_A\chi$ where χ varies with temperature and stress as

$$\chi = \begin{cases} 0.5\xi_M \sin[A_A(T - A_S) + B_A\sigma] & \text{if} \quad A_S + \sigma C_A^{-1} \leq T \leq A_f + \sigma C_A^{-1} \\ 0 & \text{Otherwise} \end{cases} \tag{4.22}$$

Similarly, the same parameters for decreasing temperature during austenite to martensite transform are $E_1 = A_M\chi$ and $E_2 = B_M\chi$, which is given by

$$\chi = \begin{cases} 0.5(1 - \xi_A)\sin[A_M(T - M_f) + B_M\sigma] & \text{if} \quad M_f + \sigma C_M^{-1} \leq T \leq M_S + \sigma C_M^{-1} \\ 0 & \text{Otherwise} \end{cases} \tag{4.23}$$

It is assumed that the volume of SMA tendon ($V_{_T}$) does not change with respect to time in this study. Therefore, the cross sectional area, length and surface area of the stiffener change, which are given by following expressions.

$$A_{cr}(t) = \frac{V_{_T}}{L(t)} \tag{4.24a}$$

$$r_{_T}(t) = \sqrt{\frac{A_{cr}(t)}{\pi}} \tag{4.24b}$$

$$A_{sur}(t) = 2\pi r(t)L(t) \tag{4.24c}$$

Using these SMA models, the control force in Eq. 4.3 is evaluated at every time instant, i.e. $F_T(t) = \sigma(t)A_{cr}(t)$, which acts against the deformation of the blade.

Following section presents the numerical analysis of onshore and offshore wind turbine to demonstrate the performance of the stiffener.

4.4 Numerical Analysis and Discussion

In this section, the performance of Horizontal Axis Wind Turbine (HAWT) blade with proposed longitudinal stiffening strategy is studied using the SMA models presented in the above section. First the analysis carried out using passive stiffening strategy, i.e. based on Graesser and Cozzarelli Model.

4.4.1 Passive Blade Stiffener

In this subsection, numerical simulation is carried out to illustrate the proposed passive response reduction strategy for the benchmark National Renewable Energy Laboratory (NREL) 5 MW wind turbine [201]. The details of this turbine and the response validation for Discrete Reduced Order Model (DROM) are presented in Section 3.3. Once the performance of the DROM is validated using standard results, it is further used to demonstrate the performance of the proposed longitudinal stiffening.

Thus, the blade responses with and without stiffener are evaluated using simulated load time-histories. The material for the SMA tendon is assumed to be Nitinol, whose Young's modulus and yield strength are 196.5 GPa and 206.84 MPa, respectively [136]. The non-dimensional constants in the G-C model, i.e. c_α, c_r, c_s, c_T and c_n are 0.0197, 2500, 0.001, 0.07 and 3, respectively. Considering these parameters, the system matrices are evaluated and responses are simulated. Fig. 4.4 and Fig. 4.5 show the unstiffened and stiffened blade responses at the rated speed in the out-of-plane and in-plane directions, respectively. Fig. 4.4a represents the displacement time history while Fig. 4.4b shows its Fourier amplitude spectrum

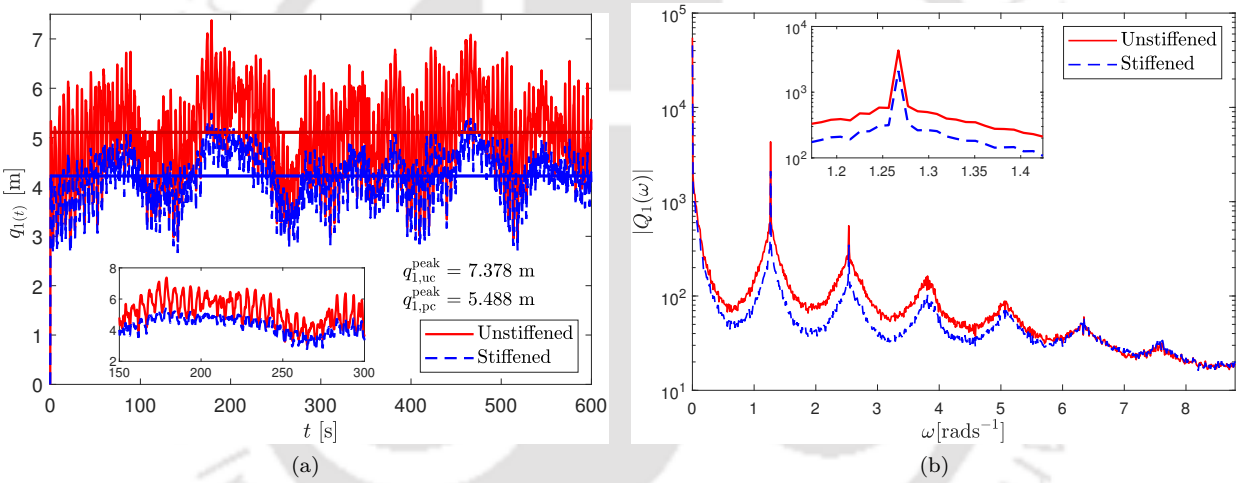

Figure 4.4: Out-of-plane blade response at rated speed; (a) displacement time history and (b) Fourier amplitude spectrum.

in the out-of-plane direction. The horizontal lines in Fig. 4.4a and Fig. 4.5a represent the mean blade response. The peak response in the out-of-plane direction is reduced by 25.62% while the mean and *rms* responses are reduced by 17.32% and 38.69%, respectively. In this context, it can be observed that the mean component of the out-of-plane response is governed by the mean of the in-flowing wind while the fluctuating component is caused by the turbulence. The large mean response in this direction (∼5 m) coupled with dynamic amplification at the rated speed not only cause significant bending followed by large deformation, it is also responsible for blade-tower impact. Therefore, any controller aiming at mitigating the out-of-plane response must address this mean component besides fluctuating part of the response. The advantage of the proposed passive stiffening strategy is reflected here, in its ability to suppress the dynamic response along with mean component as compared to other controller proposed in the literature. This point will be further discussed in the following sub-section. Fig. 4.4b shows the Fourier amplitude spectrum of the unstiffened and stiffened responses indicating the peak reduction. It also reveals that the response is dominated by the rotational frequency and its harmonics. This is due to the rotational sampling of the wind flow, where each airfoil is responsible for gust slicing. Fig. 4.5a shows the response in the in-plane direction while its Fourier amplitude spectrum is shown in Fig. 4.5b. The peak response in this case (i.e. in-plane) is reduced by 13.91% while the mean and *rms* responses are reduced by 14.42% and 8.92%, respectively. Together, these results prove the efficiency and benefit of the proposed blade stiffening strategy as a single tendon can

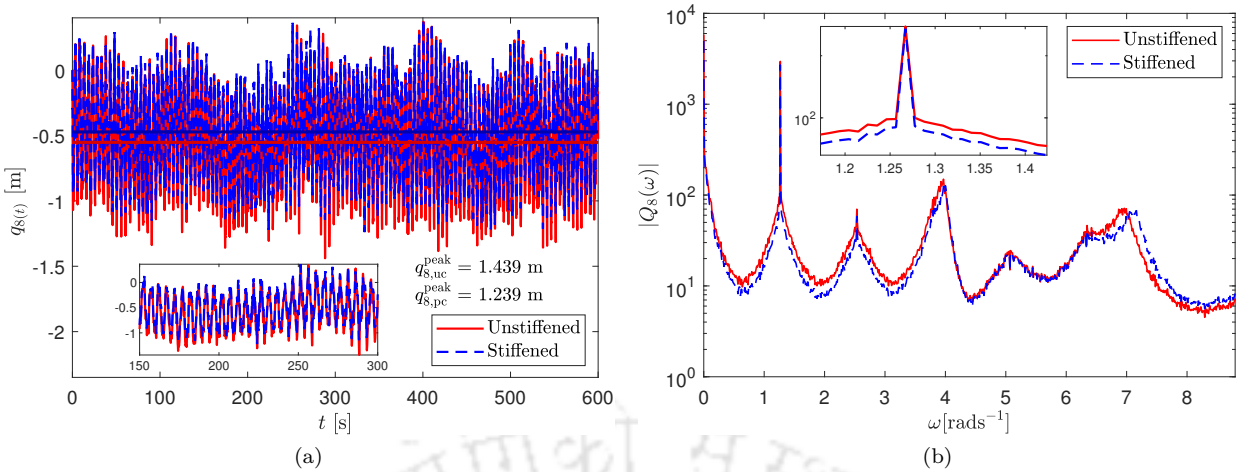

Figure 4.5: In-plane blade response at rated speed; (a) displacement time history and (b) Fourier amplitude spectrum.

reduce deformation in two orthogonal directions. This is a clear advantage over other controllers, as they demand separate controllers dedicated in each direction.

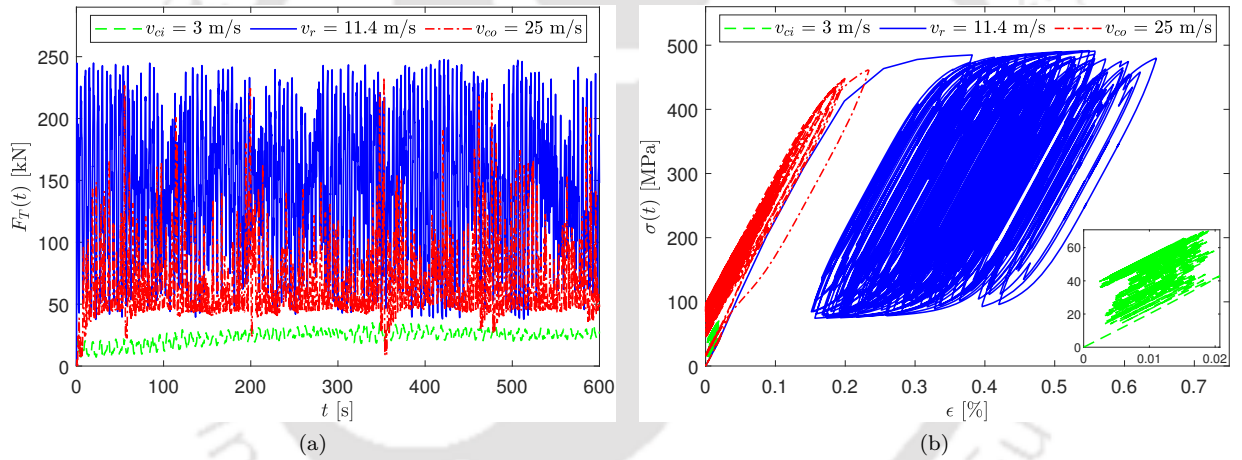

Figure 4.6: Tendon force for 1 in dia.; (a) time history and (b) stress-Strain behaviour.

Besides response reduction, further investigation is also carried out to monitor the force level in the tendon and its impact on the blade. Fig. 4.6 shows the details of the restoring force and stress-strain behaviour of the tendon. Since, the aerodynamic load is less at the cut-in speed, it is reflected in less deformation. Due to this reason, the axial strain is also less and hence the tension in the cable is less compared to other load cases. The stress-strain behaviour at this load is shown in the inset of Fig. 4.6b. The load increases as the wind speed increases up to the rated speed and hence, more force is developed in the cable. The aerodynamic load in the flapwise direction is maximum at this speed and, hence, well developed hysteresis is noticed in this load case. Once the speed crosses the rated value, the pitch controller initiates its action to keep the *rpm* same. Due to this reason, aerodynamic load reduces in the flapwise direction, which is followed by lesser blade deformation. Thus, the area under the stress-strain curve at this speed is less compared to the rated speed.

Once the response reduction at the rated speed is evaluated, the performance envelope of the proposed blade stiffening is investigated further. For this reason, a sensitivity analysis is carried out with 100 simulated turbulent time histories. The ensemble average of different performance parameters (i.e. peak, peak-to-peak, mean and *rms*) are considered here for further analysis at three different wind speeds (i.e. cut-in, rated and cut-out) covering the full spectrum of operation. Table 4.1 summarizes the performance of the proposed longitudinal stiffening based response reduction. In this table, abbreviations P, $P2P$, μ and *rms* correspond to percentage reduction of peak, peak-to-peak, mean and root mean square values, respectively

while subscripts *out* and *in* represent the out-of-plane and in-plane directions, respectively. From this table,

Table 4.1: Performance of the proposed passive longitudinal stiffening in various operating conditions

$\bar{v}$ (m/s)	Ω (rpm)	θ_p (°)	**Percentage Reduction (%)**							
			Out-of-Plane				**In-Plane**			
			P_{out}	$P2P_{out}$	μ_{out}	rms_{out}	P_{in}	$P2P_{in}$	μ_{in}	rms_{in}
3	6.9	0	6.05	7.39	4.70	8.17	2.06	1.41	5.40	1.29
11.4	12.1	0	23.19	31.51	16.45	35.57	12.39	9.54	14.27	8.77
25	12.1	23.47	16.87	16.27	8.20	10.35	9.28	9.00	12.48	6.43

it is observed that significant reduction can be achieved in terms of peak, peak-to-peak and rms response by the proposed stiffener, which clearly establishes the effectiveness of the proposed strategy. Besides peak and *rms* reduction, the mean reduction is also significant, which is an added advantage. Overall the stiffener offers impressive performance over the complete operational spectrum and in particular, at the rated speed when the effective aerodynamic load on the blade is maximum. Finally, the effect of the diameter of SMA tendon is studied and the results are shown in Fig. 4.7 and Fig. 4.8 for various sizes and wind speeds.

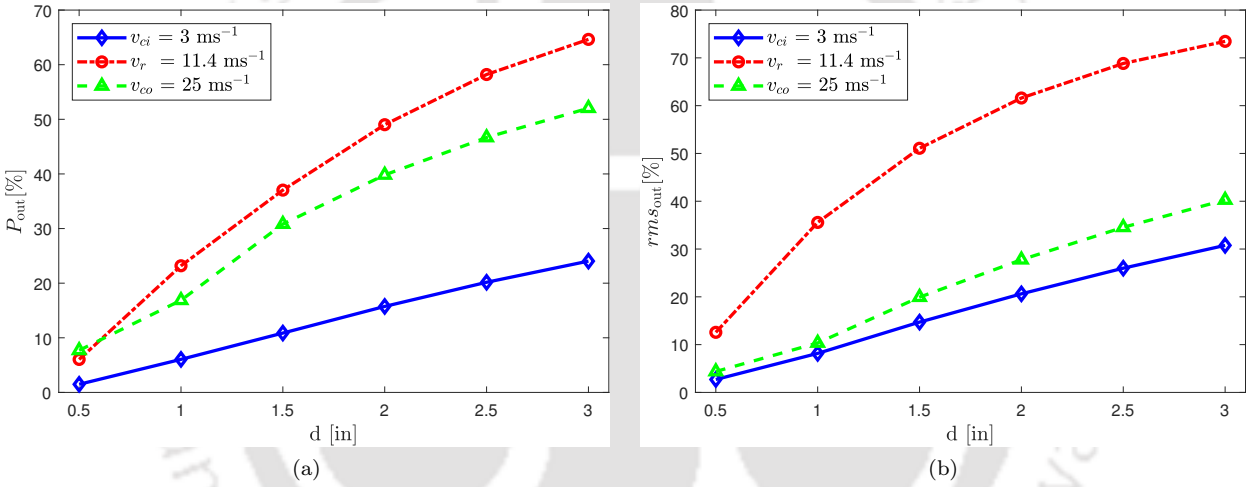

Figure 4.7: Percentage reduction in out-of-plane vs diameter of tendon; (a) peak and (b) *rms*.

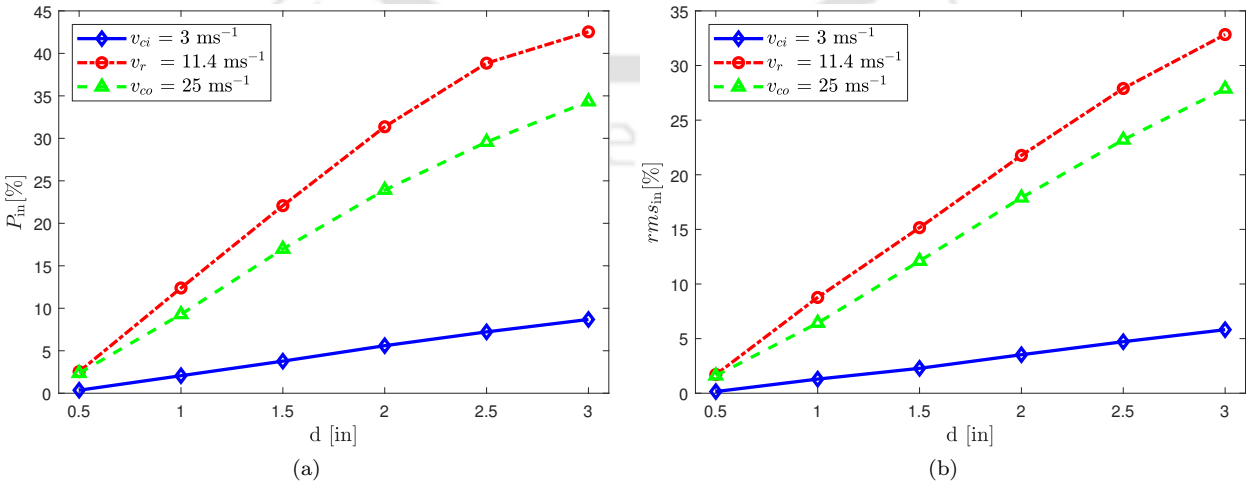

Figure 4.8: Percentage reduction in in-plane vs diameter of tendon; (a) peak and (b) *rms*.

It can be observed from these figures that as the diameter increases, the stiffener is capable of offering

more resistance, which is reflected in the higher percentage of response reduction. All these results together establish the performance spectrum of the proposed stiffening strategy for modern ultra-large wind turbine blades.

While response reduction is the main objective of this work with major emphasis on the out-of-plane performance enhancement of the blade, attention is also paid to ensure that the proposed strategy does not adversely affect the design of the blade. For this purpose, longitudinal force and stress at the blade root are investigated. Since the cable is assumed to be in taut condition, it only develops tension when the blade deforms. This axial tension in the cable primarily opposes the centrifugal force and hence, the bending deformation of the blade. Thus, the cable tension effectively reduces the longitudinal stress arising out of centrifugal force and blade bending. To prove this point, longitudinal force and stress are plotted in Fig. 4.9. Fig. 4.9a shows this force at the root with and without SMA stiffener. From this figure, it can be observed that the tension developed in the cable is always beneficial as it opposes centrifugal force and never crosses its values. Due to this reason, the axial force in the stiffened case remains less than that for the unstiffened case. Ultimately, the longitudinal stress at this location is shown in Fig. 4.9b, which indicates an overall peak reduction of 25.53% at the rated speed. This result proves the proposed stiffening strategy has no adverse effect on the blade design.

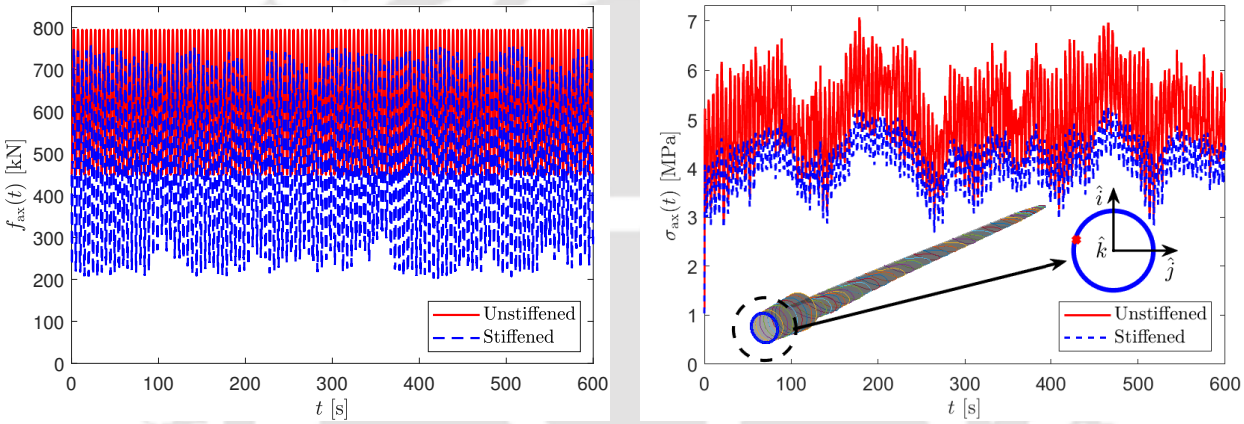

(a) (b)

Figure 4.9: Longitudinal blade response at rated speed; (a) reaction at the root and (b) axial stress at the same location.

4.4.1.1 Comparison with Other Passive Controllers

Finally, the performance of the proposed stiffening strategy is compared with other passive vibration controllers. For this purpose, three different passive controllers, i.e. Tuned Mass Damper (TMD) [73], Tuned Liquid Column Damper (TLCD) [43] and Circular Liquid Column Damper (CLCD) [77] proposed in the literature are considered here. The reason behind the selection of these references are that they use the same

Table 4.2: Comparison with other passive controllers.

Controller Type	$\bar{v}$ **(m/s)**	T_w **(%)**	**Percentage Reduction (%)**							
			Flapwise				**Edgewise**			
			P_{out}	$P2P_{out}$	μ_{out}	rms_{out}	P_{in}	$P2P_{in}$	μ_{in}	rms_{in}
TMD [73]	12	30	N.R.	N.R.	N.R.	N.R.	0.00	22	N.R.	N.R.
SMA Tendon			**25.30**	**26.98**	**16.23**	**25.88**	**10.98**	**7.99**	**13.81**	**9.61**
TLCD [43]	15	10	N.R.	N.R.	N.R.	N.R.	16.84	N.R.	N.R.	21.94
CLCD [77]			N.R.	N.R.	N.R.	N.R.	15.33	N.R.	N.R.	23.55
SMA Tendon			**20.79**	**20.57**	**13.93**	**21.19**	**16.32**	**13.54**	**12.48**	**9.59**

[N.B.: N.R. represents for *'not reported'* in the respective reference.]

NREL 5 MW blade data. The stiffened blade responses are simulated using different mean wind speed and level of turbulence as reported in those references for comparison. Table 4.2 shows the percentage response reductions of different controller and the proposed stiffening strategy. These results clearly prove that a single tendon in the proposed strategy works in both flapwise and edgewise directions. The performance in comparison to other options in terms of different dynamic response quantities are significant, which proves the superiority of the proposed stiffening strategy. In this context, it may be noted that TMD is used in the flapwise direction offers significant reduction of dynamic response [71]. However, it is not used for comparison in this table as the blade data used by Arrigan et al. [71] is different.

4.4.2 Semi-Active Blade Stiffener

In this section, the super-elastic effect of SMA is proposed to be utilized in semi-active mode (i.e. when current is supplied for Jule heating) to achieve maximum possible control. Thus, the numerical analysis of the proposed control strategy is carried out on an offshore wind turbine using Liang-Rogers SMA model. In this context, it is worth mentioning that passive mode is referred to the case when the current flow is stopped and the material is left in the ambient temperature to offer resistance against the vibration with classical elastic deformation. Both aerodynamic and hydrodynamic loads are simulated and their combined effects are considered in this analysis. A sensitivity analysis using different mean wind speeds and size of SMA tendon is carried out. The reduced order model of NREL 5 MW benchmark offshore wind turbine supported over a monopile foundation is used for this numerical analysis. The properties of this turbine are same as in Chapter 3. The wind turbine structure is considered to be mounted on a concrete monopile foundation of height 20 m from the seabed, whose properties are listed in Table 4.3.

Table 4.3: Properties of monopile and parameters related to sea profiles.

Monopile		Sea Profile	
Parameter	Value	Parameter	Value
H_p	20 m	H_s	3 m
D_p	6 m	T_P	10 s
t_p	0.06 m	C_m	1.0
ρ_p	9517.14 kg/m	C_d	1.2
K_{Px}, K_{Py}	3.89E9 N/m	ρ_w	1025 kg/m^3
ξ_{Px}, ξ_{Py}	0.6%		

Table 4.4: Properties of SMA stiffener.

Material Properties		Physical Properties		Thermodynamic Properties	
ρ_s	6450 kg/m^3	A_s	34.5°C	c_p	450 J/kg-K
$D_A - D_M$	83−28 GPa	A_f	49.0°C	Δh	30000 J/kg
$C_A - C_M$	13.8−13.8 MPa/K	M_s	18.4°C	h_c	10 W/m^{2}K
σ_{max}	900 MPa	M_f	9.0°C	T_a	25°C
ϵ_L	0.067	Θ	0.55 MPa/K	ρ_r	1 µΩ m

The wind fields for different mean velocities (i.e. 5, 11.4, 25 m/s) are generated using TurbSim [17] with 15% turbulence and the aerodynamic loads are calculated using Blade Element Momentum (BEM) theory as explained in the Section 2.4.5. Aerodynamic loads for the rated mean wind speed acting on the blades in the out-of-plane and the in-plane directions are shown in Fig. 4.10a and Fig. 4.10b respectively. Also, the Fourier spectrum of the aerodynamic thrust and torque acting at three different locations on the blades are shown in Fig. 4.10c and Fig. 4.10d respectively. In this study, the interaction between wind and wave loads is not considered. The parameters associated with the wave profile simulation are mentioned in Table 4.3. The wave loads are calculated using Morison's equation where the surface elevation of waves are simulated by Joint North Sea Wave Project (JONSWAP) spectrum for $H_s = 3$ m and $T_p = 10$ s. The simulated surface elevation PSD and the wave elevation time history are shown in Fig. 4.10e and Fig. 4.10f, respectively.

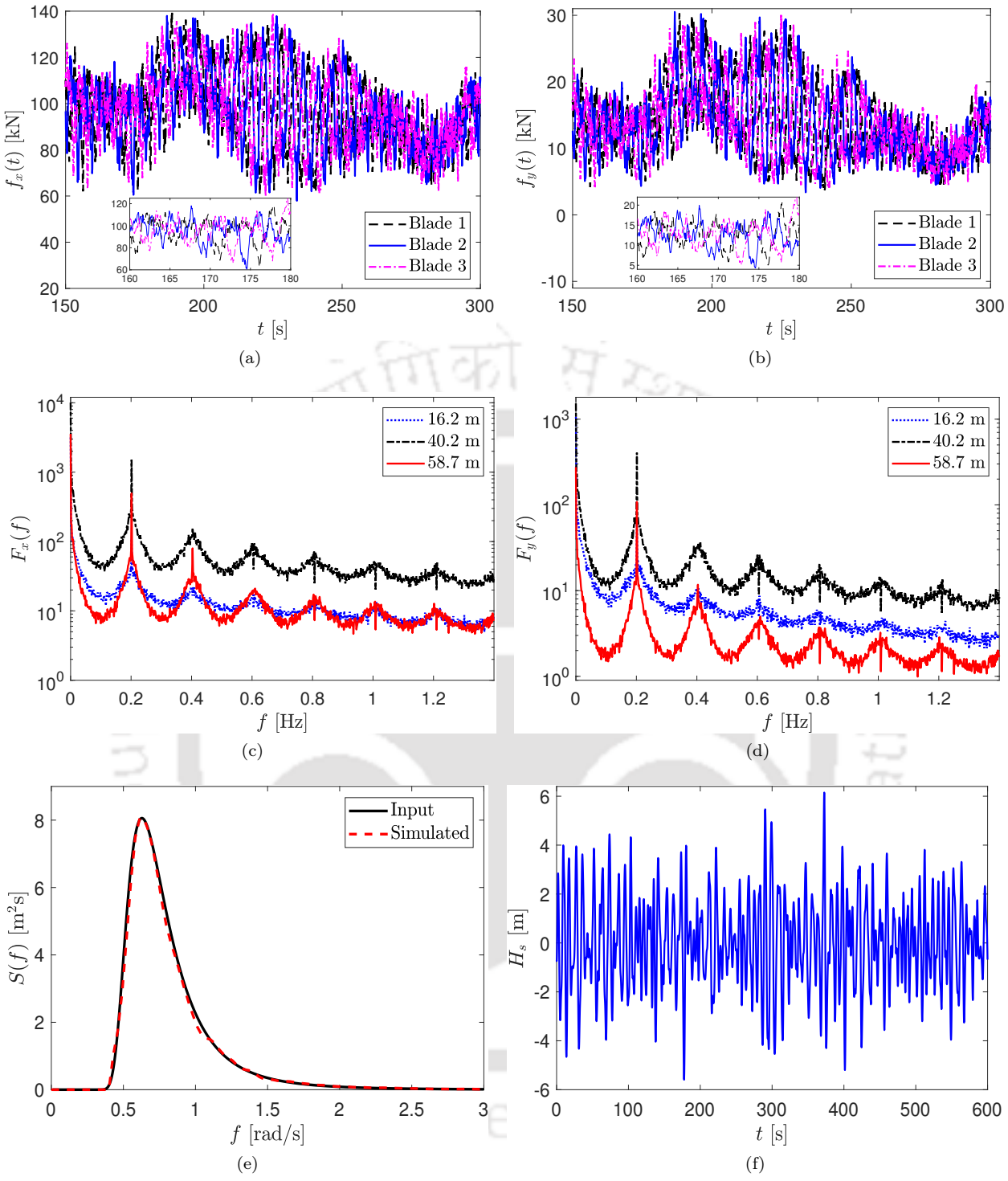

Figure 4.10: Aerodynamic loads for 11.4 m/s average wind speed at hub height; Time history in (a) out-of-plane and (b) in-plane; Fourier amplitude spectrum of (c) thrust and (d) torque; Simulated Sea Profiles; (e) surface Elevation PSD and (f) surface Elevation Time History.

The mass, stiffness and damping matrices are evaluated at each time instant and the corresponding wind and wave loads are applied to obtain the response of the system. The material properties of SMA stiffener are shown in Table 4.4. Here, it may be noted that the SMA stiffener runs from the root to the tip of the blade and hence, its length is considered to be 61.5 m in the numerical analysis. The ambient temperature and corresponding initial martensite volume fraction are assumed to be 25°C and 50%, respectively. The Young's modulus for austenite and martensite conditions are assumed to be 83 GPa and 28 GPa, respectively [153],

while the stress rate of austenite and martensite phase are assumed to be same, i.e. 13.8 MPa/K. Thermal conductivity for the austenite and martensite phases are 18 W/mK and 8.6 W/mK, respectively. The Biot number (N_{Bi}) of 12.7 mm diameter SMA tendon evaluated for the martensite phase is $N_{Bi_M} = 0.00353$ and for the austenite phase is $N_{Bi_A} = 0.00738$, which are less than 0.1 and therefore the variations of the temperature inside and the surface of the tendon is negligible. A constant current flow with voltage 44 V is applied to heat the tendon, which is switched off to allow the tendon to cool down when the martensite volume fraction is zero or the material reaches maximum allowable stress or temperature. The maximum allowable stress and temperature are assumed to be 900 MPa and 95°C, respectively. As a result, once the material is transformed to the martensite phase, the heating is initiated again.

The blade displacement time history in the out-of-plan and in-plane directions are shown in Fig. 4.11a and Fig. 4.11b, respectively for 25.4 mm diameter of tendon. In this figure, the horizontal line represents the mean response or the static component due to the non-zero mean wind flow. It is observed that the peak and Root Mean Square (RMS) displacement of the blade in the out-of-plane direction are reduced by 20.58% and 30.26% respectively in the passive mode. Whereas, the same parameters are reduced by 31.02% and 31.02%, respectively when the current is applied. Similarly, the peak and RMS displacement in the in-plane direction are reduced by 26.29% and 2.71%, respectively in the passive case, while they are 34.65% and 9.11% in the semi-active case. Table 4.5 summarizes the performance of proposed stiffener for different wind speeds. It is observed that percentage reduction increases with the increase of mean wind speed. Moreover, the semi-active stiffener always performs better than its passive version due to more stiffness offered by Joule heating. The stress-strain-temperature behavior for the passive and semi-active stiffener are shown in Fig. 4.11c and Fig. 4.11d. As there is no current flow and subsequent heating, the temperature of the tendon in passive mode remains at its ambient temperature i.e. 25°C. However in the semi-active case, when the current is applied to produce heat, the stress level in the tendon increases. As the temperature attains the austenite finish temperature, the material exhibit super-elastic effects and hence, the force in the tendon also increases, which is ultimately reflected in large reduction even at low strains. Fig. 4.11d shows this phenomenon and justifies the idea of semi-active control strategy proposed in this study. During this event (i.e. semi-active stiffening), the temperature and martensite volume fraction changes with time, which is shown in Fig. 4.11e and Fig. 4.11f, respectively. It is observed that the temperature of the tendon has reached up to 95°C in this analysis.

Table 4.5: Performance of the proposed longitudinal stiffening in various operating conditions.

$\bar{v}$	Ω	θ_p	P_{in} (%)		RMS_{in} (%)		P_{out} (%)		RMS_{out} (%)	
(m/s)	(RPM)	(°)	Passive	Semi-active	Passive	Semi-active	Passive	Semi-active	Passive	Semi-active
5	8.1	0	24.85	35.96	0.53	10.10	4.88	33.07	5.57	32.43
11.4	12.1	0	26.39	34.65	2.71	9.11	20.58	31.26	30.26	31.02
25	12.1	23.47	1.52	10.62	1.53	12.87	4.99	23.69	1.92	24.44

With the performance of SMA tendon established for simulated wind time histories, a sensitivity analysis is carried out for the different mean wind speed and diameter of the tendon. Effect of diameter on the blade response in two directions are shown in Fig. 4.12a and Fig. 4.12b, respectively. It is observed that the peak and RMS response reduction (which are denoted by P and RMS, respectively) in both these directions have increased for larger diameter of the tendon. Subscripts *in* and *out* in these figures correspond to the in-plane and out-of-plane direction, respectively. Also, it is observed that the peak and RMS response reduction for both semi-active and passive cases in these two directions increase with the diameter of the tendon, as expected. Fig. 4.13 and Fig. 4.14 show the complete performance spectrum of the proposed axial stiffening. The second subscript SA and P in these figures refer to semi-active and passive mode, respectively. It is observed that the application of pitch angle reduces the thrust and increases the torque, which in turn, reduces the response of the blade in the out-of-plane direction. Therefore, the response reduction is also less for the wind speed above the rated value. However, the peak and RMS reductions increase with the increase in diameter of the tendon and the semi-active version always offers better performance than the passive version for the entire operational range of the wind speed. These results clearly establish the fact that the proposed SMA based longitudinal stiffening using Joule heating can offer significant response reduction (in terms of mean, peak and RMS responses) for large turbine blades without affecting the aerodynamics of the system. It is a major advantage over other active or semi-active controllers proposed in the literature, which are, in principle, focused on the peak and RMS only, leaving the mean component unattended. Finally, the effect of blade pitch angle above the rated speed is studied, which is shown in Fig. 4.15. The peak and

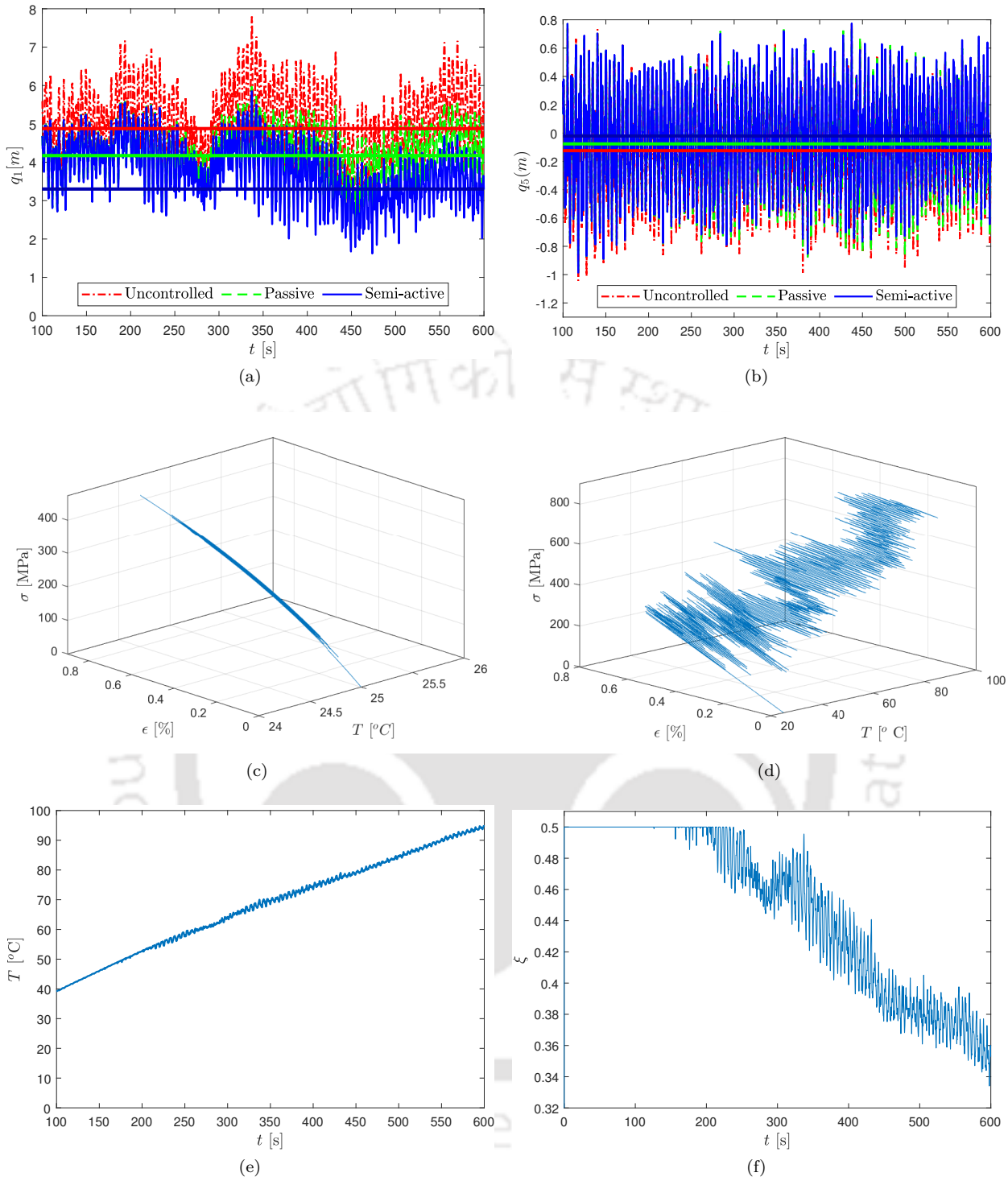

Figure 4.11: Blade response for 11.4 m/s average wind speed at hub height with 12.7 mm dia. SMA tendon; displacement time history (a) out-of-plane and (b) in-plane; hysteretic behaviour (c) passive and (d) semi-active; (e) temperature induced in SMA stiffener and (f) martensite volume fraction.

RMS response reduction have decreased in higher pitch angle in the passive case while semi-active case offers significant reduction.

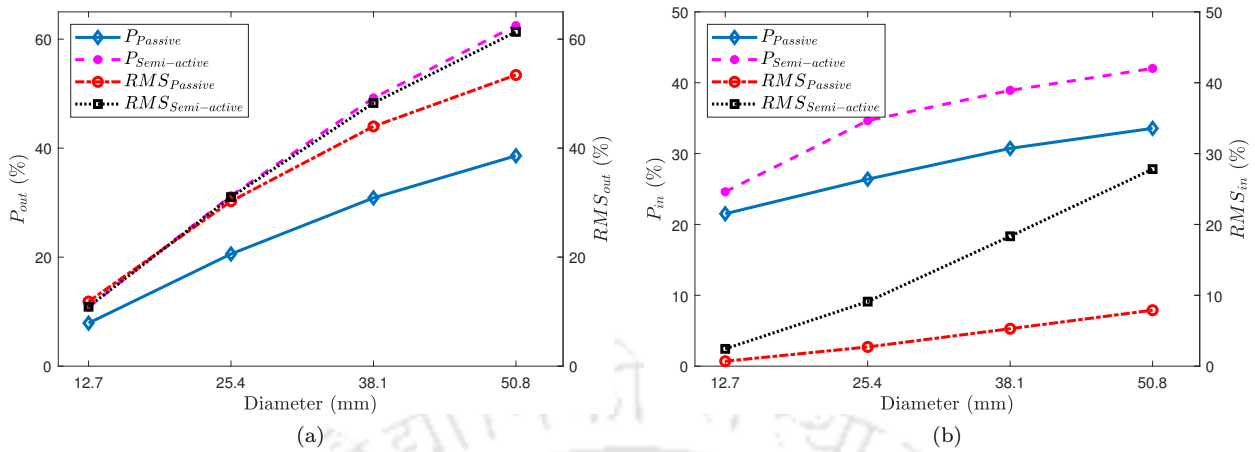

Figure 4.12: Percentage reduction in blade response for 11.4 m/s average wind speed at hub height using different diameter of SMA tendon; (a) out-of-plane and (b) in-plane.

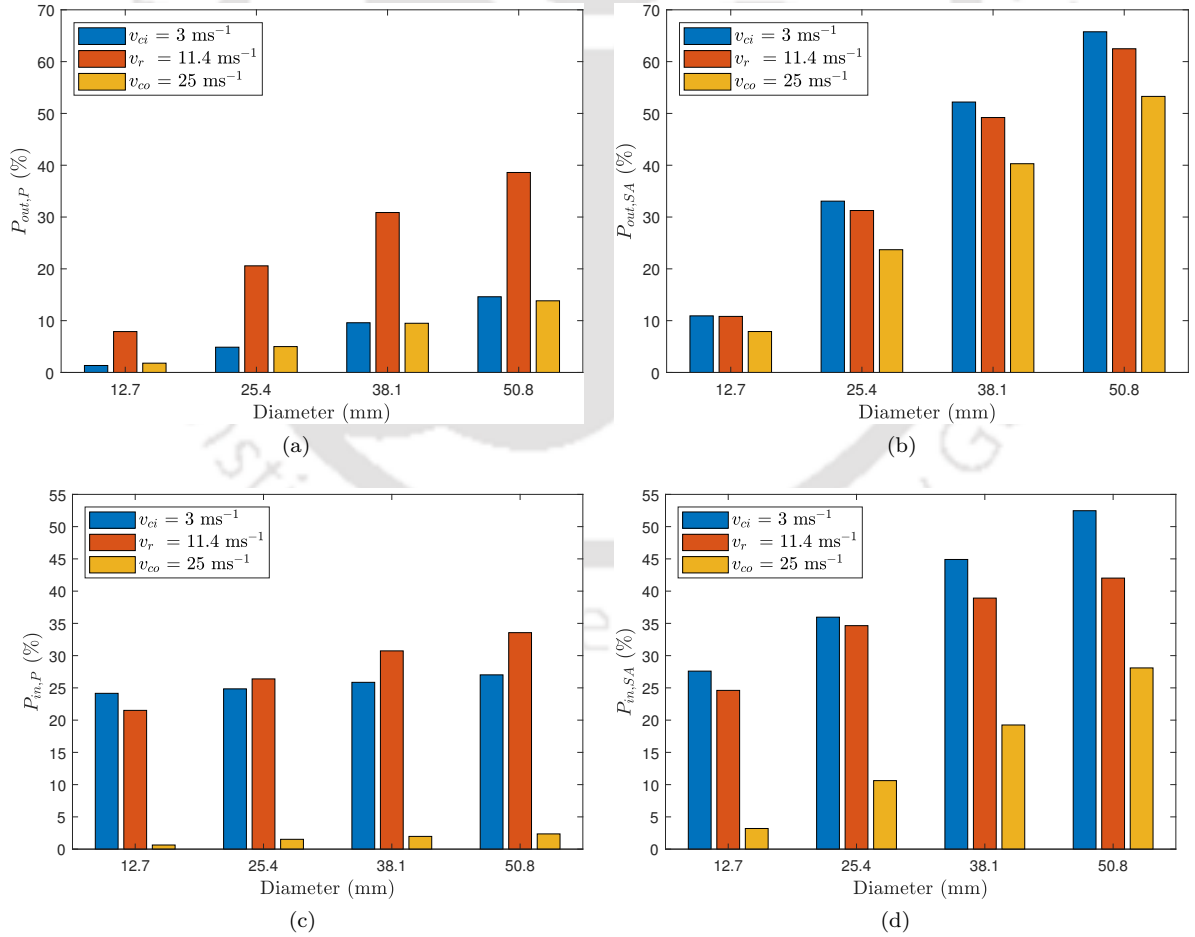

Figure 4.13: Peak Percentage reduction for different wind speed and diameter of SMA tendon; (a) out-of-plane passive, (b) out-of-plane semi-active, (c) in-plane passive and (d) in-plane semi-active.

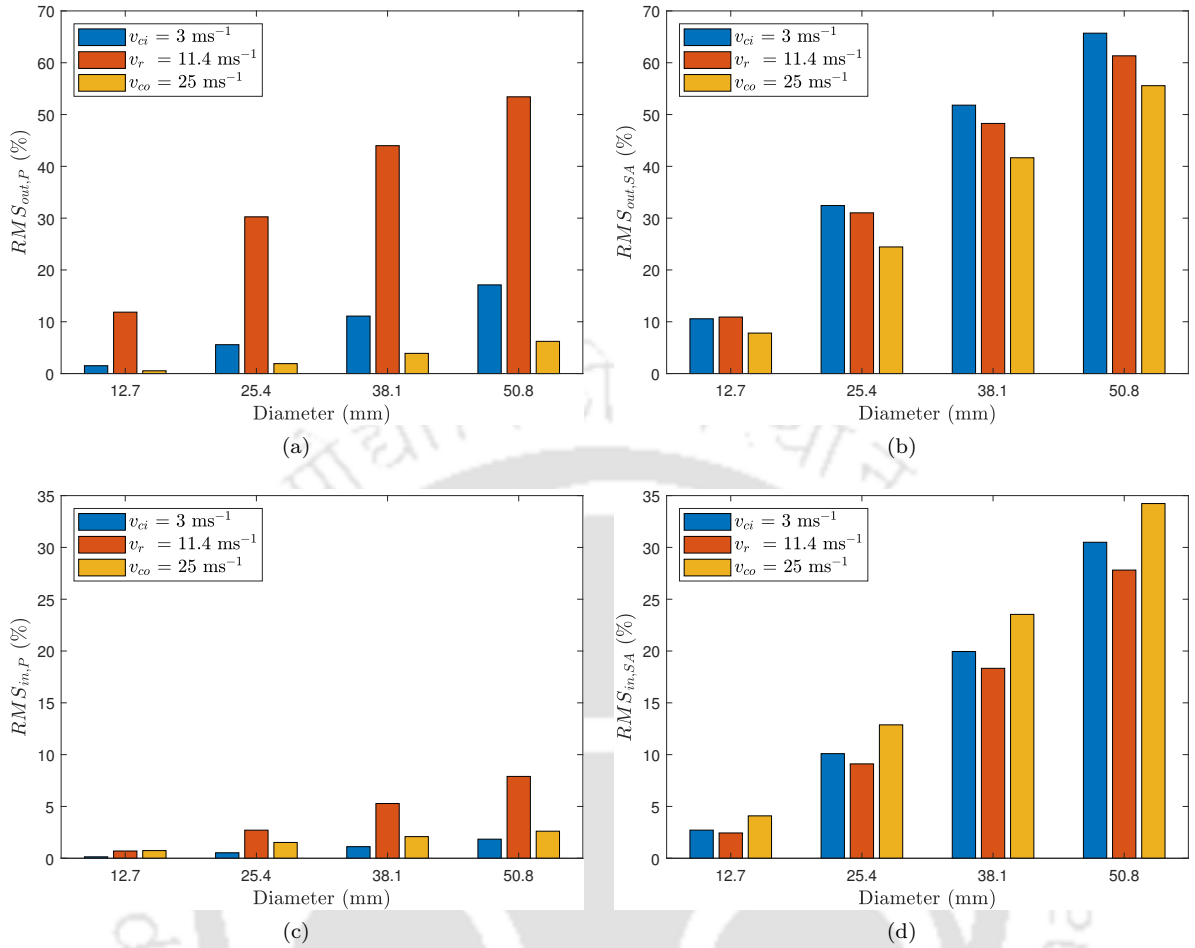

Figure 4.14: RMS Percentage reduction for different wind speed and diameter of SMA tendon; (a) out-of-plane passive, (b) out-of-plane semi-active, (c) in-plane passive and (d) in-plane semi-active.

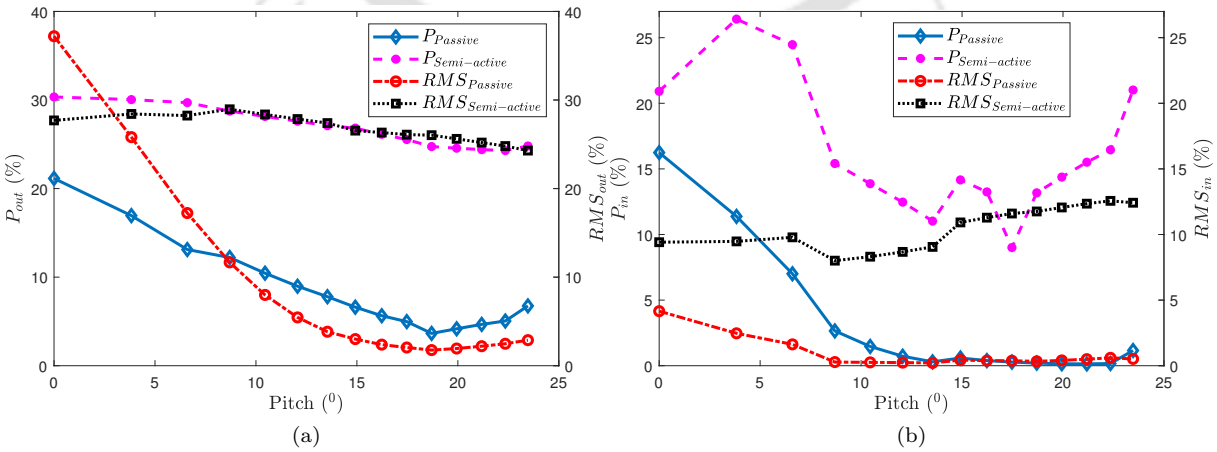

Figure 4.15: Percentage reduction for different pitch angle for above rated wind speed; (a) out-of-plane and (b) in-plane.

4.5 Summary

A novel technique to mitigate the blade vibration of HAWT using longitudinal stiffener is proposed in this chapter. The stiffener is a tendon made of shape memory alloy that offers excellent super-elastic behaviour to withstand the large strain, which is placed along the longitudinal axis of the blade. The discrete reduced order model presented in the previous chapter is further modified with stiffening force to demonstrate the performance of this proposed control strategy. Firstly, the mathematical model is developed for passive stiffener, where the behaviour of SMA is characterized by the Greaser-Cozzarelli model. Later, a new constitutive relation is derived based on the Liang-Rogers model and thermodynamic principles for applying Joule heating to obtain a better performance, i.e. semi-active mode of operation. Numerical analysis is carried out using a discrete reduced order model of the benchmark wind turbine, where the responses are simulated using equivalent aerodynamic damping in each mode of vibration. The results show that significant reduction can be achieved in both the directions (i.e. out-of-plane and in-plane) using the proposed stiffening strategy without altering the aerodynamic profile of the blade. This controller has the ability to reduce the mean component of the vibration particularly in the along-wind direction due to considerable improvement of blade stiffness. Various sensitivity analysis also demonstrate the performance envelop of the proposed stiffening strategy over the operational range of the turbine. Overall the SMA based blade stiffening helps to reduce different dynamic response components (i.e. mean, peak and RMS), which in turn, indicate an improved blade performance. This is bound to affect the blade reliability and fatigue life, which are discussed in the upcoming chapters.

Chapter 5

Reliability Analysis and Design of HAWT

5.1 Introduction

Modern blades are large flexible structure that undergo significant vibration when they are exposed to aerodynamic loads. Besides fatigue and other associated issues, excessive deformation of the blade in the along-wind direction can lead to collision with the tower. To address this issue, rotors are often tilted with pre-cone angle, as shown in Fig. 5.1a. IEC 61400-1 [18] and DNVGL-ST-0376 [212] outline the design guidelines for this purpose to avoid impact with tower due to excessive deformation. However, tilting the rotor and slow-moving shaft in the drivetrain develops additional stress on the gear tooth and bed plate that ultimately induce damage and downtime for maintenance. It also generates additional stress at the root of the blades, which need to be addressed in the analysis and design. The problem is more complex as the aerodynamic loads acting on the blades are cyclostationary in nature. So, its design must focus on two major issues - developing smart rotors that offer less deformation and analyse its performance due to cyclostationary aerodynamic loads. This chapter investigates the safety of the wind turbine blade against

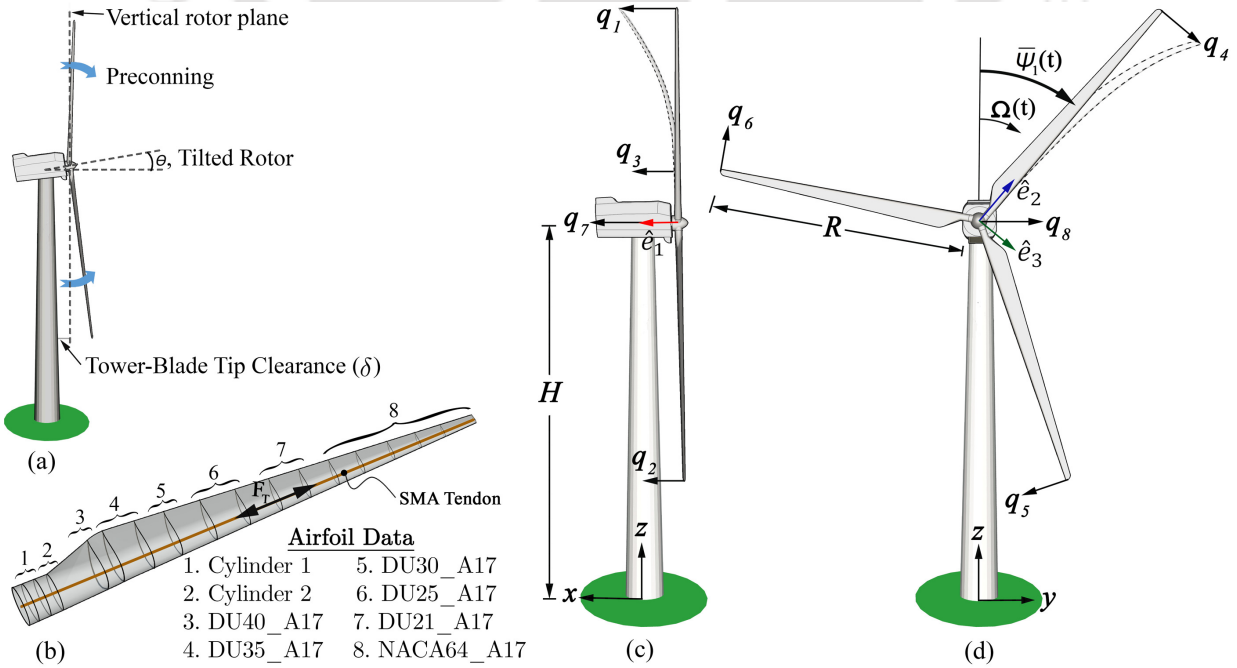

Figure 5.1: Wind turbine model: (a) tilting and pre-conning of blade, (b) airfoil distribution and centrifugal stiffener, (c) out-of-plane degrees of freedom and (d) in-plane degrees of freedom.

excessive deformation. For this purpose, the performance of the blade in the along-wind direction is improved by longitudinal stiffener made of shape memory alloy. Numerical results presented in this chapter clearly demonstrate the performance envelope of the proposed stiffener and its influence on the reliability of the blade. With this in view, following sections present the stochastic modelling and analysis of horizontal axis wind turbine.

5.2 Stochastic Structural Dynamics of HAWT

This work is primarily focused on the time-dependent reliability analysis of a wind turbine against bending deformation. For this purpose, a discrete reduced order model of the tower-blade assembly (i.e onshore wind turbine) with Shape Memory Alloy (SMA) stiffener is used as discussed in the previous chapters (i.e. 3 and 4). The following subsections briefly describe wavelet-based cyclostationary analysis and level crossing problem for performance analysis of HAWT blade.

5.2.1 Wavelet-Based Cyclostationary Analysis

In this section, cyclostationary analysis of the blade response is carried out to quantify its moment statistics. Turbine blades rotating at a constant speed in turbulent wind experience periodically varying aerodynamic loads, which lead to periodically varying non-stationary (i.e. cyclostationary) output. In this context, it may be noted that the cyclostationary process is a special case of a non-stationary process, which can be modelled and analysed in three different ways

1. Close form solution (i.e. input-output relation) within the non-stationary framework.
2. Monte-Carlo or other advanced simulations to quantify the blade response statistics.
3. Time-frequency analysis or other signal-processing tools (e.g. time series), for statistical quantification.

The first option is not applicable in this case as the governing differential equation has time-dependent coefficients, which makes it difficult for closed-form solution. As an alternative, large scale simulation is extremely time-consuming and is often impractical for field problems involving flow simulation. The last option has a trade-off between the other two, which also offer clear insight about the instantaneous frequency content of the signal. Hence, it is adopted in this study, where wavelet-based time-frequency analysis is used to characterise the response statistics. With this in view, a brief overview of the continuous wavelet transform and its use for cyclostationary response analysis of HAWT blade is presented below, which is followed by time-dependent reliability assessment.

Let, $f(t)$ be a continuous time signal in $L^2\mathbb{R}$ whose amplitude and frequency content varies with time. The continuous wavelet transform of this signal is given by [213]

$$W_\psi f(a,b) = \int_{-\infty}^{+\infty} f(t)\psi^*_{a,b}(t)dt \tag{5.1}$$

In the above equation, $*$ indicates complex conjugate while $\psi_{a,b}(t)$ represents the shifted and dilated versions of the mother wavelet $\psi(t)$ in the following form

$$\psi_{a,b}(t) = \frac{1}{|a|}\psi\left(\frac{t-b}{a}\right) \qquad a,b \in \mathbb{R}^+ \tag{5.2}$$

It may be noted that parameter a controls the filter width by adjusting its frequency content while the other parameter b localises $\psi(t)$ to extract the instantaneous features of $f(t)$. Eq. 5.1 is digitally evaluated by discretising the scale and time parameters in the following way [214]

$$\Delta a_j = \frac{1}{2}[(a_{j+1} - a_j) - (a_j - a_{j-1})] = \frac{a_j}{2}\left(\sigma - \frac{1}{\sigma}\right) \tag{5.3a}$$

$$\Delta b_\kappa = \frac{1}{2}[(b_{\kappa+1} - b_\kappa) - (b_\kappa - b_{\kappa-1})] = \Delta b \tag{5.3b}$$

In the above equations, $a_j = \sigma^j$ and $b_\kappa = (\kappa - 1)\Delta b$. Thus, the time discretised version of the inverse wavelet transform for the point-wise reconstruction of the original signal is given by the following form

$$\begin{aligned} f(t) &= \frac{1}{2\pi C_\psi} \int_{-\infty}^{+\infty} \int_{-\infty}^{+\infty} \frac{1}{a^2} W_\psi f(a,b) \psi_{a,b}(t) da db \\ &= \sum_j \sum_\kappa \frac{K \Delta b}{a_j} W_\psi f(a_j, b_\kappa) \psi \left(\frac{t - b_\kappa}{a_j} \right) \end{aligned} \tag{5.4}$$

In this study, complex Morlet wavelet is used, which is mathematically described by the following expression

$$\psi(t) = \frac{1}{\sqrt{\pi f_b}} \exp\left(i 2\pi f_c t\right) \exp\left(-t^2 / f_b\right) \tag{5.5}$$

Parameters f_c and f_b represent the central frequency and frequency bandwidth of the mother wavelet.

Once the original signal is transformed into the time-frequency domain, instantaneous moment statistics can be obtained easily. Thus, applying expectation operator on both sides of Eq. 5.4, the time-dependent mean of $f(t)$ can be evaluated as follows

$$\mu_{f(t)} = E[f(t)] = \sum_j \sum_\kappa \frac{K \Delta b}{a_j} E[W_\psi f(a_j, b_\kappa)] \psi \left(\frac{t - b_\kappa}{a_j} \right) \tag{5.6}$$

Similarly, the instantaneous second-order moment of the signal $f(t)$ can be obtained by taking the inner product of it, which can be expressed in the following form

$$\begin{aligned} \langle f(t).f(t) \rangle = \int_{-\infty}^{+\infty} f^2(t) dt &= \frac{1}{2\pi C_\psi} \int_{-\infty}^{+\infty} \int_{-\infty}^{+\infty} \frac{W_\psi^2 f(a,b)}{a^2} da db \\ &= \sum_j \sum_\kappa \frac{K \Delta b}{a_j} W_\psi^2 f(a_j, b_\kappa) \end{aligned} \tag{5.7}$$

Here, it may be noted that the wavelet transform in Eq. 5.1 localises the basis function at around $t = b_\kappa$ at a scale a_j, which has an effective bandwidth depending upon the type of the basis function used in this transformation. Therefore, the instantaneous value of the second moment of $f(t)$ can be quantified by the following expression

$$E[f^2(t)]|_{t=b_\kappa} = \sum_j \frac{K}{a_j} E[W_\psi^2 f(a_j, b_\kappa)] \tag{5.8}$$

Eq. 5.6 and Eq. 5.8 are applicable for any non-stationary signal as encountered in this work. This is also applicable for cyclostationary process, where the frequency content of the signal varies with a dominant frequency as in the case of a horizontal axis wind turbine. This wavelet-based time-frequency analysis has witnessed different applications in wind turbine design. For example, wavelet-based pitch controllers are used to enhance the performance of the wind turbine system as reported by Fitzgerald [215] and Sarkar et al. [216]. However, in this study, it is used in stochastic sense to investigate the cyclostationarity of the blade vibrations.

5.2.2 Level Crossing

Once the instantaneous first and second moment are evaluated, they can be used further for time-dependent reliability analysis. As stated in the objectives, the focus of this study is to improve blade deformation to avoid impact with tower, which leads to catastrophic consequences. To avoid this issue, blades have pre-cone at the hub, as shown in Fig. 5.1a, where clearance between the tower and blade (i.e. δ) should be sufficient to accommodate the tip deflection of the blade in its along-wind direction. This level crossing problem is addressed by the SMA stiffener that runs along the axis of the blade, which can avoid the pre-cone angle. So, the non-stationary along-wind response X_i exhibits a positive up-crossing rate of $\nu_{X_i}^+(\delta, t)$ within the

time interval $(0, t]$, which is given by the following expression [217]

$$\nu^{+}_{X_i}(\delta, t) = \int_0^{\infty} v_i(t) p_{X(t),\dot{X}_i(t)}(u_i, v_i) dv_i \qquad i = 1, 2, 3 \tag{5.9}$$

Above formulation demands the parent process $X_i(t)$ be narrow banded to quantify the peak distribution. This is logical for a wind turbine considered in this study as the along-wind cyclostationary blade tip response is primarily narrow banded, where the rotational frequency of the turbine dominates the response. This will be further demonstrated in the numerical analysis. Now, Eq. 5.9 can be simplified in the following form if the parent process is Gaussian [217] with time-varying mean and standard deviation.

$$\nu^{+}_{X_i}(\delta, t) = \frac{1}{\sqrt{2\pi}\sigma_{X_i}(t)} \exp\left[-\frac{1}{2}\left\{\frac{X_i(t) - \mu_{X_i}(t)}{\sigma_{X_i}(t)}\right\}^2\right]\left[\mu_{X_i}(t)\mathbf{\Phi}\left(\frac{\mu_{\dot{X}_i}(t)}{\sigma_{\dot{X}_i(t)}}\right) + \frac{\sigma_{\dot{X}_i(t)}}{\sqrt{2\pi}}\right] \tag{5.10}$$

Time-dependent mean and standard deviation in the above equation are represented by $\mu(t)$ and $\sigma(t)$ while the parent process and its derivative have the nomenclature X_i and $\dot{X}_i$, respectively, where $\mathbf{\Phi}(.)$ represents the standard Normal Cumulative Distribution Function (CDF). Since the time of occurrence of the extreme event is rare, it can be modelled as a Poisson process [217]. Using this model of a discrete event within the time interval $(0, t]$, the probability of occurrence of n up-crossing can be expressed as

$$P(n, t) = \frac{\nu^{+}_{X_i}(\delta, t)t}{n!} \exp(-\nu t) \tag{5.11}$$

Hence, the probability of no crossing (i.e. reliability) in the given time interval can be estimated using the above expression for different models (i.e. blade without and with SMA stiffener). This will be evaluated in the following numerical analysis to demonstrate the performance of the proposed SMA stiffener.

5.2.3 Switching Algorithm for Semi-Active Stiffener

Liang-Roger model of Shape Memory Alloy (SMA) as presented in Section. 4.3.2 is adopted here and an efficient switching algorithm is developed for its semi-active mode of operation. Using the reduced order model of the combined system, responses are evaluated, where thermo-mechanical properties of SMA are utilised to reduce the blade deformation. For this purpose, the feedback (i.e. T and σ) is utilised to evaluate the voltage to maintain the maximum possible control force. The flow chart of the proposed control algorithm is shown in Fig. 5.2. The phase transition temperature bounds of SMA and their design limits, which include maximum temperature and maximum stress, are defined as the initial input. The maximum design stress depends on the maximum recovery stress of the SMA tendon. A lesser value of stress than its allowable limit is selected as the maximum design stress to avoid any material damage. Similarly, the maximum design temperature is selected based on the allowable temperature of SMA and the surrounding materials to avoid any damage.

The time-dependent stress and temperature of SMA tendon are used and the revised (or stress-induced) thermal bounds of SMA (M^{σ}_f, M^{σ}_s, A^{σ}_s, A^{σ}_f) are evaluated using initial inputs and feedback. The current supply is switched on if the temperature is less than the bounds A^{σ}_f or $T_{\max}$. Here, it may be noted that the allowable stress limit of SMA increases in presence of electricity and thus the tendon offers more control force. The flow of current is continued until the temperature reaches its allowable limit (i.e. A^{σ}_f or $T_{\max}$) or the stress reaches its maximum design limits. Under this condition, current flow is discontinued, which initiates the fall of temperature and subsequently the stress offered by the tendon. So, the stress level reduces and as soon as the temperature goes below M^{σ}_s, current supply is restored. Also, during switching, the martensite volume fraction is evaluated at every time instant based on the stress and temperature, as explained in section 4.3.2. Then the time derivative of stress and temperature are evaluated using Eq. 4.20 and Eq. 4.21. Finally, the system responses including stress and temperature of SMA tendon are solved.

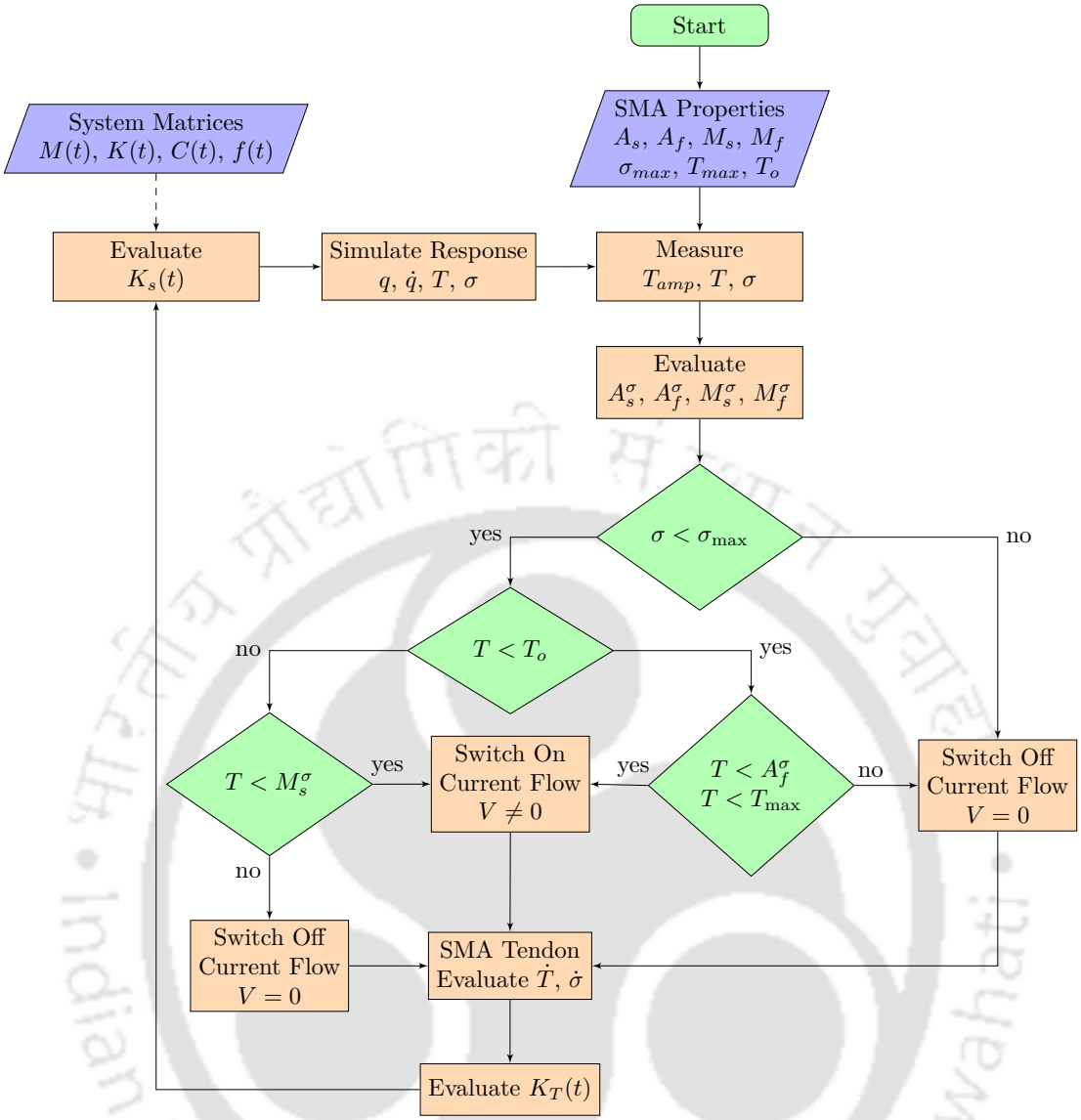

Figure 5.2: Flow chart of the switching algorithm in semi-active case

5.3 Numerical Results and Discussion

In this section, the reliability analysis using the proposed blade stiffening strategy is presented. The onshore wind turbine is modelled using only the first mode of blade and tower in out-of-plane and in-plane directions to improve computational efficiency. Therefore, the displacement in Eq. 3.1 takes the form, $\mathbf{u}(t) = [u_{11,x} \;\; u_{21,x} \;\; u_{31,x} \;\; u_{4,x} \;\; u_{11,y} \;\; u_{21,y} \;\; u_{31,y} \;\; u_{4,y} \;]^T$. Using these degrees of freedom, the reduced order model of an onshore turbine is developed as described in Chapter 3. First, the blade responses obtained using this eight degrees of freedom system are validated with FAST in the following subsection.

5.3.1 Wind Load Generation and Response Validation

The wind field is generated at the hub height using TurbSim [17] for the rated speed of 11.4 m/s with 15% turbulence, as shown in Fig. 5.3a. It is a full field turbulent wind simulation software developed by National Renewable Energy Laboratory (NREL) that generates three components (Downwind, crosswind and vertical wind) at any point in a rectangular grid around the hub. In this study, Kaimal spectrum is used to generate the wind field. Aerodynamic loads at 48 points on the blade are evaluated from the wind field using Blade Element Momentum (BEM) theory. Fig. 5.3b and Fig. 5.3c show the loads acting on the blade at a few selected nodes in the out-of-plane and in-plane directions, respectively. The tower loads in

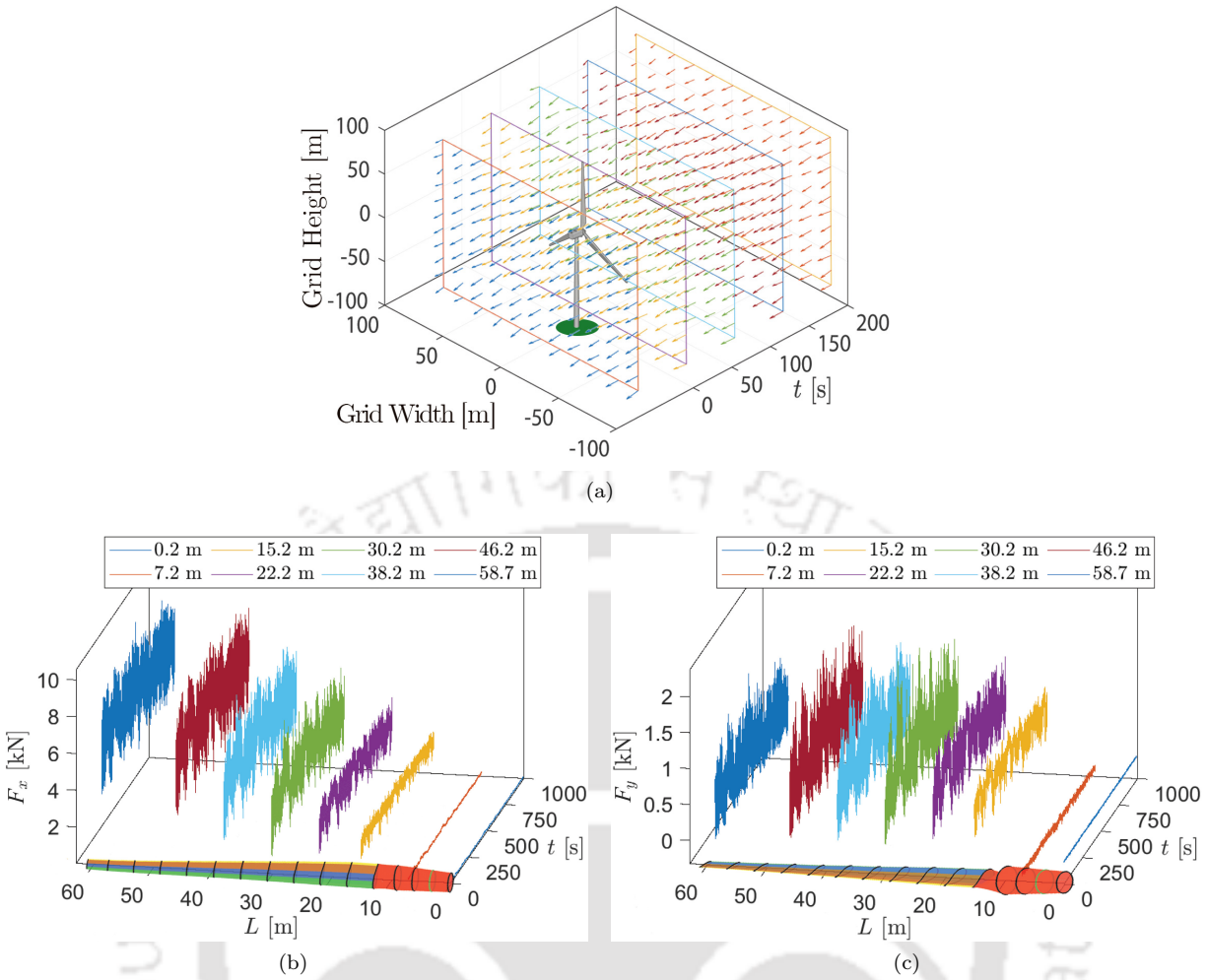

Figure 5.3: Wind field and aerodynamic loads (a) wind flow at rated speed; (b) aerodynamic loads in out-of-plane and (c) aerodynamic loads in in-plane. [N.B.: Blade orientation is schematic, not having exact pitch and aero-twist w.r.t load].

these two directions are mainly contributed by the blades, i.e. net blade loads acting at the nacelle.

The time-varying mass, stiffness and damping matrices as described in Section 5.2 are evaluated to find the response of the combined system. To validate the model, aeroelastic simulation software developed by NREL i.e. FAST [218] is used here. A steady wind flow at 11.4 m/s is generated using TurbSim and corresponding blade loads are estimated using BEM theory. The same wind field is also applied in FAST to generate the response of the wind turbine system. Fig. 5.4 shows the displacement at the blade tip in the out-of-plane and in-plane directions using the proposed Discrete Reduced Degrees of Freedom Model (DRDM) and FAST. Here, it may be noted that axial blade stiffening force is kept zero for this validation exercise. It can be observed that the reduced degrees of freedom model matches closely with FAST and hence, can be used for further to study the SMA based vibration control and reliability analysis.

5.3.2 Semi-Active Switching for Effective Control

In this study, longitudinal stiffener (i.e. SMA tendon) is used to reduce the vibration of the blade, whose material modelling is discussed in Section 4.3.2. Nitinol is used here for its excellent thermo-electro-mechanical properties, which are given in Table. 4.4. For efficient switching, the cable stress is used as feedback after the application of voltage. Hence, maximum design stress needs to be defined to avoid crossing of the maximum recoverable stress (i.e. 900 MPa). In this analysis, 825 MPa is selected as the maximum design stress value. The current flow is switched off once this limit is crossed so that there is enough gap between this value and the maximum recovery stress. Also, the heating of the SMA tendon is limited up to 95°C in order to avoid damage to the surrounding materials. This value may change depending on the properties of the

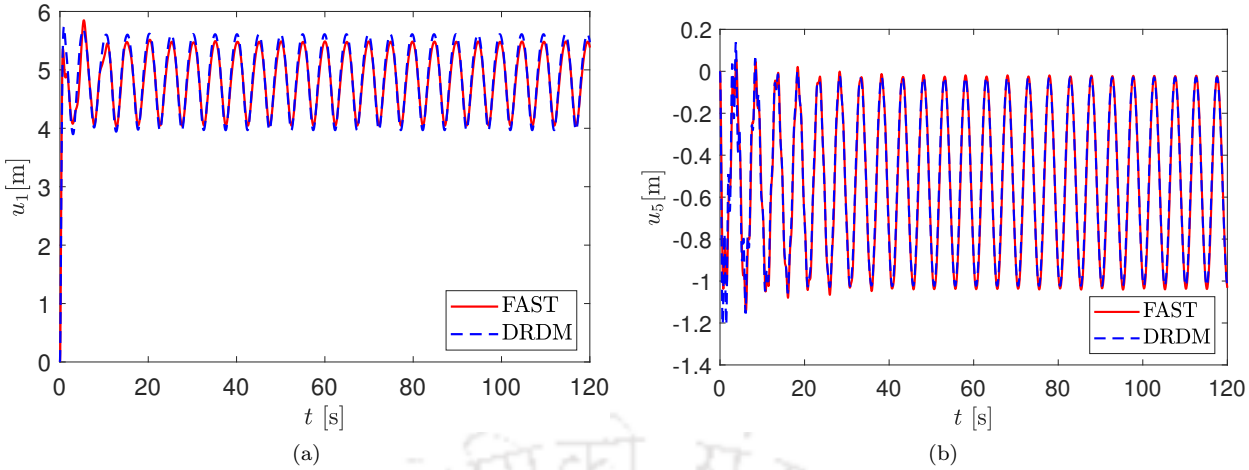

Figure 5.4: Displacement time history of the wind turbine blade at 11.4 m/s steady wind flow; (a) out-of-plane and (b) in-plane. [N.B.: OP→ out-of-plane and IP→ in-plane, DRDM→ discrete reduced degrees of freedom model].

blade material and other design requirements, if any. The ambient temperature is assumed to be 25°C. The

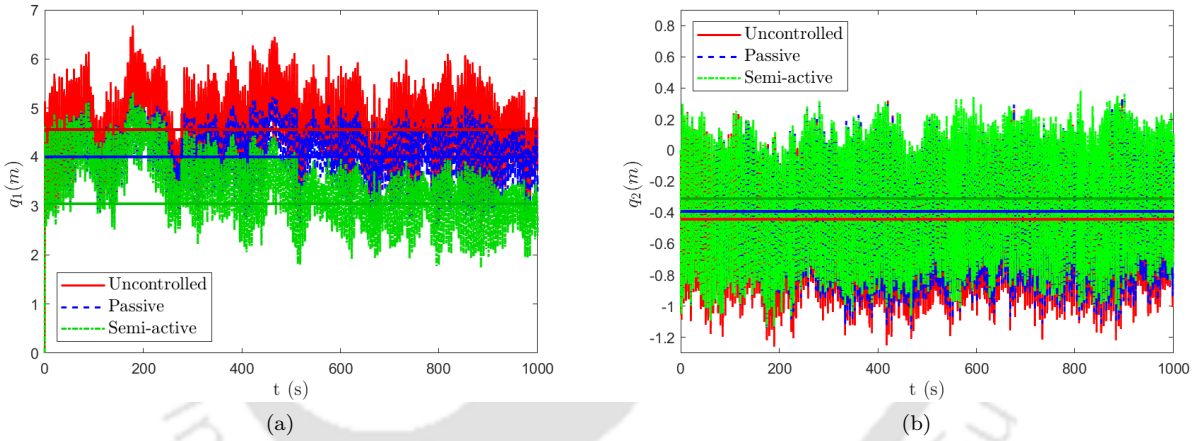

Figure 5.5: Blade response at 11.4 m/s wind speed with 25.4 mm diameter SMA tendon; (a) out-of-plane and (b) in-plane displacement time history. [N.B.: Horizontal line shows the mean response].

response analysis of the wind turbine is carried out with and without stiffener (i.e. uncontrolled and passive or semi-active controlled) and the tip displacement of the blade is shown in Fig. 5.5 for comparison. In case of passive operation, zero voltage is applied to the SMA tendon while in the semi-active case, 44 V is applied with the option of switching. Fig. 5.5a and Fig. 5.5b show the displacement response in the two orthogonal directions. The tip displacement of the blade in the out-of-plane direction is very high compared to that in the in-plane direction. The maximum displacement in the along-wind direction is ∼6 m while the same in the in-plane direction is ∼1 m at the rated speed.

Due to this reason, IEC 61400-1 [18] and DNVGL-ST-0376 [212] provide guidelines for tilt and pre-cone angle to the avoid impact with tower. In this study, the blades are modelled with zero pre-cone, which indicates the blade-tower clearance is ∼7.79 m. The tip displacement of the blade is reduced significantly due to the proposed longitudinal stiffener. The percentage reduction of the response in this study are evaluated in different modes of operation over 1000 s in which initial 450 s is used by the tendon to gain sufficient heating (∼80°C) in the semi-active mode. The figures show that peak displacement at the blade tip in the along-wind direction is reduced by 18.51% and 31.61% in passive and semi-active mode, respectively, while 5.69% and 12.75% peak displacement reduction are observed in the in-plane direction for the same mode of operation. Moreover, the mean component of the responses are also reduced significantly in both these directions when SMA stiffener is used. The mean reductions in the out-of-plane blade tip responses with

SMA tendon are 12.59% and 33.50% in two different modes of operations (i.e. passive and semi-active), respectively, while the same stiffener offers 11.33% and 29.95% mean reduction under two different modes in the in-plane direction. These are marked by the horizontal lines in Fig. 5.5. The RMS responses in the along-wind direction are reduced by 26.97% and 35.55% using passive and semi-active case, respectively, while the same in the in-plane direction are reduced by 6.00% and 12.45%, respectively.

The stress-strain-temperature behaviour of the SMA tendon is shown in Fig. 5.6a and Fig. 5.6b for passive and semi-active case, respectively. In the passive case, the tendon temperature remains same for all practical purpose compared to ambient temperature. Whereas, the temperature in the semi-active case increases with the application of current to achieve more control force, as shown in Fig. 5.6c. The SMA material can undergo ∼6-8% strain, however, the maximum strain observed in both these cases are close to 1%. This is due to the fact that the stiffener prevents blade deformation, which is reflected in the lower axial strain. This also justifies the use of SMA, which can offer large allowable stress compared to other materials in that strain range. As the current flow is switched on, the temperature is permitted to increase up to the allowable limit at around 530 s. Then the current is switched off and the tendon temperature starts to decrease slowly depending on the surrounding condition as shown in Fig. 5.6d. In this study, convective heat transfer coefficient is considered to be 10 W/m^{2}K for air-free convection and the thermal conductivity of the SMA tendon are 8.6 W/mK and 18 W/mK for martensite and austenite phase, respectively. The heating is switched on when the temperature drops by 10°C to maintain the required control force. This analysis is further continued to study the power failure during turbulent wind flow, which is a common critique for any semi-active or active control strategy. The advantage of the proposed algorithm lies in its ability to perform satisfactorily in the passive mode in case of a power failure, where it can still offer significant response reduction. This indicates that a minimum level of control is guaranteed by the proposed algorithm.

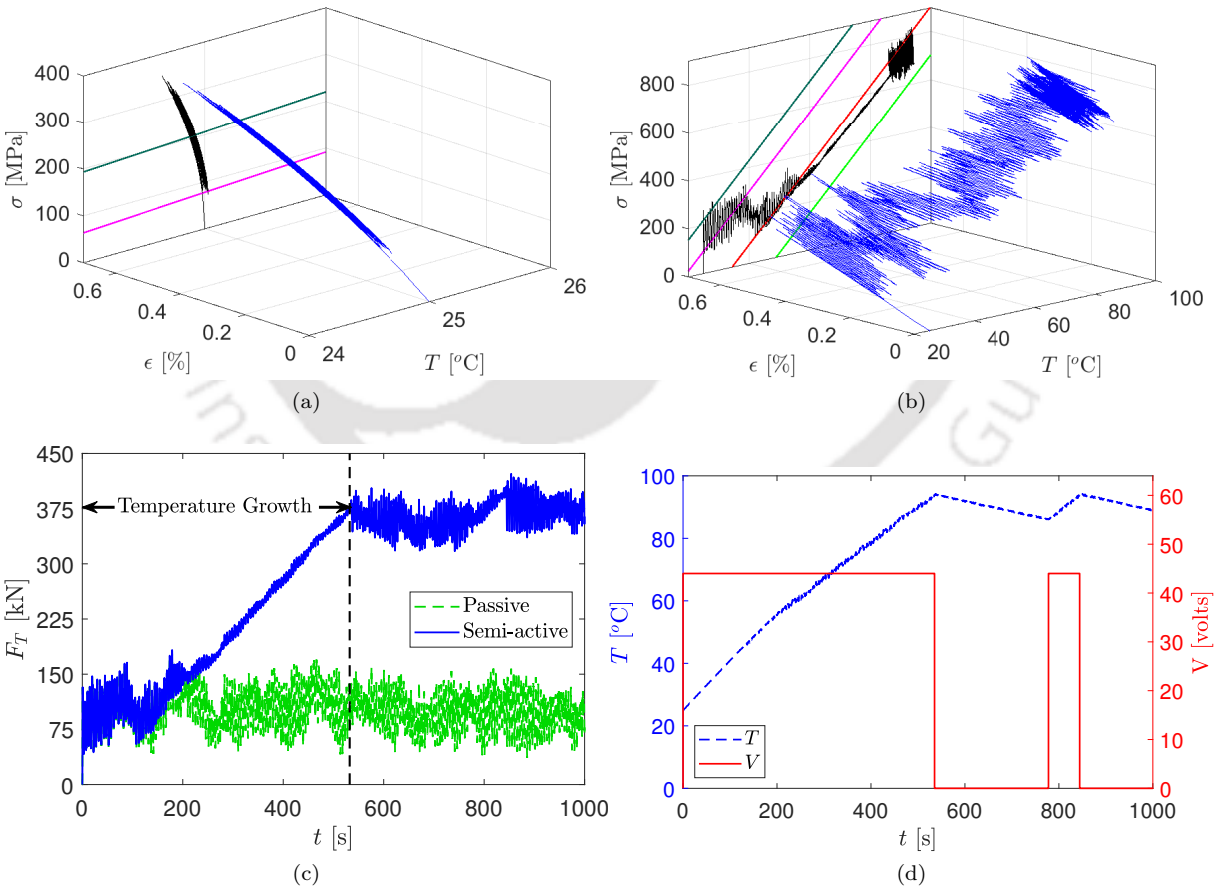

Figure 5.6: Stress and temperature variation of 25.4 mm diameter SMA tendon at 11.4 m/s average wind speed; (a) stress-strain-temperature in passive case and (b) stress-strain-temperature in semi-active case, (c) control force exerted by SMA tendon and (d) temperature applied for semi-active control. [N.B.: Straight lines in Fig. 5.6a and Fig. 5.6b represent stress rate of martensite and austenite phases, as shown in Fig. 4.3c]

A sensitivity analysis is carried out to study the performance of the SMA stiffener under various applied voltages and the results are shown in Fig. 5.7, where the zero voltage (i.e. the initial case) represents the stiffener in passive mode. The percentage reduction of peak and mean displacement response in two

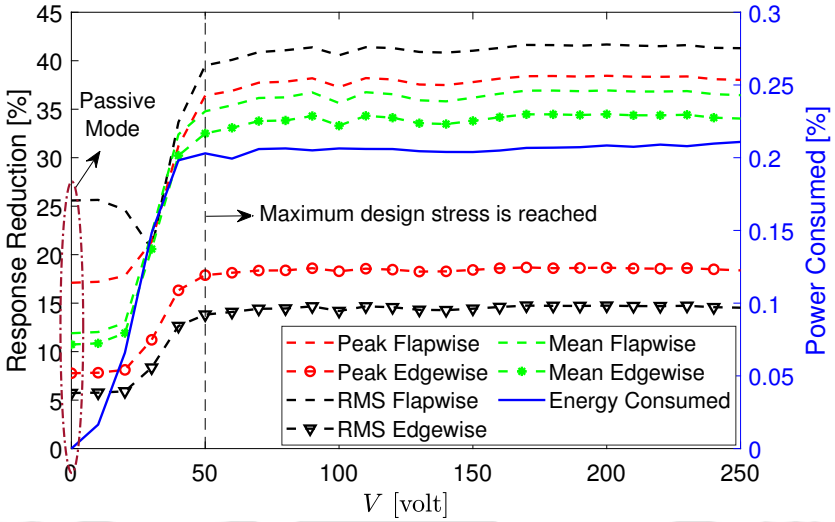

Figure 5.7: Percentage reduction in blade response and energy consumption w.r.t. voltage at rated speed for 25.4 mm diameter tendon.

orthogonal directions increase drastically with the increase of voltage from 25 V to 50 V and become stable (i.e. very little change in percentage reduction on further increase of voltage as it has already reached its maximum allowable temperature). The power consumed by the proposed controller as the percentage of the rated power of the turbine is also shown in Fig. 5.7. It can be observed that the net power consumed by the SMA tendon in the semi-active mode is 0.21% of the rated power, which is minimal for all practical purpose.

Further, the heating of tendon with different voltages are analysed to find the most favourable range for effective control with an initial temperature of 25°C, as shown in Fig. 5.8a. It is observed that starting with 40 V needs 670 s to attain the maximum allowable temperature while with 50 V reaches the same within 400 s. Similarly, 100 V and 250 V initial current reach the same temperature level in 95 s and 17 s, respectively. This indicates that higher initial voltage offers quicker heating to achieve the maximum allowable temperature, which needs frequent switching to maintain the control force.

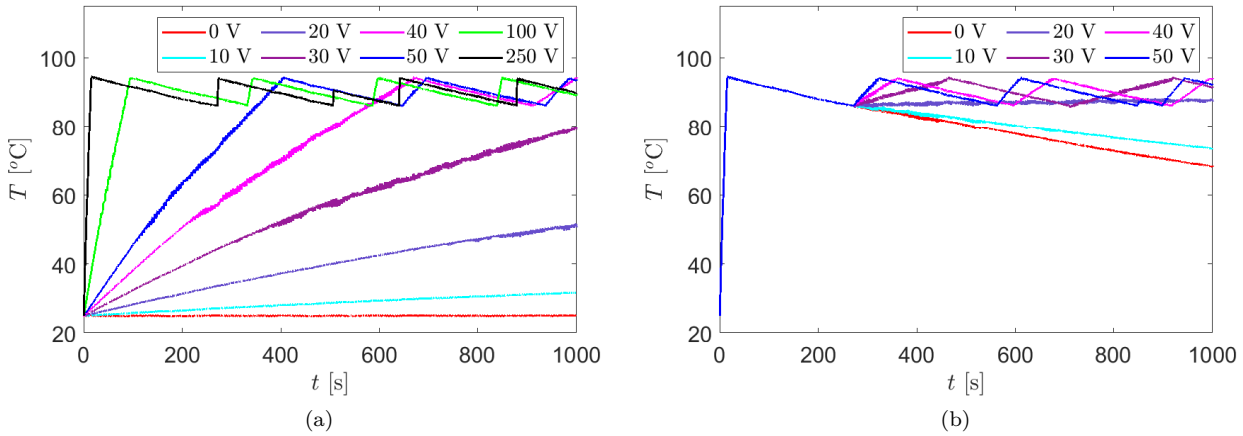

Figure 5.8: Temperature variation of 25.4 mm diameter tendon for different voltage; (a) initial temperature = 25°C and (b) initial temperature = 85°C.

To examine it further, an initial voltage of 250 V is applied to reach 95°C followed by switching. The current flow is restored after a temperature drop of 10°C, as shown in Fig. 5.8b. The voltage, which can

maintain the temperature and subsequently the stress level close to its design value, is selected as the effective voltage during the switching operation. In this case, 20 V current flow is able to maintain the temperature at the required level without frequent switching. Hence, it is considered as the effective voltage for the semi-active mode, where initial voltage is 250 V. Here, it may be noted that the designer has the option to select the mode of operation i.e. passive or semi-active. As the performance in passive mode is significant, it can be selected for regular operation, leaving the semi-active mode for extreme wind flow only. This not only helps to mitigate the demand for the extreme wind flow i.e. gust, it also helps to increase the operational lifespan of the controller due to obvious reason. In this context, the recent development of wind measurements can detect the impending gust on the rotor plane e.g. Light Detection and Ranging (LIDAR) [219]. The proposed controller can be integrated with such devices to offer optimal performance whenever necessary.

5.3.3 Level Crossing and Reliability Analysis

Once the optimal performance of the controller is established, its efficiency under uncertain wind flow is studied further. For this purpose, an ensemble of 25 wind flow field is simulated and the BEM theory is invoked in each case to simulate the corresponding aerodynamic load. Using these loads, uncontrolled and controlled responses are simulated and the performance of the proposed control strategy for different tendon diameter are summarised in Table. 5.1. From this table, it can be noted that the percentage reductions of the peak, mean and RMS displacements in the two orthogonal directions increase with the increase of tendon diameter. As obvious, the performance of the controller in the semi-active mode is significantly better than that in the passive mode. It is also observed that the controller performs better in the out-of-plane direction as compared to in-plane direction. This is due to the fact that the deformation in the in-plane direction is less compared to along-wind direction, which leads to lower axial strain.

Table 5.1: Peak, mean and Root Mean Square (RMS) response reduction in out-of-plane and in-plane directions.

Type	d	Out-of-plane			In-plane		
		Peak	Mean	RMS	Peak	Mean	RMS
	(mm)	(%)	(%)	(%)	(%)	(%)	(%)
Passive	12.70	6.26	3.98	9.51	2.84	3.58	2.06
	25.40	17.10	11.90	25.59	7.77	10.74	5.73
	38.10	26.44	19.69	38.51	12.13	17.82	8.97
	50.80	33.76	26.34	47.82	15.44	23.93	11.58
Semi-active	12.70	11.86	10.99	13.59	5.88	10.22	4.22
	25.40	34.65	33.84	37.70	17.34	31.60	13.37
	38.10	53.52	53.68	55.73	28.68	50.48	23.73
	50.80	66.68	67.19	68.30	42.90	63.71	35.88

[N.B.: Above results are based on ensemble average.]

To study the reliability of the system against excessive blade deformation, the level crossing problem is solved. For this purpose, wavelet-based time-frequency analysis, as described in Section 5.2.1, is invoked. Complex Morlet wavelet is used here, whose central frequency is 5 Hz. Fig. 5.9 shows the ensemble average of the wavelet coefficients of blade response in two orthogonal directions (i.e. out-of-plane and in-plane) under three different modes of operations (i.e. uncontrolled, passive and semi-active). This figure reveals that the response is cyclostationary, where the rotational frequency of the turbine dominates the response. Although the spectrograms show modal participation from flapwise and edgewise vibration, their contributions compared to the rotational frequency are significantly less. Furthermore, the amplitude of the expected value of the wavelet coefficients reduces in the passive mode as compared to the uncontrolled case. This reduction is more in the semi-active case, where the initial temperature growth is needed to reach the maximum allowable stress level.

Using these average wavelet coefficients, statistical moments of the blade tip response in the out-of-plane and in-plane direction are evaluated, which are shown in Fig. 5.10. From this figure, it can be concluded that the proposed control strategy offers significant response reduction in terms of time-varying mean and

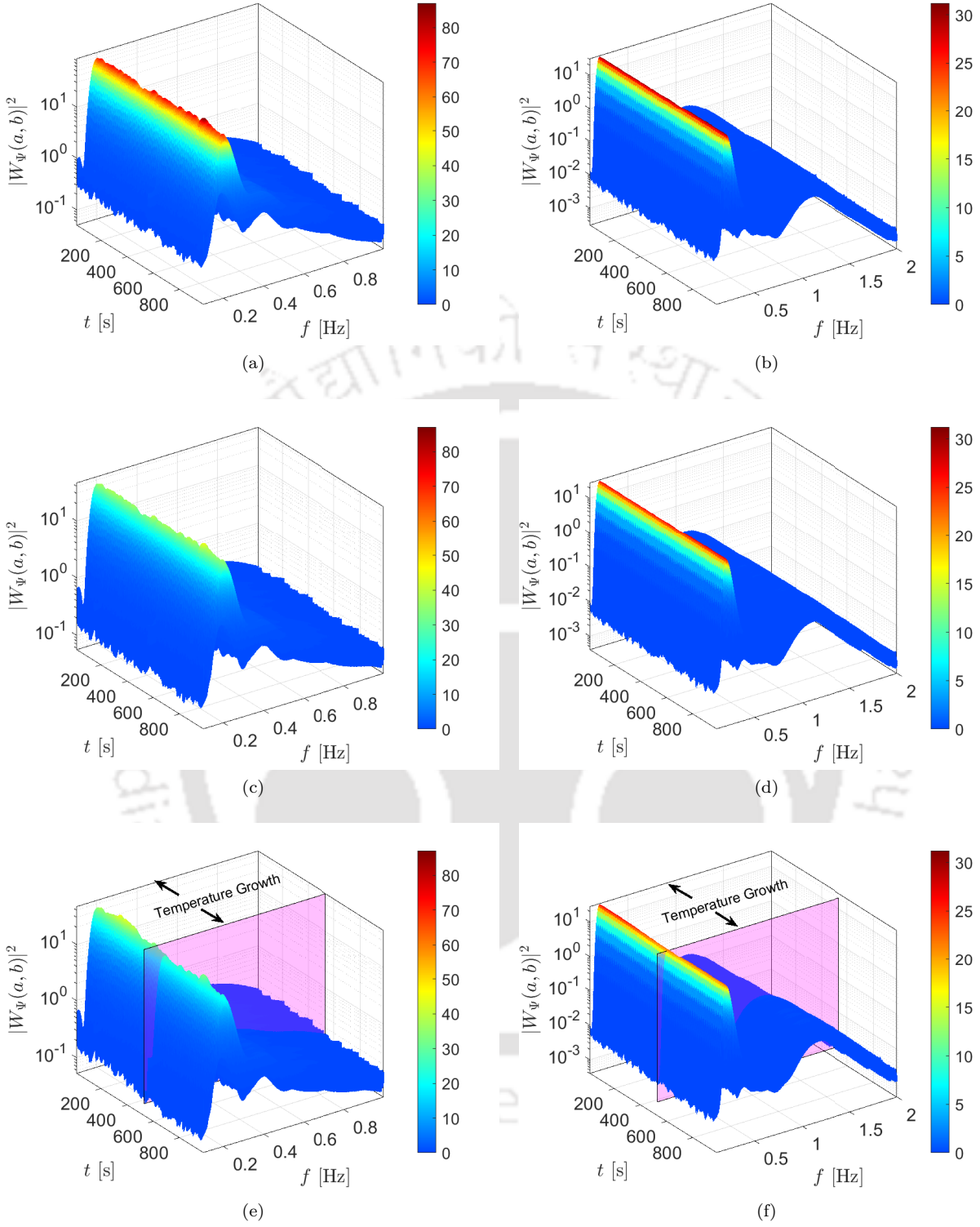

Figure 5.9: Wavelet coefficients of blade response at rated speed; (a) uncontrolled case in out-of-plane, (b) uncontrolled in in-plane, (c) passive case in out-of-plane, (d) passive case in in-plane, (e) semi-active case in out-of-plane and (f) semi-active case in in-plane.

standard deviation of the blade vibration. The level crossing problem is then solved, where the positive up crossing of the threshold (i.e. 7.79 m clearance between blade and tower) is considered for different mode of operations. Eq. 5.10 shows the time dependence of the crossing rate when the underlying stochastic process is Gaussian. Thus, the nature of the response is studied before solving the crossing rate. For this reason, four

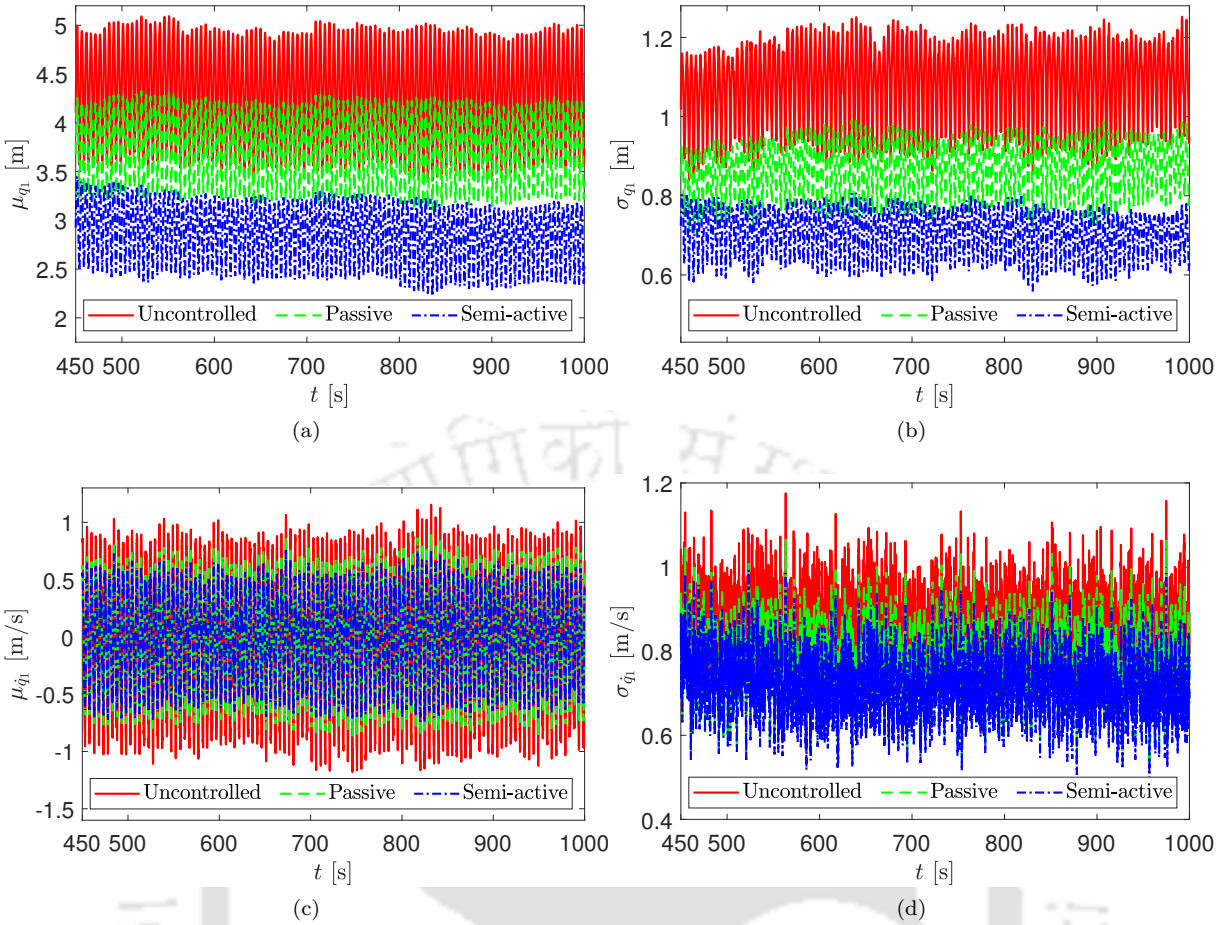

Figure 5.10: Out-of-plane blade response at rated speed for 25.4 mm diameter SMA tendon; (a) mean of displacement time history, (b) standard deviation of displacement time history, (c) mean of velocity time history and (d) standard deviation of velocity time history.

different time points are selected arbitrarily and the ensemble response at these time instants are plotted in probability paper. These are shown in Fig. 5.11a, which justify the assumption (i.e. Gaussianity) of the

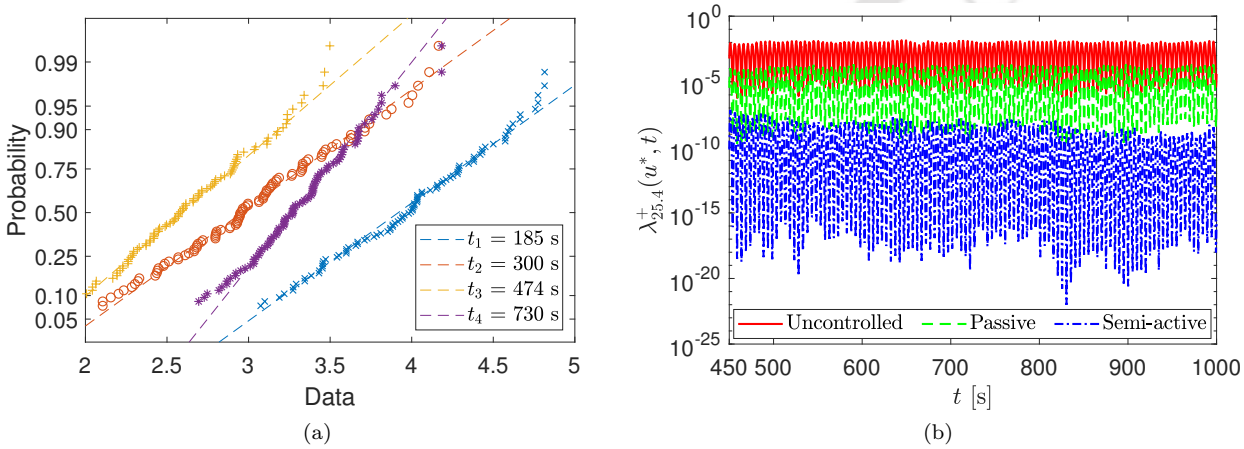

Figure 5.11: (a) Ensemble blade response in probability paper and (b) Crossing rate at rated speed for 25.4 mm diameter SMA tendon.

underlying stochastic process. Finally, the time-dependent crossing rate $\lambda^+(u,t)$ is evaluated, as shown in Fig. 5.11b for 25.4 mm diameter of the tendon. It clearly shows the improvement of the crossing rate from

the uncontrolled to passive and finally in semi-active mode. Using maximum value of the crossing rate, the probability of occurrence within the given time interval is evaluated as described in Eq. 5.11. Table. 5.2 shows the probability of zero-crossing (i.e. reliability) of the controller against allowable deformation limit. The numerical values reported in this table clearly show significant improvement of the reliability for different diameter of SMA tendon. This table also shows that performance of the controller during power failure (i.e. passive mode) is significant, which is an added advantage with this strategy.

Table 5.2: Maximum crossing rate in the along-wind direction and probability of failure.

d	$\lambda^+(u)$			p_f		
(mm)	Uncontrolled	Passive	Semi-active	Uncontrolled	Passive	Semi-active
12.70	1.48E-02	5.24E-03	1.50E-03	7.03E-04	1.58E-04	2.07E-05
25.40		2.58E-04	6.92E-08		2.47E-06	1.85E-12
38.10		2.11E-06	4.52E-20		3.90E-09	4.07E-31
50.80		2.98E-09	1.96E-47		7.09E-13	1.79E-71

5.4 Summary

The importance of blade vibration control is ever increasing, especially for large new generation rotors, as they experience considerable along-wind deformation that can lead to collision with the tower. Usually, the blades and slow moving shaft are tilted to increase the clearance between blade tip and tower. But, this creates additional stress on the gear tooth and bed plate, which often leads to damage and downtime for maintenance. Therefore, the improvement in reliability of the stiffened blade against tower strike under cyclostationary load is investigated in this chapter. For this purpose, the mathematical formulations for wavelet-based cyclostationary analysis and level crossing problem are presented. A voltage-based switching algorithm is developed to model the semi-active SMA stiffener, where the initial voltage and the voltage during switching can be adjusted depending upon the demand. With this in view, a numerical analysis is carried out using discrete reduced order model of 5 MW onshore wind turbine with and without SMA stiffener subjected to the rated wind speed and 15% turbulence at the hub height. The numerical study clearly shows the cyclostationary nature of the response, where rotational frequency predominates over other structural frequencies. The power consumption is incredibly low for this controller, which also advocates for its efficiency in semi-active mode. The study demonstrated that the proposed control strategy can significantly improve the reliability of HAWT blade. It is bound to improve the performance against the ultimate limit state and fatigue life as the blade deforms less. This issue is investigated further and the results are presented in the following chapters.

Chapter 6

Finite Element Model of HAWT Blade

6.1 Introduction

In this chapter, finite element modelling of rotating wind turbine blade with longitudinal stiffener is presented. It is further used for detailed fatigue analysis in the following chapter. A spinning body experiences Gyroscopic and Coriolis effects, which influence the dynamics of it compared to its non-spinning counterpart. Thus, the natural frequencies of a rotating blade changes with its rotational speed. Hence, the effect of spinning should be considered in the dynamic analysis of wind turbine. To address this issue, modal analysis of the spinning blade with and without the stiffener is carried out to investigate the variation of natural frequency with rotation. The response of the benchmark wind turbine is simulated using the aerodynamic loads obtained from 3D wind field using Blade Element Momentum (BEM) theory and validated with FAST. The formulations for spinning finite element model are sequentially developed as presented in the following sections.

6.2 Spinning FE Modelling of HAWT Blade

The spinning finite element method is used in this study to model a longitudinally stiffened wind turbine blade. It requires rotating co-ordinate system as shown in Fig. 6.1a. The co-ordinates of tower and nacelle are fixed while the co-ordinates for hub and rotor blade are moving. Therefore, nacelle co-ordinate can be considered as the inertial reference frame. Hub and blade rotating with an angular velocity of Ω about their y-axis, where hub y-axis (y_h) and nacelle y-axis (y_n) are parallel and rotor y-axis form the conning angle, as shown in Fig. 6.1a. Here, it may be noted that the inclined local blade axis needs co-ordinate transformation prior to assembling the component matrices where the generalised transformation matrix takes the following form

$$Tr = \begin{bmatrix} \cos\theta_{xx'} & \cos\theta_{xy'} & \cos\theta_{xz'} \\ \cos\theta_{yx'} & \cos\theta_{yy'} & \cos\theta_{yz'} \\ \cos\theta_{zx'} & \cos\theta_{zy'} & \cos\theta_{zz'} \end{bmatrix} \tag{6.1}$$

It correlates the local (i.e. xyz) and global (i.e. $x'y'z'$) axes. Thus, the nomenclature $\theta_{xy'}$, for example, represents the angle where the first subscript corresponds to the local orientation while the second one represents the global direction. The twist (θ_t) and pitch (θ_p) of the blade makes the rotation about x_b and creates an angle of θ_{pt} between other two axes of the blade and the hub. Therefore, the co-ordinate

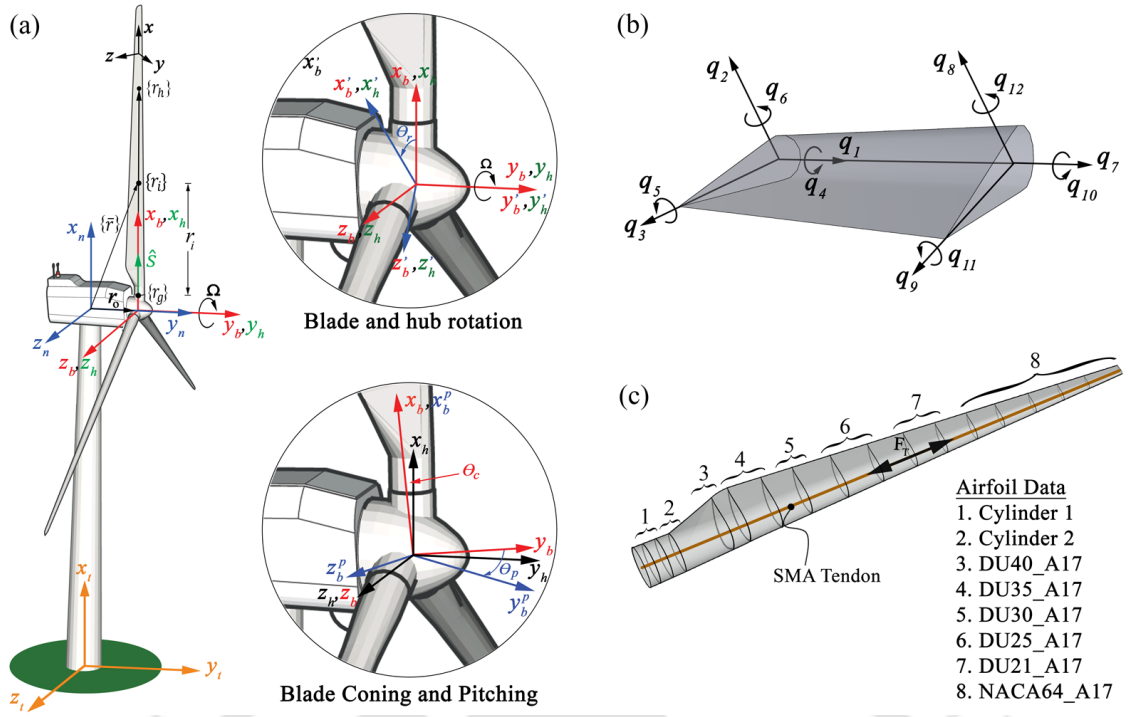

Figure 6.1: Schematic diagram of Horizontal Axis Wind Turbine (HAWT); (a) wind turbine co-ordinate system, (b) blade element degrees of freedom and (c) SMA tendon connection and airfoil distribution over the length of the blade.

transformation can be expressed for the present system as

$$Tr_p = \begin{bmatrix} 1 & 0 & 0 \\ 0 & \cos\theta_{pt} & -\sin\theta_{pt} \\ 0 & \sin\theta_{pt} & \cos\theta_{pt} \end{bmatrix} \tag{6.2}$$

The local y-axis of the blades in its present configuration are parallel to each other, with other two axes of each blade forms an angle $\theta_r = \pm 120^0$. Thus, the transformation for the blade matrices from their local orientation to the global reference frame is

$$Tr_r = \begin{bmatrix} \cos\theta_r & 0 & -\sin\theta_r \\ 0 & 1 & 0 \\ \sin\theta_r & 0 & \cos\theta_r \end{bmatrix} \tag{6.3}$$

The pre-cone of the blade makes the rotation about z_b and create an angle θ_c, therefore corresponding transformation matrix can be written as

$$Tr_c = \begin{bmatrix} \cos\theta_c & -\sin\theta_c & 0 \\ \sin\theta_c & \cos\theta_c & 0 \\ 0 & 0 & 1 \end{bmatrix} \tag{6.4}$$

In this study, pre-cone angle of the blade is assumed to be zero and hence the transformation matrix for z-axis is identity. Using the co-ordinate system as shown in Fig. 6.1a, the position of a point on the blade

in the fixed reference frame $x_n y_n z_n$ is given by

$$\begin{aligned} \{\bar{r}\} &= \{r_o\} + \{r_i\} \\ \{r_i\} &= \{r_g\} + r_i \hat{s} \qquad 0 \leq s \leq l \\ \hat{s} &= \frac{\{r_h\} - \{r_g\}}{|\{r_h\} - \{r_g\}|} \end{aligned} \tag{6.5}$$

where $\{r_i\}$ is the position vector with respect to the moving co-ordinate system, $\hat{s}$ is the unit vector along the blade pitch axis and r_o is the distance between the origins of fixed and moving co-ordinates. For a three bladed turbine system, let us consider the origin of the fixed co-ordinate coincides with the origin of the rotating co-ordinate system [i.e. $\{r_o\} = 0$]. Therefore, the position of the blade is expressed as

$$\{\bar{r}\} = \{r_g\} + r_i \hat{s} \tag{6.6}$$

6.2.1 Kinematics of Rotating Blade

The rotating hub and blade system can be described fully with respect to the inertial frame $x_n y_n z_n$ (i.e. nacelle co-ordinate). For a spinning beam as shown in Fig. 6.1a, torsional stiffness is same as non-spinning beam and it is assumed that the torsional deformation is uncoupled with the longitudinal (u) and bending (v, w) deformations. As the blade rotates about y_h axis with a constant angular speed Ω, gyroscopic effect couples different rotational degrees of freedom, which are perpendicular to the spinning axis. Thus, the spinning matrix in this case is expressed as follows

$$[\Omega] = \Omega \begin{bmatrix} 0 & 0 & 1 \\ 0 & 0 & 0 \\ -1 & 0 & 0 \end{bmatrix} \tag{6.7}$$

Using the above spinning matrix, kinematics at any location $\{r\}$ from the root of the blade can be defined with respect to the inertial frame in terms of the moving co-ordinate $x_h y_h z_h$. So, the absolute velocity vector of this point on blade takes the following form

$$\{\mathrm{v}\} = \{\dot{r}\} + [\Omega]\{r\} \tag{6.8}$$

The displacement and rotation vector along the principal axis of the blade with reference to the local co-ordinate xyz is $\mathrm{u}(x,t) = \{u, v, w\}^T$ and $\vec{\theta}(x,t) = \{\theta_x, \theta_y, \theta_z\}^T$. For an Euler-Bernoulli beam, the rotations are obtained from the differential of the displacement field i.e. $\theta_y = \partial_x w$ and $\theta_z = -\partial_x v$. Therefore, the independent variables are $\mathbf{u}(x,t) = \{u, v, w, \theta_x\}^T$. The displacement vector along the principal axis of blade with reference to the moving hub co-ordinate $x_n y_n z_n$ is given by

$$\{\bar{\mathrm{u}}\} = [R]^T \{\mathrm{u}\} \tag{6.9}$$

where $[R]$ is the transformation matrix between the global co-ordinate $x_h y_h z_h$ and the local co-ordinate xyz. Let us consider $[R]$ has the following form

$$[R] = \begin{bmatrix} \alpha_{11} & \alpha_{12} & \alpha_{13} \\ \alpha_{21} & \alpha_{22} & \alpha_{23} \\ \alpha_{31} & \alpha_{32} & \alpha_{33} \end{bmatrix} \tag{6.10}$$

The unit vector along the beam (i.e. $\hat{s}$) is equal to the first row of $[R]$, which is given by

$$\hat{s} = \begin{bmatrix} \alpha_{11} & \alpha_{12} & \alpha_{13} \end{bmatrix}^T \tag{6.11}$$

Hence, the position vector of a point on the deformed blade with respect to the reference frame $x_n y_n z_n$ is

$$\{r\} = \{r_i\} + \{\bar{u}\} = \{r_i\} + [R]^T \{u\} \tag{6.12}$$

The time derivative of the position vector is

$$\{\dot{r}\} = [R]^T \{\dot{u}\} \quad \text{since} \quad \{\dot{r}_i\} = 0 \tag{6.13}$$

Therefore, the absolute velocity vector can be evaluated by substituting this expression in Eq. 6.8, i.e.

$$\{v\} = [R]^T \{\dot{u}\} + [\Omega] \left[\{r_i\} + [R]^T \{u\}\right] \tag{6.14}$$

Since, the torsional deformation of a spinning beam is same as a non-spinning beam and is uncoupled with other deformations, the kinetic energy due to absolute velocity and torsional deformation are separately evaluated. Therefore, the total kinetic energy of the rotating blade can be written as

$$\begin{aligned}\Pi_K = \frac{1}{2}\int \rho A(x) \Big\{[R]^T \{\dot{u}\} + [\Omega]\left[\{r_i\} + [R]^T \{u\}\right]\Big\}^T \Big\{[R]^T \{\dot{u}\} + [\Omega]\left[\{r_i\} + [R]^T \{u\}\right]\Big\} dx \\ + \frac{1}{2}\int \rho A(x) R_g^2 \{\theta_x\}^T \{\theta_x\}\, dx\end{aligned} \tag{6.15}$$

where ρ is the mass density, A is the cross section area and R_g is the radius of gyration. In the above equation parameter θ_x represents the torsional deformation of the blade.

In this study, the blade is stiffened by a tendon that runs along its longitudinal axis. Fig. 6.1c shows the schematic diagram of the proposed Shape Memory Alloy (SMA) tendon for longitudinal stiffening. Therefore, the strain energy of the rotating blade with stiffener is given by

$$\begin{aligned}\Pi_P = \frac{1}{2}\int \Bigg[EA(x)\left(\frac{du}{dx}\right)^2 + EI_z(x)\left(\frac{d^2v}{dx^2}\right)^2 + EI_y(x)\left(\frac{d^2w}{dx^2}\right)^2 + GJ(x)\left(\frac{d\theta}{dx}\right)^2 + F_c(x)\left(\frac{dv}{dx}\right)^2 \\ + F_c(x)\left(\frac{dw}{dx}\right)^2 + F_g(x)\left(\frac{dv}{dx}\right)^2 + F_g(x)\left(\frac{dw}{dx}\right)^2 + F_T(x)\left(\frac{dv}{dx}\right)^2 + F_T(x)\left(\frac{dw}{dx}\right)^2\Bigg] dx\end{aligned} \tag{6.16}$$

where $EI_y(x)$ and $EI_z(x)$ are the flexural rigidity of the blade in the out-of-plane and the in-plane directions, respectively, while $EA(x)$ and $GJ(x)$ are the axial and the torsional rigidity of the blade, respectively. $F_c(x)$ and $F_g(x)$ are the centrifugal and the gravitation forces acting at a section $r_i + x$ on the blade, while F_T is the tension developed in the SMA tendon when the blade deforms.

6.2.2 Finite Element Model of Rotating Blade

In the present study, the blade is modelled in finite element frame work where it is subdivided in to a number of elements. Here, two noded beam element is used whose nodal degrees of freedom (DOF) are shown in Fig. 6.1b. Using these degrees of freedom, the displacement field $\mathbf{u}_e$ within an element is defined by interpolating the nodal Degrees of Freedom (DOF) vector $\mathbf{q}_e$ as follows

$$\{\mathbf{u}_e\} = [\Phi]\{q_e\} \tag{6.17}$$

where $\mathbf{q}_e$ is a 12×1 vector of DOF q_1,q_2...q_{12} as shown in Fig. 6.1b and the velocity field is defined as $\{\dot{\mathbf{u}}_e\} = [\Phi]\{\dot{q}_e\}$. Here, Φ is the interpolation (or shape) function matrix, i.e.

$$\Phi = \left.\begin{bmatrix} N_1 & 0 & 0 & 0 & 0 & 0 & N_7 & 0 & 0 & 0 & 0 & 0 \\ 0 & N_2 & 0 & 0 & N_5 & 0 & 0 & N_8 & 0 & 0 & N_{11} & 0 \\ 0 & 0 & N_3 & 0 & 0 & N_6 & 0 & 0 & N_9 & 0 & 0 & N_{12} \\ 0 & 0 & 0 & N_4 & 0 & 0 & 0 & 0 & 0 & N_{10} & 0 & 0 \end{bmatrix} \begin{matrix} \rightarrow N_u \\ \rightarrow N_v \\ \rightarrow N_w \\ \rightarrow N_\theta \end{matrix} \right\} H \tag{6.18}$$

where rows in the above matrix represent axial, flapwise, edgewise and torsional shape functions, respectively. In Eq. 6.18, parameter H denotes the shape function for translational deformation [i.e. $\{u\} = [H]\{q_e\}$] whereas, N_θ denotes the shape function for torsional deformation [i.e. $\{\theta_x\} = [N_\theta]\{q_e\}$]. In these formulation, axial and torsional deformation have linear shape functions while bending deformation is modelled by Hermite shape functions [220–222], as given in Table 6.1.

Table 6.1: Shape Functions.

Type	Shape Function	
	Node 1	Node 2
Axial deformation	$N_1(x) = 1 - \left(\frac{x}{l_e}\right)$	$N_7(x) = \left(\frac{x}{l_e}\right)$
Flapwise displacement	$N_2(x) = 1 - 3\left(\frac{x}{l_e}\right)^2 + 2\left(\frac{x}{l_e}\right)^3$	$N_8(x) = 3\left(\frac{x}{l_e}\right)^2 - 2\left(\frac{x}{l_e}\right)^3$
Flapwise rotation	$N_5(x) = -x\left(1 - \frac{x}{l_e}\right)^2$	$N_{11}(x) = -x\left(\left(\frac{x}{l_e}\right)^2 - \frac{x}{l_e}\right)$
Edgewise displacement	$N_3(x) = N_2(x)$	$N_9(x) = N_8(x)$
Edgewise rotation	$N_6(x) = -N_5(x)$	$N_{12}(x) = -N_{11}(x)$
Torsion deformation	$N_4(x) = N_1(x)$	$N_{10}(x) = N_7(x)$

Therefore, the kinetic energy of an element can be modified using these nomenclatures, i.e.

$$\begin{aligned}\Pi_K^e = \frac{1}{2}\int_0^{l_e} \rho A \Big(&\{\dot{q}_e\}^T H^T [R] [R]^T H \{\dot{q}_e\} + \{q_e\}^T H^T [R] [\Omega]^T [\Omega] [R]^T H \{q_e\} + \{r_i\}^T [\Omega]^T [\Omega] \{r_i\} \\ &+2\{\dot{q}_e\}^T H^T [R] [\Omega] \{r_i\} + 2\{\dot{q}_e\}^T H^T [R] [\Omega] [R]^T H \{q_e\} + 2\{r_i\}^T [\Omega]^T [\Omega] [R]^T H \{q_e\}\Big) dx \\ &+ \frac{1}{2}\int_0^{l_e} \rho A R_g^2 \{q_e\}^T [N_\theta]^T \{q_e\} [N_\theta] dx \end{aligned} \tag{6.19}$$

The transformation matrix R is an orthogonal matrix, i.e. RR^T is equal to an identity matrix. Substituting this in Eq. 6.19 and simplifying it further gives

$$\Pi_K^e = \tfrac{1}{2}\{\dot{q}_e\}^T [M_e] \{\dot{q}_e\} + \tfrac{1}{2}\{q_e\}^T [K_{\Omega e}] \{q_e\} + T_{ie} + \{\dot{q}_e\}^T \{f_e\} + \{\dot{q}_e\}^T [G_{\Omega e}] \{q_e\} + \{F_{\Omega e}\}^T \{q_e\} \tag{6.20}$$

where $[M_e]$, $[K_{\Omega e}]$ and $[G_{\Omega e}]$ are the element mass, spinning stiffness and gyroscopic damping matrices of size 12×12, respectively. Matrix $[G_{\Omega e}]$ is skew-symmetric while the other two are symmetric. These element matrices are derived as follows

$$[M_e] = \int_0^{l_e} \Phi^T [\overline{m}] \Phi dx \tag{6.21a}$$

$$[K_{\Omega e}] = \int_0^{l_e} H^T [\overline{k}_\Omega] H dx \tag{6.21b}$$

$$[G_{\Omega e}] = \int_0^{l_e} H^T [\overline{g}] H dx \tag{6.21c}$$

where l_e is the element length. In the above equation, $[\overline{m}] = diag\begin{bmatrix} \rho A(x) & \rho A(x) & \rho A(x) & \rho I_P(x) \end{bmatrix}$, $[\overline{k}_\Omega] = \rho A(x)[R] [\Omega]^T [\Omega] [R]^T$ and $[\overline{g}] = \rho A(x)[R] [\Omega] [R]^T$. Parameter I_p is the linearly varying polar moment of inertia for an element of the blade. Similarly, the strain energy of the element takes the following form

$$\Pi_P^e = \frac{1}{2}\int_0^{l_e} \Big[EA\{q_e\}^T {N_u'}^T N_u' \{q_e\} + EI_x \{q_e\}^T {N_v''}^T N_v'' \{q_e\} + EI_y \{q_e\}^T {N_w''}^T N_w'' \{q_e\} + GJ\{q_e\}^T {N_\theta'}^T N_\theta' \{q_e\} + F_c(x)\{q_e\}^T {N_v'}^T N_v' \{q_e\} + F_c(x)\{q_e\}^T {N_w'}^T N_w' \{q_e\} + F_g(x)\{q_e\}^T {N_v'}^T N_v' \{q_e\} + F_g(x)\{q_e\}^T {N_w'}^T N_w' \{q_e\} + F_T(x)\{q_e\}^T {N_v'}^T N_v' \{q_e\} + F_T(x)\{q_e\}^T {N_w'}^T N_w' \{q_e\} \Big] dx \tag{6.22}$$

After simplifying, the above equation reduces to the following form

$$\Pi_P^e = \frac{1}{2} q_e \{[K_{Ee}] + [K_{ce}] + [K_{ge}] + [K_{Te}]\} q_e \tag{6.23}$$

where $[K_{Ee}]$ is the element elastic stiffness matrix while $[K_{ce}]$, $[K_{ge}]$ and $[K_{Te}]$ are the element stiffness matrices due to centrifugal, gravitational and tendon forces, respectively. These element matrices are derived as

$$[K_{Ee}] = \int_0^{l_e} [d\Phi_K]^T \left[\bar{k}\right] [d\Phi_K]\, dx \tag{6.24a}$$

$$[K_{ce}] = \int_0^{l_e} F_c(x) [d\Phi]^T [d\Phi]\, dx \tag{6.24b}$$

$$[K_{ge}] = \int_0^{l_e} F_g(x) [d\Phi]^T [d\Phi]\, dx \tag{6.24c}$$

$$[K_{Te}] = \int_0^{l_e} F_T [d\Phi]^T [d\Phi]\, dx \tag{6.24d}$$

where $[d\Phi_K] = diag\begin{bmatrix} \frac{d}{dx} & \frac{d^2}{dx^2} & \frac{d^2}{dx^2} & \frac{d}{dx} \end{bmatrix} [\Phi]$ and $[d\Phi] = diag\begin{bmatrix} 0 & \frac{d}{dx} & \frac{d}{dx} & 0 \end{bmatrix} [\Phi]$ are the differential matrices of the shape functions and $\left[\bar{k}\right] = diag\begin{bmatrix} EA(x) & EI_y(x) & EI_z(x) & GJ(x) \end{bmatrix}$. The components of element matrices given in Eq. 6.21 and Eq. 6.24 are presented in Appendix B. Using these matrices, the governing equation of motion can be derived using Lagrange's equation, which is given by

$$\frac{d}{dt}\left(\frac{\partial L}{\partial \dot{q}_i}\right) - \frac{\partial (L)}{\partial q_i} = f_i \qquad i = 1, 2, \ldots n \tag{6.25}$$

where $L = \Pi_K - \Pi_P$. Therefore, the total kinetic energy $\Pi_K = \sum \Pi_K^e$ and the total strain energy $\Pi_P = \sum \Pi_P^e$ are substituted in Eq. 6.25, which give the governing equation of motion for a blade as follows

$$[M(t)]\{\ddot{q}\} + [C(t)]\{\dot{q}\} + ([K(t)] + [K_T(t)])\{q\} = \{f(t)\} \tag{6.26}$$

where $[M]$ and $[C]$ are the global mass and damping matrices, respectively. The damping matrix is the summation of structural $[C_s]$, aerodynamic $[C_a]$ and gyroscopic $[G_\Omega]$ damping matrices, i.e. $[C(t)] = ([C_s] + [C_a] + 2[G_\Omega(t)])$. In the above equation, $[K(t)] = [K_E] + [K_c] + [K_g(t)] - [K_\Omega]$ where $[K_E]$ and $[K_\Omega]$ are the global elastic and spinning stiffness matrices while $[K_c]$ and $[K_g]$ are the global stiffness matrices due to the centrifugal and gravitational forces, respectively. In the above equation, parameter K_T denotes the stiffness matrix due to the control force developed in the SMA tendon.

6.2.3 Damping Matrices

As stated above, the damping matrix of the wind turbine blade consists of structural ($[C_s]$), gyroscopic ($[G_\Omega]$) and aerodynamic ($[C_a]$) components. Structural damping is modelled using Rayleigh's proportionality constants [222]. Gyroscopic damping matrix is evaluated as discussed in the previous section. In this study,

aerodynamic damping of the blades are modelled using equivalent modal damping [42], which is given by

$$\xi_{ab} = \frac{\frac{1}{2}\rho_a \Omega \frac{dC_l}{d\alpha} \int_0^L r c(r) \phi_1^2(r) dr}{2 m_1 \omega_1} \tag{6.27}$$

In the above equation, the modal mass m_1 takes the following form

$$m_1 = \int_0^L m(r) \phi_1^2(r) dr \tag{6.28}$$

In this formulation, ρ_a is the density of air, $c(r)$ is the blade chord at radius r, C_l is the lift coefficient and α is the angle of attack. When blade is not in stall, the rate of change of lift coefficient with respect to angle of attack is equal to 2π [42].

6.2.4 Forces Acting on Blade Element

The forces acting on the wind turbine blades are mainly of two types i.e. due to gravity and aerodynamics of the airfoil. The relevant equations for these loads are described in Chapter 2. However, these loads are distributed over the length of the blade. Therefore, the element loads are calculated by interpolating the nodal loads using respective shape functions. For example, the normal and tangential aerodynamic forces at the i^{th} node are evaluated from Eq. 2.30, which is given by

$$p_n = \frac{1}{2} N_b \rho_a V_{rel}^2 c(r) [C_l(\alpha) \cos\varphi + C_d(\alpha) \sin\varphi] \tag{6.29}$$

$$p_t = \frac{1}{2} N_b \rho_a V_{rel}^2 c(r) [C_l(\alpha) \sin\varphi - C_d(\alpha) \cos\varphi] \tag{6.30}$$

where C_l and C_d are the lift and drag coefficients, respectively that depend on the angle of attack of the corresponding airfoil, while parameter N_b denotes the number of blades. Therefore, the element aerodynamic force vector is defined as

$$f_a^e = \int_0^{l_e} \begin{bmatrix} 0 & p_n(x) & p_t(x) & 0 \end{bmatrix} [\Phi] \, dx \tag{6.31}$$

where $p_n(x)$ and $p_t(x)$ are evaluated using linear interpolation of the nodal loads of an element in appropriate directions.

6.3 Numerical Results and Discussion

The spinning finite element model of the longitudinally stiffened HAWT blade is used here to study its dynamics and fatigue characteristics. The blade is modelled using the material properties of National Renewable Energy Laboratory (NREL) benchmark wind turbine data [201]. The distributed properties of the blade at 49 nodes including chord length, twist angle, mass per unit length and flexural rigidity are used as given in NREL Table 2-1 [201]. It consists of eight airfoils as shown in Fig. 6.1c and the distribution of their thickness is evaluated from the thickness to chord ratio given in Resor [223]. The structural damping ratio of the blade is 0.4775% in all modes and the same for the tower is 1%. The aerodynamic damping ratio of the blade is evaluated using Eq. 6.27.

6.3.1 Modal Analysis of Stiffened Blade

Using the above mentioned properties, natural frequencies of the blade are evaluated with and without tendon force to investigate the impact of the stiffener. First the blade frequency are compared with FAST and BModes when the tendon force and rotation are zero (i.e. $F_T = 0$ and $\Omega = 0$). Table 6.2 shows the frequency obtained from different sources. A close match is noticed between the frequencies where the

modelling error in each case is mentioned in the parenthesis. Fig. 6.2 shows the first six mode shapes, where first mode is in the flapwise direction, as shown in Fig. 6.2a and the second mode is in the edgewise direction, as shown in Fig. 6.2c. Based on these results, it may be concluded that the proposed finite element offers satisfactory modal performance, which can be further used to study the effects of spinning on the modal characteristics.

Table 6.2: Modal frequencies of NREL 5 MW blade in Hz.

Mode	Description	FEM	FAST	BModes
1	1^{st} Flapwise	0.6770	0.6993 (3.19%)	0.6770 (0.00%)
2	1^{st} Edgewise	1.0900	1.0793 (0.99%)	1.0858 (0.39%)
3	2^{nd} Flapwise	1.9489	1.9337 (0.79%)	1.9542 (0.27%)
4	2^{nd} Edgewise	4.0449		4.0072 (0.94%)

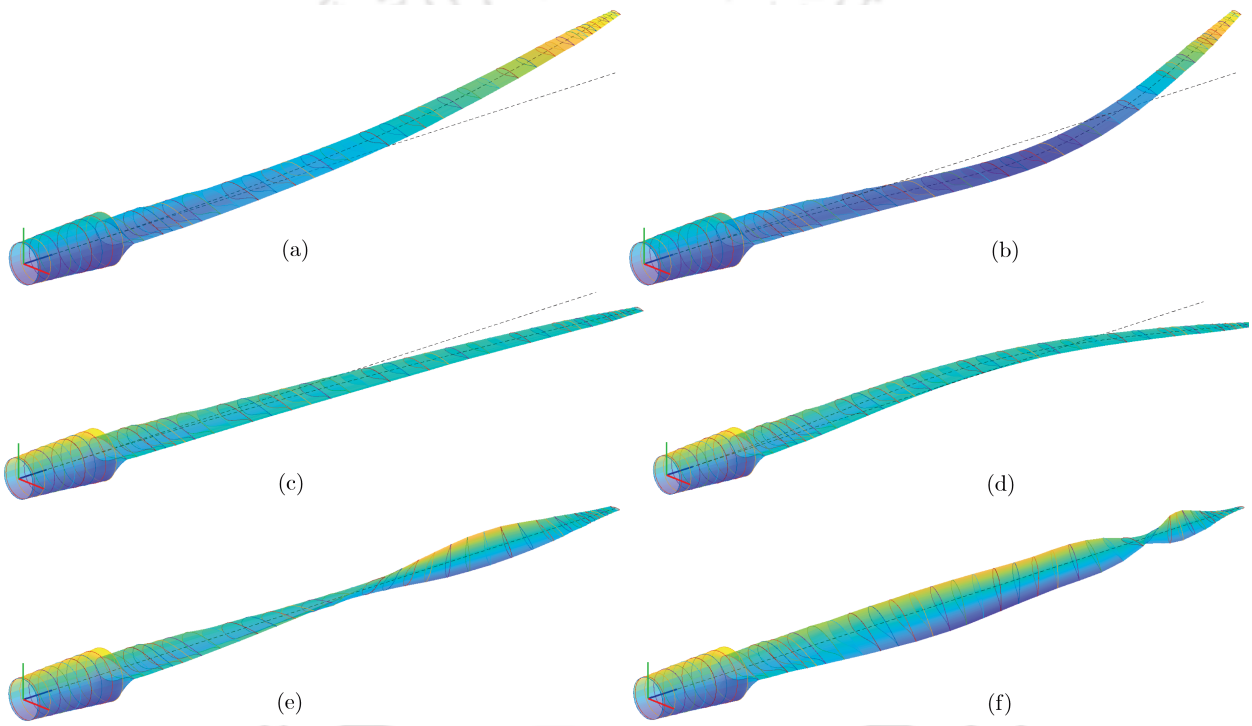

Figure 6.2: Mode shapes of NREL 5 MW HAWT blade; (a) 1^{st} flapwise, (b) 2^{nd} flapwise, (c) 1^{st} edgewise, (d) 2^{nd} edgewise, (e) 1^{st} torsional and (f) 2^{nd} torsional.

The blade natural frequencies are affected by the centrifugal force and Coriolis effect due to which the blade becomes stiffer. The effect is more pronounced as the rotational speed of the turbine increases. To study this effect, the natural frequencies are obtained by varying Ω (i.e. *rpm*) and the tendon force. The Campbell diagram (i.e. frequency vs. Ω plot) for different tendon forces are shown in Fig. 6.3. It also shows the vertical lines corresponding to cut-in, rated and cut-out speed along with the rotational speed lines (i.e. 1P, 2P etc.), which indicate resonance points (i.e. whirl frequency coincides with the blade natural frequency). It is observed that the line 1P does not cross the whirling frequency of the blade and the line 2P crosses the flapwise frequency at around 27 rpm, which is close to the cut-out speed of NREL 5 MW wind turbine without pitch control. However, the rated speed is maintained at 12.1 rpm for this turbine, which impose no threat of resonance during its regular operation. In this analysis, the effect of longitudinal stiffener is investigated with three different constant tensile forces (i.e. $F_T = 150$ kN, $F_T = 300$ kN and $F_T = 450$ kN). It is observed that the blade stiffness is significantly improved by the addition of the SMA tendon. This improved stiffness is reflected in the increase of natural frequency. However, this increase in natural frequency does not invoke resonance during its regular operation. In this context, it may be noted that first flapwise and edgewise frequencies dominate the structural response compared to all other blade frequencies during its regular operation. This, in turn, indicates that the blade dynamics are not affected by

the torsional mode within its operational range, i.e. the cut-in to cut-out speed. Once the modal frequency obtained from the spinning finite element model, it is used further to study the blade response.

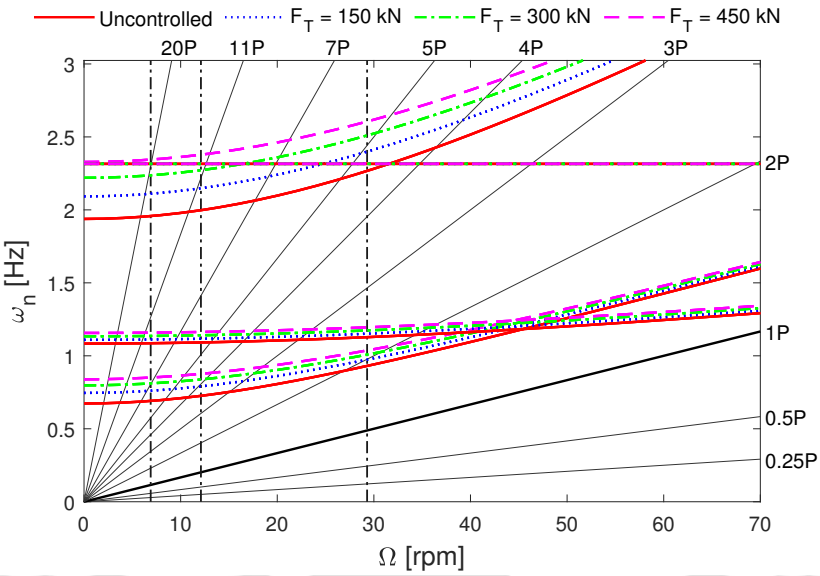

Figure 6.3: Campbell Diagram for NREL 5 MW wind turbine.

6.3.2 Response Validation and Vibration Control

In this section, the response obtained from the spinning finite element is first validated with FAST [218]. The wind loads for this numerical simulation are obtained using BEM theory from the wind field generated by TurbSim [17]. The 3D wind field is generated at the hub height over a square grid of 150 m × 150 m with 31 grid points at an equal interval along the horizontal and vertical directions. Fig. 6.4a shows the wind field for 11.4 m/s mean speed with 15% turbulence generated by TurbSim at different time instants (i.e. 0 s, 60 s, 120 s and 180 s). Fig. 6.4b and Fig. 6.4c show the wind load acting at different locations on the blade in its flapwise and edgewise directions. The aerodynamic loads along the out-of-plane and in-plane directions are evaluated using the global transformation of coordinates as discussed in Section 6.2. The Fourier amplitude spectrum of the aerodynamic loads are presented in Fig. 6.4d and Fig. 6.4e, which clearly show the rotational frequency and its integer multiple dominating the blade load time histories.

Using these loads at 49 points on the blade, its responses are solved using 4^{th} order Runge Kutta algorithm in MATLAB® [224] and the displacement response time histories obtained from the spinning FEM are compared with FAST results. For this purpose, the tension in the stiffener is kept zero. Fig. 6.5a shows the tip response of the blade in the out-of-plane direction while Fig. 6.5b shows the same in the in-plane direction. It may be noted that the responses obtained from the spinning FEM closely match with the results obtained from FAST. The little difference in response is attributed to the approximate aerodynamic damping in the spinning FEM model, as opposed to proper aeroelastic simulation in FAST. In general, the results are satisfactory and hence, the finite element analysis is further adopted to study the performance of the longitudinal stiffening and its impact on fatigue life. The tip displacement of the blade in the out-of-plane direction in Fig. 6.5a shows the peak deformation is ∼7.5 m and peak-to-peak deformation is ∼3.5 m. Similarly, the peak deformation of the blade tip in the in-plane direction is ∼1.25 m and the peak-to-peak deformation is ∼1.2 m.

In this study, SMA tendon is connected from the root to the tip, as shown in Fig. 6.1c to control blade vibration. Nitinol is proposed whose properties are shown in Table 4.4. The Young's modulus of this material in martensite phase is 83 GPa, whereas the same in austenite phase is 28 GPa [210]. The maximum allowable stress is 900 MPa. For the simulation, ambient temperature is considered to be 25°C while the maximum allowable temperature in semi-active control is set to 95°C. These values are case specific and can be adjusted depending upon the field conditions.

The response is simulated using 11.4 m/s mean wind speed with 15% turbulence with and without longitudinal stiffener as shown in Fig. 6.6. It is observed that the responses in both directions are significantly reduced due to the longitudinal stiffening. It improves the performance in terms of peak, mean and RMS

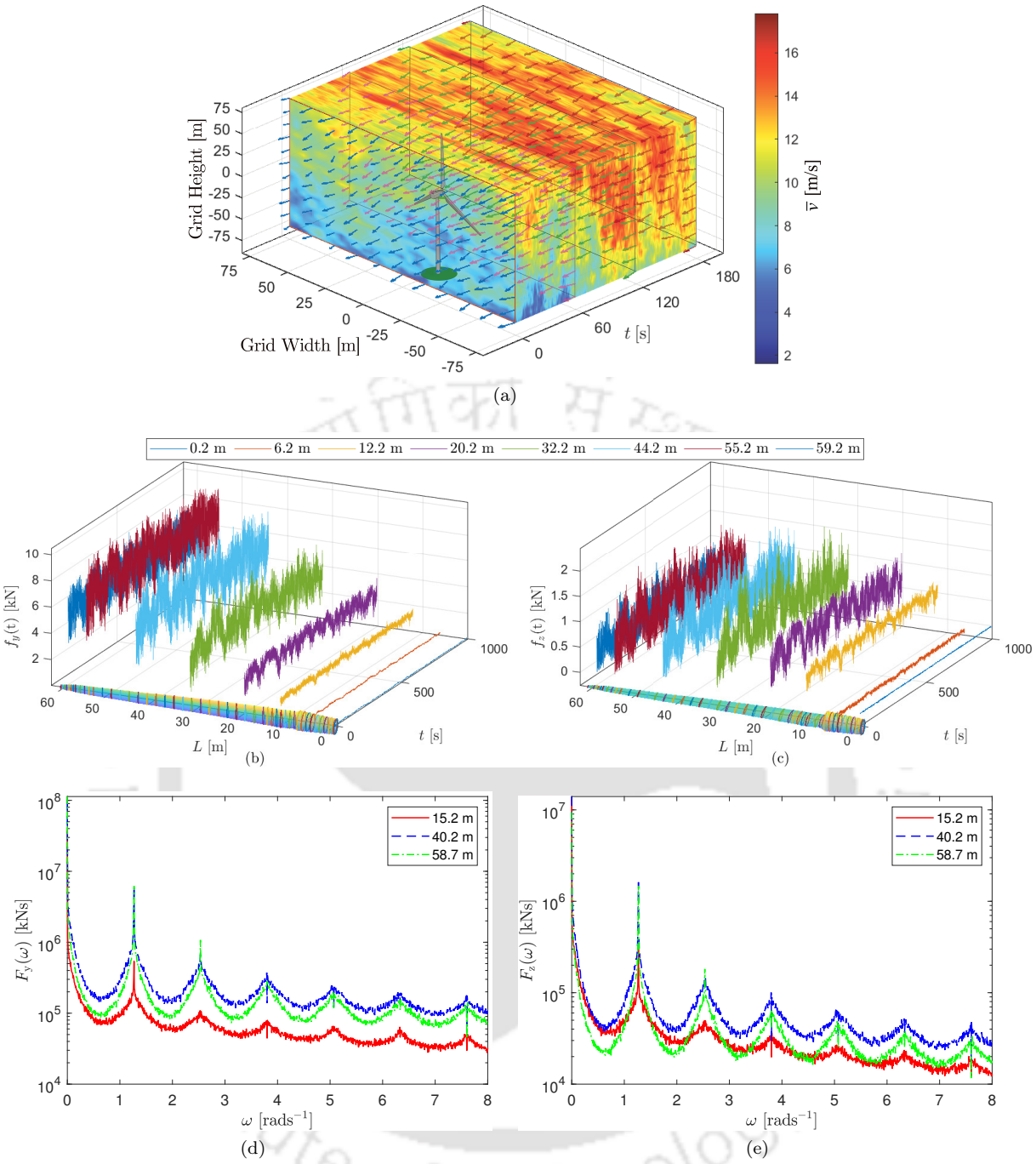

Figure 6.4: (a) Wind field for 11.4 m/s average wind speed at hub height with 15% turbulence; aerodynamic loads evaluated using BEM theory (b) out-of-plane, (c) in-plane direction, (d) Fourier amplitude of out-of-plane aerodynamic load and (e) Fourier amplitude of in-plane aerodynamic load.

response. The horizontal lines in Fig. 6.6 indicates the mean response corresponding to uncontrolled and controlled cases in passive and semi-active mode, respectively. Using passive tendon, the peak tip displacement response of the blade in the out-of-plane direction is reduced by 26.33% while same in the in-plane direction shows 13.05% reduction. The semi-active case with the application of 45 V reduces the peak tip displacement by 37.75% and 23.14% in the out-of-plane and the in-plane directions, respectively. Here, it may be noted that the applied voltage can be adjusted to have desired output. In this case, it is set in such a way that the tendon reaches maximum allowable temperature gradually in 10 min. The mean of the tip displacement is reduced by 20.76% and 14.90% in the out-of-plane and the in-plane directions, respectively in passive mode. It is further reduced to 40.94% and 31.36% in the same directions using semi-active stiffening. The RMS value of the blade tip displacement is reduced by 34.93% and 9.36% in the out-of-plane and

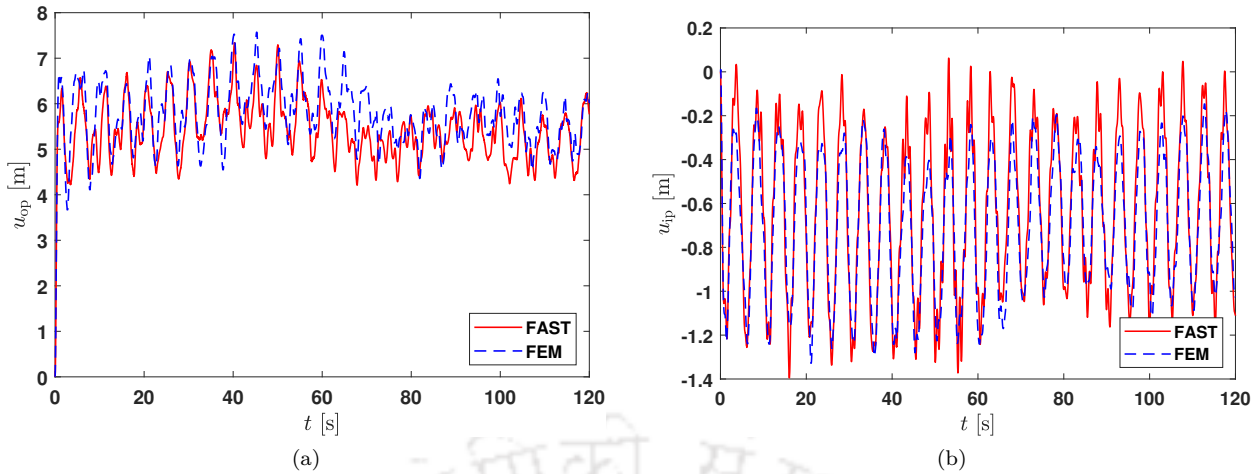

Figure 6.5: Blade tip displacement for 11.4 m/s wind with 15% turbulence (a) out-of-plane and (b) in-plane direction.

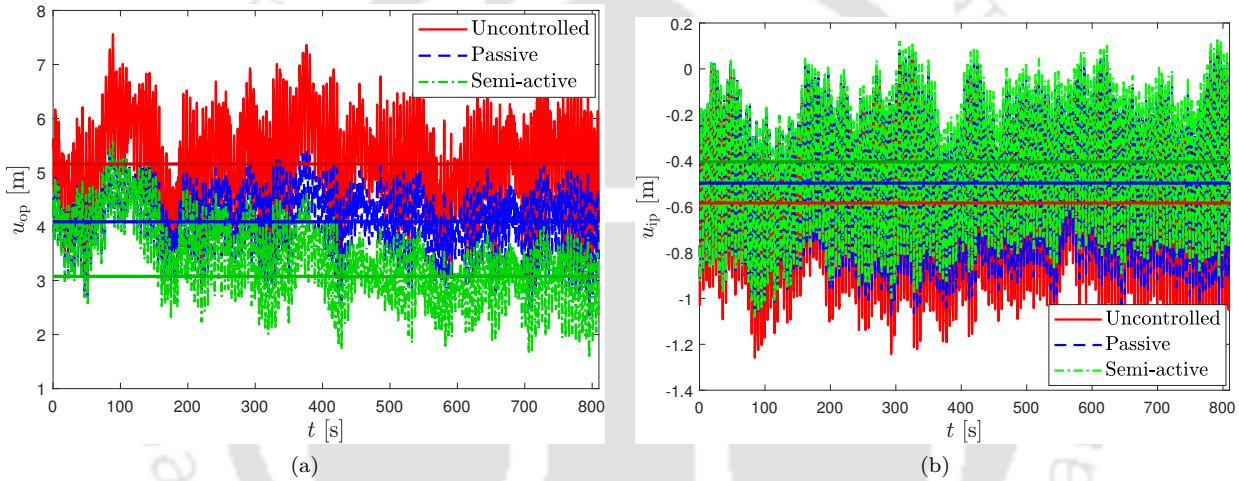

Figure 6.6: NREL 5 MW blade displacement response at the tip (a) out-of-plane and (b) in-plane.

the in-plane directions using passive version of the stiffening. While using semi-active control, it is reduced by 39.52% and 16.86% in the out-of-plane and the in-plane direction, respectively. With this, it may be concluded that the proposed longitudinal stiffening of spinning blade offers significant improvement of the response without affecting the overall aerodynamics of the airfoils used to built up the blade. Here, it should be noted that the tendons are in taut condition with no additional external force is applied. It only develops tension when the blade deforms. The tendon force stiffens the blade and acts against the centrifugal force.

6.4 Summary

A spinning blade experiences gyroscopic and Coriolis effects, which influence its modal and dynamic characteristics. Therefore, a detailed finite element model of spinning blade with longitudinal stiffener is developed in this chapter, which is used for modal and dynamic analysis. The frequencies of 5 MW benchmark turbine blade are evaluated using spinning FEM model and the results are found to be similar with BModes and FAST. The Campbell diagram, shows that the rotational effects (i.e. gyroscopic and Coriolis) must be included in modelling. Neglecting these effects may lead to the risk of resonance. Especially in case of designing vibration controllers, rotational effect must be considered to avoid the adverse consequences. Modal analysis of the rotating blade with SMA tendon shows significant improvement of stiffness, which does not invoke resonance as shown in the Campbell diagram. The response of the benchmark wind turbine is simulated using the aerodynamic loads obtained from 3D wind field and BEM theory, which is consistent

with FAST simulation. The responses obtained using spinning FE model matches with FAST, which is further used for fatigue analysis in the following chapter. The response analysis indicates that the blade vibration has reduced effectively with the addition of SMA tendon and the performance of the controller has further enhanced with the application of the heat.

Chapter 7

Fatigue Analysis of Blade

7.1 Introduction

This chapter presents a proof-of-concept for enhancing the fatigue life of the modern multi-megawatt wind turbine blade. For this purpose, the responses of the blade obtained in Section 6.3.2 are utilised to evaluate the longitudinal stresses from bi-axial bending moments and axial forces. The impact of the proposed longitudinal stiffener on the stress profile and the fatigue life of the blade are presented to demonstrate its performance. A sensitivity analysis on the reduction of peak stress and the fatigue life for different diameters of the tendon are also investigated. Further, the long-term fatigue analysis of longitudinally stiffened blade is carried out to investigate the performance under various fatigue design load cases as per IEC 61400-3 guidelines. The dynamic responses of the blade are obtained using instantaneous aeroelastic simulation and longitudinal stresses are evaluated with them. Then, short-term and long-term damages are evaluated using rainflow matrix obtained from these longitudinal stresses. Finally, the reliability of blade against fatigue failure is investigated. The numerical analysis presented in this study demonstrates the performance of longitudinal stiffening in combination with pitch angle and its advantages in reducing fatigue damage.

7.2 Fatigue Analysis of Blade

The modern multi-mega watt wind turbine blades are exposed to large amplitude of vibration and vulnerable to fatigue failure. The components of wind turbine system are subjected to various cyclic loading, which may lead to fatigue failure even when the stresses are well below the yield strength of the material. The damage due to the stress reversals often starts at the surface (i.e. extreme fibre) and eventually progresses to the fracture of the structure. Therefore, the design against fatigue failure is inevitable for structural integrity of this system. In this context, the fatigue damage assessment during the design life of a turbine is an essential task for safe operation. Thus, the longitudinal stress on the blade is estimated for various design load cases (as suggested in IEC 61400-1) and the rainflow algorithm is utilised to count the stress reversals.

In this study, the impact of longitudinal stiffening on fatigue life of NREL 5 MW wind turbine blade is investigated using rainflow algorithm. The longitudinal stress at a particular location over the blade due to the forces and moments, as shown in Fig. 7.1, during j^{th} load case is defined as

$$\sigma_j^{\text{L}}(t) = \frac{M_j^{\text{flap}}(t) z_c}{I_{\text{f}}} + \frac{M_j^{\text{edge}}(t) y_c}{I_{\text{e}}} + \sigma_j^{\text{ac}}(t) + \sigma_j^{\text{ag}}(t) + \sigma_j^{\text{a}T}(t) \tag{7.1}$$

where $M_j^{\text{flap}}(t)$ and $M_j^{\text{edge}}(t)$ are the j^{th} bending moment time history in the flapwise and edgewise direction, respectively. I_{f} and I_{e} are the second moment of area of the blade about its flapwise and edgewise axis, respectively. Parameters $\sigma_j^{\text{ac}}(t)$, $\sigma_j^{\text{ag}}(t)$ and $\sigma_j^{\text{a}T}(t)$ are the j^{th} stress time histories due to centrifugal, gravitational and control forces (F_T) in the axial direction, respectively.

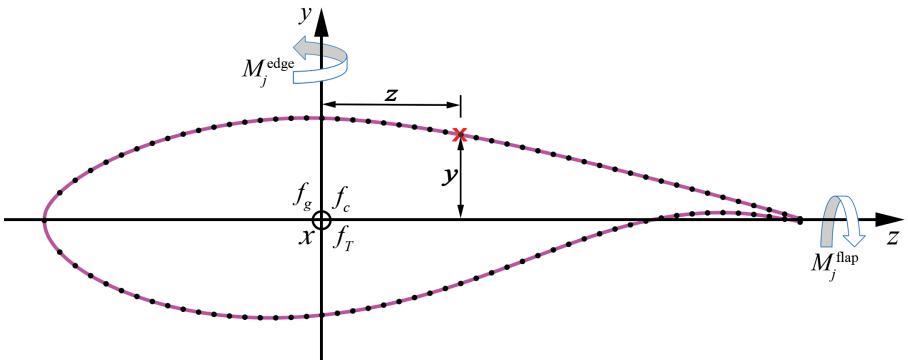

Figure 7.1: Blade bending and selected points along the airfoil for stress time history calculation.

7.2.1 Short-Term Fatigue

Once the stress time histories are evaluated, the short-term damages are estimated using the number of cycles obtained from rainflow algorithm (as proposed by Downing and Socie [225]) and S-N curve. The rainflow method produces a matrix (i.e. rainflow matrix) contains the information of number of stress reversals, mean and peak stress components for a given time history. Usually, the S-N curves are made for damage prediction from zero mean stress. But, the actual damage is accumulated when the material under compressive mean stress is less, and tensile mean stress is more compared to zero mean case. Therefore, it is important to consider the effect of mean stress while assessing the fatigue life from a time history. Thus, a mean stress correction, i.e. Goodman diagram [226] is applied to the rainflow matrix and an equivalent stress with zero mean in each cycle is evaluated to estimate the damage accumulation. Goodman diagram is a linear relation between the mean stress and alternating stress for finding the equivalent alternating stress (σ_{ji}^{ea}), which can be expressed as follows

$$\sigma_{ji}^{\mathrm{ea}} = \frac{\sigma_{ji}^{\mathrm{a}} \left(|\sigma^{\mathrm{fm}}| - \sigma^{\mathrm{u}}\right)}{|\sigma_{ji}^{\mathrm{m}}| - \sigma^{\mathrm{u}}} \tag{7.2}$$

where σ_{ji}^{a} and σ_{ji}^{m} are the alternating stress and mean stress in i^{th} cycle of the j^{th} time history from the rainflow matrix. Parameter σ^{fm} and σ^{u} are the fixed mean stress and ultimate stress of the material, respectively.

In this study, the blade is assumed to be made of Glass Fiber Reinforced Plastic (GFRP) material. Several S-N curves based on experimental data for different types of glass fibre composite materials are available in the literature [227]. Epaarachchi and Clausen [228] have suggested an empirical model for S-N curve based on two parameters λ_1 and λ_2 to calculate the fatigue behaviour of GFRP materials, which comply with the test data. They have also estimated the values of λ_1 and λ_2 for different GFRP materials. Following equations produce the S-N curve for any general GFRP material based on these parameters.

$$N = \left(\frac{\eta}{\lambda_1} + 1\right)^{\frac{1}{\lambda_2}} \tag{7.3a}$$

where

$$\eta = \left(\frac{\sigma_u}{\sigma_{ji}^{ea}} - 1\right)\left(\frac{\sigma_u}{\sigma_{ji}^{ea}}\right)^{0.6-\psi|\sin\theta_{\mathrm{f}}|} \frac{1}{(1-\psi)^{1.6-\psi|\sin\theta_{\mathrm{f}}|}} f^{\lambda_2} \tag{7.3b}$$

In the above equation, ψ is the stress ratio for reverse loading while θ_{f} is the fibre angle and f is the test frequency. Thus, the allowable number of cycles are estimated from this S-N curve using equivalent alternating stress, and the damage accumulation is obtained from Palmgren-Miner summation, i.e. the material fails after N number of allowable stress cycles. Therefore, the damage accumulated in each cycle is equal to $1/N$ and the short-term damage accumulated from the j^{th} stress time history is evaluated as

$$D_j^{ST} = \sum_i \frac{n_{ji}}{N_{ji}} \tag{7.4}$$

In above equation, n_{ji} is the rainflow cycle count during i^{th} stress reversal of j^{th} stress time history and N_{ji}

is the corresponding allowable number of cycle from the S-N curve.

Further, the Damage-equivalent Stress (DES) during a given time series is evaluated, which is used for fatigue load test. DES is defined as the constant mean and amplitude fatigue load that occurs at a fixed frequency, causing the same damage as a result of the variable spectrum load. Thus, the short-term DES is computed as [189]

$$\sigma_{\mathrm{DE}_j}^{\mathrm{ST}} = \left[\frac{\sum_i n_{ji} \left(\sigma_{ji}^{\mathrm{ea}}\right)^{\lambda}}{f^{\mathrm{eq}} T_j} \right]^{\frac{1}{\lambda}} \tag{7.5}$$

where λ is the slope of the S-N curve while f^{eq} and T_j are the frequency of DES and span of the j^{th} time series, respectively.

7.2.2 Lifetime Fatigue

Wind turbine blades are subjected to various wind speeds during their lifetime. Thus, the damage accumulation during the lifetime is estimated from the weighted summation of short-term damages under different wind speed condition according to their probability of occurrence. The probability of occurrence of hourly mean wind speed for a year is modelled by Weibull distribution [42]. In addition to probability of occurrence, an availability factor is considered to account for shut down period (i.e. maintenance) during the operational range of wind speed. Hence, the damage accumulated during the design life of the blade is evaluated as

$$D^L = \sum_j A f_j^L D_j^{ST} \tag{7.6}$$

where A is the availability factor of the wind turbine and f_j^L is the scaling factor for the j^{th} time history. The material failure occurs when the damage D^L equal to 1. The fatigue life of the material can be easily quantified once the damage accumulated over the flow period is quantified, i.e. multiplying the time span with the inverse of total damage. Further, the lifetime damage-equivalent stress is evaluated using the following expression

$$\sigma_{\mathrm{DE}}^{\mathrm{L}} = \left[\frac{\sum_j \sum_i f_j^L n_{ji} \left(\sigma_{ji}^{\mathrm{ea}}\right)^{\lambda}}{\sum_j f_j^L f^{\mathrm{eq}} T_j} \right]^{\frac{1}{\lambda}} \tag{7.7}$$

7.3 Numerical Results and Discussion

The numerical results presented in this section is mainly divided into short-term and long-term fatigue analysis, where the first part of the study is based on blade responses at the rated speed using equivalent modal aerodynamic damping. The long-term fatigue analysis involves responses using various wind speed as per IEC 61400-3 guidelines. With this in view, the following subsection presents stress and fatigue analysis of the blade.

7.3.1 Short-Term Fatigue Analysis

In this section, the fatigue life of the blade is estimated to study the effects of longitudinal stiffening using blade response at the rated speed, which is already simulated in Section 6.3.2. For this purpose, the total axial stress due to bending and different axial forces (i.e. centrifugal, component of gravity and tendon) acting at different sections of the blade are evaluated using Eq. 7.1. The cross sectional area and the second moment of area at different locations of the blade are evaluated from the airfoil data. This analysis is carried out by assuming GFRP material having density $\rho = 925.389$ kg/m^3, Young's modulus $E_y = 16.339$ GPa and $E_z = 4.902$ GPa. It may be noted that evaluation of I_f and I_e involve accurate knowledge of the blade geometry. For this purpose, thickness of the NREL 5 MW blade suggested by Borrman [229] is considered here along with its airfoil configuration. The bending moment in the flapwise and edgewise directions are evaluated at every node to estimate the flexural stress. Bending moment at the root of the blade is shown in Fig. 7.2. It can be observed that the bending moment in the flapwise direction is higher than the edgewise direction due to large deformation. In addition to flexural stress, axial stress due to the centrifugal,

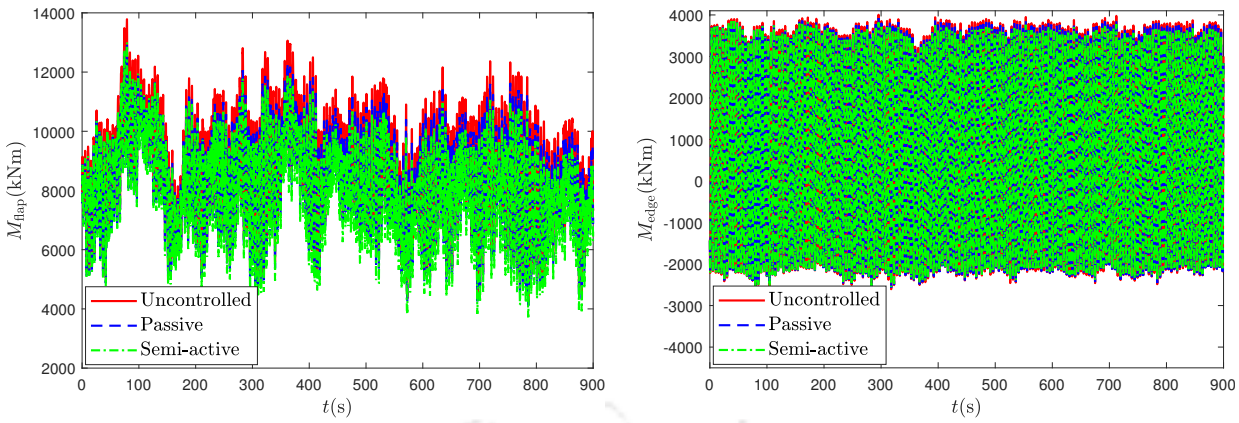

Figure 7.2: Bending moment time history at the root of the blade (a) flapwise and (b) edgewise.

gravitational and tendon forces are evaluated using cross sectional area of the airfoil. The tendon force acts towards the root while the centrifugal force acts opposite to it. The gravity force on the blade creates a time dependent cosine component in its axial direction.

The stress profile over the entire blade is evaluated using 100 points on the airfoil at every location. The time instant at which the axial stress over the uncontrolled blade becomes maximum is evaluated from the complete stress. The stress contours over the deflected blade at this time instant are shown in Fig. 7.3. The maximum stress is observed at 8.20 m from the root where the circular section (i.e. Cylinder-2 airfoil) start changing to non-circular section (i.e. DU40_A17 airfoil). The region between the midspan and the third quarter of length towards the tip also indicates very high stress as shown in Fig. 7.3(a). This is mainly due to the huge out-of-plane deformation of the large cantilever blade. In further analysis, maximum stress at this region is observed to be at 44.2 m from the root. The stress profile over the controlled blade is investigated and observed that it is significantly reduced by passive and semi-active Shape Memory Alloy (SMA) tendon, as shown in Fig. 7.3(b) and Fig. 7.3(c), respectively. Here, it may be noted that the reduction in blade deformation is caused by SMA tendon, which alleviates the stress over the region after the midspan. The

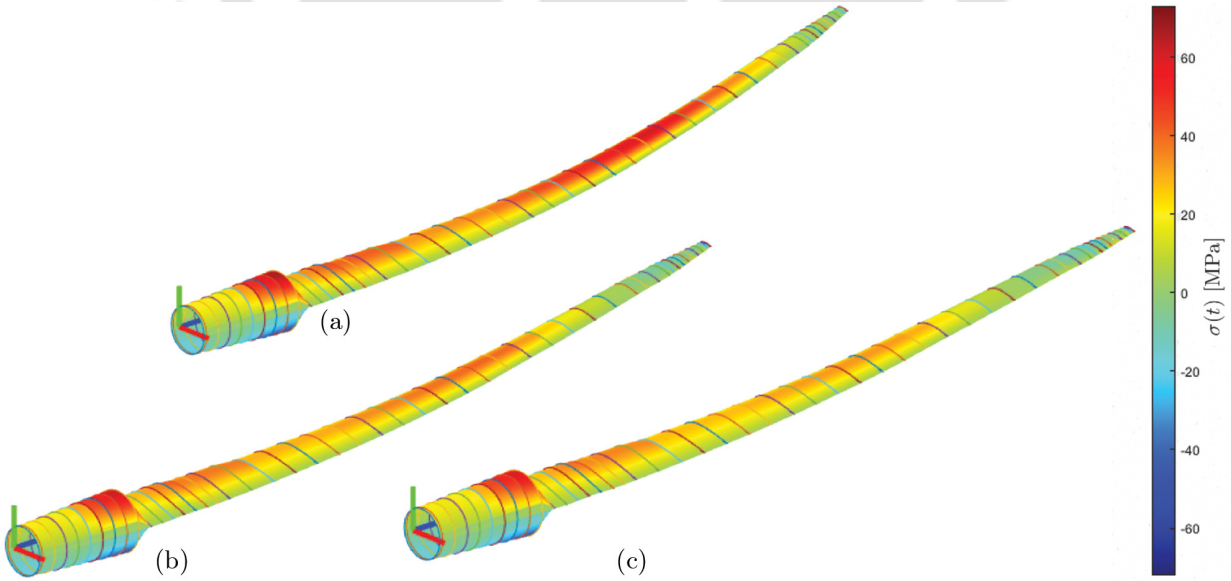

Figure 7.3: Stress contour at time instant of peak uncontrolled stress; (a) uncontrolled, (b) passive controlled and (c) semi-active controlled.

stress time histories of the blade at root, 8.20 m and 44.20 m are shown in Fig. 7.4. The peak stress at the root of the blade without the controller is 20.80 MPa and with controller shows ∼5-8% reduction using passive and semi-active tendon as observed in Fig. 7.4a. This clearly indicates that the proposed controller

does not create additional stress at the root, rather it is reduced as the developed tendon force always acts against the centrifugal force. The peak stress at 8.20 m from the root is 72.88 MPa. The stress time history of the maximum stress point is shown in Fig. 7.4b, where the stress is reduced by ∼7-13% with the addition of longitudinal stiffener as can be observed from the figure. The peak stress of the blade at 44.2 m from the blade root is 64.31 MPa as shown in Fig. 7.4c which is reduced by 40% and 58% using passive and semi-active SMA stiffener, respectively.

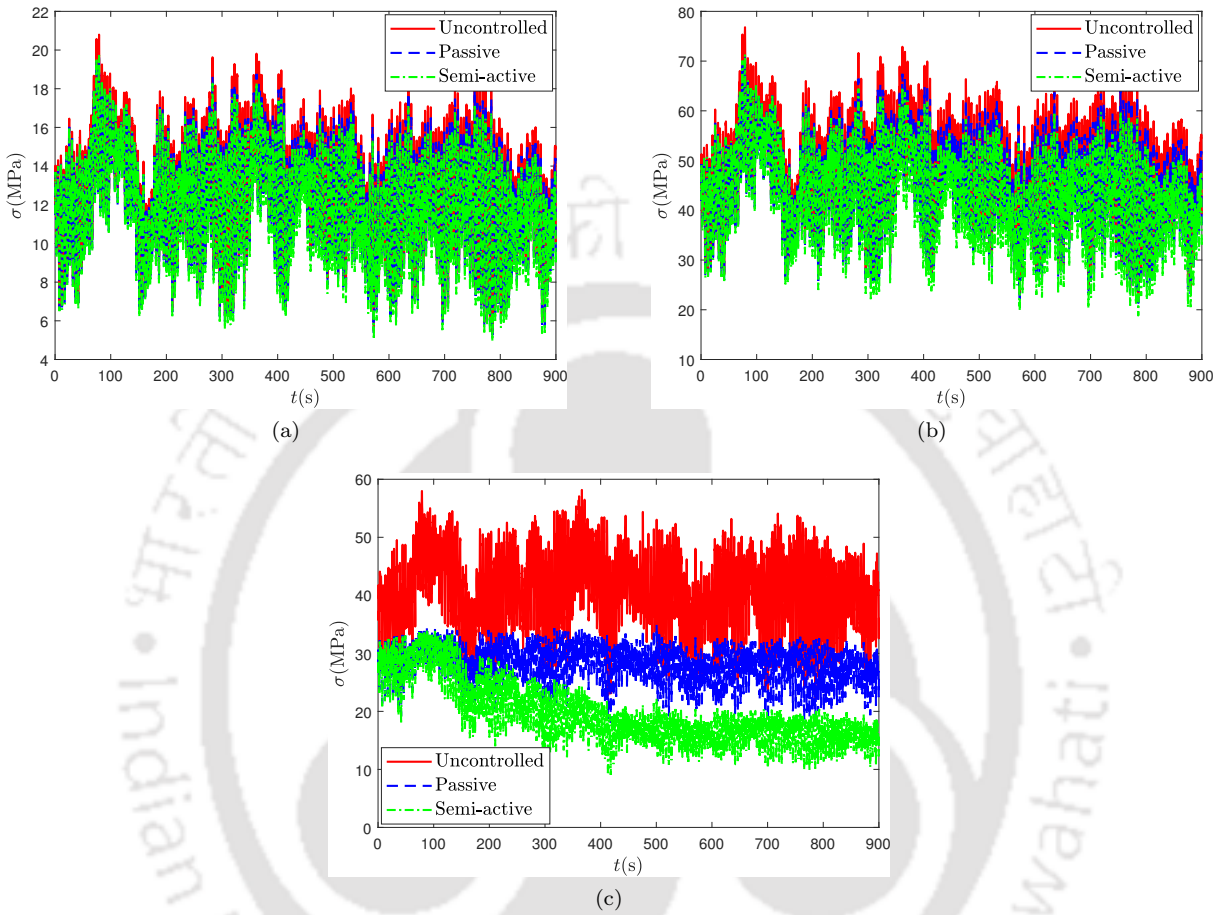

Figure 7.4: Stress response with and without controller at (a) root, (b) maximum stress point (8.2 m from root) and (c) midspan (34.2 m from root).

Further, the fatigue life of the blade is investigated. In this context, the number and frequency of cycles, mean and range of stress are estimated at each nodes over the blade using rainflow algorithm. Fig. 7.5 shows the rainflow cycle count histogram for blade axial stress at 8.2 m from the blade root (i.e. maximum uncontrolled stress location). For this purpose, the cycle count distribution obtained from the rainflow algorithm is placed into cycle count bins based on the mean and range of the stress. The total number of stress cycles have increased from 371.5 to 421.5 using passive controller as compared to uncontrolled case while it is further increased to 425.5 in semi-active case. It can be noted that the mean and range of the stress are significantly reduced using the proposed controller.

The damage accumulation is estimated using Palmgren-Miner's hypothesis (i.e. Eq. 7.4). The S-N curve parameters (i.e. λ_1 and λ_2 in Eq. 7.3) are considered to be 0.1173 and 0.231 with the fibre angle 90^o. The ultimate stress of the GFRP is assumed to be 185 MPa [228]. Fig. 7.6 shows the S-N curve for this material considered in this analysis. Finally, the service life of the blade is estimated at all points on the blade using the damage index D. The minimum fatigue life of the uncontrolled blade is estimated to be 15.29 years at 8.2 m from the root and a distance of 2.16 m and 1.11 m away from the centre of gravity along y-axis and z-axis, respectively. The corresponding peak stress is evaluated as 72.86 MPa. The displacement and stress response of the blade are significantly reduced with the addition of longitudinal stiffener as discussed above. Hence, the fatigue analysis of the blade using passive and semi-active stiffener are carried out and the fatigue life has improved to 32.45 years and 44.50 years, respectively by 25.4 mm (i.e. 1in) diameter

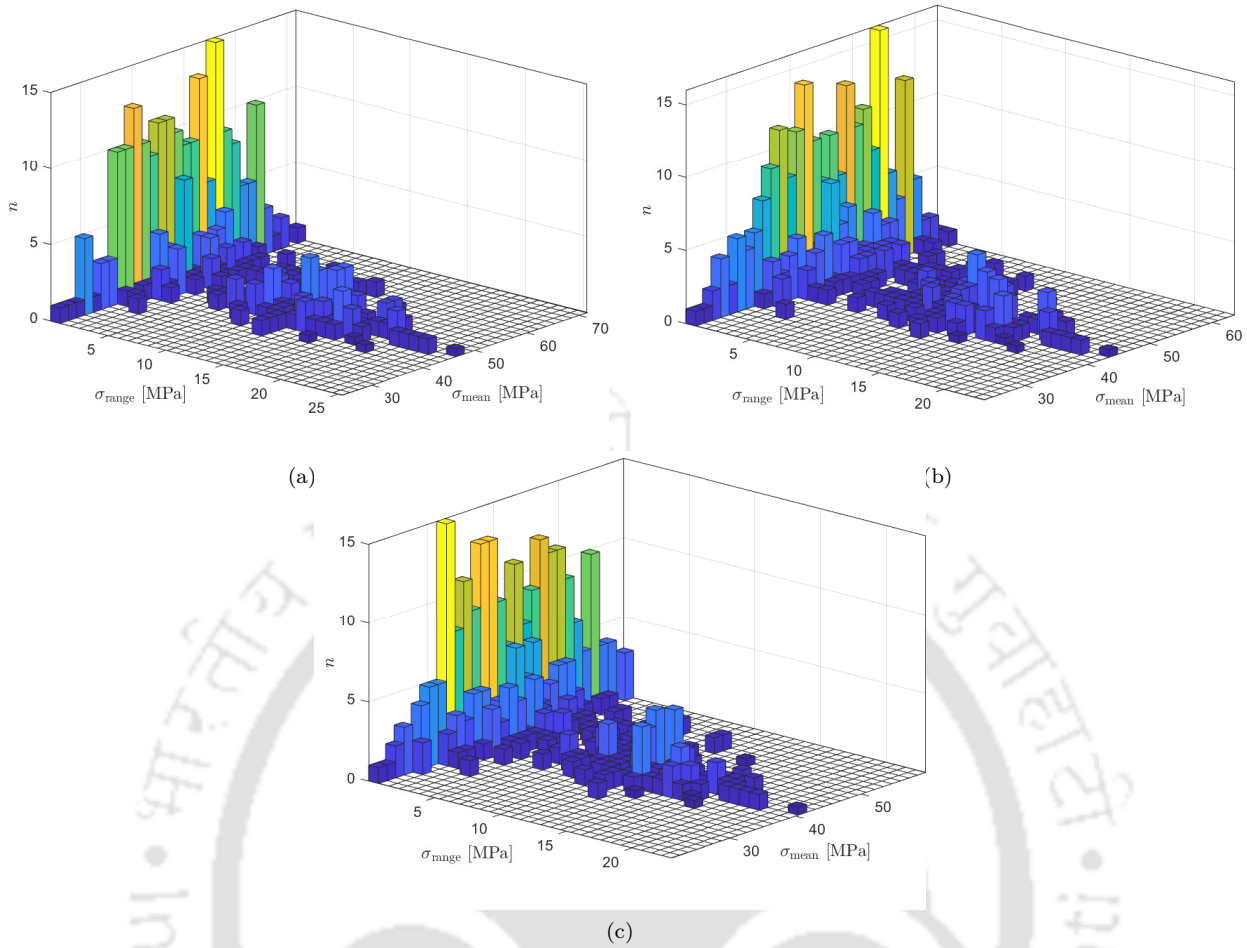

Figure 7.5: Rainflow cycle count histogram at maximum stress point (8.2 m from root); (a) uncontrolled, (b) passive controlled and (c) semi-active controlled.

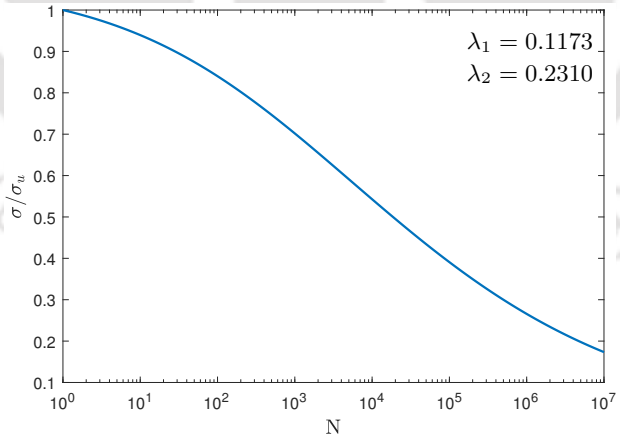

Figure 7.6: S-N curve for GFRP material.

SMA tendon. The peak stress at the critical location is reduced to 67.43 MPa and 64.68 MPa using passive and semi-active SMA stiffener, respectively.

Further, the sensitivity of the blade stress is investigated for different diameters of tendon, as shown in Fig. 7.7. The peak stress of the blade reduces further with the increase of tendon diameter in the passive version and the location of peak stress remains same as that in the uncontrolled case (i.e. $x = 8.20$ m, $y = 2.16$ m, $z = 1.023$ m). While the semi-active case gives more reduction of peak stress at critical location with increase of tendon diameter, at the same time the stress at the tip of the blade increases due to increase

in control force. In Fig. 7.7b, it can be observed that the 25.4 mm diameter tendon gives better control when compared to its passive version and other semi-active diameter cases. The semi-active case for higher diameter (38.1 mm and 50.8 mm) leads to increase in peak stress at the tip of the blade when compared to the passive case. Moreover, the peak stress at blade tip using 50.8 mm diameter tendon shows higher axial stress value when compared to the uncontrolled case. As mentioned earlier, the tip displacement response of the blade reduces with the increase of tendon diameter in both passive and semi-active cases. Also, the peak stress of the blade location away from the tip in semi-active case has huge reduction when compared to uncontrolled and passive case. Therefore, the effective performance of the semi-active controller can be obtained from the sensitivity analysis using different control force.

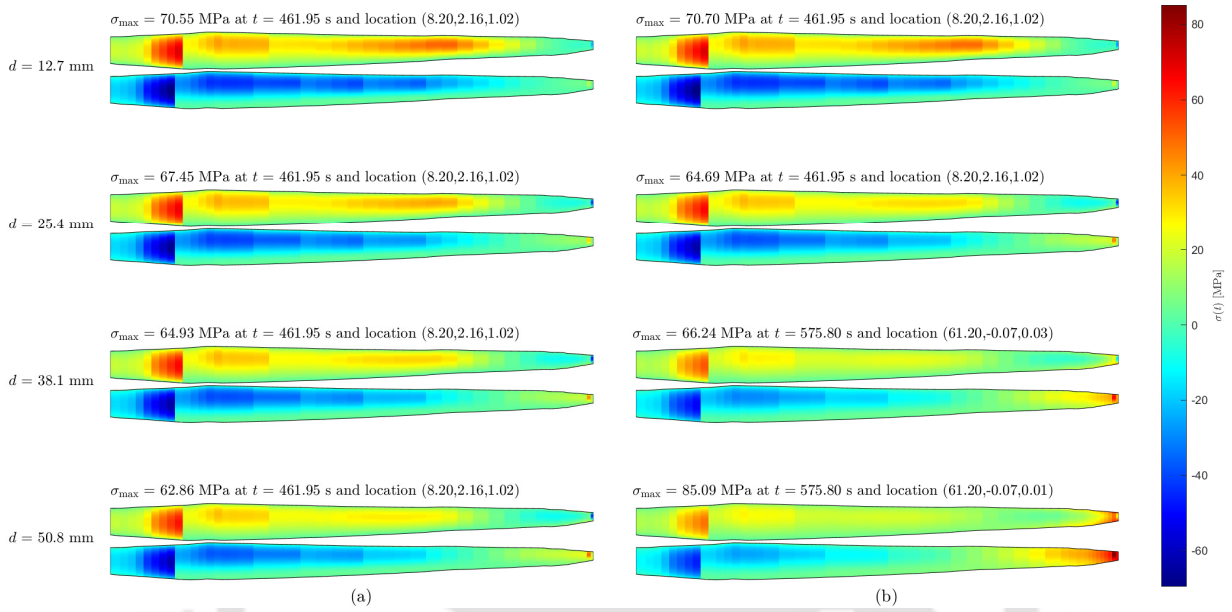

Figure 7.7: Stress contour at a time instant of peak stress for different diameter cases (a) passive controlled and (b) semi-active controlled.

Finally, the variation of fatigue life for different diameter of tendon is investigated as given in Table 7.1. It is observed that the fatigue life of the blade increases with increase of tendon diameter in both passive and semi-active cases while the peak stress at critical location decreases with the same. Also, the semi-active case shows more peak stress reduction and corresponding fatigue life improvement when compared to its passive version. In both passive and semi-active case, it may be noted that the number of cycles are increased with the increase of tendon diameter. However, the amplitude of vibration is less in controlled cases, which result in improved fatigue life.

Table 7.1: Peak stress and fatigue life of the blade with and without controller.

Type	d (mm)	σ^c_{max} (MPa)	n (-)	λ (years)
Uncontrolled	-	72.86	371.50	15.29
Passive	12.70	70.53	393.50	21.48
	25.40	67.43	421.50	32.45
	38.10	64.92	443.50	46.59
	50.80	62.68	450.50	62.83
Semi-active	12.70	70.68	382.50	20.01
	25.40	64.68	425.50	44.50
	38.10	58.85	467.50	95.23
	50.80	53.53	517.50	210.48

In stress sensitivity analysis, the semi-active tendon with 38.1 mm and 50.8 mm diameter have produced

more stress at the tip when compared to other locations as shown in Fig. 7.7b. However, the minimum fatigue life of the blade is observed at 8.2 m from the root (i.e. uncontrolled critical location) for both these diameters. The reason for this is further demonstrated in Fig. 7.8, which shows the stress time history of the semi-active case at the critical location and at to the tip. In Fig. 7.8a and Fig. 7.8b, the stress at the tip increases with time due to increase of control force. Once the temperature reach allowable limit, it is maintained at this level by adjusting the current flow. Therefore, the stress developed at the tip also reaches a constant level. In case of 25.4 mm diameter tendon (i.e. Fig. 7.8a), even though the number of stress cycles are more near the tip (i.e. 61.2 m) as shown in inset, the peak, mean and range of stress are less compared to the critical location. While the same stress using 50.8 mm diameter tendon is shown in Fig. 7.8b, where the peak, mean and number of cycles of stress are more compared to critical location but the range is significantly less. All these factors affect the overall fatigue life of the blade. Hence, the minimum fatigue life of the blade is observed at 8.2 m from the blade root in both the cases (i.e. diameter 25.4 mm and 50.8 mm).

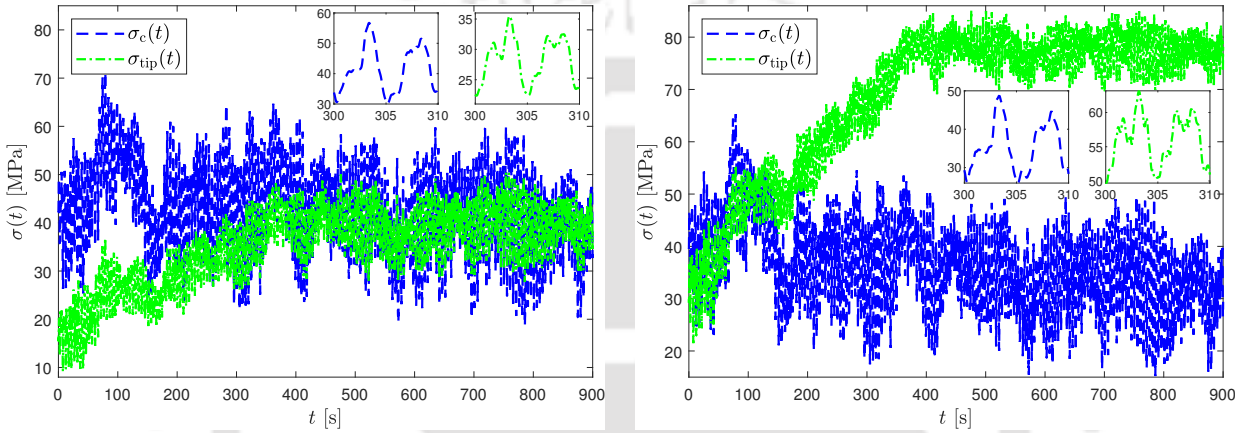

Figure 7.8: Stress time history at critical point and near to tip (i.e. 61.2 m from root) in semi-active controlled blade (a) tendon diameter, $d = 25.4$ mm and (b) tendon diameter, $d = 50.8$ mm.

7.3.2 Long-Term Fatigue Analysis

In this section, the fatigue analysis is carried out based on IEC 61400-3 [19] design guidelines. For this purpose, the dynamic responses of the blade with and without the stiffener are simulated under various design load cases using spinning finite element model presented in the previous chapter. Besides structural damping, real time aero-elastic simulation is adopted here to model the instantaneous aerodynamic damping acting on the rotor. Since long-term fatigue estimation involves various response analysis for longer time duration, the aeroelastic spinning Finite Element (FE) model is developed in Fortran. Thus, the aeroelastic loads and responses obtained using spinning FE model are validated with FAST at various wind speeds. In this context, the details of design load cases and wind fields are described in the following subsection.

7.3.2.1 Wind Field

The design load cases for fatigue analysis involves various wind flow conditions, including operating (i.e. between cut-in and cut-out) and non-operating (i.e. below cut-in and above cut-out) regions of the turbine as per IEC 61400-3 [19]. In this study, these fatigue load cases are selected as per the data given in Upwind Design Basis [230], which includes 17 load cases as given in Table 7.2 where $\bar{v}$ and T_w are the mean wind speed and turbulence intensity at the hub height, respectively. The frequency of occurrence for each load cases are evaluated using Weibull probability density function, as shown in Fig. 7.9 where scale and shape parameters are set to c = 11.31 m/s and k = 1.97, respectively [230].

The guideline also recommends a single one-hour response time-history or six simulations of ten minutes each for damage assessment. In this study, the time for heating the SMA material to achieve maximum control in semi-active mode is ∼400 s. During this time, the material is heated to a maximum temperature of 95 °C using a voltage difference of 45 V so that the temperature change is gradual and does not damage

Table 7.2: Wind parameters.

Load Cases	$\bar{v}$ [m/s]	T_w [%]	Load Cases	$\bar{v}$ [m/s]	T_w [%]
LC1	2	29.2	LC10	20	13.4
LC2	4	20.4	LC11	22	13.3
LC3	6	17.5	LC12	24	13.1
LC4	8	16.0	LC13	26	12.0
LC5	10	15.2	LC14	28	11.9
LC6	12	14.6	LC15	30	11.8
LC7	14	14.2	LC16	32	11.8
LC8	16	13.9	LC17	34-42	11.7
LC9	18	13.6			

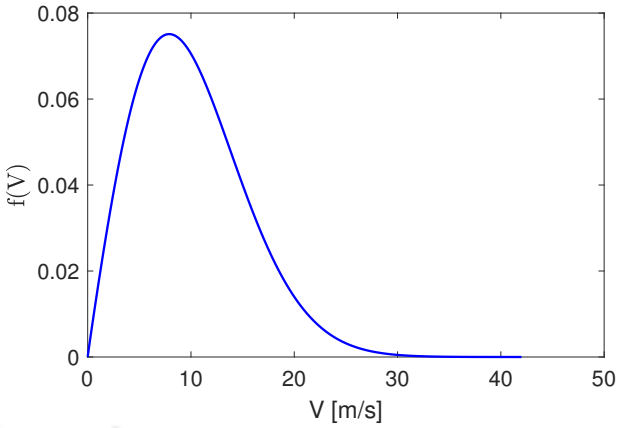

Figure 7.9: Weibull distribution of wind speed.

the material or its surroundings. The wind field in each load case is simulated for 4000 s with a time step of 0.5 s using TurbSim [16], which is a full field turbulent wind simulator developed by NREL [17]. In this wind fields simulation, 1D Kaimal spectrum is used. The complete flow field has three velocity components (i.e. downwind, crosswind and vertical wind) at each point in a rectangular grid around the hub.

Fig. 7.10 shows the 3D wind fields generated using TurbSim for steady and 15% turbulence at cut-in, rated and cut-out speed. In steady wind flow condition, both vertical and cross velocity components are zero, and the downwind velocity changes only with height due to shear exponent, as observed in Fig. 7.10a, Fig. 7.10c and Fig. 7.10e. Hence, the range of velocity variation is less in steady flow compared to turbulent case where all wind components are present, as shown in Fig. 7.10b, Fig. 7.10d and Fig. 7.10f. Further, these wind fields are used for validating the aeroelastic response simulated using spinning finite element model developed in this study.

7.3.2.2 Model Validation

For model validation, the blade tip displacement in the out-of-plane and in-plane directions are compared with FAST [209], which is an aeroelastic simulation package developed by NREL [218]. First, the instantaneous aerodynamic loads are evaluated using BEM theory from the 3D wind field, as discussed in Subsection 6.2.4. Then, the responses are simulated using these aerodynamic loads. Fig. 7.11 shows the comparison of aeroelastic loads from the model developed in this study and FAST in the out-of-plane and in-plane directions at a few selected locations on the blade for the different steady wind flow. In this figure, the dotted line refers to the load simulated in Fortran, which perfectly matches with the values obtained from FAST, i.e. the solid line. Since there is no turbulence in this case, the load is mostly governed by the mean wind speed and the rotational frequency of the turbine. Hence, the load time-histories under the steady flow condition are pure sinusoid, whose values obtained from two different codes (i.e. Fortran and FAST) match with each other.

The blade tip deformation corresponding to these velocities are also shown in Fig. 7.12. From these figures, it may be noted that the results of the FEM model closely match with FAST at different velocities. The inset in each sub figure of Fig. 7.12 shows the comparison of dotted line (i.e. response from the code developed in this study) with firm line (i.e. FAST Result). The percentage differences between the response quantities obtained from the two codes are given in Table 7.3. The maximum difference in case of blade out-of-plane response under steady wind flow is 2.38% (corresponding to peak-peak deformation under 3 m/s wind speed) and the same in the in-plane direction is 2.43% (corresponding to peak deformation under 25 m/s wind speed). The difference in all other cases are lower and practically insignificant. Thus, the model performs satisfactorily under steady flow condition.

Further, the performance of the spinning FE model is investigated for turbulent wind condition. Fig. 7.13 and Fig. 7.15 show the aerodynamic loads and blade tip displacements for 15% turbulence, respectively. In this case also the aerodynamic load generated by the Fortran code is very close to the same obtained from FAST. Fig. 7.14 shows the aerodynamic load at location 48.20 m from root of the blade. The peak, mean and dominant frequency of the load time history match with each other. The difference between the magnitude of loads obtained from these two codes are well within 5% and hence the turbulent load simulation is considered

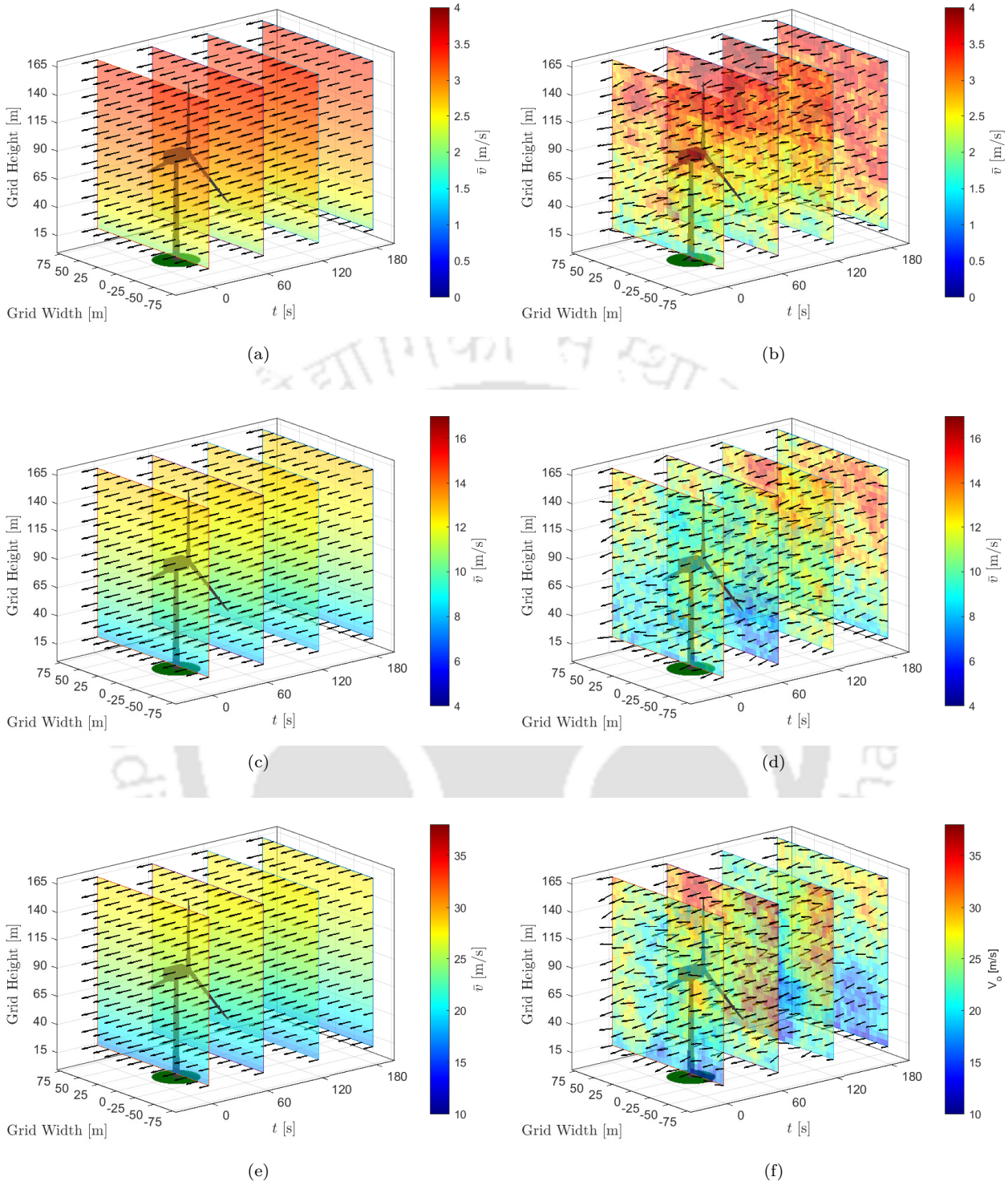

Figure 7.10: Wind field for cut-in, rated and cut-out mean wind speed at hub height; (a) 3 m/s steady flow, (b) 3 m/s with 15% turbulence, (c) 11.4 m/s steady flow, (d) 11.4 m/s with 15% turbulence, (e) 25 m/s steady flow and (f) 25 m/s with 15% turbulence.

satisfactory. Using these loads, the response of the blade is simulated, which is shown in Fig. 7.15. The response simulated by both these codes are nearly identical and there is no significant phase lag between these two time histories. The maximum difference in case of blade out-of-plane response under 15% turbulent wind flow is 3.95% (corresponding to peak-peak deformation under 3 m/s wind speed) and the same in the in-plane direction is 1.97% (corresponding to rms deformation under 11.4 m/s wind speed), as shown in

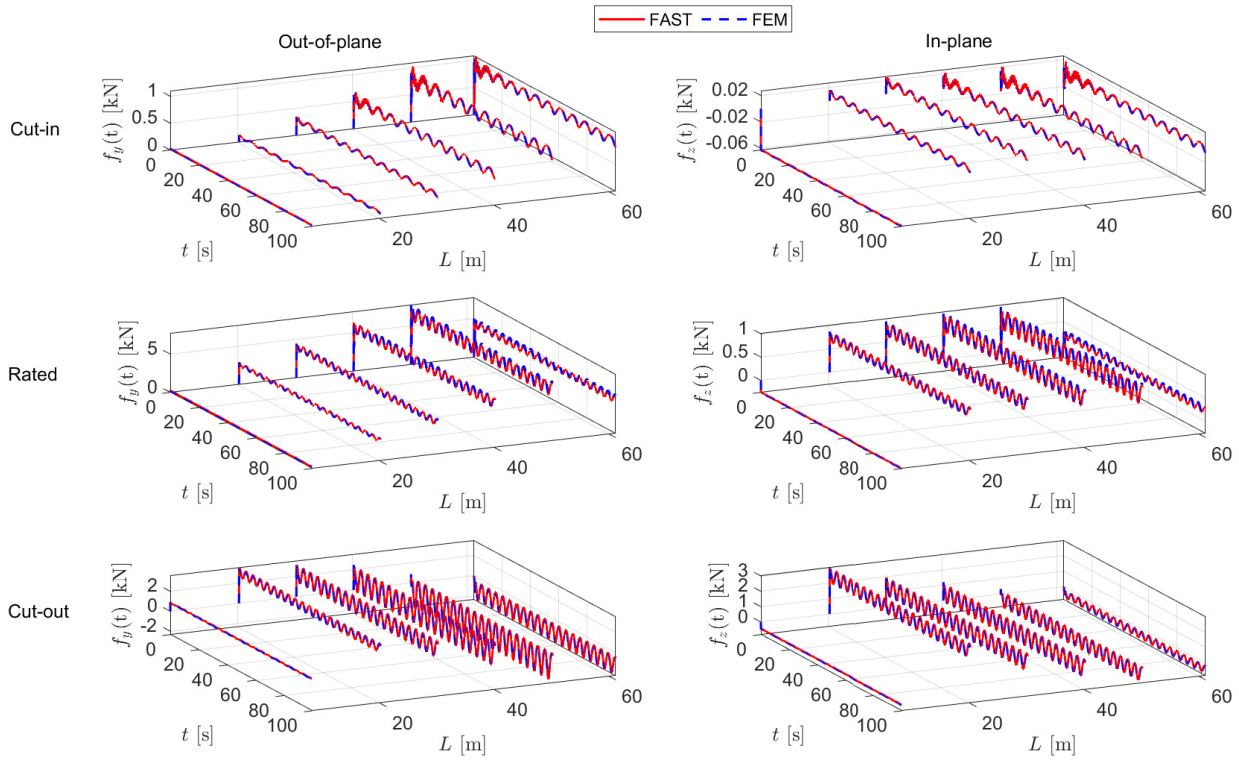

Figure 7.11: Aerodynamic loads at different locations of the blade for different mean wind speed and steady flow condition.

Table 7.3. The difference in all other cases are less and hence, the performance of the Fortran code is satisfactory. Therefore, the spinning FEM model and aeroelastic simulator developed in Fortran can be used for further analysis for long-term fatigue reliability of blade.

Here, it may be noted that the maximum blade tip response in the out-of-plane direction is observed at the rated speed compared to cut-in and cut-out while the same in the in-plane direction is observed at cut-out wind speed.

7.3.2.3 Response Reduction Using Longitudinal Stiffening

Once the spinning FE model is validated, it is further used to investigate the performance of longitudinal stiffening for fatigue life enhancement. The longitudinal tendon is assumed to be made of Nitinol with 25.4 mm diameter. Its Youngs modulus in austenite and martensite phases are 83 GPa and 28 GPa, respectively. The density and maximum recoverable strain of this material are 6450 kg/m^3 and 0.067, respectively. The voltage in semi-active control is set to 45 V and the details of other physical and thermodynamic properties may be found in Table 4.4.

Table 7.3: Percentage difference between the response from spinning FEM and FAST.

Wind Type	V [m/s]	Out-of-plane				In-plane			
		Peak	Mean	RMS	Peak-Peak	Peak	Mean	RMS	Peak-Peak
Steady	3.0	0.03	0.08	0.40	2.38	1.10	0.21	1.11	1.73
	11.4	1.02	0.20	0.99	0.98	0.17	0.39	1.28	1.12
	25.0	1.93	0.32	1.72	1.68	2.43	0.55	1.32	2.02
TI=15%	3.0	0.12	0.14	0.62	3.95	0.94	0.29	1.05	1.53
	11.4	1.23	0.30	1.53	1.64	1.16	0.55	1.97	0.85
	25.0	0.98	1.20	2.05	1.48	1.25	1.63	1.26	0.19

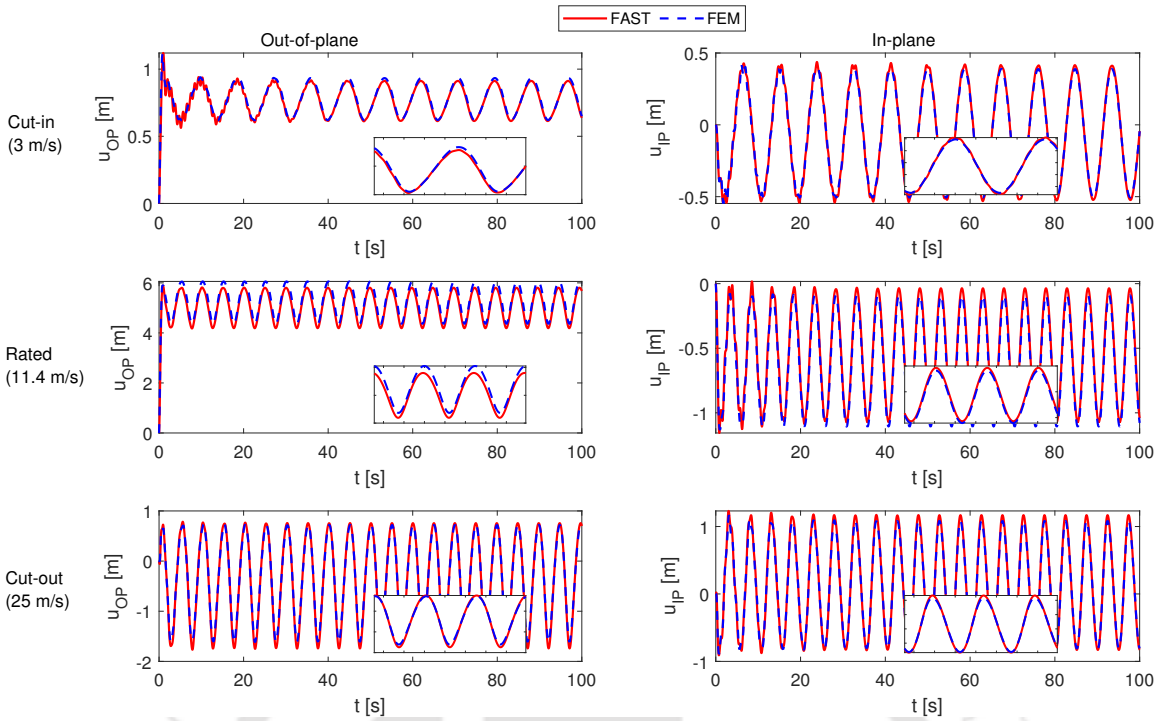

Figure 7.12: Blade tip deformation time history for different mean wind speed and steady flow condition.

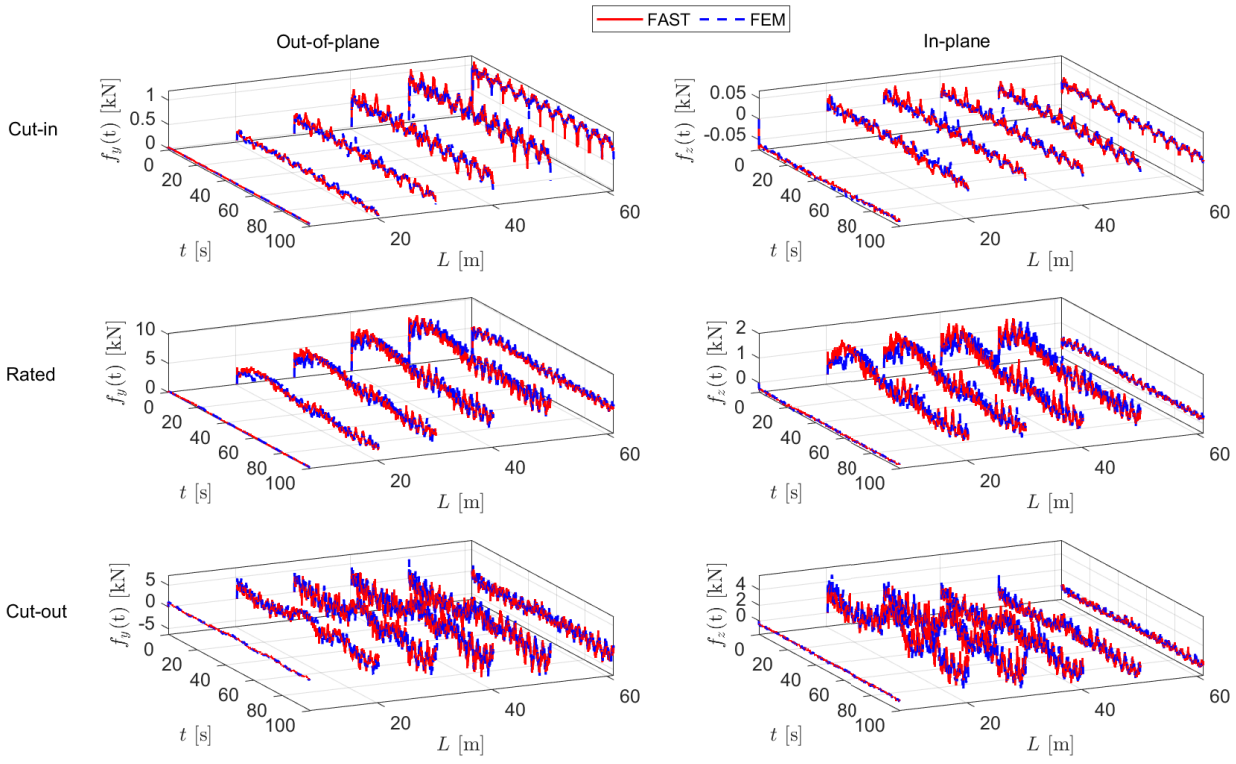

Figure 7.13: Aerodynamic load time histories for different mean wind speeds with 15% turbulence at various locations of the blade.

The responses of the NREL 5 MW benchmark turbine blade is simulated for each load case given in Table 7.2 with and without the stiffening force. Fig. 7.16a and Fig. 7.16b show the blade tip displacement time history in the out-of-plane and in-plane direction, respectively for 6^{th} load case (i.e. LC6), which is close to rated speed. Table 7.4 shows the details of the different response quantities along the out-of-plane and

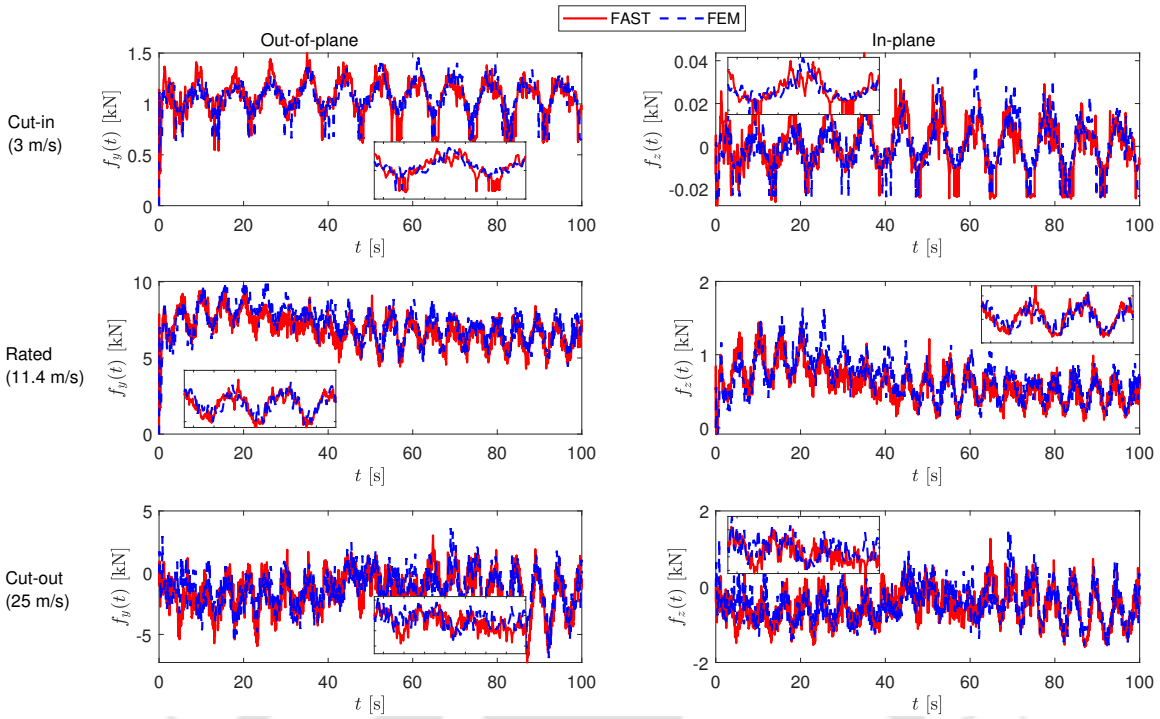

Figure 7.14: Aerodynamic load time histories for different mean wind speeds and 15% turbulence at 48.20 m from root of the blade.

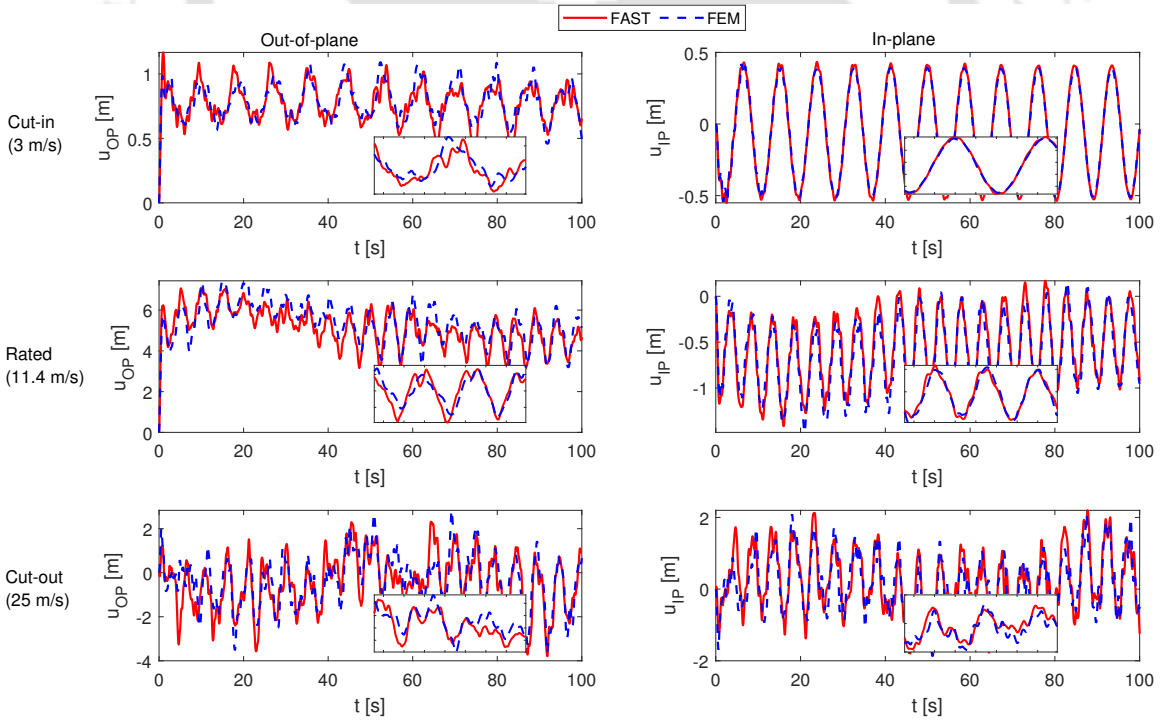

Figure 7.15: Blade tip deformation time history for wind speeds with turbulence 15%.

in-plane directions. It may be noted that the magnitude of peak, mean and peak-to-peak deformations in out-of-plane direction are significantly higher compared to the same in the in-plane direction. Moreover, the mean response among these quantities is governed by the mean wind speed at the hub-height. The remaining quantities (peak, peak-to-peak and *rms*) are governed to the fluctuating component of the inflowing turbulent wind. Here, it is worth mentioning that different controllers discussed in the literature review can control the dynamic response of the blade in either of the two orthogonal direction leaving the mean component

Table 7.4: Blade deformation corresponding to LC6

Type	Out-of-plane [m]				In-plane [m]			
	Peak	Mean	RMS	Peak-Peak	Peak	Mean	RMS	Peak-Peak
Uncontrolled	6.887	3.988	4.086	6.074	1.669	-0.684	0.797	1.929
Passive	5.402	3.438	3.497	4.614	1.448	-0.603	0.707	1.695
Semi-active	3.923	2.306	2.362	3.545	1.178	-0.427	0.533	1.440

unattended. However, the fatigue life is affected by the magnitude of the stress reversal and its number besides the mean stress level. Therefore, any controller aims to improve fatigue life must mitigate both of them, as demonstrated by the proposed blade stiffening. The advantage of the proposed longitudinal stiffening is reflected here in its ability to suppress all dynamic components (i.e. peak, mean, rms and peak-to-peak) of the blade deformations significantly in both out-of-plane and in-plane directions. The peak, mean, rms and peak-to-peak deformations in out-of-plane direction are reduced by 21.57%, 13.80%, 14.41% and 24.04%, respectively in passive mode, which are further improved to 43.04%, 42.17%, 42.19% and 41.63%, respectively in semi-active mode. While the same response parameters along the in-plane direction are reduced by 13.24%, 11.85%, 11.28% and 12.12%, respectively in passive case, which are improved to 29.45%, 37.55%, 33.09% and 25.36%, respectively with the application of Joule heating in semi-active mode of operation.

The Fourier amplitude spectrum of the blade tip displacement in the out-of-plane and in-plane directions are assessed for LC6 using the responses, as illustrated in Fig. 7.16c and Fig. 7.16d, respectively. The rotational frequency of the turbine and its harmonics (i.e. 1P, 2P, 3P, etc.) are found to dominate the vibration of the blade. Furthermore, the Fourier amplitude of the blade response corresponding to 1P is significantly more than the same corresponding to higher harmonics and blades natural frequencies. This is due to the fact that the blades are designed in such a way that their fundamental frequency is well above 3P of the turbine's rotational frequency. Fig. 7.16c and Fig. 7.16d also reveal the same. These figures also show that the proposed longitudinal stiffening has the ability to reduce the amplitude of vibration significantly at the dominant frequencies, as shown in the insets of Fig. 7.16c and Fig. 7.16d and also in Table 7.5, due to improved blade stiffness.

Table 7.5: Percentage reduction of peak Fourier amplitude of blade response for LC6

Harmonics of Ω	Out-of-plane		In-plane	
	Passive	Semi-active	Passive	Semi-active
1P	29.25	44.31	8.29	19.32
2P	13.53	34.82	9.21	27.22
3P	11.37	27.97	2.77	15.04

[N.B.: Response amplitudes are insignificant beyond 3P and hence, they are neglected.]

Further, the performance of this blade stiffening over the complete range of design load cases are demonstrated using box-whisker plot, as shown in Fig. 7.17a and Fig. 7.17b. It is observed that the peak displacement at the blade tip increases with the increase of wind speed. However, the peak and mean responses are reduced due to the application of pitch angle for load cases above the rated speed. Finally, the blade response parameters are reduced once the wind speed crosses its cut-out mark where breaks are applied while the pitch angle is set to 90°.

Once the response time histories are ready, the instantaneous bending moments in two orthogonal directions are evaluated at each node along the length of the blade. The longitudinal stresses over the blade profile are evaluated using these values of bending moment and axial forces (i.e. centrifugal, gravitational and tendon) for all design load cases. The variation of dynamic stress components at the critical location is shown in Fig. 7.18a. It may be noted that the amplitude of stress increases with higher wind velocities, which is finally reduced above the rated speed. The range of stress (i.e. $\sigma_{max} - \sigma_{min}$) increases significantly up to LC12. Beyond this point brakes are applied and the turbine is parked with 90° pitch angle. Fig. 7.18b shows the variation of uncontrolled and controlled stress response of the blade at 42.4 m from the root. It clearly shows the capability of the passive and semi-active longitudinal stiffening in reducing all dynamic components, especially the range of stress, which has major roll on fatigue damage.

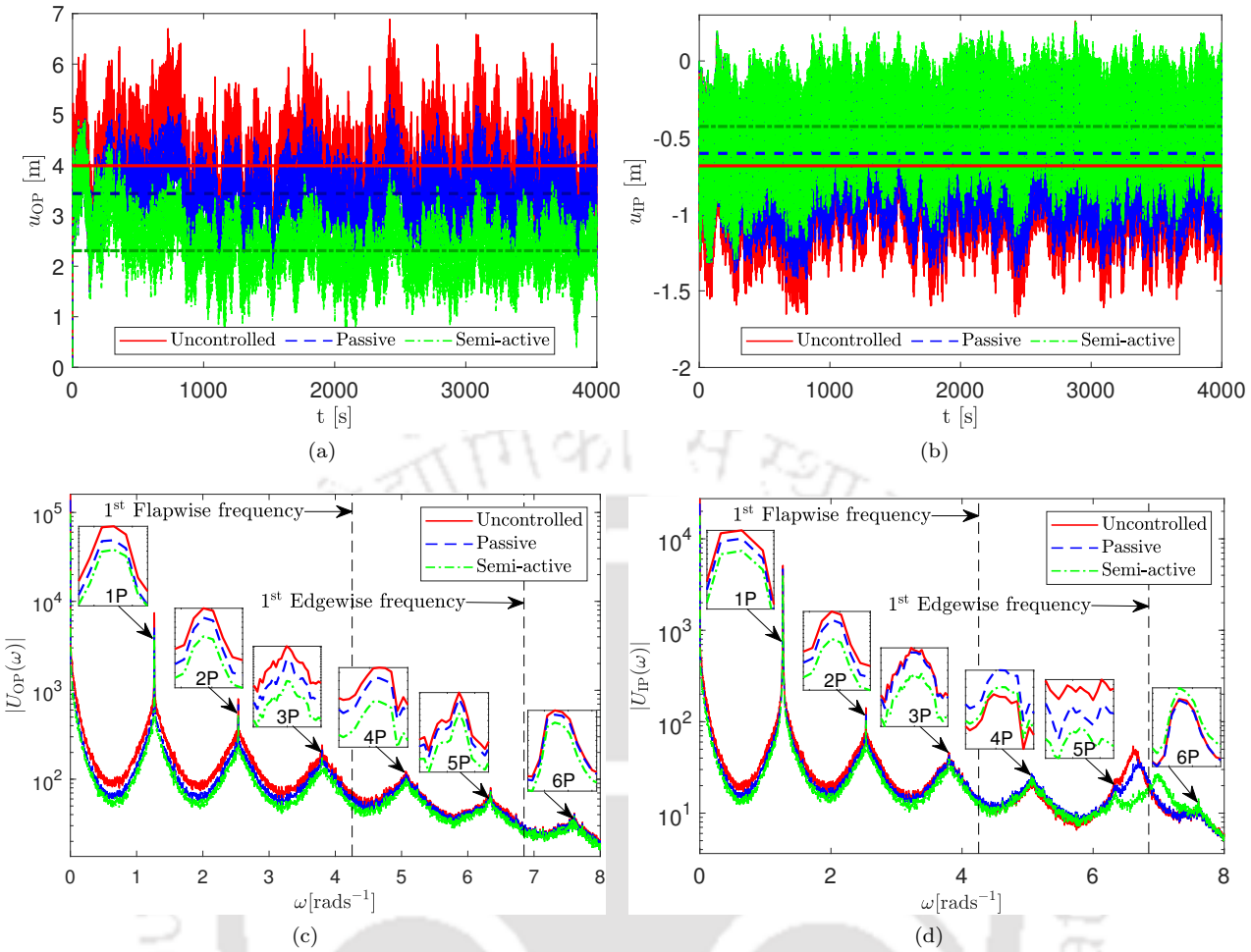

Figure 7.16: Response at the tip of the blade for load case 6; (a) out-of-plane displacement, (b) in-plane displacement, (c) Fourier amplitude spectrum of out-of-plane displacement and (d) Fourier amplitude spectrum of in-plane displacement.

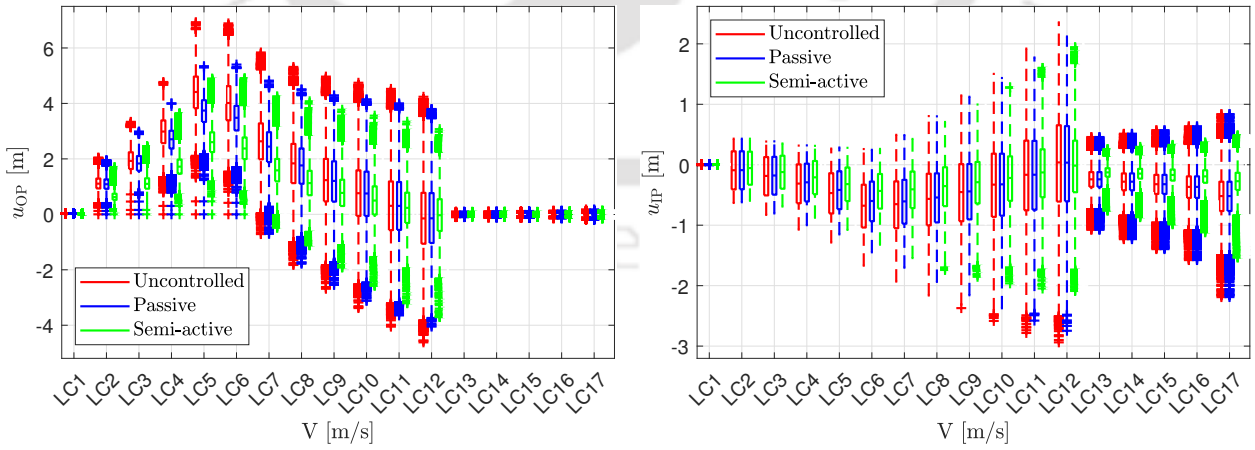

Figure 7.17: Box and Whisker plot of displacement for different load cases; (a) out-of-plane and (b) in-plane.

7.3.2.4 Fatigue Life Estimation

The longitudinal stresses obtained in Section 7.3.2.3 are further utilized to estimate the fatigue life of the blade. For this purpose, the partial safety factor is set to 1.8. With this, the rainflow matrices are evaluated for each design load case and the corresponding number of cycles from the S-N curve are evaluated using

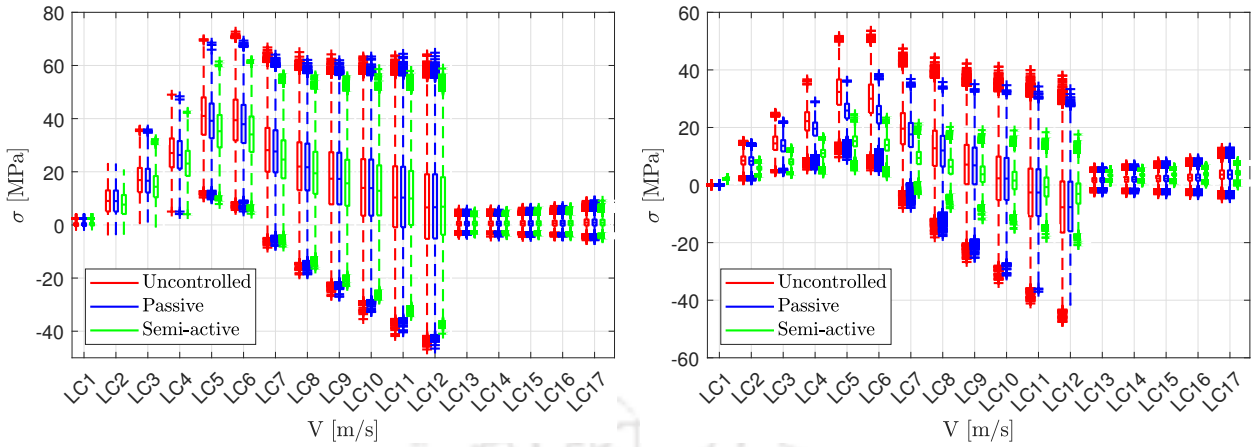

Figure 7.18: Box and Whisker plot of stress variations for different load cases; (a) at critical point and (b) at 42.4 m from root.

mean corrected equivalent alternating stress. Then, the short-term damages are estimated using Eq. 7.4, as shown in Fig. 7.19a. It is observed that the short-term damage increases significantly with load case up to

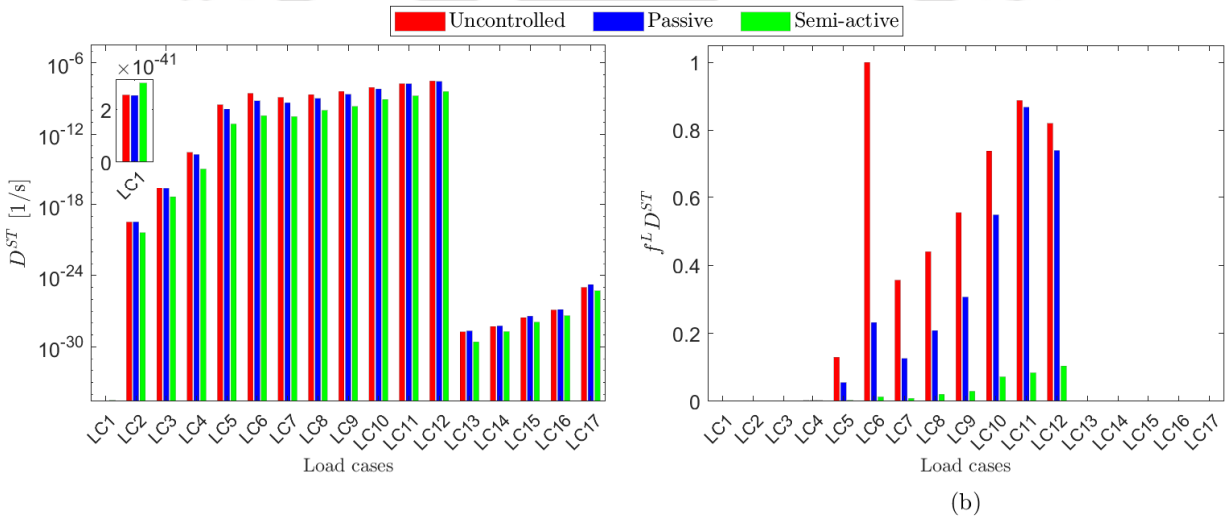

(b)

Figure 7.19: Damage of blade at critical location; (a) short-term damage, (b) relative short-term damage weighted with probability of occurrence.

LC12. Beyond this point, as the turbine is parked, the short-term damages are reduced. Comparatively, the passive and semi-active stiffening show less damage in all load cases below cut-out speed. Further, these short-term damages are weighted according to the probability of occurrence of the load cases. Fig. 7.19b shows the relative short-term damage weighted with probability of occurrence. It is clearly visible that the maximum damage occurs during the 6^{th} load case, which is close to the rated speed, due to its high probability of occurrence compared to the higher velocity load cases. The contribution of damage during the lifetime is comparatively smaller for the wind flow below the rated speed due to less short-term damage with a lower probability of occurrence.

Once short-term damages are estimated, the damage equivalent stresses are evaluated using Eq. 7.5, which is shown in Fig. 7.20a. This information is necessary for fatigue load test. It is observed that the maximum short-term DES corresponds to 12^{th} load case, which is close to the cut-out speed of the turbine. However, the frequency of occurrence of this load case is less compared to the rated speed. Hence, the relative short-term DES weighted with probability of occurrence, as shown in Fig. 7.20b illustrates maximum weighted DES corresponding to the 6^{th} load case. Finally, the accumulation of damages during the design life and corresponding fatigue life are estimated using these short-term damages. For this purpose, the design life

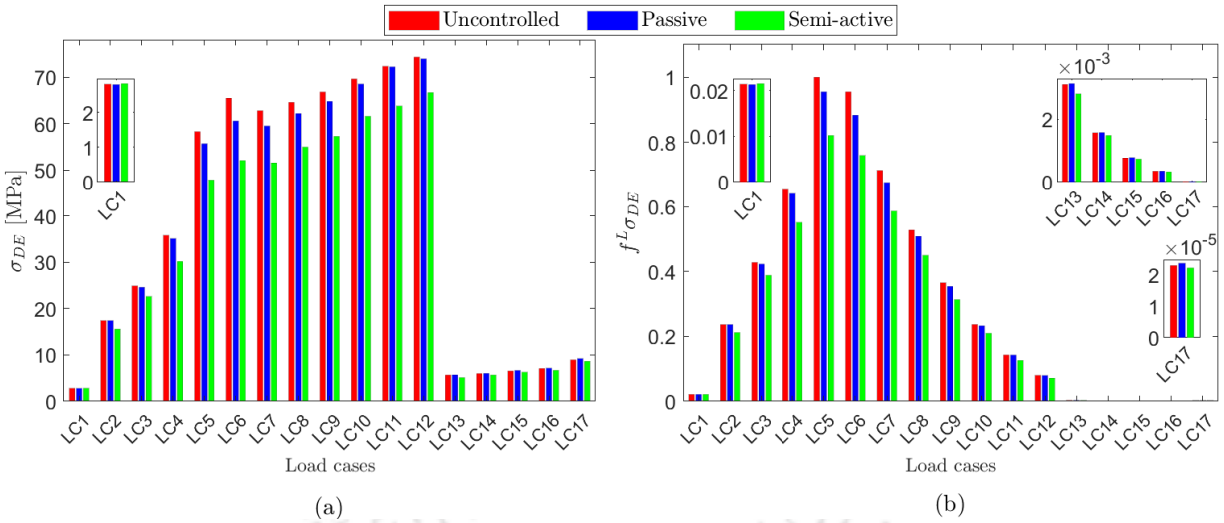

Figure 7.20: DES of blade at critical location; (a) short-term DES, (b) relative short-term DES weighted with probability of occurrence.

of the blade is assumed to be 20 years. In case of blade without stiffener, the lifetime damage is found to be 1.010 and corresponding fatigue life is 19.82 years. This is further improved to 0.633 and 0.069 using passive and semi-active longitudinal stiffening, respectively and the corresponding fatigue life are found to be 31.58 years and 290.78 years. The lifetime damage equivalent stress for fatigue design in uncontrolled case is 89.00 MPa, while the same for passive and semi-active cases are 87.10 MPa and 79.00 MPa, respectively. Besides performance evaluation of the proposed stiffening strategy, further attempts are made to investigate the impact of this blade stiffening on its reliability and extended design life.

7.3.3 Reliability Analysis

To study the impact of longitudinal stiffening further, the reliability of the blade against fatigue damage is also demonstrated with a statistical analysis using 100 samples of response for each load case. Using these responses, the performance of stiffened blade are summarised in Table 7.6. It is observed that the passive stiffening is not effective in non-operating region of the wind speed (i.e. below cut-in and above cut-out). This is due to less deformation of the blade, which in turn develops less tendon force. In general, the passive and semi-active stiffened blade perform well in the operational range of the turbine.

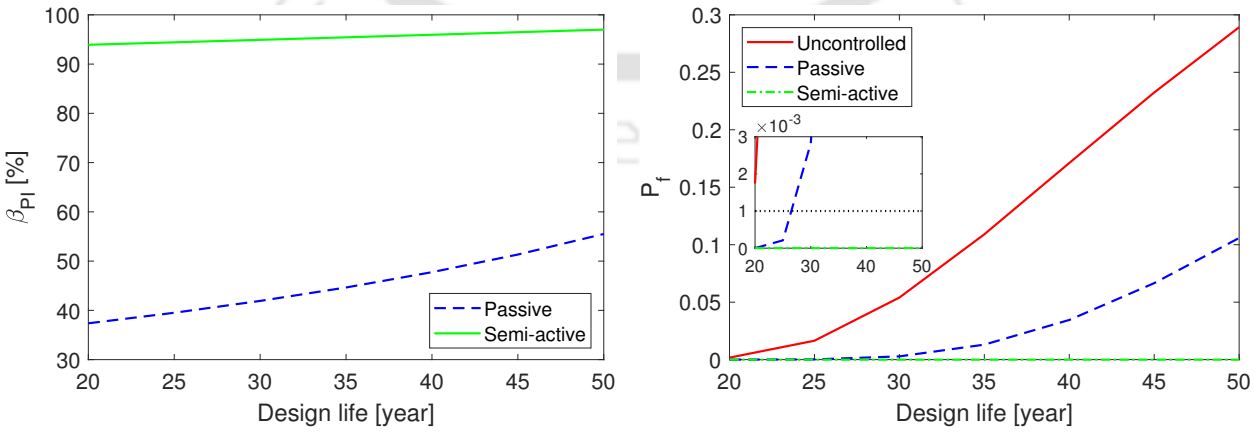

Figure 7.21: (a) Improvement in reliability index and (b) Probability of failure.

The limit state function for reliability analysis takes the form $g(x) = D_a^L - D_f^L$ where D_a^L is the allowable damage accumulation and D_f^L is the fatigue damage during the design life of blade. In this analysis, the

Table 7.6: Performance of the longitudinal stiffening in terms of percentage reduction in passive and semi-active mode of operation.

$\bar{v}$	Passive								Semi-active							
m/s	u^{op}_{peak}	u^{op}_{mean}	u^{op}_{rms}	u^{op}_{p2p}	u^{ip}_{peak}	u^{ip}_{mean}	u^{ip}_{rms}	u^{ip}_{p2p}	u^{op}_{peak}	u^{op}_{mean}	u^{op}_{rms}	u^{op}_{p2p}	u^{ip}_{peak}	u^{ip}_{mean}	u^{ip}_{rms}	u^{ip}_{p2p}
2	0.00	0.00	0.00	0.00	0.00	0.00	0.00	0.00	45.15	44.23	44.61	45.39	35.91	35.28	35.46	35.83
4	4.98	2.17	5.42	5.65	1.61	1.98	0.49	0.96	43.90	44.87	44.11	43.30	20.79	40.99	14.45	16.33
6	10.33	5.32	12.57	12.17	3.75	4.16	1.54	2.55	43.62	44.12	44.14	42.55	23.14	36.65	15.21	18.30
8	15.89	9.81	21.41	19.58	6.53	7.17	3.56	4.98	43.57	43.45	44.29	42.82	24.02	34.34	16.37	19.27
10	22.75	15.59	30.89	28.33	11.33	11.40	7.18	9.01	42.74	42.38	43.38	41.84	23.92	33.34	17.94	19.15
12	22.26	13.88	27.96	25.81	14.55	11.90	9.65	12.50	42.04	41.64	42.67	41.24	29.50	37.01	21.58	24.99
14	18.31	8.57	17.05	17.08	13.35	8.02	8.11	10.73	41.26	41.41	41.60	40.34	32.22	39.27	25.56	29.39
16	16.23	6.16	10.61	13.09	12.46	5.89	6.15	9.33	40.86	40.73	41.10	40.08	33.28	39.12	28.51	31.98
18	14.78	5.01	6.87	11.53	11.72	4.77	4.56	8.87	40.36	39.39	40.68	39.82	33.48	37.66	30.75	33.36
20	13.94	4.58	5.13	11.38	11.26	4.20	3.72	9.14	39.96	36.77	40.42	39.76	33.50	34.47	32.51	34.39
22	13.12	4.01	4.48	11.67	10.65	3.17	3.47	9.77	39.53	26.84	40.11	39.63	33.35	24.18	33.86	35.23
24	12.74	8.94	4.71	12.16	9.74	2.19	3.80	10.45	39.35	84.30	39.89	39.52	32.94	18.91	34.94	35.83
26	0.01	0.00	0.00	0.00	0.01	0.00	0.00	0.01	24.83	62.72	25.97	19.56	45.34	49.52	44.53	43.96
28	0.00	0.00	0.00	0.00	0.01	0.00	0.00	0.01	23.84	62.63	26.03	17.88	45.18	49.50	44.42	43.75
30	0.02	0.00	0.00	0.00	0.01	0.00	0.00	0.01	26.89	62.54	26.13	19.50	45.04	49.49	44.31	43.58
32	0.00	0.00	0.00	0.00	0.01	0.00	0.01	0.00	27.50	62.50	26.03	19.86	44.89	49.48	44.21	43.43
38	0.01	0.01	0.00	0.00	0.02	0.01	0.01	0.02	28.50	62.35	25.89	19.94	44.42	49.45	43.91	42.92

[N.B.: Insignificant reduction in passive case under parked condition due to very less blade deformation. However, Joule heating in semi-active mode increases the stiffness significantly and hence, offers significant reduction.]

design life is assumed to be 20 years and the corresponding damage accumulation index is set to $D^L_a = 1$. The Cornell reliability index is then evaluated for the blade with and without stiffening and the corresponding probability of failure [i.e. $p_f = \Phi(-\beta)$] is evaluated. The reliability index for blade without longitudinal stiffening is found to be $\beta = 2.92$ and corresponding probability of failure is $p_f = 1.74 \times 10^{-3}$. In case of longitudinally stiffened blades, this is improved to $\beta = 4.67$ and $p_f = 1.54 \times 10^{-6}$ in the passive mode of operation (i.e. ∼37% increase in β and ∼99% improvement of p_f). While the reliability index in semi-active mode of operation increased by ∼94% and the corresponding probability of failure is very small for obvious reason. In this context, it is worth to study how the reliability index and probability of failure varies with higher design life. Therefore, the fatigue analysis is repeated for design life varying from 20-50 years. Fig. 7.21a and Fig. 7.21b show the improvement of reliability index and probability of failure for different design life. It is observed that the blade with passive stiffening improves reliability index by ∼45% for the range of design life used in this analysis, while the semi-active stiffening improves the same by ∼95%. From Fig. 7.21b, it may be noted that the design life of the blade can be extended using the longitudinal stiffening, which can operate either in passive mode or in semi-active mode depending up on the situation.

7.4 Summary

In this chapter, the impact of SMA tendon based longitudinal stiffening on the fatigue life of the horizontal axis wind turbine blade is investigated using spinning finite element method. For this purpose, the longitudinal stresses are evaluated and it is found that the highest stress concentration is at the location where blade geometry changes from circular to non-circular. The peak stress at this locations is significantly reduced with the addition of SMA stiffener to the blade and a remarkable stress alleviation is noticed around the midspan of the blade. In the semi-active mode of operation, the application of higher diameter SMA tendon improves the blade performance in terms of deformation but it also increases the stress concentration at the tip of the blade. Hence, the heating of the tendon should be limited to an optimal level to avoid the damage due to stress build-up at the tip.

Further, this study is extended for long-term fatigue analysis. For this purpose, the response of blade are simulated for various fatigue design load cases as per IEC guidelines, which includes wind speed in operational and parked conditions. The performance of the proposed stiffening strategy at those load cases are studied. It is observed that passive stiffener is effective in operational wind speed (i.e. between cut-in and cut-out wind speed), while its semi-active version is effective in all design load cases (i.e. operational and parked condition of the turbine). With these responses, longitudinal stresses are evaluated and observed

significant reduction in all dynamic components. Then, short-term and long-term damages are evaluated using rainflow matrix obtained from these longitudinal stresses. Finally, fatigue life and reliability against fatigue are estimated. This long-term fatigue and reliability analysis advocate the proposed blade stiffening strategy for improved design life. Overall, the numerical results presented in this study clearly indicate the significant improvement of blade performance in terms of longitudinal stress, fatigue life and reliability.

Chapter 8

Concluding Remarks

The work presented in this thesis primarily contributes to the theoretical development of a novel control technique for improving the performance of large horizontal axis wind turbine blades. Overall, the performance of the proposed scheme is investigated to study its impact on the modal, dynamic, fatigue and reliability characteristics of wind turbine blades. With this in view, the major contributions from this study along with their plausible extension in the future are reported in the following sections.

8.1 Conclusions

The wind turbine blade vibration control is need of the hour, especially for large new generation rotors as they experience significant deformation. To address this issue, a 5 MW benchmark wind turbine blade is longitudinally stiffened by a SMA tendon. The material property of the tendon is modelled by combining the constitutive relationship with the principles of thermodynamics. A voltage based switching algorithm is developed to model the semi-active mode of operation. It is observed that the proposed stiffener has significantly improved the performance of the blade. The major findings and the advantages of the proposed control strategy are listed below

- A single stiffener is effective in two orthogonal directions (i.e. out-of-plane and in-plane) as opposed to other passive controllers proposed in the literature (i.e. TMD, TLCD, CLCD), that primarily operate in one direction only. The magnitude of response reduction in terms of critical response parameters (i.e. peak, peak-to-peak, mean and RMS) are significant over the complete operational envelope of the turbine.
- The proposed longitudinal stiffening primarily enhances the stiffness of the blade without affecting any other design parameters. This, in turn, helps to reduce large deformation in terms of peak, peak-to-peak, mean and RMS value, which is otherwise difficult to mitigate. It significantly improves the reliability of the blade against bending, which is the natural consequence of response reduction.
- The proposed control algorithm works even in the passive mode when the current flow is stopped. It is an advantage of this control strategy in case of any power failure as opposed to other active or semi-active controller. The sensitivity analysis conducted in this study clearly demonstrates this issue under extreme condition and proves the strategy to be promising for vibration control of large blades.
- In the semi-active mode, an efficient switching algorithm is developed where the initial voltage and the voltage during switching can be adjusted depending upon the demand experienced by the turbine. Therefore, the controller can be designed in passive mode to meet the regular serviceability requirements while the semi-active mode can be invoked during any emergency. This offers flexibility to the operator for mode switching where the minimum level of performance is always guaranteed. In this context, the power requirement in the semi-active mode is extremely low, which also advocates for the efficiency of the proposed controller in the light of energy consumption.
- This study offers the mathematical framework for cyclostationary analysis of blade response. The numerical results clearly shows the cyclostationary nature of the response where rotational frequency

predominates over other structural frequencies. The wavelet based time-frequency analysis offers perfect solution to identify the instantaneous frequency content of the response. Using these wavelet coefficients, time varying response statistics can be quantified, which is otherwise difficult for wind turbine system using conventional input-output relation in non-stationary random vibration framework as the system matrices are time dependent.

- Once the response statistics are quantified, they are further used to model the level crossing problem. This is one of the important aspect of blade design as its collision with tower can be catastrophic. The numerical results obtained in this study clearly shows the response is Gaussian and hence, the crossing rate can be modelled using Rice formula where the failure can be modelled as a Poisson process. It is observed that the proposed control strategy can significantly enhance the reliability of the turbine against blade-tower collision. Hence, it can be used as an alternative to tilting the rotor and blade, which brings in additional stress at the blade root and gear tooth.
- The modal analysis of the rotating blade shows significant improvement of the blade stiffness due to centrifugal force and Coriolis effect. The application of longitudinal stiffener with various constant tendon forces shows a considerable increase in blade stiffness. The Campbell diagram indicates that the applied tendon forces do not invoke resonance during its operational window. Moreover, this tendon force can be modified with the application of heat in an actual scenario to avoid the chance for resonance using a control algorithm.
- The sensitivity analysis of the blade stress with respect to diameter of the tendon shows that the stress level decreases in passive case which is further enhanced by the semi-active case. But, this may also increase the peak stress at the blade tip due to higher control force. In an actual scenario, the heating of the tendon can be limited to an optimal level to avoid the stress growth at the tip.
- Fatigue analysis of the blade shows remarkable improvement of fatigue life using longitudinal stiffening. This signifies the major contribution of this study where the stiffening action of the cable in longitudinal direction is utilised without applying any additional external force (i.e. tendon is in taut condition that develops force as the blade forms).
- The stress analyses under various design load cases reveal that stiffening of the blade shows significant improvement in terms of all performance parameters (i.e. peak, mean, RMS and peak-to-peak). The stiffened blade's performance with pitch angle is remarkable, especially peak-to-peak deformation, which is a major component in the fatigue damage.
- The short-term fatigue analysis of the blade under various design load cases indicates that the maximum damage accumulation during the design life occurs at the rated speed due to its higher frequency of occurrence. In this context, it may be noted that the stiffening strategy proposed here shows its best performance in reducing fatigue damage at this velocity. In other hand, the performance of this controller increases against larger deformation. The damage equivalent stress corresponding to each load case is evaluated, which is a key parameters for the fatigue design. The reliability analysis of the blade against fatigue limit state shows significant improvement when axial stiffener is used.

Based on the above discussion, it can be concluded that the proposed longitudinal stiffening using SMA tendon can control the blade response in both out-of-plane and in-plane direction offering significant reduction of peak, peak-to-peak, mean and RMS values. Its impact on the reliability and fatigue life of the blade are remarkable.

8.2 Future Work

The above section outlines the key contributions of this research work. It lays a promising proof-of-concept for horizontal axis wind turbine blade vibration control using SMA stiffener. Although various performance analysis conducted in this study are promising, the proposed stiffening strategy have the scope for further developments. With this in view, the following areas are identified for future work

1. The theoretical model shows impressive control output, this has to be validated with appropriate experiments. Also, the material properties of Shape Memory Alloy (SMA) can be optimized for enhancing the performance of longitudinally stiffened blade. For example, the performance in passive case can be improved with austenite finish temperature of the material less than ambient temperature,

so that it will undergo super-elastic behaviour. The SMA wires can be trained for different phase transition temperature to investigate its optimal performance.

2. The present study developed a spinning finite element model of SMA based stiffened blade, where the bending-torsion coupling is not addressed. Thus, the spinning Finite Element (FE) model of the blade can be modelled for dynamic coupling or/and elastic coupling. Moreover, the impact of the proposed stiffening strategy on blade flutter under unsteady aerodynamic load can be studied with this updated spinning FE model considering bending-torsion coupling.

3. Vibration control of wind turbine blade using SMA-based inerter may be studied. This option can harvest energy along with vibration control. Its performance under cyclostationary load, and impact on fatigue life and reliability can be investigated. Also, the application of SMA stiffener along with other controllers (i.e. pitch control, trailing edge flap) may enhance the performance of modern multi-megawatt turbine blade.

4. The spinning FE model developed in this study has only rotating blade, this required to be extend for complete wind turbine system, including drivetrain, tower, foundation in multi-body framework. With multi-body spinning FE model, coupled blade-tower interaction can be studied. Also, this high fidelity model can be extended with different types of foundation, e.g. monopile foundation with soil-structure interaction.

5. SMA materials can be used as a coating or layer in various parts of blade to improve their strength. It can be applied over the spar of the wind turbine blade to enhance fatigue life and reliability. Also, SMA wires can be embedded within the Glass Fiber Reinforced Plastic (GFRP) composite layer of the blade to improve its strength. It can be used to maintain the temperature over blade surface to avoid icing in extreme climate besides strength enhancement.

6. In this study, SMA tendon is used to stiffen the blade in longitudinal direction, which can be applied for transverse morphing of the blade. With this, the shape of airfoil can be adjusted to reduce the extreme load on the blade. Enhancing lift-drag ratio with the transverse morphing can improve the power production with reduced structural vibration.

7. Wind turbines are subjected to non-linear deformations, which is more prominent when the aerodynamic loads are non-stationary. Therefore, non-linear analysis of wind turbine with various uncertainties under non-stationary loading can be studied. Besides excitation uncertainties, modelling also has inherent uncertainties. For example, the drivetrain used in this study has witnessed lot of improvements over time. Also, the baseline controller has evolved to handle more complex situations. All these issues in the light of uncertainties need further investigation.

8. In this study, the performance of longitudinal stiffener is investigated using aerodynamic loads simulated by Blade Element Momentum (BEM) theory. A detailed performance analysis using Computational Fluid Dynamics (CFD) can be conducted using ANSYS or similar software. In this study the tendon can be modelled using phenomenological material model.

9. The application of the pitch controller to reduce blade vibration also affect power production. Therefore, the blade's pitch control and longitudinal stiffening may improve the power production with reduced blade vibration. This can be studied by implementing a baseline pitch controller along with the blade stiffening strategy.

Appendix A

DROM-System Matrices of Blade-Drivetrain-Tower assembly

The mass, damping and stiffness matrices of the combined blade-tower-drivetrain system is given by

$$M = \begin{bmatrix}
m_{21_x} & 0 & 0 & 0 & 0 & 0 & m_{11_x} & 0 & 0 & 0 & 0 & 0 & 0 & 0 & 0 & 0 \\
0 & m_{22_x} & 0 & 0 & 0 & 0 & m_{12_x} & 0 & 0 & 0 & 0 & 0 & 0 & 0 & 0 & 0 \\
0 & 0 & m_{21_x} & 0 & 0 & 0 & m_{11_x} & 0 & 0 & 0 & 0 & 0 & 0 & 0 & 0 & 0 \\
0 & 0 & 0 & m_{22_x} & 0 & 0 & m_{12_x} & 0 & 0 & 0 & 0 & 0 & 0 & 0 & 0 & 0 \\
0 & 0 & 0 & 0 & m_{21_x} & 0 & m_{11_x} & 0 & 0 & 0 & 0 & 0 & 0 & 0 & 0 & 0 \\
0 & 0 & 0 & 0 & 0 & m_{22_x} & m_{12_x} & 0 & 0 & 0 & 0 & 0 & 0 & 0 & 0 & 0 \\
m_{11_x} & m_{12_x} & m_{11_x} & m_{12_x} & m_{11_x} & m_{12_x} & m_{4x} & 0 & 0 & 0 & 0 & 0 & 0 & 0 & 0 & 0 \\
0 & 0 & 0 & 0 & 0 & 0 & 0 & m_{21_y} & 0 & 0 & 0 & 0 & 0 & m_{11}^1 & m_{0_1} & 0 \\
0 & 0 & 0 & 0 & 0 & 0 & 0 & 0 & m_{22_y} & 0 & 0 & 0 & 0 & m_{12}^1 & m_{0_2} & 0 \\
0 & 0 & 0 & 0 & 0 & 0 & 0 & 0 & 0 & m_{21_y} & 0 & 0 & 0 & m_{11}^2 & m_{0_1} & 0 \\
0 & 0 & 0 & 0 & 0 & 0 & 0 & 0 & 0 & 0 & m_{22_y} & 0 & 0 & m_{12}^2 & m_{0_2} & 0 \\
0 & 0 & 0 & 0 & 0 & 0 & 0 & 0 & 0 & 0 & 0 & m_{21_y} & 0 & m_{11}^3 & m_{0_1} & 0 \\
0 & 0 & 0 & 0 & 0 & 0 & 0 & 0 & 0 & 0 & 0 & 0 & m_{22_y} & m_{12}^3 & m_{0_2} & 0 \\
0 & 0 & 0 & 0 & 0 & 0 & 0 & m_{11}^1 & m_{12}^1 & m_{11}^2 & m_{12}^2 & m_{11}^3 & m_{12}^3 & m_{4y} & 0 & 0 \\
0 & 0 & 0 & 0 & 0 & 0 & 0 & m_{0_1} & m_{0_2} & m_{0_1} & m_{0_2} & m_{0_1} & m_{0_2} & 0 & J_r & 0 \\
0 & 0 & 0 & 0 & 0 & 0 & 0 & 0 & 0 & 0 & 0 & 0 & 0 & 0 & 0 & J_g
\end{bmatrix} \tag{A.1}$$

where $m_{1j_x} = \int_0^R \mu(r)\Phi_j^{b_x}\mathrm{dr}$; $m_{2j_x} = \int_0^R \mu(r)\Phi_j^{b_x\,2}\mathrm{dr}$; $m_{1j_y} = \int_0^R \mu(r)\Phi_j^{b_y}\mathrm{dr}$; $m_{2j_y} = \int_0^R \mu(r)\Phi_j^{b_y\,2}\mathrm{dr}$; $m_{4x} = m_{4y} = 3\int_0^R \mu(r)dr + M^s$; $m_{0_j} = \int_0^R r\mu(r)\Phi_{y_j}^b$; $m_{1j}^i = m_{1j_y}\cos\Psi_i$; $i = 1, 2, 3$ and $j = 1, 2$.

$$K_s = \begin{bmatrix}
K^1_{x,11} & K^1_{x,12} & 0 & 0 & 0 & 0 & 0 & K_{xy_1} & 0 & 0 & 0 & 0 & 0 & 0 & 0 & 0 \\
K^1_{x,21} & K^1_{x,22} & 0 & 0 & 0 & 0 & 0 & 0 & K_{xy_2} & 0 & 0 & 0 & 0 & 0 & 0 & 0 \\
0 & 0 & K^2_{x,11} & K^2_{x,12} & 0 & 0 & 0 & 0 & 0 & K_{xy_1} & 0 & 0 & 0 & 0 & 0 & 0 \\
0 & 0 & K^2_{x,21} & K^2_{x,22} & 0 & 0 & 0 & 0 & 0 & 0 & K_{xy_2} & 0 & 0 & 0 & 0 & 0 \\
0 & 0 & 0 & 0 & K^3_{x,11} & K^3_{x,12} & 0 & 0 & 0 & 0 & 0 & K_{xy_1} & 0 & 0 & 0 & 0 \\
0 & 0 & 0 & 0 & K^3_{x,21} & K^3_{x,22} & 0 & 0 & 0 & 0 & 0 & 0 & K_{xy_2} & 0 & 0 & 0 \\
0 & 0 & 0 & 0 & 0 & 0 & K_{tx} & 0 & 0 & 0 & 0 & 0 & 0 & 0 & 0 & 0 \\
K_{xy_1} & 0 & 0 & 0 & 0 & 0 & 0 & K^1_{y,11} & K^1_{y,12} & 0 & 0 & 0 & 0 & 0 & 0 & 0 \\
0 & K_{xy_2} & 0 & 0 & 0 & 0 & 0 & K^1_{y,21} & K^1_{y,22} & 0 & 0 & 0 & 0 & 0 & 0 & 0 \\
0 & 0 & K_{xy_1} & 0 & 0 & 0 & 0 & 0 & 0 & K^2_{y,11} & K^2_{y,12} & 0 & 0 & 0 & 0 & 0 \\
0 & 0 & 0 & K_{xy_2} & 0 & 0 & 0 & 0 & 0 & K^2_{y,21} & K^2_{y,22} & 0 & 0 & 0 & 0 & 0 \\
0 & 0 & 0 & 0 & K_{xy_1} & 0 & 0 & 0 & 0 & 0 & 0 & K^3_{y,11} & K^3_{y,12} & 0 & 0 & 0 \\
0 & 0 & 0 & 0 & 0 & K_{xy_2} & 0 & 0 & 0 & 0 & 0 & K^3_{y,21} & K^3_{y,22} & 0 & 0 & 0 \\
0 & 0 & 0 & 0 & 0 & 0 & 0 & K^1_{t,11} & K^1_{t,12} & K^2_{t,11} & K^2_{t,12} & K^3_{t,11} & K^3_{t,12} & K_{ty} & 0 & 0 \\
0 & 0 & 0 & 0 & 0 & 0 & 0 & 0 & 0 & 0 & 0 & 0 & 0 & 0 & k_0 & -\frac{k_0}{N} \\
0 & 0 & 0 & 0 & 0 & 0 & 0 & 0 & 0 & 0 & 0 & 0 & 0 & 0 & -\frac{k_0}{N} & \frac{k_0}{N^2}
\end{bmatrix} \tag{A.2}$$

where $K^i_{x,jj} = K_{e,jj,x} + K_{c,jj,x} + K_{g,jj,x}\cos\Psi_i + K_{T,jj,x}$; $K^i_{x,jk} = K_{c,jk,x} + K_{g,jk,x}\cos\Psi_i + K_{T,jk,x}$ for $j \neq k$; $K^i_{y,jj} = K_{e,jj,y} + K_{c,jj,y} - \Omega^2 m_{2j_y} + K_{g,jj,y}\cos\Psi_i + K_{T,jj,y}$; $K^i_{y,jk} = K_{c,jk,y} + K_{g,jk,y}\cos\Psi_i + K_{T,jk,y}$ for $j \neq k$; $K^i_{t,1j} = -\Omega^2 m_{1j_y}\cos\Psi_i$; $k = 1, 2$. In case of uncontrolled system, K can be obtained from K_s using the conditions $K_{T,jj,x} = K_{T,jk,x} = K_{T,jj,y} = K_{T,jj,y} = 0$.

$$C = \begin{bmatrix}
C_{bx_1} & 0 & 0 & 0 & 0 & 0 & 0 & 0 & 0 & 0 & 0 & 0 & 0 & 0 & 0 & 0 \\
0 & C_{bx_2} & 0 & 0 & 0 & 0 & 0 & 0 & 0 & 0 & 0 & 0 & 0 & 0 & 0 & 0 \\
0 & 0 & C_{bx_1} & 0 & 0 & 0 & 0 & 0 & 0 & 0 & 0 & 0 & 0 & 0 & 0 & 0 \\
0 & 0 & 0 & C_{bx_2} & 0 & 0 & 0 & 0 & 0 & 0 & 0 & 0 & 0 & 0 & 0 & 0 \\
0 & 0 & 0 & 0 & C_{bx_1} & 0 & 0 & 0 & 0 & 0 & 0 & 0 & 0 & 0 & 0 & 0 \\
0 & 0 & 0 & 0 & 0 & C_{bx_2} & 0 & 0 & 0 & 0 & 0 & 0 & 0 & 0 & 0 & 0 \\
0 & 0 & 0 & 0 & 0 & 0 & C_{tx} & 0 & 0 & 0 & 0 & 0 & 0 & 0 & 0 & 0 \\
0 & 0 & 0 & 0 & 0 & 0 & 0 & C_{by_1} & 0 & 0 & 0 & 0 & 0 & 0 & 0 & 0 \\
0 & 0 & 0 & 0 & 0 & 0 & 0 & 0 & C_{by_2} & 0 & 0 & 0 & 0 & 0 & 0 & 0 \\
0 & 0 & 0 & 0 & 0 & 0 & 0 & 0 & 0 & C_{by_1} & 0 & 0 & 0 & 0 & 0 & 0 \\
0 & 0 & 0 & 0 & 0 & 0 & 0 & 0 & 0 & 0 & C_{by_2} & 0 & 0 & 0 & 0 & 0 \\
0 & 0 & 0 & 0 & 0 & 0 & 0 & 0 & 0 & 0 & 0 & C_{by_1} & 0 & 0 & 0 & 0 \\
0 & 0 & 0 & 0 & 0 & 0 & 0 & 0 & 0 & 0 & 0 & 0 & C_{by_2} & 0 & 0 & 0 \\
0 & 0 & 0 & 0 & 0 & 0 & 0 & C^1_{11} & C^1_{12} & C^2_{11} & C^2_{12} & C^3_{11} & C^3_{12} & C_{ty} & 0 & 0 \\
0 & 0 & 0 & 0 & 0 & 0 & 0 & 0 & 0 & 0 & 0 & 0 & 0 & 0 & 0 & 0 \\
0 & 0 & 0 & 0 & 0 & 0 & 0 & 0 & 0 & 0 & 0 & 0 & 0 & 0 & 0 & 0
\end{bmatrix} \tag{A.3}$$

where $C^i_{1j} = -2\Omega m_{1j_y}\sin\Psi_i$. C_b and C_t denote the damping associated with the blades and tower, respectively.

Appendix B

Finite Element Matrices

B.1 Mass Matrix

The components of 12×12 element mass matrix in Eq. 6.21a after the integration is given by

$$
\begin{aligned}
M_e(1,1) &= \frac{l_e}{12}(3m_i + m_{i+1}) & M_e(1,7) &= \frac{l_e}{12}(m_i + m_{i+1}) \\
M_e(2,2) &= \frac{l_e}{35}(10m_i + 3m_{i+1}) & M_e(2,6) &= \frac{l_e^2}{420}(15m_i + 7m_{i+1}) \\
M_e(2,8) &= \frac{9l_e}{140}(m_i + m_{i+1}) & M_e(2,12) &= -\frac{l_e^2}{420}(7m_i + 6m_{i+1}) \\
M_e(3,3) &= \frac{l_e}{35}(10m_i + 3m_{i+1}) & M_e(3,5) &= -\frac{l_e^2}{420}(15m_i + 7m_{i+1}) \\
M_e(3,9) &= \frac{9l_e}{140}(m_i + m_{i+1}) & M_e(3,11) &= \frac{l_e^2}{420}(7m_i + 6m_{i+1}) \\
M_e(4,4) &= \frac{l_e}{12}\left(3I_{m_i} + I_{m_{i+1}}\right) & M_e(4,10) &= \frac{l_e}{12}\left(I_{m_i} + I_{m_{i+1}}\right) \\
M_e(5,5) &= \frac{l_e^3}{840}(5m_i + 3m_{i+1}) & M_e(5,9) &= -\frac{l_e^2}{420}(6m_i + 7m_{i+1}) \\
M_e(5,11) &= -\frac{l_e^3}{280}(m_i + m_{i+1}) & & \\
M_e(6,6) &= \frac{l_e^3}{840}(5m_i + 3m_{i+1}) & M_e(6,8) &= \frac{l_e^2}{420}(6m_i + 7m_{i+1}) \\
M_e(6,12) &= -\frac{l_e^3}{280}(m_i + m_{i+1}) & & \\
M_e(7,7) &= \frac{l_e}{12}(m_i + 3m_{i+1}) & & \\
M_e(8,8) &= \frac{l_e}{35}(3m_i + 10m_{i+1}) & M_e(8,12) &= -\frac{l_e^2}{420}(7m_i + 15m_{i+1}) \\
M_e(9,9) &= \frac{l_e}{35}(3m_i + 10m_{i+1}) & M_e(9,11) &= \frac{l_e^2}{420}(7m_i + 15m_{i+1}) \\
M_e(10,10) &= \frac{l_e}{12}\left(I_{m_i} + 3I_{m_{i+1}}\right) & & \\
M_e(11,11) &= \frac{l_e^3}{840}(3m_i + 5m_{i+1}) & & \\
M_e(12,12) &= \frac{l_e^3}{840}(3m_i + 5m_{i+1}) & &
\end{aligned}
$$

where I_{m_i} and $I_{m_{i+1}}$ are the polar mass moment of inertia, i.e.

$$I_{m_i} = m_i \frac{I_{p1}}{A_i} \qquad I_{m_{i+1}} = m_{i+1} \frac{I_{p2}}{A_{i+1}}$$

where I_p is the polar moment of inertia of the cross section area A. Subscript $i, i+1$ represent the root and tip of the i^{th} element respectively.

B.2 Elastic Stiffness Matrix

The components of 12×12 element elastic stiffness matrix in Eq. 6.24a after the integration is given by

$$K_{Ee}(1,1) = \frac{E(A_i + A_{i+1})}{2l_e} \qquad K_{Ee}(1,7) = \frac{-E(A_i + A_{i+1})}{2l_e}$$
$$K_{Ee}(2,2) = \frac{6E(I_{y_i} + I_{y_{i+1}})}{l_e^3} \qquad K_{Ee}(2,6) = \frac{2E(2I_{y_i} + I_{y_{i+1}})}{l_e^2}$$
$$K_{Ee}(2,8) = \frac{-6E(I_{y_i} + I_{y_{i+1}})}{l_e^3} \qquad K_{Ee}(2,12) = \frac{2E(I_{y_i} + 2I_{y_{i+1}})}{l_e^2}$$
$$K_{Ee}(3,3) = \frac{6E(I_{z_i} + I_{z_{i+1}})}{l_e^3} \qquad K_{Ee}(3,5) = \frac{-2E(2I_{z_i} + I_{z_{i+1}})}{l_e^2}$$
$$K_{Ee}(3,9) = \frac{-6E(I_{z_i} + I_{z_{i+1}})}{l_e^3} \qquad K_{Ee}(3,11) = \frac{-2E(I_{z_i} + 2I_{z_{i+1}})}{l_e^2}$$
$$K_{Ee}(4,4) = \frac{G\,(J_i + J_{i+1})}{2l_e} \qquad K_{Ee}(4,10) = \frac{-G\,(J_i + J_{i+1})}{2l_e}$$
$$K_{Ee}(5,5) = \frac{E(3I_{z_i} + I_{z_{i+1}})}{l_e} \qquad K_{Ee}(5,9) = \frac{2E(2I_{z_i} + I_{z_{i+1}})}{l_e^2}$$
$$K_{Ee}(5,11) = \frac{E(I_{z_i} + I_{z_{i+1}})}{l_e} \qquad K_{Ee}(6,6) = \frac{E(3I_{y_i} + I_{y_{i+1}})}{l_e}$$
$$K_{Ee}(6,8) = \frac{-2E(2I_{y_i} + I_{y_{i+1}})}{l_e^2} \qquad K_{Ee}(6,12) = \frac{E(I_{y_i} + I_{y_{i+1}})}{l_e}$$
$$K_{Ee}(7,7) = \frac{E(A_i + A_{i+1})}{2l_e} \qquad K_{Ee}(8,8) = \frac{6E(I_{y_i} + I_{y_{i+1}})}{l_e^3}$$
$$K_{Ee}(8,12) = \frac{-2E(I_{y_i} + 2I_{y_{i+1}})}{l_e^2} \qquad K_{Ee}(9,9) = \frac{6E(I_{z_i} + I_{z_{i+1}})}{l_e^3}$$
$$K_{Ee}(9,11) = \frac{2E(I_{z_i} + 2I_{z_{i+1}})}{l_e^2} \qquad K_{Ee}(10,10) = \frac{G\,(J_i + J_{i+1})}{2l_e}$$
$$K_{Ee}(11,11) = \frac{E(I_{z_i} + 3I_{z_{i+1}})}{l_e} \qquad K_{Ee}(12,12) = \frac{E(I_{y_i} + 3I_{y_{i+1}})}{l_e}$$

B.3 Spinning Stiffness Matrix

The components of 12×12 element spinning stiffness matrix in Eq. 6.21b after the integration is given by

$$K_{\Omega e}(1,1) = \frac{\Omega^2 a_{11} l_e}{12}(3m_i + m_{i+1}) \qquad K_{\Omega e}(1,2) = \frac{\Omega^2 a_{12} l_e}{60}(16m_i + 5m_{i+1})$$
$$K_{\Omega e}(1,3) = \frac{\Omega^2 a_{13} l_e}{60}(16m_i + 5m_{i+1}) \qquad K_{\Omega e}(1,5) = \frac{-\Omega^2 a_{13} l_e^2}{60}(2m_i + m_{i+1})$$
$$K_{\Omega e}(1,6) = \frac{\Omega^2 a_{12} l_e^2}{60}(2m_i + m_{i+1}) \qquad K_{\Omega e}(1,7) = \frac{\Omega^2 a_{11} l_e}{12}(m_i + m_{i+1})$$
$$K_{\Omega e}(1,8) = \frac{\Omega^2 a_{12} l_e}{60}(4m_i + 5m_{i+1}) \qquad K_{\Omega e}(1,9) = \frac{\Omega^2 a_{13} l_e}{60}(4m_i + 5m_{i+1})$$
$$K_{\Omega e}(1,11) = \frac{\Omega^2 a_{13} l_e^2}{60}(m_i + m_{i+1}) \qquad K_{\Omega e}(1,12) = \frac{-\Omega^2 a_{12} l_e^2}{60}(m_i + m_{i+1})$$

$$K_{\Omega e}(2,2) = \frac{\Omega^2 a_{22} l_e}{35}(10m_i + 3m_{i+1}) \qquad K_{\Omega e}(2,3) = \frac{\Omega^2 a_{23} l_e}{35}(10m_i + 3m_{i+1})$$
$$K_{\Omega e}(2,5) = \frac{-\Omega^2 a_{23} l_e^2}{420}(15m_i + 7m_{i+1}) \qquad K_{\Omega e}(2,6) = \frac{\Omega^2 a_{22} l_e^2}{420}(15m_i + 7m_{i+1})$$
$$K_{\Omega e}(2,7) = \frac{\Omega^2 a_{21} l_e}{60}(5m_i + 4m_{i+1}) \qquad K_{\Omega e}(2,8) = \frac{9\Omega^2 a_{22} l_e}{140}(m_i + m_{i+1})$$
$$K_{\Omega e}(2,9) = \frac{9\Omega^2 a_{23} l_e}{140}(m_i + m_{i+1}) \qquad K_{\Omega e}(2,11) = \frac{\Omega^2 a_{23} l_e^2}{420}(7m_i + 6m_{i+1})$$
$$K_{\Omega e}(2,12) = \frac{-\Omega^2 a_{22} l_e^2}{420}(7m_i + 6m_{i+1})$$
$$K_{\Omega e}(3,3) = \frac{\Omega^2 a_{33} l_e}{35}(10m_i + 3m_{i+1}) \qquad K_{\Omega e}(3,5) = \frac{-\Omega^2 a_{33} l_e^2}{420}(15m_i + 7m_{i+1})$$
$$K_{\Omega e}(3,6) = \frac{\Omega^2 a_{32} l_e^2}{420}(15m_i + 7m_{i+1}) \qquad K_{\Omega e}(3,7) = \frac{\Omega^2 a_{31} l_e}{60}(5m_i + 4m_{i+1})$$
$$K_{\Omega e}(3,8) = \frac{9\Omega^2 a_{32} l_e}{140}(m_i + m_{i+1}) \qquad K_{\Omega e}(3,9) = \frac{9\Omega^2 a_{33} l_e}{140}(m_i + m_{i+1})$$
$$K_{\Omega e}(3,11) = \frac{\Omega^2 a_{33} l_e^2}{420}(7m_i + 6m_{i+1}) \qquad K_{\Omega e}(3,12) = \frac{-\Omega^2 a_{32} l_e^2}{420}(7m_i + 6m_{i+1})$$
$$K_{\Omega e}(5,5) = \frac{\Omega^2 a_{33} l_e^3}{840}(5m_i + 3m_{i+1}) \qquad K_{\Omega e}(5,6) = \frac{-\Omega^2 a_{32} l_e^3}{840}(5m_i + 3m_{i+1})$$
$$K_{\Omega e}(5,7) = \frac{-\Omega^2 a_{31} l_e^2}{60}(m_i + m_{i+1}) \qquad K_{\Omega e}(5,8) = \frac{-\Omega^2 a_{32} l_e^2}{420}(6m_i + 7m_{i+1})$$
$$K_{\Omega e}(5,9) = \frac{-\Omega^2 a_{33} l_e^2}{420}(6m_i + 7m_{i+1}) \qquad K_{\Omega e}(5,11) = \frac{-\Omega^2 a_{33} l_e^3}{280}(m_i + m_{i+1})$$
$$K_{\Omega e}(5,12) = \frac{\Omega^2 a_{32} l_e^3}{280}(m_i + m_{i+1})$$
$$K_{\Omega e}(6,6) = \frac{\Omega^2 a_{22} l_e^3}{840}(5m_i + 3m_{i+1}) \qquad K_{\Omega e}(6,7) = \frac{\Omega^2 a_{21} l_e^2}{60}(m_i + m_{i+1})$$
$$K_{\Omega e}(6,8) = \frac{\Omega^2 a_{22} l_e^2}{420}(6m_i + 7m_{i+1}) \qquad K_{\Omega e}(6,9) = \frac{\Omega^2 a_{23} l_e^2}{420}(6m_i + 7m_{i+1})$$
$$K_{\Omega e}(6,11) = \frac{\Omega^2 a_{23} l_e^3}{280}(m_i + m_{i+1}) \qquad K_{\Omega e}(6,12) = \frac{-\Omega^2 a_{22} l_e^3}{280}(m_i + m_{i+1})$$
$$K_{\Omega e}(7,7) = \frac{\Omega^2 a_{11} l_e}{12}(m_i + 3m_{i+1}) \qquad K_{\Omega e}(7,8) = \frac{\Omega^2 a_{12} l_e}{60}(5m_i + 16m_{i+1})$$
$$K_{\Omega e}(7,9) = \frac{\Omega^2 a_{13} l_e}{60}(5m_i + 16m_{i+1}) \qquad K_{\Omega e}(7,11) = \frac{\Omega^2 a_{13} l_e^2}{60}(m_i + 2m_{i+1})$$
$$K_{\Omega e}(7,12) = \frac{-\Omega^2 a_{12} l_e^2}{60}(m_i + 2m_{i+1})$$
$$K_{\Omega e}(8,8) = \frac{\Omega^2 a_{22} l_e}{35}(3m_i + 10m_{i+1}) \qquad K_{\Omega e}(8,9) = \frac{\Omega^2 a_{23} l_e}{35}(3m_i + 10m_{i+1})$$
$$K_{\Omega e}(8,11) = \frac{\Omega^2 a_{23} l_e^2}{420}(7m_i + 15m_{i+1}) \qquad K_{\Omega e}(8,12) = \frac{-\Omega^2 a_{22} l_e^2}{420}(7m_i + 15m_{i+1})$$
$$K_{\Omega e}(9,9) = \frac{\Omega^2 a_{33} l_e}{35}(3m_i + 10m_{i+1}) \qquad K_{\Omega e}(9,11) = \frac{\Omega^2 a_{33} l_e^2}{420}(7m_i + 15m_{i+1})$$
$$K_{\Omega e}(9,12) = \frac{-\Omega^2 a_{32} l_e^2}{420}(7m_i + 15m_{i+1})$$
$$K_{\Omega e}(11,11) = \frac{\Omega^2 a_{33} l_e^3}{840}(3m_i + 5m_{i+1}) \qquad K_{\Omega e}(11,12) = \frac{-\Omega^2 a_{32} l_e^3}{840}(3m_i + 5m_{i+1})$$
$$K_{\Omega e}(12,12) = \frac{\Omega^2 a_{22} l_e^3}{840}(3m_i + 5m_{i+1})$$

B.4 Centrifugal Stiffness Matrix

The element centrifugal stiffness matrix in Eq. 6.24b is a 12×12 symmetric matrix after the integration, whose components are

$$
\begin{aligned}
K_{ce}(2,2) &= \frac{6F_{\Omega_i}}{5l_e} - \frac{3\Omega^2 a}{35}(5m_i + 2m_{i+1}) - \frac{\Omega^2 b l_e}{70}(7m_i + 5m_{i+1}) \\
K_{ce}(2,6) &= \frac{F_{\Omega_i}}{10} - \frac{\Omega^2 a l_e}{140}(9m_i + 5m_{i+1}) - \frac{\Omega^2 b l_e^2}{420}(8m_i + 7m_{i+1}) \\
K_{ce}(2,12) &= \frac{F_{\Omega_i}}{10} - \frac{\Omega^2 a l_e}{70}(m_i - m_{i+1}) + \frac{\Omega^2 b l_e^2}{420}(m_i + 5m_{i+1}) \\
K_{ce}(5,5) &= \frac{2F_{\Omega_i} l_e}{15} - \frac{\Omega^2 a l_e^2}{210}(5m_i + 2m_{i+1}) - \frac{\Omega^2 b l_e^3}{2520} l_e^2 (13m_i + 11m_{i+1}) \\
K_{ce}(5,11) &= \frac{-F_{\Omega_i} l_e}{30} + \frac{\Omega^2 a l_e^2}{420}(4m_i + 3m_{i+1}) + \frac{\Omega^2 b l_e^3}{2520} l_e^2 (7m_i + 11m_{i+1}) \\
K_{ce}(11,11) &= \frac{2F_{\Omega_i} l_e}{15} - \frac{\Omega^2 a l_e^2}{70}(4m_i + 3m_{i+1}) - \frac{\Omega^2 b l_e^2}{2520}(43m_i + 65m_{i+1})
\end{aligned}
$$

$$
\begin{aligned}
&K_{ce}(2,8) = -K_{ce}(2,2) \quad K_{ce}(3,3) = K_{ce}(2,2) \quad K_{ce}(3,5) = -K_{ce}(2,6) \\
&K_{ce}(3,9) = -K_{ce}(3,3) \quad K_{ce}(3,11) = -K_{ce}(2,12) \quad K_{ce}(5,9) = K_{ce}(2,6) \\
&K_{ce}(6,6) = K_{ce}(5,5) \quad K_{ce}(6,8) = -K_{ce}(2,6) \quad K_{ce}(6,12) = K_{ce}(5,11) \\
&K_{ce}(8,8) = K_{ce}(2,2) \quad K_{ce}(8,12) = -K_{ce}(2,12) \quad K_{ce}(9,9) = K_{ce}(2,2) \\
&K_{ce}(9,11) = K_{ce}(2,12) \quad K_{ce}(12,12) = K_{ce}(11,11)
\end{aligned}
$$

where F_{Ω_i} is the centrifugal force acting at the root of the element.

B.5 Gravitational Stiffness Matrix

The components of 12×12 element stiffness matrix due to gravitational force along longitudinal axis of the blade, in Eq. 6.24c after the integration is given by

$$
\begin{aligned}
K_{ge}(2,2) &= \frac{6F_{go}}{5l_e} + \frac{3gm_i}{14} + \frac{3gm_{i+1}}{35} & K_{ge}(2,6) &= \frac{F_{go}}{10} + \frac{9gl_e m_i}{280} + \frac{gl_e m_{i+1}}{56} \\
K_{ge}(2,12) &= \frac{F_{go}}{10} + \frac{gl_e m_i}{140} - \frac{gl_e m_{i+1}}{140} & K_{ge}(5,5) &= \frac{56F_{go}l_e}{420} + \frac{5gl_e m_i}{420} + \frac{2gl_e m_{i+1}}{420} \\
K_{ge}(5,11) &= -\frac{28F_{go}l_e}{840} + \frac{4gl_e m_i}{840} + \frac{3gl_e m_{i+1}}{840} & K_{ge}(11,11) &= \frac{56F_{go}l_e}{420} + \frac{12gl_e m_i}{420} + \frac{9gl_e m_{i+1}}{420}
\end{aligned}
$$

$$
\begin{aligned}
&K_{ge}(2,8) = -K_{ge}(2,2) \quad K_{ge}(3,3) = K_{ge}(2,2) \quad K_{ge}(3,5) = -K_{ge}(2,6) \\
&K_{ge}(3,9) = -K_{ge}(3,3) \quad K_{ge}(3,11) = -K_{ge}(2,12) \quad K_{ge}(5,9) = K_{ge}(2,6) \\
&K_{ge}(6,6) = K_{ge}(5,5) \quad K_{ge}(6,8) = -K_{ge}(2,6) \quad K_{ge}(6,12) = K_{ge}(5,11) \\
&K_{ge}(8,8) = K_{ge}(2,2) \quad K_{ge}(8,12) = -K_{ge}(2,12) \quad K_{ge}(9,9) = K_{ge}(2,2) \\
&K_{ge}(9,11) = K_{ge}(2,12) \quad K_{ge}(12,12) = K_{ge}(11,11)
\end{aligned}
$$

where F_{go} is the gravitational force acting at the root of the element.

B.6 Tendon Force Stiffness Matrix

The components of 12×12 element stiffness matrix due to tendon force in Eq. 6.24d after the integration is given by

$$K_{Te}(2,2) = \frac{6F_T}{5l_e} \qquad K_{Te}(2,6) = \frac{F_T}{10}$$
$$K_{Te}(5,5) = \frac{2F_T l_e}{15} \qquad K_{Te}(5,11) = \frac{-F_T l_e}{30}$$

$K_{Te}(2,8) = -K_{Te}(2,2)$ $K_{Te}(2,12) = K_{Te}(2,6)$ $K_{Te}(3,3) = K_{Te}(2,2)$ $K_{Te}(3,5) = -K_{Te}(2,6)$

$K_{Te}(3,9) = -K_{Te}(3,3)$ $K_{Te}(3,11) = -K_{Te}(2,6)$ $K_{Te}(5,9) = K_{Te}(2,6)$ $K_{Te}(6,6) = K_{Te}(5,5)$

$K_{Te}(6,8) = -K_{Te}(2,6)$ $K_{Te}(6,12) = K_{Te}(5,11)$ $K_{Te}(8,8) = K_{Te}(2,2)$ $K_{Te}(8,12) = -K_{Te}(2,6)$

$K_{Te}(9,9) = K_{Te}(2,2)$ $K_{Te}(9,11) = K_{Te}(2,6)$ $K_{Te}(11,11) = K_{Te}(5,5)$ $K_{Te}(12,12) = K_{Te}(5,5)$

B.7 Gyroscopic Damping Matrix

The components of 12×12 element gyroscopic damping matrix in Eq. 6.21c after the integration is given by

$$G_{\Omega e}(1,2) = \frac{\Omega b_1 l_e}{60}(16m_i + 5m_{i+1}) \qquad G_{\Omega e}(1,3) = \frac{\Omega b_2 l_e}{60}(16m_i + 5m_{i+1})$$
$$G_{\Omega e}(1,5) = \frac{-\Omega b_2 l_e^2}{60}(2m_i + m_{i+1}) \qquad G_{\Omega e}(1,6) = \frac{\Omega b_1 l_e^2}{60}(2m_i + m_{i+1})$$
$$G_{\Omega e}(1,8) = \frac{\Omega b_1 l_e}{60}(4m_i + 5m_{i+1}) \qquad G_{\Omega e}(1,9) = \frac{\Omega b_2 l_e}{60}(4m_i + 5m_{i+1})$$
$$G_{\Omega e}(1,11) = \frac{\Omega b_2 l_e^2}{60}(m_i + m_{i+1}) \qquad G_{\Omega e}(1,12) = \frac{-\Omega b_1 l_e^2}{60}(m_i + m_{i+1})$$
$$G_{\Omega e}(2,3) = \frac{\Omega b_3 l_e}{35}(10m_i + 3m_{i+1}) \qquad G_{\Omega e}(2,5) = \frac{-\Omega b_3 l_e^2}{420}(15m_i + 7m_{i+1})$$
$$G_{\Omega e}(2,7) = \frac{\Omega b_1 l_e}{60}(5m_i + 4m_{i+1}) \qquad G_{\Omega e}(2,9) = \frac{9\Omega b_3 l_e}{140}(m_i + m_{i+1})$$
$$G_{\Omega e}(2,11) = \frac{\Omega b_3 l_e^2}{420}(7m_i + 6m_{i+1})$$
$$G_{\Omega e}(3,6) = \frac{-\Omega b_3 l_e^2}{420}(15m_i + 7m_{i+1}) \qquad G_{\Omega e}(3,7) = \frac{-\Omega b_2 l_e}{60}(5m_i + 4m_{i+1})$$
$$G_{\Omega e}(3,8) = \frac{-9\Omega b_3 l_e}{140}(m_i + m_{i+1}) \qquad G_{\Omega e}(3,12) = \frac{\Omega b_3 l_e^2}{420}(7m_i + 6m_{i+1})$$
$$G_{\Omega e}(5,6) = \frac{\Omega b_3 l_e^3}{840}(5m_i + 3m_{i+1}) \qquad G_{\Omega e}(5,7) = \frac{\Omega b_2 l_e^2}{60}(m_i + m_{i+1})$$
$$G_{\Omega e}(5,8) = \frac{\Omega b_3 l_e^2}{420}(6m_i + 7m_{i+1}) \qquad G_{\Omega e}(5,12) = \frac{-\Omega b_3 l_e^3}{280}(m_i + m_{i+1})$$
$$G_{\Omega e}(6,7) = \frac{-\Omega b_1 l_e^2}{60}(m_i + m_{i+1}) \qquad G_{\Omega e}(6,9) = \frac{\Omega b_3 l_e^2}{420}(6m_i + 7m_{i+1})$$
$$G_{\Omega e}(6,11) = \frac{\Omega b_3 l_e^3}{280}(m_i + m_{i+1})$$
$$G_{\Omega e}(7,8) = \frac{\Omega b_1 l_e}{60}(5m_i + 16m_{i+1}) \qquad G_{\Omega e}(7,9) = \frac{\Omega b_2 l_e}{60}(5m_i + 16m_{i+1})$$
$$G_{\Omega e}(7,11) = \frac{\Omega b_2 l_e^2}{60}(m_i + 2m_{i+1}) \qquad G_{\Omega e}(7,12) = \frac{-\Omega b_1 l_e^2}{60}(m_i + 2m_{i+1})$$
$$G_{\Omega e}(8,9) = \frac{\Omega b_3 l_e}{35}(3m_i + 10m_{i+1}) \qquad G_{\Omega e}(8,11) = \frac{\Omega b_3 l_e^2}{420}(7m_i + 15m_{i+1})$$
$$G_{\Omega e}(9,12) = \frac{\Omega b_3 l_e^2}{420}(7m_i + 15m_{i+1})$$
$$G_{\Omega e}(11,12) = \frac{\Omega b_3 l_e^3}{840}(3m_i + 5m_{i+1})$$

References

[1] T. A. Shemmeri, Wind Turbines, Book Boon, 2010.

[2] H. M. Kojabadi, L. Chang, Wind Turbines, InTech, 2011.

[3] B. Fox, Wind power integration: connection and system operational aspects, Vol. 50, Iet, 2007.

[4] M. O. Hansen, Aerodynamics of wind turbines, Routledge, 2015.

[5] J. F. Manwell, J. G. McGowan, A. L. Rogers, Wind energy explained: theory, design and application, John Wiley and Sons, 2010.

[6] TheCapitol.Net, Energy: Wind, The History of Wind Energy, Electricity Generation from the Wind, Types of Wind Turbines, Wind Energy Potential, Offshore Wind Technology, Wind Power on Federal Land, Small Wind Turbines, Economic and Policy Issues, Tax Policy, Government Series,TheCapitol.Net, 2010.

[7] H. Pörtner, D. Roberts, V. Masson-Delmotte, P. Zhai, M. Tignor, E. Poloczanska, K. Mintenbeck, A. Alegría, M. Nicolai, A. Okem, J. Petzold, B. Rama, N. W. (eds.), Ipcc special report on the ocean and cryosphere in a changing climate, Tech. rep., In press (2019).

[8] W. Tong, Wind power generation and wind turbine design, WIT press, 2010.

[9] N. Veritas, Guidelines for design of wind turbines, Wind Energy Department, RisøNational Laboratory, 2002.

[10] P. J. Schubel, R. J. Crossley, Wind turbine blade design, Energies 5 (9) (2012) 3425–3449.

[11] A. Betz, Introduction to the theory of flow machines, Elsevier, 2014.

[12] M. Hazari, M. Mannan, S. Muyeen, A. Umemura, R. Takahashi, J. Tamura, Stability augmentation of a grid-connected wind farm by fuzzy-logic-controlled DFIG-based wind turbines, Applied Sciences 8 (1) (2017) 20.

[13] S. Muyeen, J. Tamura, T. Murata, Stability augmentation of a grid-connected wind farm, Springer Science and Business Media, 2008.

[14] Haliade-x offshore turbine, https://www.ge.com/renewableenergy/wind-energy/offshore-wind/haliade-x-offshore-turbine, [Accessed on 26-November-2020].

[15] NWTC Information Portal (IECWind), https://nwtc.nrel.gov/IECWind, [Last modified 28-September-2014 ; Accessed 01-April-2020].

[16] NWTC Information Portal (TurbSim), https://nwtc.nrel.gov/TurbSim, [Last modified 14-June-2016; Accessed 13-November-2019] (2008).

[17] B. J. Jonkman, TurbSim user's guide: Version 1.50, Tech. rep., National Renewable Energy Laboratory (NREL), Golden, CO (United States) (2009).

[18] I. E. Commission, et al., Iec 61400-1: Wind turbines part 1: Design requirements, International Electrotechnical Commission.

[19] IEC 61400-3, Wind turbines: Part 3: Design requirements for offshore wind turbines, International Electrotechnical Commission.

[20] R. W. Thresher, A. Wright, E. Hershberg, A computer analysis of wind turbine blade dynamic loads, Journal of solar energy engineering 108 (1) (1986) 17–25.

[21] A. Wright, M. Buhl, R. Thresher, Flap (force and loads analysis program) code development and validation, Tech. rep., Solar Energy Research Inst., Golden, CO (USA) (1988).

[22] NWTC information portal (AeroDyn), https://nwtc.nrel.gov/AeroDyn, [Last modified 25-May-2017; Accessed 04-December-2019].

[23] H. Glauert, The analysis of experimental results in the windmill brake and vortex ring states of an airscrew, HM Stationery Office, 1926.

[24] M. L. Buhl Jr, New empirical relationship between thrust coefficient and induction factor for the turbulent windmill state, Tech. rep., National Renewable Energy Lab.(NREL), Golden, CO (United States) (2005).

[25] Z. Du, M. Selig, A 3D stall-delay model for horizontal axis wind turbine performance prediction, in: 1998 ASME Wind Energy Symposium, 1998, p. 21.

[26] A. Eggers, K. Chaney, R. Digumarthi, An assessment of approximate modeling of aerodynamic loads on the UAE rotor, in: ASME 2003 Wind Energy Symposium, American Society of Mechanical Engineers Digital Collection, 2003, pp. 283–292.

[27] S. A. Ning, A simple solution method for the blade element momentum equations with guaranteed convergence, Wind Energy 17 (9) (2014) 1327–1345.

[28] M. Robinson, M. Hand, D. Simms, S. Schreck, Horizontal axis wind turbine aerodynamics: three-dimensional, unsteady, and separated flow influences, Tech. rep., National Renewable Energy Lab., Golden, CO (US) (1999).

[29] Y. Song, CFD simulation of the flow around NREL phase VI wind turbine.

[30] E. P. Duque, M. D. Burklund, W. Johnson, Navier-Stokes and comprehensive analysis performance predictions of the NREL phase VI experiment, J. Sol. Energy Eng. 125 (4) (2003) 457–467.

[31] N. Goundarzi, Computational fluid dynamics methods for wind turbines performance analysis, in: Advanced Wind Turbine Technology, Springer, 2018, pp. 47–58.

[32] W. J. Pierson Jr, L. Moskowitz, A proposed spectral form for fully developed wind seas based on the similarity theory of SA Kitaigorodskii, Journal of geophysical research 69 (24) (1964) 5181–5190.

[33] K. Hasselmann, T. Barnett, E. Bouws, H. Carlson, D. Cartwright, K. Enke, J. Ewing, H. Gienapp, D. Hasselmann, P. Kruseman, et al., Measurements of wind-wave growth and swell decay during the Joint North Sea Wave Project (JONSWAP), Ergänzungsheft 8-12.

[34] P. Jamieson, T. Camp, D. Quarton, Wind turbine design for offshore, in: Proceedings of the Offshore Wind Energy in Mediterranean and European Seas Conference, CEC/EWEA/IEA Sicily, 2000, pp. 405–414.

[35] A. Leung, T. Fung, Spinning finite elements, Journal of Sound and Vibration 125 (3) (1988) 523–537.

[36] A. Hansen, D. Laino, User's guide to the wind turbine dynamics computer programs YawDyn and AeroDyn for ADAMS version 11.0, Mech. Eng. Dept. University of Utah, Golden, Colorado.

[37] S. M. Larwood, Dynamic analysis tool development for advanced geometry wind turbine blades, Citeseer, 2009.

[38] L. Komzsik, A. Vollan, Computational techniques of rotor dynamics with the finite element method, CRC Press, 2012.

[39] D. I. Chortis, Structural Analysis of Composite Wind Turbine Blades: Nonlinear Mechanics and Finite Element Models with Material Damping, Vol. 1, Springer Science & Business Media, 2013.

[40] R. Ganguli, Finite Element Analysis of Rotating Beams, Springer, 2017.

[41] R. Ganguli, V. Panchore, The Rotating Beam Problem in Helicopter Dynamics, Springer, 2018.

[42] T. Burton, N. Jenkins, D. Sharpe, E. Bossanyi, Wind energy handbook, John Wiley and Sons, 2011.

[43] Z. Zhang, B. Basu, S. R. Nielsen, Tuned liquid column dampers for mitigation of edgewise vibrations in rotating wind turbine blades, Structural Control and Health Monitoring 22 (3) (2015) 500–517.

[44] Z. Zhang, S. R. Nielsen, B. Basu, J. Li, Nonlinear modeling of tuned liquid dampers (TLDs) in rotating wind turbine blades for damping edgewise vibrations, Journal of Fluids and Structures 59 (2015) 252–269.

[45] V. N. Dinh, B. Basu, S. Nagarajaiah, Semi-active control of vibrations of spar type floating offshore wind turbines, Smart Struct Syst 18 (4) (2016) 683–705.

[46] Y. K. Lin, G. Q. Cai, Probabilistic structural dynamics: advanced theory and applications, McGraw-Hill Inc.,US, 1995.

[47] W. A. Gardner, Cyclostationarity in communications and signal processing, Tech. rep., STATISTICAL SIGNAL PROCESSING INC YOUNTVILLE CA (1994).

[48] S. Holm, B. Josefson, J. DeMaré, T. Svensson, Prediction of fatigue life based on level crossings and a state variable, Fatigue and Fracture of Engineering Materials and Structures 18 (10) (1995) 1089–1100.

[49] A. McCormick, A. Nandi, Cyclostationarity in rotating machine vibrations, Mechanical systems and signal processing 12 (2) (1998) 225–242.

[50] W. A. Gardner, A. Napolitano, L. Paura, Cyclostationarity: Half a century of research, Signal processing 86 (4) (2006) 639–697.

[51] J. Antoni, F. Bonnardot, A. Raad, M. El Badaoui, Cyclostationary modelling of rotating machine vibration signals, Mechanical systems and signal processing 18 (6) (2004) 1285–1314.

[52] J. Antoni, Cyclostationarity by examples, Mechanical Systems and Signal Processing 23 (4) (2009) 987–1036.

[53] F. Chaari, M. Haddar, Modeling of gear transmissions dynamics in non-stationary conditions, in: Cyclostationarity: Theory and Methods, Springer, 2014, pp. 109–124.

[54] R. U. Maheswari, R. Umamaheswari, Trends in non-stationary signal processing techniques applied to vibration analysis of wind turbine drive train–a contemporary survey, Mechanical Systems and Signal Processing 85 (2017) 296–311.

[55] Z. Ma, Y. Liu, D. Wang, W. Teng, A. Kusiak, Cyclostationary analysis of a faulty bearing in the wind turbine, Journal of Solar Energy Engineering 139 (3) (2017) 031006.

[56] W. Teng, X. Ding, Y. Zhang, Y. Liu, Z. Ma, A. Kusiak, Application of cyclic coherence function to bearing fault detection in a wind turbine generator under electromagnetic vibration, Mechanical Systems and Signal Processing 87 (2017) 279–293.

[57] M. H. Hansen, Aeroelastic instability problems for wind turbines, Wind Energy: An International Journal for Progress and Applications in Wind Power Conversion Technology 10 (6) (2007) 551–577.

[58] K. Thomsen, J. T. Petersen, E. Nim, S. Øye, B. Petersen, A method for determination of damping for edgewise blade vibrations, Wind Energy: An International Journal for Progress and Applications in Wind Power Conversion Technology 3 (4) (2000) 233–246.

[59] V. Riziotis, S. Voutsinas, E. Politis, P. Chaviaropoulos, Aeroelastic stability of wind turbines: the problem, the methods and the issues, Wind Energy: An International Journal for Progress and Applications in Wind Power Conversion Technology 7 (4) (2004) 373–392.

[60] P. Murtagh, B. Basu, B. Broderick, Along-wind response of a wind turbine tower with blade coupling subjected to rotationally sampled wind loading, Engineering structures 27 (8) (2005) 1209–1219.

[61] P. Murtagh, A. Ghosh, B. Basu, B. Broderick, Passive control of wind turbine vibrations including blade/tower interaction and rotationally sampled turbulence, Wind Energy 11 (4) (2008) 305–317.

[62] S. Colwell, B. Basu, Tuned liquid column dampers in offshore wind turbines for structural control, Engineering Structures 31 (2) (2009) 358–368.

[63] M. A. Lackner, M. A. Rotea, Passive structural control of offshore wind turbines, Wind energy 14 (3) (2011) 373–388.

[64] M. A. Lackner, M. A. Rotea, Structural control of floating wind turbines, Mechatronics 21 (4) (2011) 704–719.

[65] B. Fitzgerald, B. Basu, Active tuned mass damper control of wind turbine nacelle/tower vibrations with damaged foundations, in: Key Engineering Materials, Vol. 569, Trans Tech Publ, 2013, pp. 660–667.

[66] Z. L. Zhang, J. B. Chen, J. Li, Theoretical study and experimental verification of vibration control of offshore wind turbines by a ball vibration absorber, Structure and Infrastructure Engineering 10 (8) (2014) 1087–1100.

[67] M. Rezaee, A. M. Aly, Vibration control in wind turbines for performance enhancement: A comparative study, Wind and Structures 22 (1).

[68] C. Sun, V. Jahangiri, Bi-directional vibration control of offshore wind turbines using a 3D pendulum tuned mass damper, Mechanical Systems and Signal Processing 105 (2018) 338–360.

[69] C. Anderson, H. Heerkes, R. Yemm, The use of blade-mounted dampers to eliminate edgewise stall vibration, in: EWEC-CONFERENCE-, 1999, pp. 207–211.

[70] C. Huang, J. Arrigan, S. Nagarajaiah, B. Basu, Semi-active algorithm for edgewise vibration control in floating wind turbine blades, in: Earth and Space 2010: Engineering, Science, Construction, and Operations in Challenging Environments, 2010, pp. 2097–2110.

[71] J. Arrigan, V. Pakrashi, B. Basu, S. Nagarajaiah, Control of flapwise vibrations in wind turbine blades using semi-active tuned mass dampers, Structural Control and Health Monitoring 18 (8) (2011) 840–851.

[72] J. Arrigan, C. Huang, A. Staino, B. Basu, S. Nagarajaiah, A frequency tracking semi-active algorithm for control of edgewise vibrations in wind turbine blades, Smart Structures and Systems 13 (2) (2014) 177–201.

[73] B. Fitzgerald, B. Basu, S. R. Nielsen, Active tuned mass dampers for control of in-plane vibrations of wind turbine blades, Structural Control and Health Monitoring 20 (12) (2013) 1377–1396.

[74] B. Fitzgerald, B. Basu, Cable connected active tuned mass dampers for control of in-plane vibrations of wind turbine blades, Journal of Sound and Vibration 333 (23) (2014) 5980–6004.

[75] Z. Zhang, J. Li, S. R. Nielsen, B. Basu, Mitigation of edgewise vibrations in wind turbine blades by means of roller dampers, Journal of Sound and Vibration 333 (21) (2014) 5283–5298.

[76] Z. Zhang, S. R. Nielsen, Edgewise vibration control of wind turbine blades using roller and liquid dampers, in: Journal of Physics: Conference Series, Vol. 524, IOP Publishing, 2014, p. 012037.

[77] B. Basu, Z. Zhang, S. R. Nielsen, Damping of edgewise vibration in wind turbine blades by means of circular liquid dampers, Wind Energy 19 (2) (2016) 213–226.

[78] J. K. Rice, M. Verhaegen, Robust and distributed control of a smart blade, Wind Energy: An International Journal for Progress and Applications in Wind Power Conversion Technology 13 (2-3) (2010) 103–116.

[79] S. Krenk, M. N. Svendsen, J. Høgsberg, Resonant vibration control of three-bladed wind turbine rotors, AIAA journal 50 (1) (2012) 148–161.

[80] A. Staino, B. Basu, S. R. Nielsen, Actuator control of edgewise vibrations in wind turbine blades, Journal of Sound and Vibration 331 (6) (2012) 1233–1256.

[81] A. Staino, B. Basu, Dynamics and control of vibrations in wind turbines with variable rotor speed, Engineering Structures 56 (2013) 58–67.

[82] A. Staino, B. Basu, Emerging trends in vibration control of wind turbines: a focus on a dual control strategy, Philosophical Transactions of the Royal Society A: Mathematical, Physical and Engineering Sciences 373 (2035) (2015) 20140069.

[83] C. Cong, Stochastic vibrations control of wind turbine blades based on wireless sensor, Wireless Personal Communications 102 (4) (2018) 3503–3515.

[84] Z. Zhang, B. Chen, S. R. Nielsen, Coupled-mode flutter of wind turbines and its suppression using torsional viscous damper, Procedia engineering 199 (2017) 3254–3259.

[85] B. Chen, Z. Zhang, X. Hua, S. R. Nielsen, B. Basu, Enhancement of flutter stability in wind turbines with a new type of passive damper of torsional rotation of blades, Journal of Wind Engineering and Industrial Aerodynamics 173 (2018) 171–179.

[86] A. Dixit, S. Suryanarayanan, Towards pitch-scheduled drive train damping in variable-speed, horizontal-axis large wind turbines, in: Proceedings of the 44$^{\text{th}}$ IEEE Conference on Decision and Control, IEEE, 2005, pp. 1295–1300.

[87] C. Van Dam, D. E. Berg, S. J. Johnson, Active load control techniques for wind turbines., Tech. rep., Sandia National Laboratories (2008).

[88] S. Rehman, M. Alam, L. M. Alhems, M. M. Rafique, et al., Horizontal axis wind turbine blade design methodologies for efficiency enhancementa review, Energies 11 (3) (2018) 506.

[89] E. Bossanyi, Wind turbine control for load reduction, Wind Energy: An International Journal for Progress and Applications in Wind Power Conversion Technology 6 (3) (2003) 229–244.

[90] E. Van der Hooft, P. Schaak, T. Van Engelen, et al., Wind turbine control algorithms, DOWEC project-DOWEC-F1W1-EH-03-094/0, Task-3 report.

[91] A. D. De Corcuera, A. Pujana-Arrese, J. M. Ezquerra, E. Segurola, J. Landaluze, h_∞ based control for load mitigation in wind turbines, Energies 5 (4) (2012) 938–967.

[92] P. Fleming, J. W. Wingerden, A. Wright, Comparing state-space multivariable controls to multi-siso controls for load reduction of drivetrain-coupled modes on wind turbines through field-testing, in: 50$^{\text{th}}$ AIAA Aerospace Sciences Meeting including the New Horizons Forum and Aerospace Exposition, 2012, p. 1152.

[93] P. Anderson, A. Bose, Stability simulation of wind turbine systems, IEEE transactions on power apparatus and systems (12) (1983) 3791–3795.

[94] M. A. Lackner, An investigation of variable power collective pitch control for load mitigation of floating offshore wind turbines, Wind Energy 16 (4) (2013) 519–528.

[95] E. A. Bossanyi, Individual blade pitch control for load reduction, Wind Energy: An International Journal for Progress and Applications in Wind Power Conversion Technology 6 (2) (2003) 119–128.

[96] A. Kusiak, W. Li, Z. Song, Dynamic control of wind turbines, Renewable energy 35 (2) (2010) 456–463.

[97] S. Zuo, Y. Song, L. Wang, Q. W. Song, Computationally inexpensive approach for pitch control of offshore wind turbine on barge floating platform, The Scientific World Journal 2013.

[98] Z. Zhang, S. R. Nielsen, F. Blaabjerg, D. Zhou, Dynamics and control of lateral tower vibrations in offshore wind turbines by means of active generator torque, Energies 7 (11) (2014) 7746–7772.

[99] R. Agarwala, P. I. Ro, Separated pitch control at tip: innovative blade design explorations for large MW wind turbine blades, Journal of Wind Energy 2015.

[100] V. Maldonado, J. Farnsworth, W. Gressick, M. Amitay, Active control of flow separation and structural vibrations of wind turbine blades, Wind Energy: An International Journal for Progress and Applications in Wind Power Conversion Technology 13 (2-3) (2010) 221–237.

[101] S. J. Johnson, J. P. Baker, C. Van Dam, D. Berg, An overview of active load control techniques for wind turbines with an emphasis on microtabs, Wind Energy: An International Journal for Progress and Applications in Wind Power Conversion Technology 13 (2-3) (2010) 239–253.

[102] M. A. Lackner, G. van Kuik, A comparison of smart rotor control approaches using trailing edge flaps and individual pitch control, Wind Energy: An International Journal for Progress and Applications in Wind Power Conversion Technology 13 (2-3) (2010) 117–134.

[103] C. L. Bottasso, A. Croce, F. Gualdoni, P. Montinari, Load mitigation for wind turbines by a passive aeroelastic device, Journal of Wind Engineering and Industrial Aerodynamics 148 (2016) 57–69.

[104] M. Zhang, B. Tan, J. Xu, Smart fatigue load control on the large-scale wind turbine blades using different sensing signals, Renewable Energy 87 (2016) 111–119.

[105] D. G. Wilson, D. E. Berg, D. W. Lobitz, J. R. Zayas, Optimized active aerodynamic blade control for load alleviation on large wind turbines, in: AWEA WINDPOWER 2008 Conference and Exhibition, Houston, TX, June, 2008, pp. 1–4.

[106] D. G. Wilson, D. E. Berg, M. F. Barone, J. C. Berg, B. R. Resor, D. W. Lobitz, Active aerodynamic blade control design for load reduction on large wind turbines, in: European Wind Energy Conference, Marseille, France, Vol. 26, 2009, pp. 643–678.

[107] G. Pechlivanoglou, J. Wagner, C. Nayeri, C. Paschereit, Active aerodynamic control of wind turbine blades with high deflection flexible flaps, in: 48$^{\text{th}}$ AIAA Aerospace Sciences Meeting Including the New Horizons Forum and Aerospace Exposition, 2010, p. 644.

[108] R. Nelson, T. Corke, H. Othman, M. Patel, S. Vasudevan, T. Ng, A smart wind turbine blade using distributed plasma actuators for improved performance, in: 46$^{\text{th}}$ AIAA Aerospace Sciences Meeting and Exhibit, 2008, p. 1312.

[109] F. O. Thomas, T. C. Corke, M. Iqbal, A. Kozlov, D. Schatzman, Optimization of dielectric barrier discharge plasma actuators for active aerodynamic flow control, AIAA journal 47 (9) (2009) 2169–2178.

[110] X. Lachenal, S. Daynes, P. M. Weaver, Review of morphing concepts and materials for wind turbine blade applications, Wind energy 16 (2) (2013) 283–307.

[111] D. E. Berg, D. G. Wilson, B. R. Resor, M. F. Barone, J. C. Berg, S. Kota, G. Ervin, Active aerodynamic blade load control impacts on utility-scale wind turbines., Tech. rep., Sandia National Lab.(SNL-NM), Albuquerque, NM (United States) (2009).

[112] M. Capuzzi, A. Pirrera, P. Weaver, A novel adaptive blade concept for large-scale wind turbines. part ii: Structural design and power performance, Energy 73 (2014) 25–32.

[113] M. Capuzzi, A. Pirrera, P. M. Weaver, A novel adaptive blade concept for large-scale wind turbines. part i: Aeroelastic behaviour, Energy 73 (2014) 15–24.

[114] M. Capuzzi, A. Pirrera, P. Weaver, Structural design of a novel aeroelastically tailored wind turbine blade, Thin-Walled Structures 95 (2015) 7–15.

[115] W. Wang, S. Caro, F. Bennis, O. R. Salinas Mejia, A simplified morphing blade for horizontal axis wind turbines, Journal of solar energy engineering 136 (1).

[116] W. Hu, I. Han, S. C. Park, D. H. Choi, Multi-objective structural optimization of a HAWT composite blade based on ultimate limit state analysis, Journal of mechanical science and technology 26 (1) (2012) 129–135.

[117] K. Cox, A. Echtermeyer, Structural design and analysis of a 10 MW wind turbine blade, Energy Procedia 24 (2012) 194–201.

[118] A. Dal Monte, M. R. Castelli, E. Benini, Multi-objective structural optimization of a HAWT composite blade, Composite Structures 106 (2013) 362–373.

[119] T. H. Cheng, M. Ren, Z. Z. Li, Y. D. Shen, Vibration and damping analysis of composite fiber reinforced wind blade with viscoelastic damping control, Advances in Materials Science and Engineering 2015.

[120] S. Hurlebaus, L. Gaul, Smart structure dynamics, Mechanical systems and signal processing 20 (2) (2006) 255–281.

[121] R. Jain, S. Majumder, B. Ghosh, S. Saha, Deflection control for piezoelectric actuator through voltage signal and its application in micromanipulation, Mechanical Systems and Signal Processing 62 (2015) 305–323.

[122] S. Pietrzko, Q. Mao, Control of structural sound radiation and vibration using shunt piezoelectric materials, Journal of System Design and Dynamics 5 (5) (2011) 752–764.

[123] Q. Mao, S. Pietrzko, Control of noise and structural vibration, Springer, 2013.

[124] M. M. Sajeer, A. Chakraborty, Optimal placement of piezoelectric patch for passive vibration control, in: 13th International Conference on Vibration Problems, 2017.

[125] M. M. Sajeer, A. Chakraborty, Optimal location of piezoelectric patch in passive vibration control, in: Advances in Rotor Dynamics, Control, and Structural Health Monitoring, Springer, 2020, pp. 579–591.

[126] Y. H. Qiao, J. Han, C. Y. Zhang, J. P. Chen, K. C. Yi, Finite element analysis and vibration suppression control of smart wind turbine blade, Applied Composite Materials 19 (3-4) (2012) 747–754.

[127] J. D. Tippmann, F. L. di Scalea, Vibration control experiments using piezoelectric transducers on a wind turbine blade, in: Sensors and Smart Structures Technologies for Civil, Mechanical, and Aerospace Systems 2013, Vol. 8692, International Society for Optics and Photonics, 2013, p. 86921H.

[128] T. Liu, Classical flutter and active control of wind turbine blade based on piezoelectric actuation, Shock and Vibration 2015.

[129] T. Liu, G. Liu, Vibration control of rotating piezo-composite blade beam with cus configuration based on optimal lqg controller, Journal of Vibroengineering 20 (1) (2018) 427–447.

[130] N. Pern, J. Jacob, R. Lebeau, Characterization of zero mass flux flow control for separation control of an adaptive airfoil, in: 3rd AIAA Flow Control Conference, 2006, p. 3032.

[131] S. Sarkar, A. Chakraborty, Optimal design of semiactive MR-TLCD for along-wind vibration control of horizontal axis wind turbine tower, Structural Control and Health Monitoring 25 (2) (2018) e2083.

[132] F. Bolat, S. Sivrioglu, Active control of a small-scale wind turbine blade containing magnetorheological fluid, Micromachines 9 (2) (2018) 80.

[133] J. Chen, C. Yuan, J. Li, Q. Xu, Semi-active fuzzy control of edgewise vibrations in wind turbine blades under extreme wind, Journal of Wind Engineering and Industrial Aerodynamics 147 (2015) 251–261.

[134] O. Ozbulut, C. Mir, M. Moroni, M. Sarrazin, P. Roschke, A fuzzy model of superelastic shape memory alloys for vibration control in civil engineering applications, Smart materials and structures 16 (3) (2007) 818.

[135] O. Ozbulut, S. Hurlebaus, R. Desroches, Seismic response control using shape memory alloys: a review, Journal of Intelligent Material Systems and Structures 22 (14) (2011) 1531–1549.

[136] E. Graesser, F. Cozzarelli, Shape-memory alloys as new materials for aseismic isolation, Journal of engineering mechanics 117 (11) (1991) 2590–2608.

[137] E. Graesser, F. Cozzarelli, A proposed three-dimensional constitutive model for shape memory alloys, Journal of Intelligent Material Systems and Structures 5 (1) (1994) 78–89.

[138] K. Wilde, P. Gardoni, Y. Fujino, Base isolation system with shape memory alloy device for elevated highway bridges, Engineering structures 22 (3) (2000) 222–229.

[139] F. Auricchio, Shape memory alloys: Applications, micromechanics, macromodelling and numerical simulations., PhD Dissertation, Department of Civil and Environmental Engineering, The University of California at Berkeley.

[140] C. Liang, C. Rogers, One-dimensional thermomechanical constitutive relations for shape memory materials, Journal of intelligent material systems and structures 8 (4) (1997) 285–302.

[141] T. Duerig, A. Pelton, D. Stockel, The use of superelasticity in medicine, Metall-Heidelberg 50 (9) (1996) 569–574.

[142] D. Mantovani, Shape memory alloys: Properties and biomedical applications, Jom 52 (10) (2000) 36–44.

[143] T. Yoneyama, S. Miyazaki, Shape memory alloys for biomedical applications, Elsevier, 2008.

[144] L. Petrini, F. Migliavacca, Biomedical applications of shape memory alloys, Journal of Metallurgy 2011.

[145] S. Saadat, J. Salichs, M. Noori, Z. Hou, H. Davoodi, I. Bar On, Y. Suzuki, A. Masuda, An overview of vibration and seismic applications of niti shape memory alloy, Smart materials and structures 11 (2) (2002) 218.

[146] L. Miková, S. Medvecká-Beňová, M. Kelemen, F. Trebuňa, I. Virgala, Application of shape memory alloy (SMA) as actuator, Metalurgija 54 (1) (2015) 169–172.

[147] W. Van Moorleghem, D. Otte, The use of shape memory alloys for fire protection, Butterworth-Heinemann, Oxford, 1990.

[148] D. J. Hartl, D. C. Lagoudas, Aerospace applications of shape memory alloys, Proceedings of the Institution of Mechanical Engineers, Part G: Journal of Aerospace Engineering 221 (4) (2007) 535–552.

[149] K. Dhanalakshmi, M. Umapathy, Active vibration control of SMA actuated structures using fast output sampling based sliding mode control, Instrumentation Science and Technology 36 (2) (2008) 180–193.

[150] M. M. Khan, D. C. Lagoudas, Modeling of shape memory alloy pseudoelastic spring elements using preisach model for passive vibration isolation, in: Smart Structures and Materials 2002: Modeling, Signal Processing, and Control, Vol. 4693, International Society for Optics and Photonics, 2002, pp. 336–347.

[151] S. B. Choi, C. C. Cheong, Vibration control of a flexible beam using shape memory alloy actuators, Journal of Guidance, Control, and Dynamics 19 (5) (1996) 1178–1180.

[152] M. Walber, S. Jose, A. Lima, C. Araujo, W. Valenzula, Measurement and control of deformation on a flexible beam using shape memory alloy, ABCM Symposium Series in Mechatronics 3 (2008) 535–542.

[153] A. R. Shahin, P. H. Meckl, J. D. Jones, Modeling of SMA tendons for active control of structures, Journal of Intelligent Material Systems and Structures 8 (1) (1997) 51–70.

[154] E. Choi, T. Nam, J. Oh, B. Cho, An isolation bearing for highway bridges using shape memory alloys, Materials Science and Engineering: A 438 (2006) 1081–1084.

[155] G. Song, N. Ma, H. N. Li, Applications of shape memory alloys in civil structures, Engineering structures 28 (9) (2006) 1266–1274.

[156] A. M. Sharabash, B. O. Andrawes, Application of shape memory alloy dampers in the seismic control of cable-stayed bridges, Engineering Structures 31 (2) (2009) 607–616.

[157] O. Ozbulut, P. Roschke, P. Lin, C. Loh, GA-based optimum design of a shape memory alloy device for seismic response mitigation, Smart Materials and Structures 19 (6) (2010) 065004.

[158] M. Küçük, N. S. Çetin, C. Emeksiz, Stress analysis of shape memory alloys used in wind turbine blade root connection, Energy Education Science and Technology Part A: Energy Science and Research 30 (2012) 667–676.

[159] S. Gur, S. K. Mishra, S. Chakraborty, Performance assessment of buildings isolated by shape-memory-alloy rubber bearing: Comparison with elastomeric bearing under near-fault earthquakes, Structural Control and Health Monitoring 21 (4) (2014) 449–465.

[160] S. Das, S. K. Mishra, Optimal performance of buildings isolated by shape-memory-alloy-rubber-bearing (SMARB) under random earthquakes, International Journal for Computational Methods in Engineering Science and Mechanics 15 (3) (2014) 265–276.

[161] S. Gur, S. K. Mishra, S. Chakraborty, Stochastic optimization of shape-memory-alloy rubber bearing (smarb) for isolating buildings against random earthquake, Structural Control and Health Monitoring 21 (9) (2014) 1222–1239.

[162] P. D. Mondal, A. D. Ghosh, S. Chakraborty, Control of underground blast induced building vibration by shape-memory-alloy rubber bearing (SMARB), Structural Control and Health Monitoring 24 (10) (2017) e1983.

[163] D. Exarchos, P. Dalla, I. Tragazikis, K. Dassios, N. Zafeiropoulos, M. Karabela, C. De Crescenzo, D. Karatza, D. Musmarra, S. Chianese, et al., Development and characterization of high performance shape memory alloy coatings for structural aerospace applications, Materials 11 (5) (2018) 832.

[164] A. Patriota, E. Fernandes, J. Silva, J. da Rocha Neto, Deformation closed-loop control of a flexible beam by means of a shape memory alloy, in: 2018 IEEE International Instrumentation and Measurement Technology Conference (I2MTC), IEEE, 2018, pp. 1–6.

[165] P. Haghdoust, S. Cinquemani, A. L. Conte, Preliminary studies on SMA embedded wind turbine blades for passive control of vibration, in: Active and Passive Smart Structures and Integrated Systems XII, Vol. 10595, International Society for Optics and Photonics, 2018, p. 105953B.

[166] D. T. R. Pasala, S. Nagarajaiah, Adaptive-length pendulum smart tuned mass damper using shape-memory-alloy wire for tuning period in real time, Smart Structures and Systems 13 (2) (2014) 203.

[167] M. T. Contreras, D. T. R. Pasala, S. Nagarajaiah, Adaptive length SMA pendulum smart tuned mass damper performance in the presence of real time primary system stiffness change, Smart Structures and Systems 13 (2) (2014) 219–233.

[168] S. B. Kumbhar, S. Chavan, S. Gawade, Adaptive tuned vibration absorber based on magnetorheological elastomer-shape memory alloy composite, Mechanical Systems and Signal Processing 100 (2018) 208–223.

[169] S. K. Mouleeswaran, Y. Mani, P. Keerthivasan, J. Veeraragu, Vibration control of small horizontal axis wind turbine blade with shape memory alloy, SMART STRUCTURES AND SYSTEMS 21 (3) (2018) 257–262.

[170] V. Jagadeesh, M. Yuvaraja, A. Chandhru, P. Viswanathan, et al., Investigations on vibration characteristics of SMA embedded horizontal axis wind turbine blade, in: IOP Conference Series: Materials Science and Engineering, Vol. 310 (1), IOP Publishing, 2018, p. 012067.

[171] P. R. Greaves, R. G. Dominy, G. L. Ingram, H. Long, R. Court, Evaluation of dual-axis fatigue testing of large wind turbine blades, Proceedings of the Institution of Mechanical Engineers, Part C: Journal of Mechanical Engineering Science 226 (7) (2012) 1693–1704.

[172] J.-S. Chou, C.-K. Chiu, I.-K. Huang, K.-N. Chi, Failure analysis of wind turbine blade under critical wind loads, Engineering Failure Analysis 27 (2013) 99–118.

[173] N. Dervilis, M. Choi, S. Taylor, R. Barthorpe, G. Park, C. Farrar, K. Worden, On damage diagnosis for a wind turbine blade using pattern recognition, Journal of sound and vibration 333 (6) (2014) 1833–1850.

[174] H. G. Lee, M. G. Kang, J. Park, Fatigue failure of a composite wind turbine blade at its root end, Composite Structures 133 (2015) 878–885.

[175] P. U. Haselbach, R. D. Bitsche, K. Branner, The effect of delaminations on local buckling in wind turbine blades, Renewable Energy 85 (2016) 295–305.

[176] C. Zhang, H. P. Chen, T. L. Huang, Fatigue damage assessment of wind turbine composite blades using corrected blade element momentum theory, Measurement 129 (2018) 102–111.

[177] L. Tenghiri, Y. Khalil, F. Abdi, A. Bentamy, Structural design and analysis of a small wind turbine blade using simple load model, FAST-MLife codes, and ANSYS nCode DesignLife, Wind Engineering (2019) 0309524X19882430.

[178] B. Fitzgerald, S. Sarkar, A. Staino, Improved reliability of wind turbine towers with active tuned mass dampers (ATMDs), Journal of Sound and Vibration 419 (2018) 103–122.

[179] S. Sarkar, B. Fitzgerald, B. Basu, A. Chakraborty, Magneto-rheological tuned liquid column dampers to improve reliability of wind turbine towers, in: 13$^{\text{th}}$ International Conference on Vibration Problems, International Conference on Vibration Problems, 2017.

[180] N. K. Dimitrov, Structural reliability of wind turbine blades: Design methods and evaluation.

[181] W. Tao, B. Basu, J. Li, Reliability analysis of active tendon-controlled wind turbines by a computationally efficient wavelet-based probability density evolution method, Structural Control and Health Monitoring 25 (3) (2018) e2078.

[182] Z. Jiang, W. Hu, W. Dong, Z. Gao, Z. Ren, Structural reliability analysis of wind turbines: A review, Energies 10 (12) (2017) 2099.

[183] W. Hu, Reliability-based design optimization of wind turbine systems, in: Advanced Wind Turbine Technology, Springer, 2018, pp. 1–45.

[184] L. Liu, H. Bian, Z. Du, C. Xiao, Y. Guo, W. Jin, Reliability analysis of blade of the offshore wind turbine supported by the floating foundation, Composite Structures 211 (2019) 287–300.

[185] Y. Wang, Lighting analysis of wind turbines, in: Advanced Wind Turbine Technology, Springer, 2018, pp. 143–173.

[186] I. IEC 61400-24., Wind turbine generator systems–part 24: Lightning protection for wind turbines.

[187] Wind farm turbines wear sooner than expected, https://www.telegraph.co.uk/news/earth/energy/windpower/9770837/Wind-farm-turbines-wear-sooner-than-expected-says-study.html, [Accessed on 10-October-2019].

[188] G. Hayman, M. Buhl Jr, Mlife users guide for version 1.00, National Renewable Energy Laboratory, Golden, CO 74 (75) (2012) 112.

[189] G. Hayman, Mlife theory manual for version 1.00, National Renewable Energy Laboratory, Golden, CO 74 (75) (2012) 106.

[190] P.-C. Ma, Y. Zhang, Perspectives of carbon nanotubes/polymer nanocomposites for wind blade materials, Renewable and Sustainable Energy Reviews 30 (2014) 651–660. doi:10.1016/j.rser.2013.11.008.

[191] E. Simley, L. Pao, N. Kelley, B. Jonkman, R. Frehlich, Lidar wind speed measurements of evolving wind fields, in: 50th AIAA Aerospace Sciences Meeting including the New Horizons Forum and Aerospace Exposition, 2012, p. 656.

[192] J. D. Holmes, Wind loading of structures, CRC press, 2018.

[193] C. G. Justus, Winds and wind system performance, Franklin Institute Press, Philadelphia, PA.

[194] J. Counihan, Adiabatic atmospheric boundary layers: a review and analysis of data from the period 1880–1972, Atmospheric Environment (1967) 9 (10) (1975) 871–905.

[195] Global modeling and assimilation office (GMAO), MERRA-2, http://www.soda-pro.com/web-services/meteo-data/merra, [Accessed on 12-July-2019] (2015).

[196] G. K. Gugliani, A. Sarkar, C. Ley, V. Matsagar, Identification of optimum wind turbine parameters for varying wind climates using a novel month-based turbine performance index, Renewable Energy 171 (2021) 902–914. doi:10.1016/j.renene.2021.02.141.
URL https://doi.org/10.1016%2Fj.renene.2021.02.141

[197] O. K. G. Tietjens, L. Prandtl, Applied hydro-and aeromechanics: based on lectures of L. Prandtl, Vol. 2, Courier Corporation, 1957.

[198] M. McWilliam, C. Crawford, The behavior of fixed point iteration and newton-raphson methods in solving the blade element momentum equations, Wind Engineering 35 (1) (2011) 17–31. doi:10.1260/0309-524x.35.1.17.
URL https://doi.org/10.1260%2F0309-524x.35.1.17

[199] I. Masters, J. C. Chapman, M. R. Willis, J. A. C. Orme, A robust blade element momentum theory model for tidal stream turbines including tip and hub loss corrections, Journal of Marine Engineering & Technology 10 (1) (2011) 25–35. doi:10.1080/20464177.2011.11020241.
URL https://doi.org/10.1080%2F20464177.2011.11020241

[200] Z. Zhang, Passive and active vibration control of renewable energy structures, Ph.D. thesis, PhD thesis, Aalborg University, Denmark (2015).

[201] J. Jonkman, S. Butterfield, W. Musial, G. Scott, Definition of a 5 MW reference wind turbine for offshore system development, Tech. rep. (2009).

[202] O. Faltinsen, Sea loads on ships and offshore structures, Vol. 1, Cambridge university press, 1993.

[203] R. Shirzadeh, C. Devriendt, M. A. Bidakhvidi, P. Guillaume, Experimental and computational damping estimation of an offshore wind turbine on a monopile foundation, Journal of Wind Engineering and Industrial Aerodynamics 120 (2013) 96–106.

[204] P. Gujer, Overall damping for piled offshore support structures, GL RC Guideline for the Certification of Offshore Wind Turbines, Edition.

[205] M. F. Cook, J. K. Vandiver, et al., Measured and predicted dynamic response of a single pile platform to random wave excitation, in: Offshore Technology Conference, Offshore Technology Conference, 1982.

[206] N. J. Tarp-Johansen, C. Mørch, L. Andersen, E. D. Christensen, S. T. Frandsen, Comparing sources of damping of cross-wind motion, in: The European Offshore Wind Conference and Exhibition, The European Wind Energy Association, 2009.

[207] C. Chen, P. Duffour, Modelling damping sources in monopile-supported offshore wind turbines, Wind Energy 21 (11) (2018) 1121–1140.

[208] G. Bir, User's guide to bmodes (software for computing rotating beam-coupled modes), Tech. rep., National Renewable Energy Lab.(NREL), Golden, CO (United States) (2005).

[209] NWTC Information Portal (FAST v8), https://nwtc.nrel.gov/FAST8, [Last modified 04-January-2018; Accessed 04-December-2019].

[210] A. Rao, A. R. Srinivasa, J. N. Reddy, Design of shape memory alloy (SMA) actuators, Vol. 3, Springer, 2015. doi:10.1007/978-3-319-03188-0.

[211] T. L. Bergman, A. Lavine, F. P. Incropera, D. P. Dewitt, Fundamentals of heat and mass transfer, John Wiley and Sons New York, 2017.

[212] DNVGL-ST-0376, Rotor blades for wind turbines.

[213] Y. Chan, Wavelet basics, Springer Science and Business Media, 1994.

[214] B. Basu, V. K. Gupta, Seismic response of sdof systems by wavelet modeling of nonstationary processes, Journal of Engineering Mechanics 124 (10) (1998) 1142–1150.

[215] B. Fitzgerald, A. Staino, B. Basu, Wavelet-based individual blade pitch control for vibration control of wind turbine blades, Structural Control and Health Monitoring 26 (1) (2019) e2284.

[216] S. Sarkar, L. Chen, B. Fitzgerald, B. Basu, Multi-resolution wavelet pitch controller for spar-type floating offshore wind turbines including wave-current interactions, Journal of Sound and Vibration 470 (2020) 115170.

[217] L. D. Lutes, S. Sarkani, Random vibrations: analysis of structural and mechanical systems, Butterworth-Heinemann, 2004.

[218] J. M. Jonkman, M. L. Buhl Jr, et al., FAST users guide, Tech. rep. (2005).

[219] M. Harris, M. Hand, A. Wright, Lidar for turbine control, National Renewable Energy Laboratory, Golden, CO, Report No. NREL/TP-500-39154.

[220] J. N. Reddy, An introduction to the finite element method, McGraw-Hill Mechanical Engineering, 1993.

[221] T. R. Chandrupatla, A. D. Belegundu, T. Ramesh, C. Ray, Introduction to finite elements in engineering, Vol. 10, Prentice Hall Upper Saddle River, NJ, 2002.

[222] K. J. Bathe, Finite element procedures, PHI Learning Private Limited, Delhi, India, 2006.

[223] B. R. Resor, Definition of a 5 MW/61.5 m wind turbine blade reference model, Albuquerque, New Mexico, USA, Sandia National Laboratories, SAND2013-2569 2013.

[224] The MathWorks Inc, version 9.6, Ordinary Differential Equation Toolbox, Natick, Massachusetts (2019).

[225] S. D. Downing, D. Socie, Simple rainflow counting algorithms, International journal of fatigue 4 (1) (1982) 31–40.

[226] J. Goodman, Mechanics applied to engineering, Longmans, Green, 1918.

[227] J. Mandell, D. Samborsky, DOE/MSU composite material fatigue database: Test methods, materials, and analysis, Tech. rep. (dec 1997). doi:10.2172/578635.
URL https://doi.org/10.2172%2F578635

[228] J. A. Epaarachchi, P. D. Clausen, An empirical model for fatigue behavior prediction of glass fibre-reinforced plastic composites for various stress ratios and test frequencies, Composites Part A: Applied science and manufacturing 34 (4) (2003) 313–326.

[229] R. Borrmann, Structural design of a wood-CFRP wind turbine blade model, Tech. rep., Wind Energy Technology Institute (2016).

[230] T. Fischer, W. De Vries, B. Schmidt, UpWind design basis (WP4: Offshore foundations and support structures), Upwind.

Index